DEVELOPMENT OF DUCTILE IRONS FOR HIGH-TEMPERATURE APPLICATIONS: CHARACTERIZATION IN THE AS-CAST AND OXIDIZED STATES

by

Carl Rudolph Cvetnic, B. Eng, Ryerson University, 2002

A Thesis
presented to Ryerson University
in partial fulfillment of the
requirement for the degree of

Masters of Applied Science

In the program of
Mechanical Engineering

Toronto, Ontario, Canada, 2004

AUTHOR'S DECLARATION

I hereby declare that I am the sole author of this thesis.

I authorize Ryerson University to lend this thesis to other institutions or individuals for the purpose of scholarly research.

Carl R. Cvetnic

I further authorize Ryerson University to reproduce this thesis by photocopying or by other means, in total or in part, at the request of other institutions or individuals for the purpose of scholarly research.

Carl R. Cvetnic

BORROWER'S PAGE

Name (last, first)	**Address**	**Date** (day/month/year)

ABSTRACT

Development of Ductile Irons for
High-Temperature
Applications:
Characterization in the As-Cast and Oxidized States

© Carl Rudolph Cvetnic, 2004

Masters of Applied Science

In the program of
Mechanical Engineering

Toronto, Ontario, Canada, 2004

Ductile iron alloyed with molybdenum and different levels of aluminum and silicon was cast to determine the proper combination of elements to increase the temperature range of operation. Four alloys containing 1.5wt.% molybdenum and different combinations of aluminum and silicon (i.e., 3.5Si-2.0Al, 3.5Si-3.0Al, 4.5Si-2.0Al and 4.5Si-3.0Al) were cast at 1350, 1400 and 1450°C into step blocks. The effects of alloy chemistry, pouring temperature and casting thickness in the as-cast and oxidized conditions were studied. Results from the as-cast condition show that graphite morphology (i.e., size, count and sphericity) improved with lower Si/Al ratios and intermediate pouring temperatures. Higher silicon and lower aluminum contents accompanied by intermediate pouring temperatures reduced the onset of surface and sub-surface defects. Results from the oxidized condition show that maximum oxidation resistance was achieved in alloys containing higher aluminum and silicon contents. This also increased the critical α-ferrite to γ-austenite phase transformation temperature range.

RÉSUMÉ

Développement de fontes ductiles pour des
applications à
haute température:
étude d'échantillons moulés oxydés et non oxydés

© Carl Rudolph Cvetnic, 2004

Maîtrise en science appliquée

Dans le programme du
Génie mécanique

Toronto, Ontario, Canada, 2004

Une fonte ductile, alliée avec du molybdène et différentes quantités d'aluminium et de silicium a été fondue et mise en forme pour déterminer la composition chimique optimale permettant d'augmenter la température d'utilisation. Quatre alliages contenant 1,5% en masse de molybdène et différentes combinaisons de concentrations d'aluminium et de silicium (3,5Si-2,0Al; 3,5Si-3,0Al; 4,5Si-2,0Al; 4,5Si-3,0Al) ont été coulés dans un moule en forme d'escalier à 1350°C, 1400°C et 1450°C. Les effets de la composition chimique, de la température de coulée et de l'épaisseur de l'échantillon moulé ont été étudiés sur des échantillons oxydés et non oxydés. L'analyse des échantillons non oxydés a montré que la morphologie des nodules de graphite (taille, nombre et sphéricité) est meilleure avec des ratios Si/Al faibles et des températures de coulée intermédiaires. Pour des températures de coulée intermédiaires, des concentrations de silicium élevées et d'aluminium faibles conduisent à une réduction des défauts à la surface et à l'intérieur de l'échantillon. Les résultats obtenus avec les échantillons oxydés montrent que la résistance à l'oxydation est maximale pour les alliages contenant de fortes concentrations en aluminium et en silicium. Ces conditions permettent également d'augmenter la température de changement de phase des α-ferrite en γ-austénite.

ACKNOWLEDGEMENTS

The author would like to take this opportunity to express his sincerest gratitude and appreciation to Dr. C. Ravindran for his time, wisdom, guidance, encouragement, motivation and advice.

The author would like to acknowledge Dr. A. McLean of the University of Toronto for his invaluable discussions, advice and support.

The author would like to express his gratitude and appreciation to Mr. Alan Machin for his continued support, advice, motivation and many discussions.

The author is grateful to Materials Manufacturing Ontario (MMO) and in particular to Mr. Harvey Pellegrini and Mr. Frank de Lint for initial financial support.

The author would like to thank Wescast Industries Inc., in particular Dr. R. Perrin, Dr. G. Burger and Dr. Gangjun Liao. Their initiative and collaboration inspired this study and will hopefully lead to future cooperative research projects.

Special consideration and appreciation is given to Dr. Y. Yang and Dr. R. Roy of the University of Toronto and Mr. Tom Pang for their invaluable discussions. The author would also like to thank Mr. Joseph Amankrah for his technical assistance.

The author wishes to thank Ms. Amandine Salles, Mr. Lukas Bichler, Mr. Alex Androus, Mr. Uttam Jagoo and Mr. Nitin Dhingra for their support in the laboratory and discussions. The author also wishes to thank Mr. Rich Pulcini and Mr. John Roith for their assistance.

Finally, the author would like to express heartfelt gratitude to his family, in particular to his parents and sister. Their patience, spontaneous support and prayers led to the successful completion of this thesis.

Dedicated to my Family and to the memory of Karol Cvetnic

TABLE of CONTENTS

LIST of TABLES

LIST of FIGURES

NOMENCLATURE

Symbols		Units
A	Original surface area	mm^2
C	Mass change per unit area	mg/mm^2
dC	Change in the concentration gradient	kg/m^3
dt	Change in time	
dW	Change in oxygen quantity or change in scale weight	mg
dx	Change in distance	m
dy	Change in oxide scale thickness	μm
D	Self-diffusion coefficient	m^2/s
D_o	Frequency factor	m^2/s
$\Delta G°$	Free energy of formation	J
H	Oxide scale thickness according to Pilling and Bedworth	μm
$\Delta H°$	Standard enthalpy change	J
J	Diffusion flux	kg/m^2-s
k_o	Frequency factor constant for parabolic rate constant	m^2/s
k_{PB}	Parabolic rate constant according to Pilling and Bedworth	mg^2/cm^4-s
k_t	Parabolic rate constant according to Tammann	cm^2/s
M_{metal}	Molecular weight of the metal	g/mol
M_{oxide}	Molecular weight of the oxide	g/mol
p	Proportionality constant according to Tammann	cm^2/s
p_{O_2}	Oxygen pressure	1 atmosphere
Q	Activation energy for diffusion	J/mol
R	Gas constant	8.314 J/mol-K
$\Delta S°$	Standard entropy change	J/K
t	Time	
t_f	Final time after mould is poured	
t_o	Initial time at tap out	
T	Temperature	

W_{PB}	Weight gain per unit area according to Pilling and Bedworth	mg/mm^2
W_F	Final mass	mg
W_O	Original mass	mg
y	Oxide scale thickness according to Tammann	μm

Greek Letters

α	Ferrite phase	
α_{exp}	Coefficient of thermal expansion	
ε	Aluminum carbide phase	
γ	Austenite phase	
ρ_{metal}	Density of the metal	g/cm^3
ρ_{oxide}	Density of the oxide	g/cm^3

Element Abbreviations

H	Hydrogen
Be	Beryllium
B	Boron
C	Carbon
N	Nitrogen
O	Oxygen
Mg	Magnesium
Al	Aluminum
Si	Silicon
P	Phosphorus
S	Sulphur
Ca	Calcium
Ti	Titanium
V	Vanadium
Cr	Chromium

Fe	Iron
Ni	Nickel
Cu	Copper
As	Arsenic
Sr	Strontium
Y	Yttrium
Zr	Zirconium
Nb	Niobium
Mo	Molybdenum
Sb	Antimony
Te	Tellurium
Ba	Barium
La	Lanthanum
Ce	Cerium
Pr	Praseodymium
Nd	Neodymium
Pb	Lead
Bi	Bismuth

Compound Abbreviations

Fe_3C	Cementite
$MgO{\cdot}SiO_2$	Enstatite
$2FeO{\cdot}SiO_2$	Fayalite
Mg_2SiO_4	Forsterite
Fe_2O_3	Haematite
Fe_3O_4	Magnetite
FeO	Wüstite

Abbreviations

ASTM	American Society for Testing and Materials
BCC	Body-Centered Cubic
CAD	Computer Aided Design
CE	Carbon Equivalent
CEL	Carbon Equivalent Liquidus
DAS	Data Acquisition System
EDS	Energy Dispersive Spectrometry
FCC	Face-Centered Cubic
MCA	Moisture Content Analyzer
NA	Nodules per unit Area
ppm	parts per million
SE	Secondary Electrons
SEM	Scanning Electron Microscope
SiE	Silicon Equivalent
SPEED	Selective Potentiostatic Etching by Electrolytic Dissolution
SSM	Sand Strength Machine
wt.%	weight percent

Chapter 1

Introduction

Developed in the late 1940's, ductile cast irons have evolved into an essential class of engineering materials. Castability, ease of machining, in-service reliability, vibration damping, high-strength and toughness are some characteristics that have made this material a popular option among many leading industries, including the automotive sector [1].

Ductile iron is a multi-constituent iron-carbon alloy with a carbon content ranging from 3 to 4.5 wt.%. Referred to as nodular or spheroidal graphite iron, ductile irons contain concentrations of graphite in the form of minute spheres within a predominantly ferritic matrix. During solidification, eutectic graphite separates from the molten iron. With the addition of certain reagents to the molten metal before it is cast, the graphite precipitates into nodules rather than lamellae. The spherical shape of the graphite creates fewer discontinuities and reduces stress concentrations within the alloy thereby producing a strong naturally occurring composite. The spheroidal geometry of the graphite gives ductile irons an incredible combination of elongation, tensile strength and proof stress [1].

Magnesium bearing ferrosilicon tends to be the most common spheroidizing agent presently in use; however, additional spheroidizing agents such as unalloyed magnesium, nickel-based nodulizers and cerium are used to promote the nodularization of graphite as well [1]. These nodularizing additives can also aid in restricting the deleterious effects of elements such as antimony, lead, titanium, tellurium, bismuth and zirconium, which prevent the developing graphite from nodularizing.

Mechanical properties of ductile irons may be enhanced by additions of boron, chromium, cerium, copper, molybdenum, nickel, niobium, phosphorus, vanadium and zirconium [2-7]. Furthermore, thermo-mechanical properties of ductile irons can be increased by controlled additions of aluminum and silicon [8-18]. Many of these elements have a significant influence on the precipitation of ferrite, pearlite and carbides, which are material property determining phases.

Ductile cast iron is generally used in applications where respectable thermo-mechanical properties are required at an economical cost. But, its use is slowly being phased out by newly emerging alloys yielding similar strength properties at a fraction of the weight. In automobiles, for example, cylinder heads are being replaced by various aluminum alloy-composites and intake manifolds are being replaced with magnesium alloys. However, high-operating temperatures have prevented any new lightweight alloy from replacing the exhaust manifold or turbochargers. Exposed to extreme temperatures exceeding 700°C, the exhaust manifold would virtually melt aluminum and magnesium alloys. The only material that can withstand such extremely high temperatures at an economical cost is ductile cast iron.

There is an ongoing quest in the automotive industry for possible methods of reducing fuel consumption. The approach to this problem by the industry has been two-fold. One is to reduce the overall weight of the vehicle. An important component of this approach is to reduce the section thickness of castings. The second approach is to increase the engine operating temperature, thereby enhancing the efficiency. The latter approach also enables complete combustion of fuel; effectively reducing harmful emissions [19,20].

Increasing operating temperatures has a profound effect on current engine components cast from ductile iron, such as exhaust manifolds and turbochargers. Surface oxidation and spalling at high temperatures severely reduce the life of current ductile cast iron components. As a result, a new family of ductile irons has emerged. Alloyed with aluminum, molybdenum and silicon, these alloys were developed for the next generation exhaust manifold and turbochargers. Its resistance to high temperature oxidation and enhanced thermo-mechanical fatigue resistance during thermal cycling have made this type of iron an ideal candidate for high-temperature applications. However, choices in material composition, treatment additions and process conditions necessary to produce sound castings for elevated temperature regimes are not completely understood. In effect, these prevent mass production of such cast irons. This research project demonstrates the correlation of these variables through experimental study.

The present research is focused on determining the precise concentration and combination of alloying elements that will enable the next generation of ductile cast irons to withstand surface and sub-surface oxidation and spallation at operating temperatures in excess of 700°C. With this material requirement, principal as-cast defects such as slag,

dross, pinholes and shrinkage were controlled. Process variables included different pouring temperatures, section sizes and chemical compositions. Post-process variables included critical oxidizing and phase transformation temperatures. The effect of select process parameters were studied using optical and scanning electron microscopes and computational digital image analysis software.

Chapter 2

Literature Review

Current studies are focused on extending the usefulness of ductile iron alloys into applications requiring thermal stability at high temperatures [15]. The literature to follow is a review of ductile cast iron metallurgy relevant to high temperature applications. Metallurgical studies performed to understand the processing of ductile iron and its alloys will be examined in this review with a view to extending these fundamentals into developing a ductile cast iron alloy for applications in excess of 700°C.

2.1 METALLURGICAL CHARACTERISTICS of DUCTILE IRONS

The microstructure and properties of ductile cast iron depend extensively on composition, rate of solidification and molten metal processing [1,21-24]. More specifically, chemical composition is the primary driving force in shaping the final microstructure and obtaining the desired properties for any elevated temperature application. Alloying elements have a direct effect on the ability of ductile cast irons to withstand high temperatures through graphite morphology and the relative amounts of ferrite and pearlite [15,25]. Alloying elements generally used to enhance the thermal properties of ductile cast irons and negate the effects of deleterious elements include carbon, aluminum, silicon, molybdenum, boron, chromium, nickel, copper and vanadium [7,22,26]. Elements used to influence graphite morphology include magnesium, calcium, cerium and other rare earths. Other elements introduced into ductile cast iron during processing may include hydrogen, nitrogen and oxygen [27].

Controlled additions of these elements into ductile cast iron can offer the best potential in meeting the following requirements for elevated temperature applications [1,6,8-10,12-16,22,25,28]:

1. Resistance to Oxidation and Spalling

2. Resistance to α-ferrite→γ-austenite Phase Transformation
3. High-Temperature Fatigue Strength
4. High-Temperature Creep Resistance
5. Low Thermal Conductivity
6. Low Thermal Expansion Coefficients
7. Dimensional Stability at Elevated Temperatures

2.1.1 Effect of CARBON and CARBON EQUIVALENT in Ductile Iron Processing

The carbon content in ductile cast iron can range anywhere from 3 to 4.5wt.%. However, the carbon content in commercial grade ductile cast irons generally ranges from 3.5 to 3.9wt.% [22]. Under conditions of slow cooling or near equilibrium conditions, phase transformations in unalloyed ductile cast iron can be explained using the Fe-C binary phase diagram illustrated in Figure 2.1. In BCC α-ferrite, maximum carbon solubility is about 0.02wt.% C, whereas the maximum carbon solubility limit in FCC γ-austenite is approximately 0.65wt.% C [29]. This discrepancy in carbon solubility results from the shape and size of the crystals themselves. Since the interstitial positions are much larger in a FCC crystal, it is much easier to accommodate carbon atoms. The temperature of this transformation is critical in improving the ability of the cast iron to operate at elevated temperatures. By increasing the α→γ critical transformation temperature, excess carbon in suspension will yield higher levels of graphite, and this in turn will improve internal resistance to oxidation. Furthermore, this will ensure dimensional stability as the working temperature range of the cast iron is increased. From the Fe-C phase diagram in Figure 2.1, the working range of an unalloyed cast iron is approximately 738°C, which can be increased through the addition of elements such as silicon and aluminum [25].

Carbon's primary influence on the microstructure in ductile cast iron is the nodule count and the formation of ferrite and pearlite [30,31]. Higher concentrations of carbon offer increased strength and resistance to thermal fatigue at the expense of reduction in hardness, tensile strength and yield strength [1,3,22].

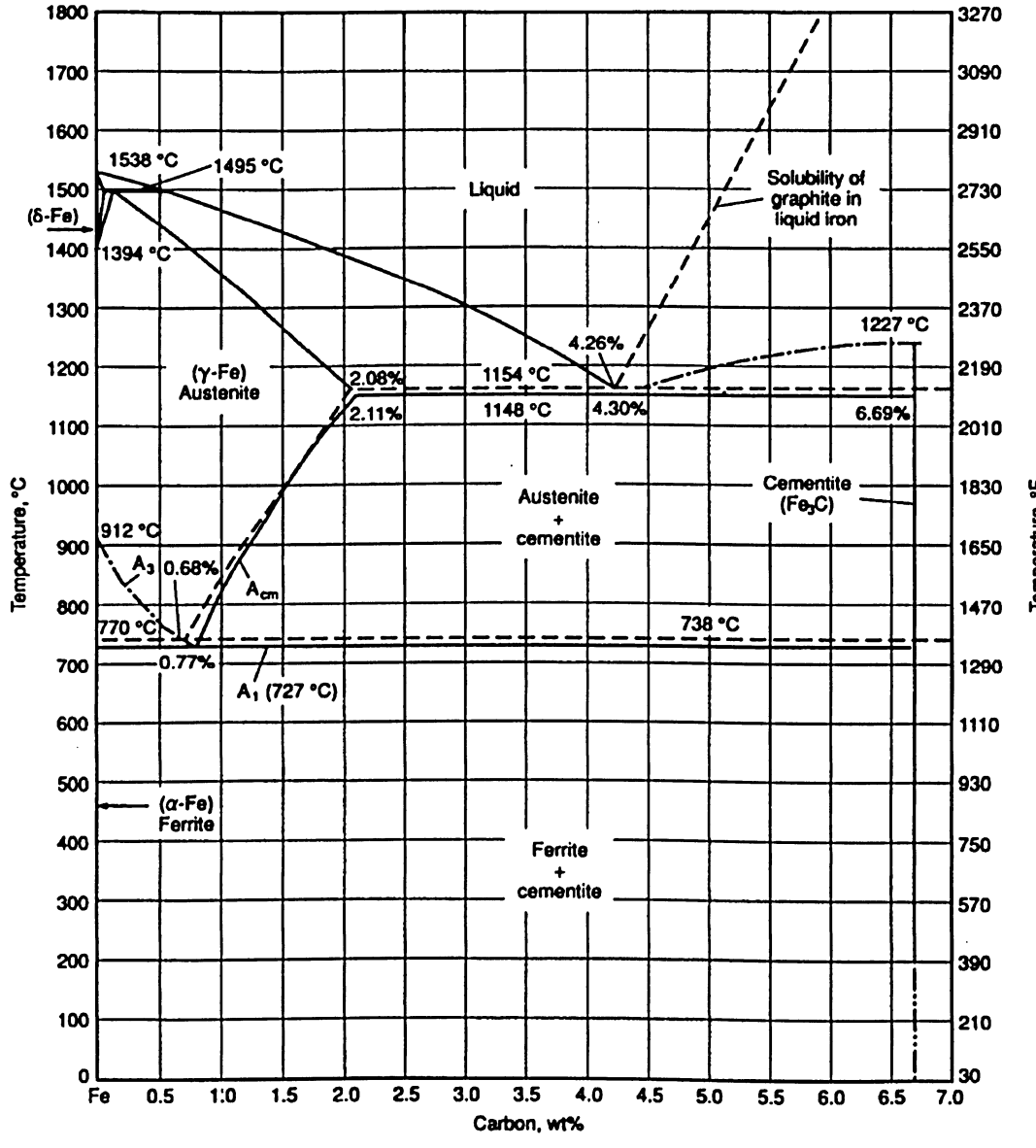

Figure 2.1: Iron-carbon equilibrium diagram, where solid curves represent the metastable system Fe-Fe_3C and the dashed lines represent the iron-graphite stable system [1].

The fluidity of molten iron and mould fillability are influenced by carbon [1]. Fluidity of liquid iron is reduced when excess carbon is in suspension and not in solution. Further, fluidity is reduced when the carbon content exceeds 2.2wt.% [10]. Mould fillability is affected by the volumetric expansion of graphite during solidification [1,22]. During eutectic solidification, carbon in solution transforms into graphite. Since the volume of graphite is 3.5 times the volume of iron, this phase transformation will cause a net volumetric

expansion of the iron. As a consequence of this thermo-physical process, mould fillability enhances during solidification and defects such as shrinkage and porosity can be prevented. The amount of carbon necessary to cause this phenomenon can be approximated using the Henderson Diagram in Figure 2.2. To avoid excessive shrinkage, Henderson [32] established a lower threshold limit for carbon equivalent (*CE*):

$$CE = \%C + \frac{\%Si}{7} = 3.9\% \qquad \text{Equation 2.1}$$

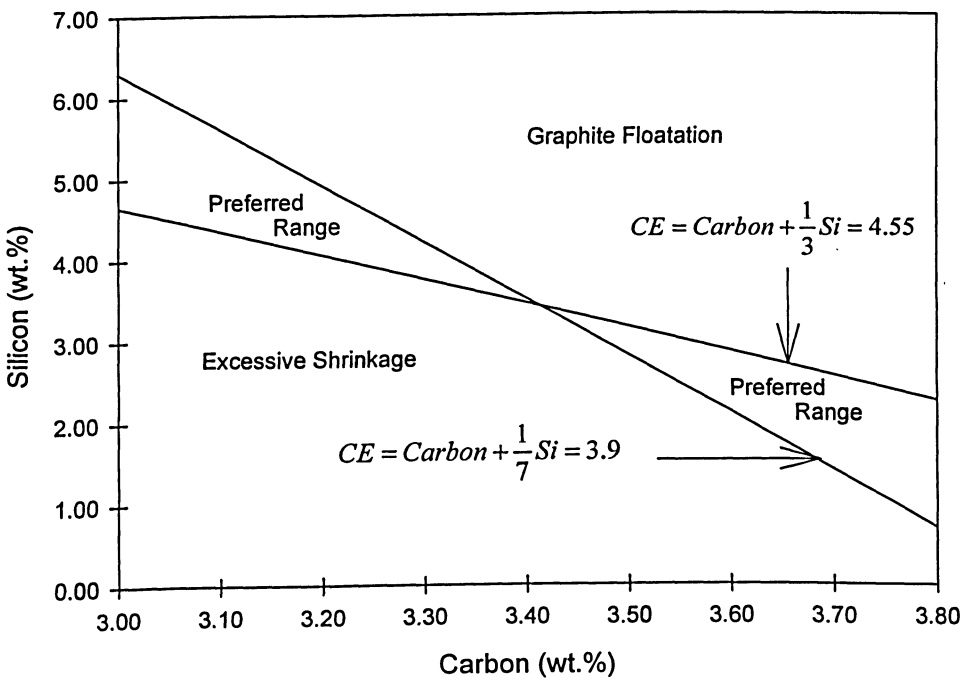

Figure 2.2: Carbon and silicon ranges for ductile cast iron used to minimize processing defects (Henderson [32]).

To prevent carbon floatation (a defect involving a localized concentration of carbon in the upper portion of the mould during solidification), an upper *CE* threshold limit was established. This is expressed as:

$$CE = \%C + \frac{\%Si}{3} = 4.55\% \qquad \text{Equation 2.2}$$

Silicon does not effectively substitute for carbon during graphite nucleation and growth; however, it is considered to be an effective graphitizing agent [1,3,30]. Therefore, it is the *CE* value that ultimately determines whether the cast iron alloy will contain a hypoeutectic, eutectic or hypereutectic structure, not the base carbon content.

2.1.2 Effect of SILICON in Ductile Iron Processing

The addition of silicon to ductile cast iron increases its ability to operate in a high temperature environment [1,22,25]. The addition of silicon to the Fe-C binary systems destabilizes the cementite (Fe_3C) phase, promotes graphitization, increases nodule count, decreases carbide formation, promotes formation of ferrite and raises the critical α-ferrite to γ-austenite transformation temperature [1,3,8,25,31,33,34,35]. The addition of silicon to cast iron will result in a ternary Fe-C-Si alloy, which will ultimately shift the eutectic and eutectoid points to lower carbon concentrations. This effect can be seen from the equilibrium phase diagram in Figure 2.3 for a Fe-C binary alloy containing 2wt.% silicon. The Fe-C-Si ternary equilibrium phase diagrams in Figure 2.4 further illustrate the effect of increasing silicon concentrations on the eutectic and eutectoid carbon contents and temperatures at which they occur. The phases in Figure 2.4 include graphite, α-ferrite, γ-austenite, C_1 (cementite, Fe_3C), C_2 (iron silicon carbide), C_3 (silicon carbide, SiC) and L (liquid).

The silicon contents in alloyed ductile cast irons can range from 1.8 to 2.8wt.%, with some compositional systems containing as much as 8wt.% [22,25,35]. However, silicon contents are generally limited to within 4wt.% providing a respectable equilibrium between high temperature oxidation resistance and embrittlement [1].

Silicon has an exceptional ability to increase ductile cast iron resistance to oxidation and spalling at high temperatures while maintaining dimensional stability. It forms a compact adhering oxide scale that protects the cast iron from further oxidation [25,34]. By increasing the silicon content, the oxide layer progressively transforms from iron oxide to iron silicate. This transformation provides a higher resistance to the transport of oxygen atoms into the metal from the surface. Conversely, the diffusion of metal atoms through the oxide layer into the atmosphere is progressively slowed down. Therefore, the rate of oxidation can be gradually reduced by increasing the concentration of silicon [2,36].

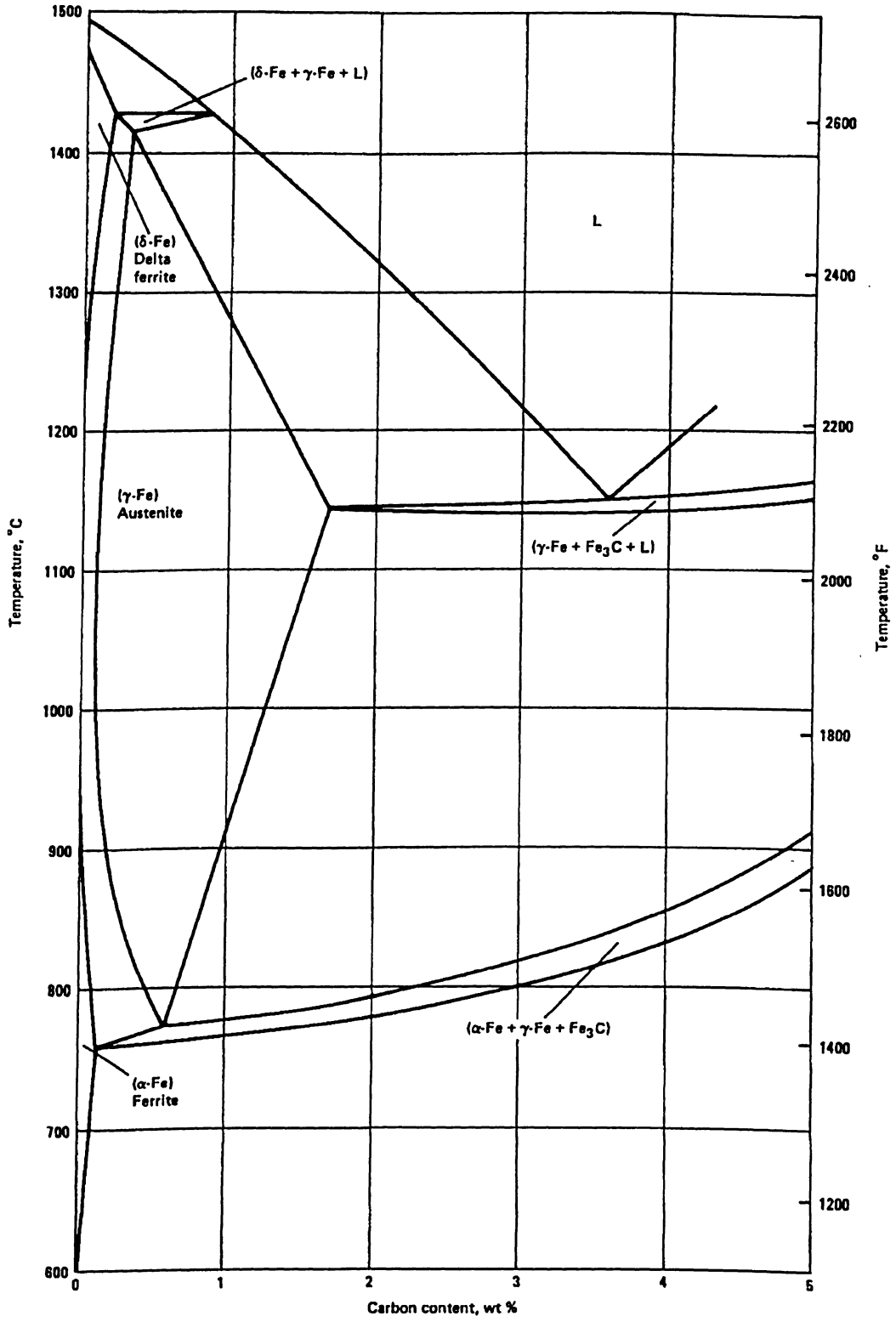

Figure 2.3: Influence of 2wt.% silicon on the eutectic and eutectoid points in a Fe-C binary alloy [1].

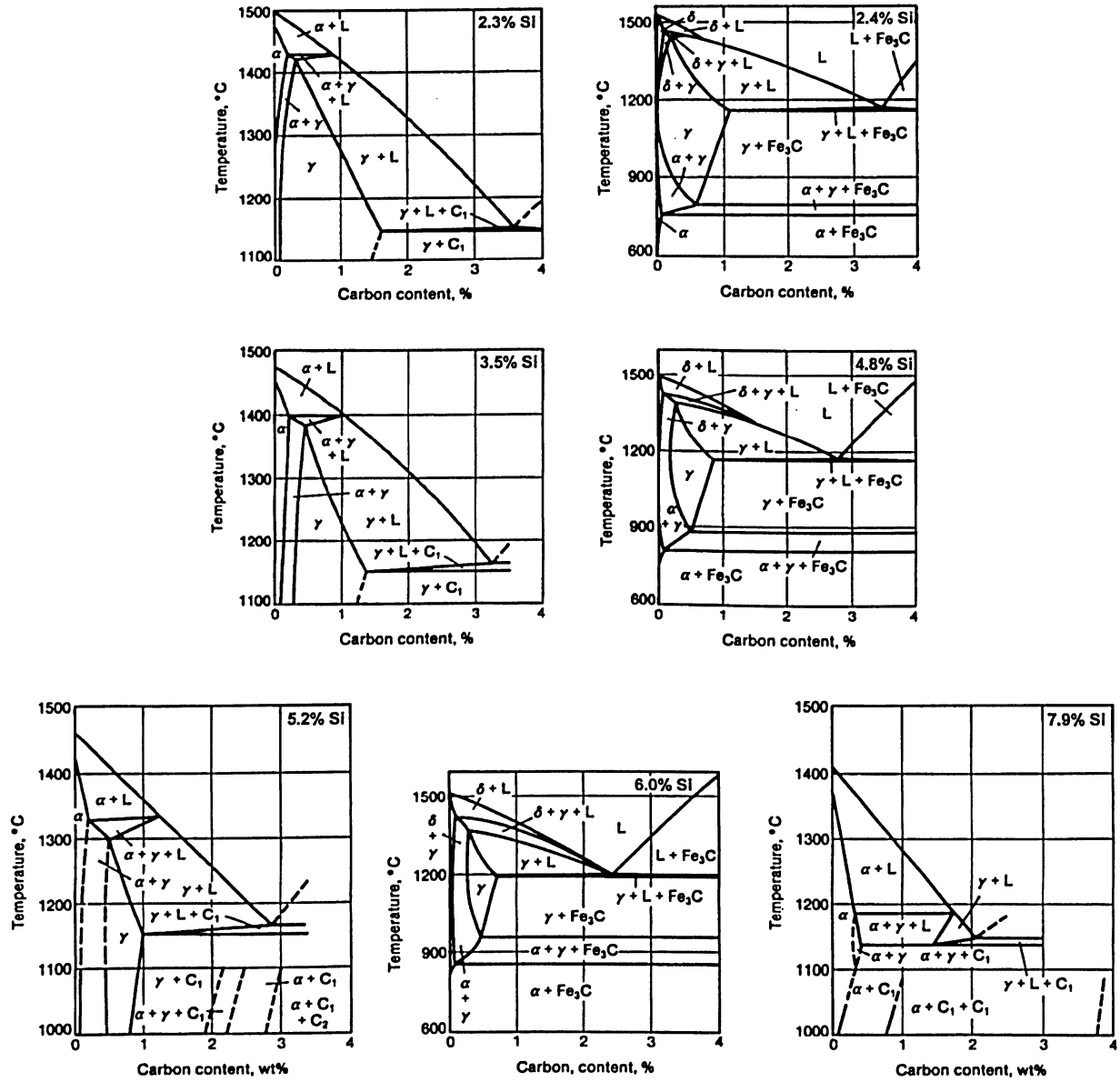

Figure 2.4: Influence of various silicon concentrations on the iron-carbon equilibrium system [1].

The Silicon Equivalent (*SiE*) (a correlation between the amount of silicon and aluminum) is often used to evaluate the resistance of a cast iron to oxidation by only one numerical quantity. The silicon equivalent is expressed through the following equation [17]:

$$SiE = Si + 0.8Al \qquad \text{Equation 2.3}$$

According to Reynauld and Roberge [17], a ductile cast iron possessing an *SiE* of 6.0 or higher would not experience any oxidation.

Silicon's ability to increase the critical $\alpha \rightarrow \gamma$ transformation temperature enhances the useful operating temperature range for ductile cast iron. A linear relationship exists between the silicon concentration and the critical transformation temperature. This correlation can be approximated from the following expression [37]:

$$Critical\ Temperature = 730 + 28 \times (\%Si)^{o}C \qquad \text{Equation 2.4}$$

The range of temperature that promotes this phase transformation is of considerable importance. First, it determines the carbon available for graphitization during solidification and second, it influences the dimensional stability of the cast iron at high temperatures.

2.1.3 Effect of MOLYBDENUM in Ductile Iron Processing

Addition of molybdenum enhances the resistance to oxidation and the mechanical properties of ductile cast irons at elevated temperatures; these include tensile strength, stress rupture and creep strength and resistance to thermo-mechanical fatigue [1,6,14,22,25,34]. Molybdenum can cause shrinkage problems [3]. It's also prone to segregating near the grain boundaries in the form of stable carbides [1]. This element causes precipitation of various carbidic phases including the Fe+Fe_xMo_yC and Fe+M_yC-type [38]. Investigators have stipulated that such phases can be responsible for giving ductile iron alloys dimensional stability at elevated temperatures [15]. Several carbidic phases including Fe_2MoC, M_2C, M_6C and $M_{23}C$ can co-exist within the cast iron alloy, which are identified by the Fe-Mo-C ternary phase equilibrium diagram illustrated in Figure 2.5.

Some investigators [18] have observed that additions of molybdenum above 0.3% lead to an increase in pearlite concentration. Increasing molybdenum will reduce the formation of free ferrite by initiating a volume fraction increase in pearlite through the formation of free carbides [2]. However, recent studies have indicated that this could be misleading. The $Fe_xM_yC_z$ type phases can be mistaken for pearlite [15]. As a result, careful analysis (e.g., via electron microscopy) is necessary.

Ductile cast irons have been alloyed with molybdenum contents ranging from 0.6wt.% to 2.5wt.% [25]. The most effective concentration range is from 0.5wt.% to 1wt.%. In this range, molybdenum is most effective in improving creep and stress rupture strength [17]. Automobile turbochargers currently contain 0.6wt.% to 0.75wt.% of molybdenum alloyed with 4wt.% silicon, while cast irons alloyed with 1wt.% molybdenum and 4wt.% silicon are typically used for exhaust manifolds [25].

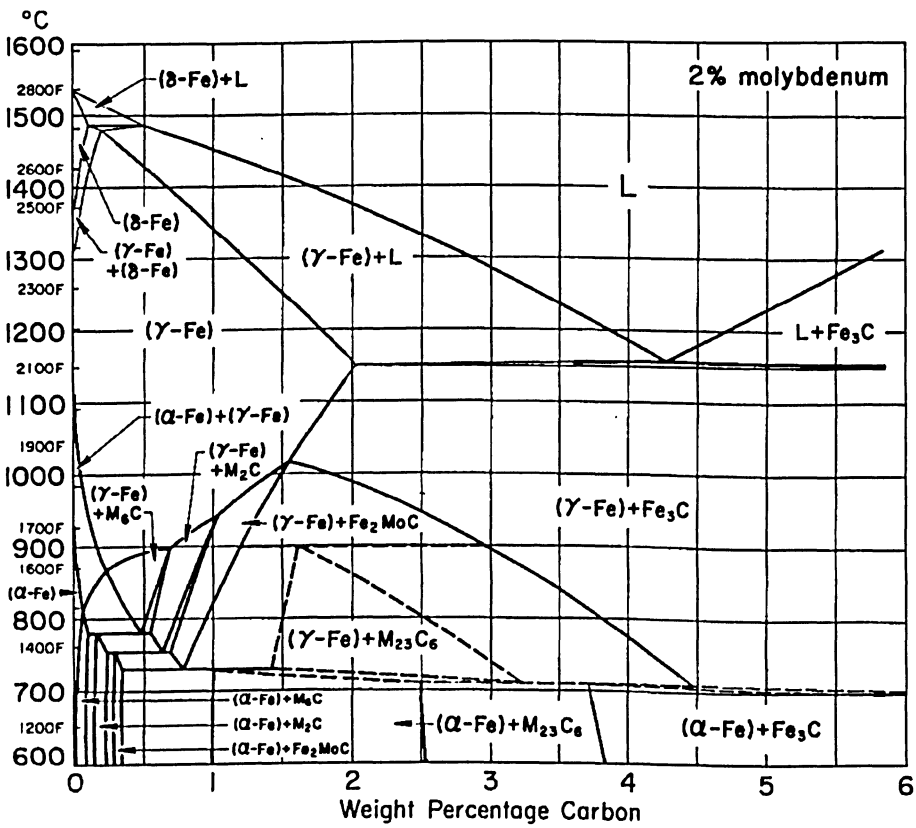

Figure 2.5: Fe-Mo-C ternary alloy equilibrium phase diagram for 2wt.% molybdenum [35].

2.1.4 Effect of ALUMINUM in Ductile Iron Processing

The effect of aluminum in ductile cast iron is two-fold. The addition of aluminum enhances the degree of resistance to oxidation at high temperatures and it raises the critical α-ferrite to γ-austenite critical transformation temperature [8,9,12,14,17,25,34]. Aluminum protects the cast iron from oxidation by producing a thin impervious film that prevents further diffusion of oxygen in iron. Since the critical α→γ phase transformation temperature

is increased, the scaling tendency of the aluminum oxide layer is decreased, thereby providing protection throughout the thermal cycling life of the material. Approximately 1wt.% of aluminum can increase this critical temperature by 50-60°C [14,34].

Aluminum also affects the graphitization of cast irons [34]. In cast irons containing up to 3 to 4wt.% aluminum, carbon in suspension develops as graphite [12]. As this concentration of aluminum is progressively increased, its effectiveness as a graphitizer diminishes. At 10wt.%, aluminum becomes a carbide stabilizer [12,39]. The existence of a hard brittle ferro-magnetic phase called ε-carbide (a complex iron-aluminum carbide) has been detected in cast irons containing 9 to 19wt.% aluminum [8,40,41,42]. However, the application of such cast irons is limited due to the brittleness of the material [8,43]. Cast irons containing 10 to 18wt.% Al are referred to as white cast iron because of their inability to form graphite. Graphite formation resumes in cast irons having aluminum concentration in excess of 18wt.% [9,12,25].

There are many drawbacks to the use of aluminum. In molten ductile cast iron, aluminum is very reactive and exposure to ambient air and moisture will cause the formation of dross and other microstructural defects [25]. Moreover, higher concentrations of aluminum make ductile irons more susceptible to gas porosity.

2.1.5 Effect of Combining Al, Si and Mo in Ductile Iron Processing

The operating temperature of ductile cast irons can be improved by alloying with Al, Si or Mo. But, by combining these elements, optimal thermal performance can be achieved by counteracting damaging properties such as embrittlement, and enhancing favourable properties such as dimensional stability at high temperatures. If ductile cast iron alloyed with excessive amounts of silicon (>4wt.%) is continuously heated and cooled, induced thermal stresses will cause cracking and ultimate failure due to thermal fatigue [14,34]. Moreover, excessive amounts of aluminum in Fe-C cast alloys will yield large microstructural defects, such as dross and porosity. In view of that, a ductile cast iron alloyed with controlled amounts of Al, Mo and Si can be produced to effectively endure high temperatures and maintain dimensional stability.

Sponseller et al. [14] observed that a cast iron alloyed with 4wt.% silicon, 2wt.% molybdenum and 0.75wt.% aluminum produced an effective material for elevated temperature applications. This particular combination yielded a Fe-C alloy with a critical $\alpha \rightarrow \gamma$ phase transformation temperature of 816°C. Furthermore, this material exhibited exceptional resistance to oxidation, particularly when the aluminum content was increased from 0.55 to 0.90wt.%.

Reynauld and Roberge [17] investigated high temperature ductile irons with higher amounts of aluminum at operating temperatures in excess of 900°C. Several elemental combinations were proposed by Reynauld and Roberge [17]; 4.2-4.4wt.% Si, 1.5-1.7wt.% Al and 0.8-1.0wt.% Mo have been developed to operate at temperatures up to 900°C; 4.7-5.1wt.% Si, 2.1-2.3wt.% Al and 0.8-1.0wt.% Mo for operating temperatures up to 950°C; 5.2-5.4wt.% Si, 2.1-2.3wt.% Al and 0.8-1.0wt.% Mo for operating temperatures up to 1000°C.

Investigators have also studied a ductile iron alloy containing 3wt.% silicon, 2wt.% molybdenum and 5.5wt.% aluminum [25]. This particular combination exhibited a low rate of scaling and exceptional tensile properties at 925°C. Exposed to 925°C for 1000 hours, a thin oxide layer on the base iron alloy formed whose penetration depth was 0.008 mm. However, ductile cast irons alloyed with 2wt.% Si produced an oxide layer with a penetration depth of approximately 0.15 mm. A 1wt.% decrease in silicon considerably reduced the materials resistance to oxidation. This illustrated the importance of maintaining a predetermined level of silicon at or above 3wt.%.

Nofal et al. [8] also investigated a new family of high temperature cast irons that contained 9wt.% aluminum and different concentrations of silicon (i.e., 2, 3.5 and 5wt.%). The oxidation resistance at 9wt.% Al was observed to be exceptionally high at the surface. Furthermore, sub-surface oxidation decreased due to the increase in the critical $\alpha \rightarrow \gamma$ phase transformation temperature. However, it was observed that at lower silicon concentrations, the microstructure of thin sections consisted primarily of fine carbides and eutectoid products consisting of ferrite and graphite flakes. But, with slower cooling, there was marked coarsening of the carbide phase (together with the eutectoid agglomerates). This resulted in increasing the volume of ferrite by reducing the carbide phase. Further reduction in the carbide phase and a consequent increase of the ferrite matrix was observed by alloying the

iron with 1wt.% copper and inoculating with 1wt.% CaSi. It was also noted by Nofal et al. [8] that the formation of carbides was dependent on the silicon concentration. As a result, increasing the silicon content to 5wt.% eliminated both free and eutectoid carbides.

Yaker et al. [9] investigated the high temperature characteristics of ductile cast irons alloyed with different combinations of silicon and aluminum. The combination of compositions proposed included; 2.1wt.% Si and 1.25wt.% Al; 2.1wt.% Si and 3.8wt.% Al; 1.6wt.% Si and 5.9wt.% Al. It was observed that the strength of ductile irons alloyed with aluminum increased at higher temperatures as the concentration of aluminum increased, even at lower silicon concentrations. Moreover, the aluminum improved resistance to decarburization. Alloy combinations with lower amounts of aluminum exhibited surface oxide layers that were thicker than 0.1mm after longer periods of time at 760°C or shorter periods of time at 871°C. Petitbon and Wallace [12], with similar aluminum concentrations, observed comparable results. Increased amounts of aluminum produced a very thin, tight, adherent and protective oxide film at temperatures as high as 982°C in air. But, as the aluminum content decreased, the thickness of the oxide scale increased, thus decreasing the adherence and protection provided by the film. Petitbon and Wallace [12] demonstrated that irons containing 20wt.% to 25wt.% aluminum had the best resistance to oxidation at high temperatures. However, susceptibility to carbide formation, increasing the thermal expansion coefficient of the alloy and production economics obviates high aluminum concentrations.

2.1.6 Individual Effects of B, Cu, Cr, Nb, Ni and V on Ductile Iron Processing

Additions of boron, copper, chromium, niobium, nickel and vanadium to ductile cast irons have been made by investigators to enhance specific properties [1-3,7,17,22,44]. These elements can improve the strength, wear resistance, thermo-mechanical fatigue, creep and resistance to corrosion at ambient and elevated temperatures. However, due to high costs associated with some elements, the moderate usefulness of others and the direct application in consideration (i.e., exhaust manifolds and turbocharger housings), it is not practical to use these elements.

Boron is a carbide stabilizer and pearlite promoter [1,2,22]. Small amounts of boron will promote the segregation of boron carbides along grain boundaries while higher concentrations will effectively create an actual network-like structure [22]. Baligidad and Radhakrishna [7] observed that additions of boron to a base Fe-Al-C alloy increased the room temperature ultimate tensile strength by 9MPa and decreased the yield strength by 20MPa. Similarly, elevated temperature ultimate tensile strength increased by 20MPa and the yield strength increased by 26MPa.

Copper improves graphitization and promotes pearlite [1,3,22]. It destabilizes the ferrite phase and favours pearlite formation. Copper also impedes the annealing of pearlite. In cast ferritic irons, the amount of copper is restricted to approximately 0.03wt.%. The solubility of copper in cast iron is approximately 3wt.% to 3.5wt.% [2]. Copper, in the presence of molybdenum, can effectively increase the hardenability of irons [22]. Copper has a tendency of reducing the carbon content by about 0.075wt.% for every percent of copper. Alloyed with nickel, copper can suppress the formation of carbides and increase graphitization. Moreover, nickel and copper do not promote pearlitic stability at temperatures exceeding 450°C. However, copper will prevent the development of ferrite and will decrease the critical $\gamma \rightarrow \alpha$ transformation temperature [1,2].

Chromium is a powerful carbide and pearlite stabilizer [1,3,22]. It neutralizes the effects of elements such as molybdenum. To maintain a ferritic matrix, chromium levels must be kept below 0.04wt.%. However, a pearlitic matrix will be observed if chromium concentrations are increased to 0.10wt.%. Chromium will increase the carbon content of the iron-carbon eutectic by approximately 0.06wt.% for every 1wt.% of chromium added up to 9wt.%. Furthermore, when alloyed with elements such as silicon and aluminum, chromium will increase the cast iron's resistance to oxidation. In fact, for every 1wt.% of chromium that is added to iron, the critical $\alpha \rightarrow \gamma$ transformation temperature will be raised by as much as 40°C [2,17]. Low concentrations of chromium are generally of limited value. Concentrations of chromium ranging from 15-30wt.% are particularly suitable for temperatures up to 900°C and a range of 24-35wt.% is suitable for even higher operating temperatures. Chromium is generally used in white cast irons to enhance abrasion resistance and stabilize the structure for high temperature applications [1].

Recent studies have shown that additions of niobium to Fe-C-Al alloys, namely high carbon steels, could improve high temperature strength and creep resistance [7]. Similar applications could include cast irons. Moderate increases in room temperature hardness and yield strengths have been reported as a result of Nb additions. Correspondingly, moderate increases in elevated temperature strengths have also been observed with the ultimate tensile strength being increased by 15MPa and the yield strength by 20MPa.

Nickel increases the hardness and fraction of pearlite in cast irons [1]. Nickel is typically added to ductile irons at levels ranging from 0.5-36wt.% [22]. Nickel is an excellent graphitizing element. It facilitates in reducing the solubility of carbon in liquid iron and solid iron and it reduces the eutectic carbon content by approximately 0.06wt.% for every 1wt.% of nickel [2,22]. Nickel has a graphitizing ability that is one third that of silicon. Nickel has a tendency of decreasing the critical $\alpha \rightarrow \gamma$ critical transformation temperature [37]. In fact, the addition of 1% nickel to iron can reduce this critical temperature by approximately 17°C. Applications of cast irons alloyed with nickel include components in need of high wear resistance, corrosion resistance or high temperature resistance [1,2].

Vanadium is frequently added to steels to substantially improve strength properties of tools and dies which are subject to severe forging processes. Vanadium forms very stable carbides and facilitates in promoting pearlitic structures [1,3,44]. However, vanadium has a superior resistance to creep. It can be alloyed in small amounts with cast irons to help increase the operating temperatures at an appreciable cost. Sage and Dawson [3] investigated the addition of vanadium to gray cast irons and concluded that addition of 0.5wt.% V to iron increased the tensile strength by 125MPa. Furthermore, they concluded that resistance to thermal fatigue was not reduced and that chills did not form even in sections as thin as 3mm. But, this was attributed to the higher silicon contents. Sage and Dawson [3] also reported that vanadium can be used as a graphite refiner.

2.1.7 Spheroidizing Elements

There are many elements that have demonstrated the ability to spheroidize graphite. Specific examples include Group IA elements (i.e., lithium, sodium and potassium), Group

IIA elements (i.e., beryllium, magnesium, calcium, strontium and barium) and Group IIIB elements (yttrium and rare earths) [1,22].

Magnesium is a key constituent in the nodularization of graphite in ductile irons. Magnesium concentrations of approximately 0.02 to 0.08wt.% are needed to produce spheroidal graphite [22]. Irons that have low sulfur concentrations (<0.015wt.%) only need approximately 0.04wt.% Mg to nodularize graphite. The effectiveness of magnesium as a nodularizer fades with time, primarily due to the oxidation of magnesium. Magnesium can effectively deoxidize the base iron. As a result of this deoxidation, magnesium oxide (MgO) will form. MgO is very stable, has a very high melting temperature, low density, and low solubility in iron. As a result of its low density, when combined with other elements such as Si and Fe, MgO dross will settle near the top of the cope in the iron casting.

The amount of magnesium added to ductile cast iron is very important. If it is too low the graphite will not undergo spheroidal transformation. On the other hand, if the concentration of magnesium is too high, it will promote the formation of brittle primary carbides [1,23]. However, the effect of high magnesium concentrations can be suppressed by appropriately inoculating the cast iron [8]. This will increase the nodule counts which will counteract the formation of carbides [45].

Takanezawa et al. [6] observed that magnesium was not only an effective nodularizer, but was also the root cause of grain boundary fracture. Magnesium had a tendency of segregating at the grain boundaries, which resulted in the deterioration of elongation for the ductile iron. It was further observed that additions of phosphorus actually suppressed the segregation of magnesium at the boundaries. However, it was concluded that a specific Mg/P ratio of 1.5 should never be exceeded.

Other effective nodularizing compounds include mischmetal, rare earth silicide, Mg-bearing ferrosilicon (Mg-FeSi) and calcium silicide with copper [8,22]. The latter has been proven to be very effective [46]. Cerium and lanthanum are also very effective nodulizers [1].

Calcium can be used in spheroidizing treatments. Calcium, like other spheroidizing elements, forms oxides (CaO) that generally float to the cope of the casting. With levels above 0.03%, Ca will promote a carbidic structure when added with Mg. Below 0.03wt.%,

Ca helps to increase the nodule count. Calcium also helps to reduce the volatility of a Mg reaction [22].

Cerium is generally used as a supplement to magnesium to help increase nodule count and reduce the effects of deleterious elements, including aluminum [22,45]. The oxides and sulfides produced by Ce in the reaction are very stable. Only about 0.035wt.% Ce is needed to produce spheroidal graphite. Ce will offset the negative effects of Ti, Pb, Sb and As. But, large amounts of Ce will result in graphite flotation, exploded graphite formation and chunky graphite in large sections of the casting.

Lanthanum, combined with MgFeSi, is favoured primarily for its influence on promoting a fully ferritic matrix and developing a high nodule count [45]. Lanthanum has been linked to having an impact on spheroidizing graphite in ductile irons, but it has also been linked to promoting brittle carbides as well [1,22].

Many investigators have challenged the use of other rare earths including neodymium, praseodymium and yttrium. It has been reported that neodymium and praseodymium are very heavy carbide stabilizers. Yttrium on the other hand has proven beneficial in creating graphitic nodules but it has not been widely accepted due to excessive cost [22].

2.1.8 Matrix Phase Structures in the As-Cast Ductile Iron

2.1.8.1 Ferrite

The BCC α-ferrite iron is a solid solution with 0.022wt.% carbon (maximum) [29]. This phase is stable up to the eutectoid temperature of 738°C [47]. This can be observed from the Fe-C phase equilibrium diagram illustrated in Figure 2.1. A detailed discussion on the ferrite structure is given by Voigt and Loper [2].

The bright white constituent in the micrograph (Figure 2.6) is ferrite. Ferritic ductile cast irons are favoured over pearlitic cast irons for high temperature applications. The decomposition of cementite (Fe_3C) associated with pearlitic cast irons can cause excessive surface spalling at temperatures in excess of 700°C, thereby reducing the life of the component [15]. Addition of Si to cast iron can promote, stabilize and harden this phase [25].

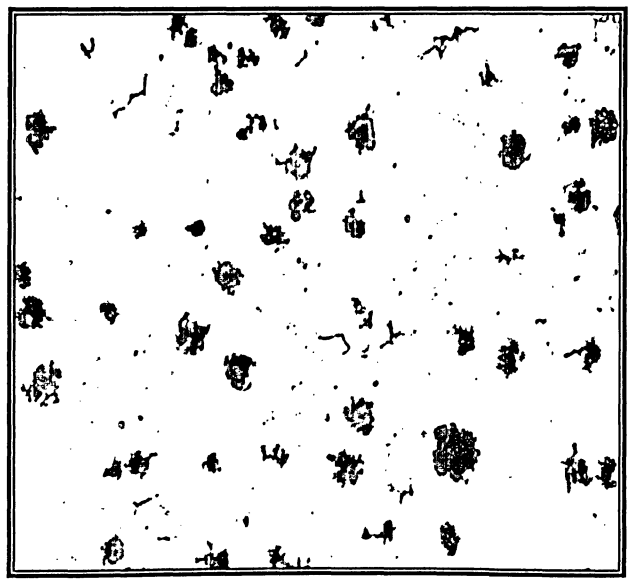

Figure 2.6: Optical micrograph of as-cast ferritic ductile iron alloy [current research]. 100X. Nital etched.

2.1.8.2 Pearlite

The pearlite microstructure in ductile cast iron is composed of alternating layers of α-iron and metastable cementite (Fe_3C) [47]. During the formation of pearlite, diffusion of carbon atoms occurs over small lamel distances. The austenite-to-pearlite transformation takes place at temperatures lower than those for austenite-to-ferrite transformation [48]. Furthermore, pearlite formation increases with increased cooling rates [23,49]. A detailed discussion on the pearlite structure and eutectoid transformation of austenite is given by Voigt and Loper [29] and Lieteart [50].

The bright white rings surrounding the graphite in Figure 2.7(a) is ferrite and the dark compound surrounding the ring of ferrite is pearlite. Since cementite is a metastable compound, exposing the cast iron to high temperatures will cause pearlite to decompose into α-ferrite and graphite. The resulting microstructure is illustrated in Figure 2.7(b). When the cementite phase decomposes, the resulting expansion will cause the oxide layer to break at high temperatures. It has been observed that for every 0.1wt.% of carbon combined as cementite in pearlite, a volumetric increase of 0.3% will occur [15]. To further support this occurrence, Gilbert [51] determined that after aging ductile cast iron for 64 weeks at 500°C, the material increased linearly by 0.5%. In summary, the onset of repetitive plastic strains

resulting from the decomposition of pearlite will lead to fatigue cracking of the oxide scale and ultimate failure of the component [52].

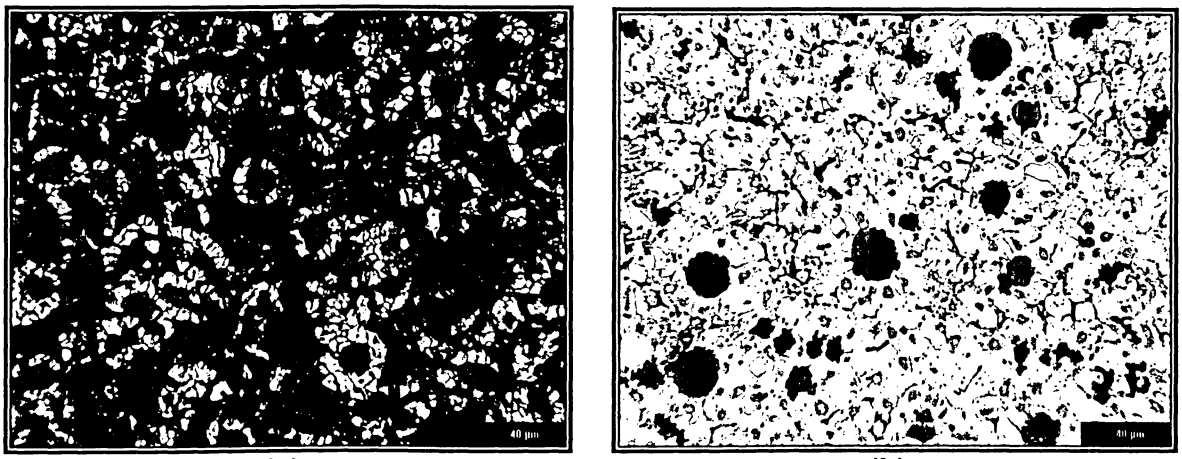

Figure 2.7: Optical micrographs of (a) as-cast pearlitic ductile iron alloy and (b) as-cast ductile iron alloy annealed for 500 hours at 800°C [current research]. 200X. Nital etched.

2.1.9 Formation of γ-Austenite and Graphite in Ductile Cast Iron during Solidification

During solidification of ductile cast iron through the eutectic (1150°C→1100°C), two distinct solid phases develop: γ-austenite and graphite [53]. The nucleation and growth process of these two phases is the least understood phenomena in cast iron metallurgy [21].

Nucleation and growth of austenite is believed to occur through the formation of dendrites [53-57]. These dendrites consist of primary and secondary arms, which grow perpendicular to the surface of the casting. A complex network of austenitc dendrites is illustrated in Figure 2.8. The length and number of dendrites depends on the rate of solidification. As the rate of solidification decreases the dendrites become shorter and less in number. This is illustrated in Figure 2.9. Further discussion and in depth analysis on austenitic dendrites including exogeneous and endogeneous growth can be found elsewhere [58-63].

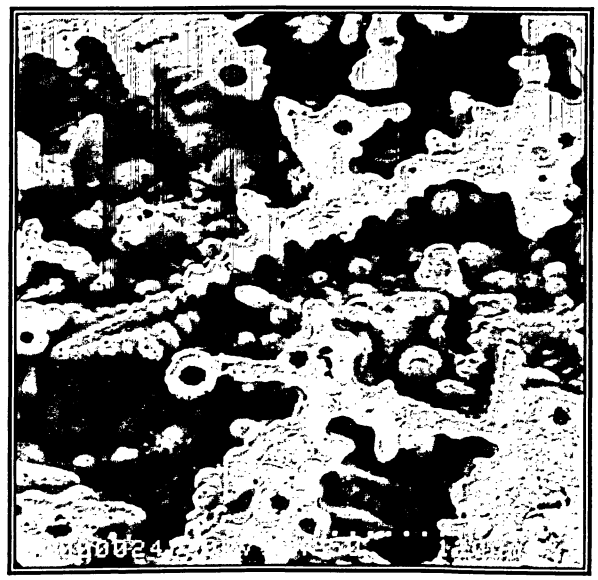

Figure 2.8: SEM micrograph of austenitic dendrites that formed during solidification [current research]. 250X. Nital etched.

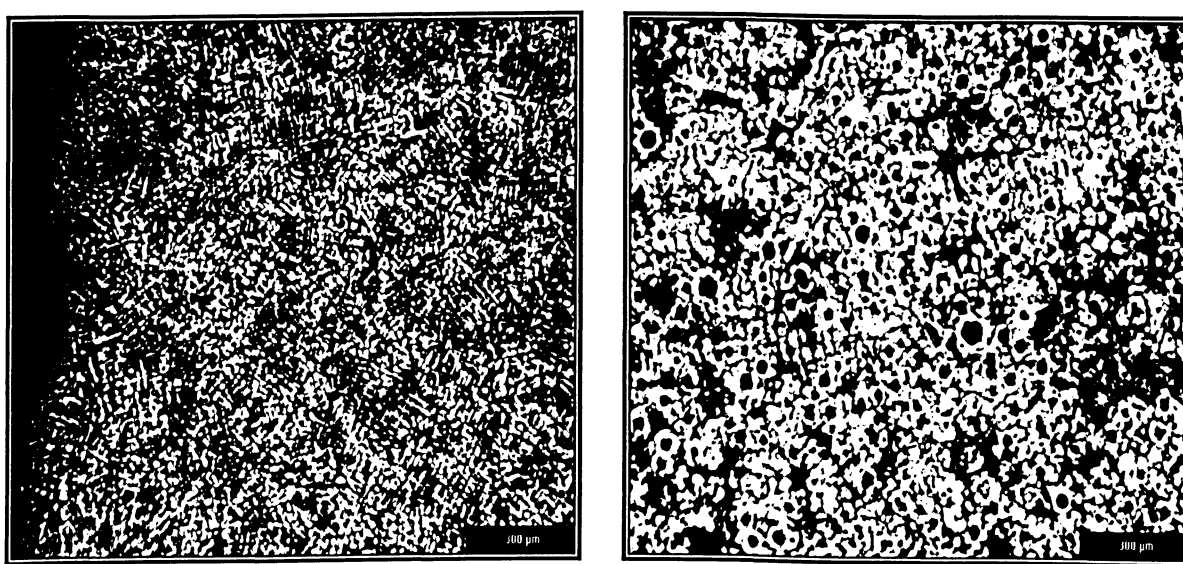

(a) (b)

Figure 2.9: Optical micrographs of (a) 4mm thick specimen and (b) 7mm thick specimen [current research]. 50X. Nital etched.

It is well accepted that austenite develops through the formation of dendrites during solidification; however, much ambiguity still exists in the theories developed to explain the

nucleation of graphite. The more widely accepted theories include the Cementite Theory, Austenite Theory and Melt Theory, with the latter being most convincing.

The Cementite Theory is one of the earliest theories developed to explain the nucleation of graphite. Morrogh [64] postulated that graphite nodules formed by the decomposition of cementite. Furthermore, Dunphy and Pellini [65] suggested that the decomposition of Fe_3C developed in the vicinity of dendrites immediately before the start of the eutectic reaction, thereby forming nodules in the neighbourhood of existing dendrites. However, it was later determined that graphite formation only took place in the austenitic phase, not in cementite.

Supported by De Sy [66] and Wittmoser [67], the Austenite Theory suggested that graphite precipitated within the austenitic dendrites, with further growth taking place by a peritectic transformation. Since they found that dendrites contained the same chemical composition as the base metal, it was believed that ductile iron solidified without eutectic but in a mixed crystal system formed by supersaturated austenite. However, Falkenhagen and Hofmann [68] proved that this theory was not practical because supersaturated austenite never really existed.

The longest surviving and most rigorously tested theory is the Melt Theory. Scheil and Hutter [69] postulated that graphite nodules formed within the eutectic melt away from existing austenitic dendrites. Nucleation and growth were believed to occur on a substrate within the melt and once a critical size was reached they would be encapsulated by an austenitic shell. Further growth of graphite nodules would progress by diffusion of carbon from the melt through the austenite and to the existing nodules. Support for this theory was further provided by Loper and Heine [70,71,72] with similar conclusions made by Stefanescu [57], Oldfield and Humphreys [73] and Kempers [74]. However, in later studies, Oldfield [75] and Sato et al. [76] observed that no trace of an austenite shell surrounding graphite nodules existed and concluded that graphite nodules formed in direct contact with the molten iron. Patterson [77] also suggested a modified version of Scheil's and Hutter's [69] hypothesis. Patterson [77] proposed that the graphite nodule formed directly from the melt in the interstitial positions of the austenitic dendrite arms where the melt was supersaturated. A detailed discussion on the support for the Melt Theory is given by Van de Velde [78].

Though theories on graphite nucleation are still open to debate, researchers have found some common ground on the substrate responsible for the heterogeneous nucleation of graphite nodules in the melt. Heterogeneous nucleation of graphite during solidification begins with the formation of complex sulfides, which serve as nuclei for complex oxides. The end product serves as nuclei for spheroidal graphite [79]. De Sy [80] hypothesized that the decomposition of a complex magnesium silicon-carbide can act as a substrate for nucleation. Bakkerus and Rosenstiel [81] have discovered inclusions within graphite, thereby postulating the possibility of inclusions acting as nucleation sites. Itofuji et al. [82] found inclusions of the type Mg-Ca-S-SiO at the centre of the graphite nodules. Lalich and Hitchings [83] have also observed and concluded that inclusions could be a possible source for nucleation. They also suggested that complex silicates, sulfides and rare earth metals are potential substrates for nucleation.

2.1.10 Structure of Graphite

The crystal structure of graphite is HCP. Bound by low index planes, the normally observed bounding planes in a graphite crystal that has formed from the iron-carbon melt are (0001) and $(10\bar{1}0)$. This is illustrated in Figure 2.10. Possible growth directions for crystalline graphite are labelled as A and C in Figure 2.10. Graphite that precipitates out of the iron-carbon melt has a layer-like type of structure with very strong covalent bonds (i.e., 4.19×10^5 to 5×10^5 J/mol) between atoms in the same layer. However, weak molecular forces subsist between each layer of the graphite structure. Moreover, every atom also contains three electron bonds with each of its neighbouring atoms on the same plane. The remaining fourth electron is common to the layer, thus giving it the metallic properties of graphite. Strength and hardness are generally higher in the C-direction, as depicted in Figure 2.10 [79].

Graphite precipitates from carbon. Depending on the chemical composition of the cast iron, a variety of graphite shapes can emerge. Figure 2.11 illustrates some of the various graphite geometries that may develop during solidification.

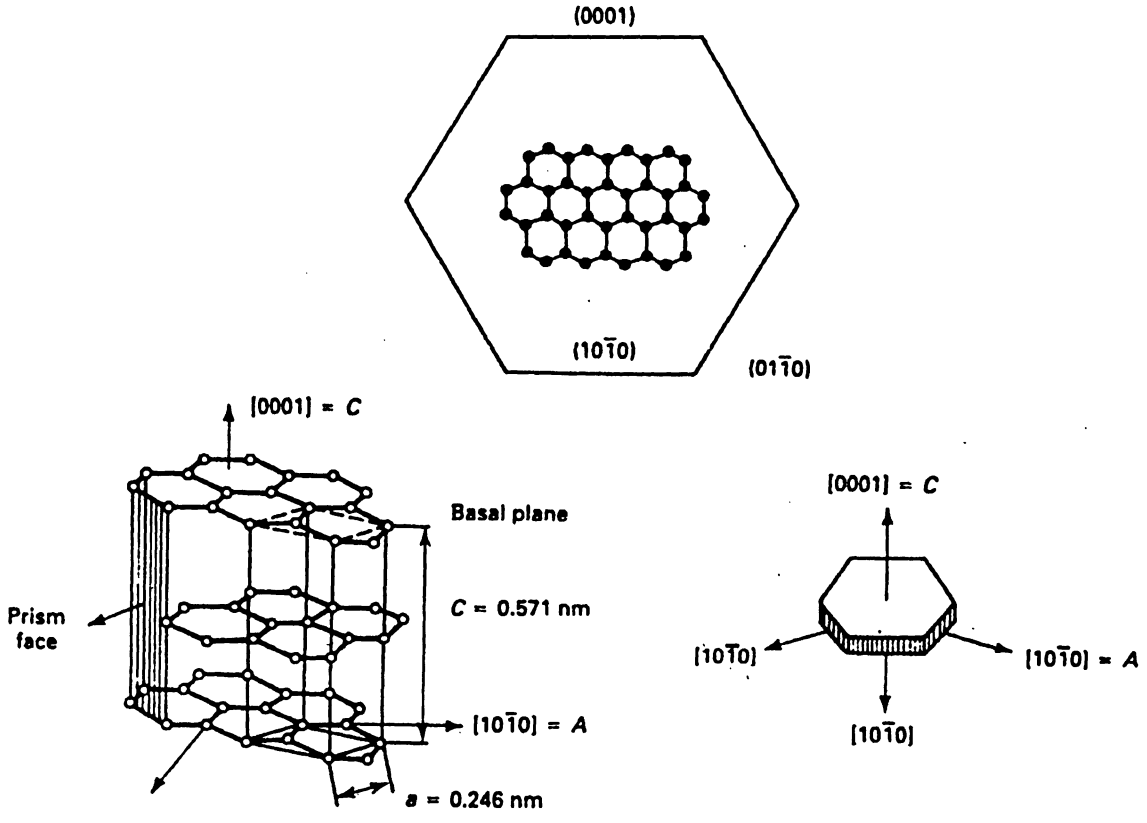

Figure 2.10: Crystalline structure of graphite [84].

2.1.10.1 Graphite Shape Parameters

Cast iron components designed for high temperature applications (i.e., exhaust manifolds and turbochargers) must contain spheroidal graphite. This ensures that stresses induced during thermal cycling are distributed within the iron matrix along the nodules (not concentrated at a single point), so as to eliminate the onset of fatigue failure due to microcracking. Two factors must be considered when analyzing the shape of a graphite nodule; sphericity (S) and compactness (C) [85]:

$$Sphericity = \frac{4\pi(Area)}{(perimeter)^2} \qquad \text{Equation 2.5}$$

$$Compactness = \frac{4\pi(Area)}{(convex\ perimeter)^2} \qquad \text{Equation 2.6}$$

Figure 2.12 illustrates how the *perimeter* and *convex perimeter* are determined.

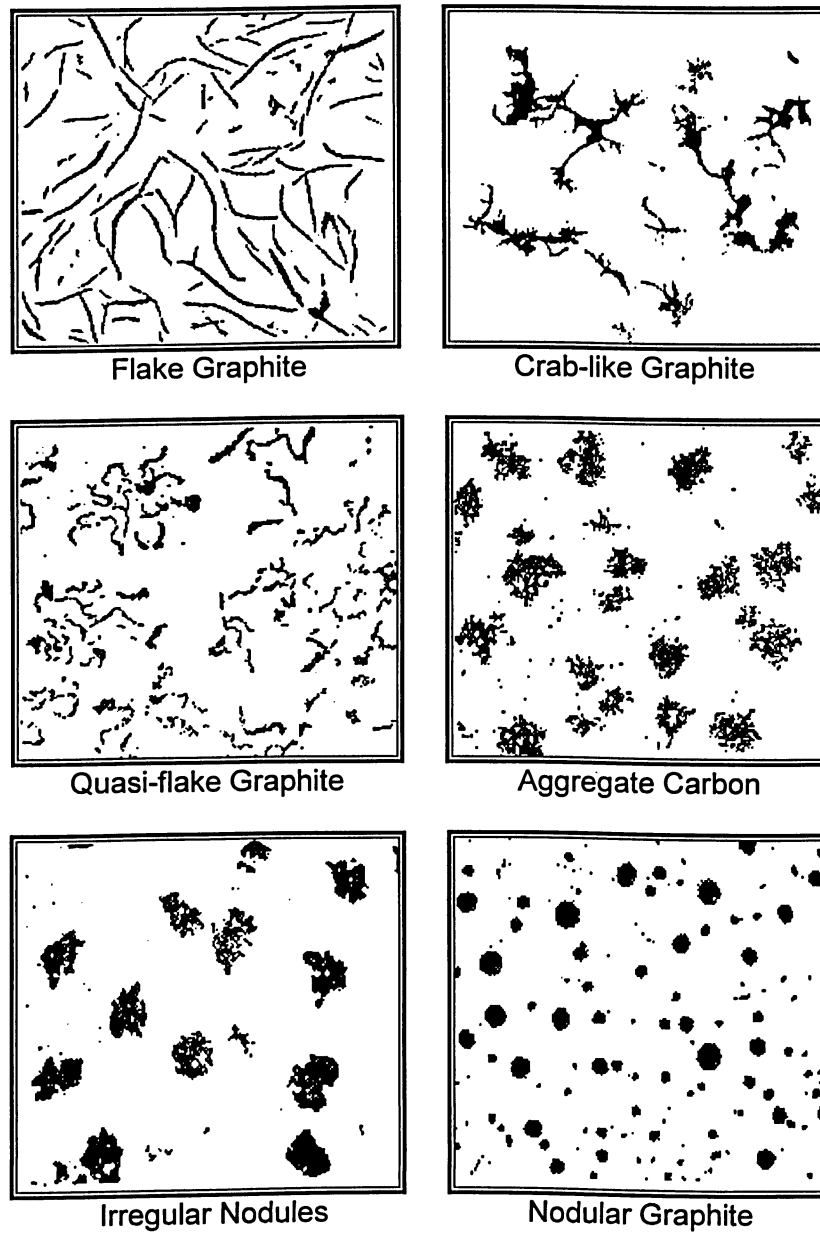

Figure 2.11: Various graphite geometries in a purely ferritic matrix (graphite classification based on ISO standards) [2].

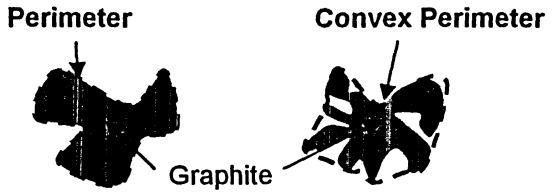

Figure 2.12: Schematic illustration of perimeter and convex perimeter used in Equations 2.5 and 2.6 according to Ruxanda, Stefanescu and Piwonka [85].

An acceptable nodule will have $S>0.65$ and $C>0.7$. The use of Equations 2.5 and 2.6 will depend on the quality of the shaped graphite and the magnification at which the analysis is carried out.

2.1.10.2 Graphite Nodule Count

Once graphite nucleation is initiated, the development of a sufficient number of graphite nodules becomes the most significant aspect of the solidification process [24]. The graphite nodule distribution will affect the final properties of ductile cast iron. Factors that dictate the number of nodules that will form are carbon equivalent, section size and type of spheroidizing treatment used [21,23,24,45]. The distribution of graphite nodules is most conveniently expressed as the number of nodules per unit area, *NA*. High carbon equivalents (i.e., > 4.65) will lead to low nodule counts. Similarly, the number of nodules per unit area will decrease with increasing section thicknesses. The addition of magnesium (a spheroidizing agent) will increase the *NA*. A decrease in the *NA* value below a certain threshold limit will hinder the feeding ability of a casting. This can eventually lead to shrinkage. Furthermore, if the *NA* value is low enough, primary carbides will form. It has also been shown that if graphite nodules are fine and uniformly distributed, a larger fraction of ferrite will be retained within the matrix. Conversely, if the graphite nodules are large and broadly spaced, pearlite and carbides will grow between the nodules. High nodule counts can also suppress the growth of dendrites, thereby reducing the possibility of interdendritic defects. To have a ductile cast iron of varying thickness that will maintain a reasonable level of strength at room and elevated temperatures, it is vital to establish a critical threshold limit for *NA*.

2.2 CASTING DEFECTS

Ductile cast iron alloys are ideal for elevated temperature use with respectable mechanical properties to compliment them. But, due to the high alloying concentrations and subsequent deleterious effects of some elements, this family of ductile irons is difficult to cast, resulting in many surface and subsurface defects. To help eliminate and prevent such defects from occurring, process parameters such as melt chemistry, melt temperatures, pouring, gating and moulding must be examined. Defects of primary concern include graphite floatation, dross and slag, pinhole porosity and shrinkage.

2.2.1 Graphite Floatation

The density of graphite is significantly less than that of iron. As a result, when iron is in its molten state, the precipitating graphite will float to the cope of the casting during solidification [24,86]. An example of graphite segregation at the cope surface is shown in Figure 2.13. Mechanical properties such as tensile strength are significantly reduced in cast irons containing localized regions of high carbon concentrations.

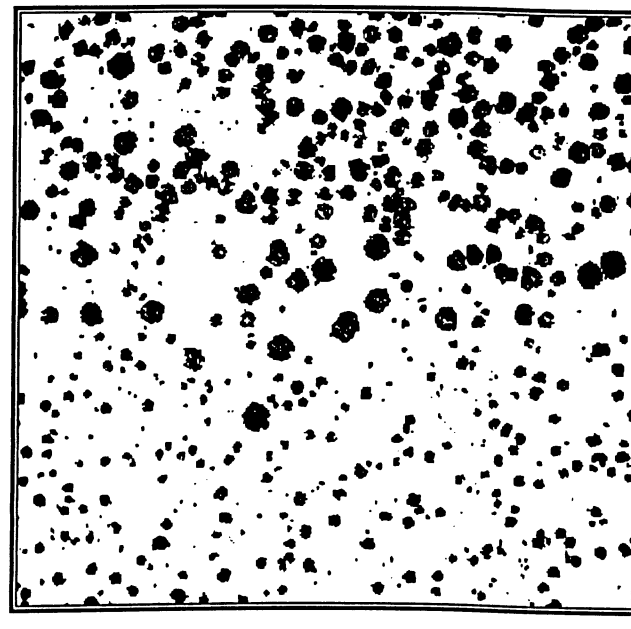

Figure 2.13: Graphite floatation in ductile cast iron [1].

Factors responsible for graphite floatation include the carbon equivalent (*CE*), section size and solidification rate [1,21,23,24,86]. If the carbon equivalent exceeds 4.5%, nodules will become sufficiently large, and thus subjected to significant buoyant forces. This will result in graphite nodules segregating near the upper portion of a casting. Graphite floatation effects are generally restricted to thicker cast sections that take longer to solidify.

It is vital to control the chemistry of the base melt before spheroidizing and inoculation treatments are added. To minimize the risk of graphite floatation, Equations 2.1 and 2.2 must be used to control the carbon and silicon contents. A similar relationship was developed by investigators involving the liquidus arrest temperature [86]. The carbon equivalent liquidus (*CEL*) relationship accounted for the effect of carbon, silicon and phosphorus (if present) upon the liquidus arrest temperature to prevent floatation [30,86]:

$$CEL = \%C + \frac{\%Si}{4} + \frac{\%P}{2} \qquad \text{Equation 2.7}$$

It is critical that the *CEL* value is not exceeded for a particular section size. Maximum *CEL* values for specific section sizes and pouring temperatures are given in Table 2.1.

Table 2.1: Maximum *CEL* values for specific section thicknesses and pouring temperatures [86].

Pouring Temperature (°C)	CEL Value			
	20mm	30mm	50mm	80mm
1315	4.56	4.52	4.44	4.31
1340	4.53	4.49	4.41	4.27
1370	4.50	4.46	4.38	4.24
1400	4.47	4.43	4.35	4.21
1425	4.45	4.40	4.32	4.19
1455	4.42	4.37	4.29	4.15

2.2.2 Dross and Slag

Dross and slag defects typically develop in grey, malleable and ductile cast irons during molten metal processing [86-91]. The predominant constituents of slag and dross are various oxides. Sources that promote the formation of these oxides include furnace refractories, fuel ash, ladle linings, oxidation during melting and oxidation or re-oxidation during pouring [88]. Much of the slag and dross is produced during the nodularization and subsequent inoculation of the cast iron.

Slag and dross contain oxides of iron (FeO) in addition to SiO_2, MnO (if manganese is present), MgO, Mg_2SiO_4 (fosterite), $2FeO{\cdot}SiO_2$ (fayalite), $MgO{\cdot}SiO_2$ (enstatite), Al_2O_3, FeO, CaO and Ce oxides [21,90,91]. If the carbon equivalent is high enough, certain slag films (that melt at high temperatures) can accompany the graphite nodules during floatation [21,92]. Once the casting has solidified, these types of slag films can be easily removed by grinding the cast surface. Conversely, lower melting slags can cause severe surface damage resulting in cavities. These slags change into dross, which is fluffy and occurs as chunks on the surface and sub-surface of a casting. Figure 2.14 illustrates typical slag and dross defects.

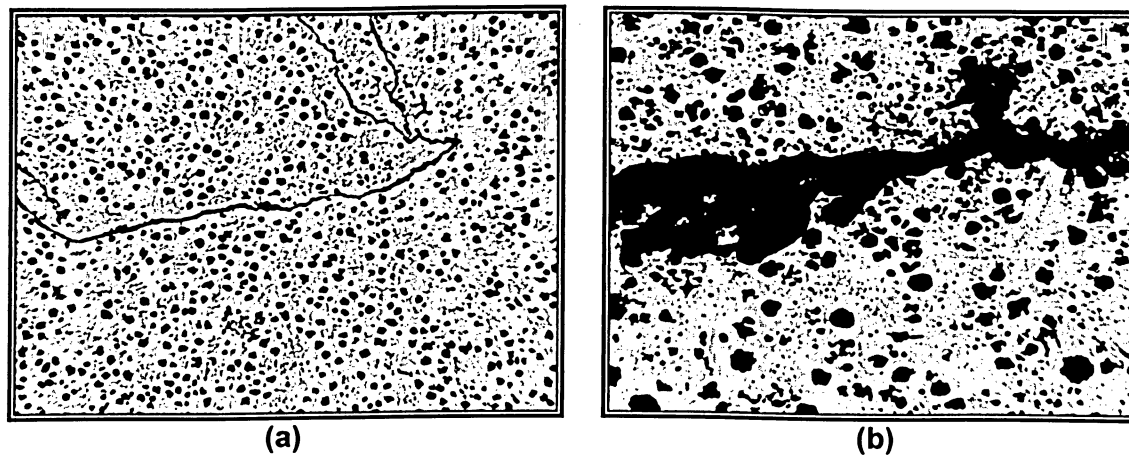

Figure 2.14: Optical micrographs of (a) slag and (b) dross [current research]. 50X.

Slag formation is temperature dependent [21]. It forms by re-oxidation as temperature decreases during tapping, pouring and within the mould cavity. Principal oxidation reactions involved in producing slag and dross are:

$$C + O_2 \rightarrow CO_2$$ Equation 2.8

$$\underline{C} + \underline{O} \rightarrow CO$$ Equation 2.9

$$Si + O_2 \rightarrow SiO_2$$ Equation 2.10

$$\underline{Si} + 2\underline{O} \rightarrow SiO_2$$ Equation 2.11

$$2Fe + O_2 \rightarrow 2FeO$$ Equation 2.12

$$2Fe + 2\underline{O} \rightarrow 2FeO$$ Equation 2.13

$$\frac{4}{3}Al + O_2 \rightarrow \frac{2}{3}Al_2O_3$$ Equation 2.14

$$2Mg + O_2 \rightarrow 2MgO$$ Equation 2.15

where $\underline{C}$, $\underline{Si}$ and $\underline{O}$ are, respectively, carbon, silicon and oxygen in solution. When the temperature of cast iron increases during heating through the eutectic and into the molten state, principal reduction reactions taking place include:

$$SiO_2 + \underline{C} \rightarrow \underline{Si} + 2CO$$ Equation 2.16

$$FeO + \underline{C} \rightarrow \underline{Fe} + CO$$ Equation 2.17

$$Al_2O_3 + 3\underline{C} = 2\underline{Al} + 3CO$$ Equation 2.18

where $\underline{Fe}$ and $\underline{Al}$ are, respectively, iron and aluminum in solution.

According to the Ellingham Diagram [93] (discussed in section 2.3.1), when liquid iron is above 1550°C, carbon monoxide gas (CO) is more stable than silicon dioxide (SiO_2). Consequently, carbon is preferentially oxidized and is lost at a higher rate than silicon. Silicon only begins to oxidize when a sufficient amount of carbon is used up. As a result, the liquid iron surface will remain film free, and any traces of SiO_2 will dissociate into free silicon (Equation 2.16) and dissolve into the melt forming CO [94]. The CO eventually escapes into the atmosphere. When the temperature of the melt falls below 1550°C, the relative stabilities of carbon monoxide and silicon dioxide are reversed. As temperatures reach 1400°C, a crusty film (slag) begins to form on the surface of the melt. With falling temperatures, the slag becomes a mixture of a solid phase (SiO_2) and a liquid phase (FeO), which eventually approaches the fayalite composition ($2FeO{\cdot}SiO_2$). Other constituents of the slag may include Al_2O_3 and CaO. A detailed discussion on slag formation is given by Heine [21].

2.2.3 Pinhole Porosity

Pinhole porosity is frequently observed in ductile cast irons. Variables that have a strong influence on this defect include metal chemistry, solidification rates, mould additions and gating design [95]. Pinhole porosity may arise through decreased solubility of dissolved gases in the solidifying melt, entrapment of gases in cores and moulds under pressure and the reaction of carbon with oxygen in the liquid metal [96]. In general, these defects are produced from gaseous by-products such as magnesium vapour, hydrogen, nitrogen or carbon monoxide.

2.2.3.1 Effect of Magnesium on the Formation of Pinhole Porosity

Pinholes develop when magnesium concentrations are high (~0.061wt.%) and pouring temperatures are low (<1345°C) [2,86,90]. Kaczmarek et al. [90] showed that pinholes in cast irons can be minimized by keeping magnesium levels low (approximately 0.035wt.%) and pouring temperatures high (approximately 1429°C). The area surrounding magnesium induced pinholes consists primarily of pearlite with minute traces of carbide [86].

Higher pouring temperature and alloying the magnesium with rare earth metals, such as cerium and lanthanum, can significantly reduce this type of defect. These increase the fluidity of the molten iron, thereby allowing the gases to escape more quickly.

Molten metal containing magnesium concentration up to 0.1wt.% has a tendency to absorb hydrogen from the walls of green sand moulds [95]. The presence of a strong deoxidizer such as magnesium will increase hydrogen availability by reacting with water vapour or steam produced during pouring [97]:

$$Mg + H_2O \rightarrow MgO + 2H$$ Equation 2.19

It has been observed that melts containing magnesium concentration above 0.1% continue to absorb hydrogen (Equation 2.19); however, pinhole formation at this magnesium concentration is suppressed. Dawson et al. [96] suggested the possibility of a diffusion barrier of magnesium oxide, but this did not account for the excess hydrogen. Naik and Wallace [95] suggested that the composition of the nodularizing compound may affect the reduction in hydrogen pickup at higher Mg concentrations. Some suggest the use of a Ni-Mg alloy for the nodularization of cast iron to reduce the susceptibility of hydrogen pickup by magnesium [98].

2.2.3.2 Effect of Hydrogen on the Formation of Pinhole Porosity

Pinhole porosity resulting from hydrogen is a common defect in cast irons [95,96]. The hydrogen content in cast iron typically varies between 0.00005% and 0.00025% [99]. However, this range is far exceeded when hydrogen is absorbed into the melt from the surrounding casting environment. Hydrogen absorption by liquid iron is associated with the dissociation of water vapour from the atmosphere or mould [90,96,100]. Some of the reactions may include [95,97,101,102,]:

$$C + H_2O \rightarrow CO + 2H$$ Equation 2.20

$$Fe + H_2O \rightarrow FeO + 2H$$ Equation 2.21

$$2Al + 3H_2O \rightarrow Al_2O_3 + 6H$$ Equation 2.22

The degree of H_2O dissociation and the solubility of hydrogen increase with an increase in the temperature of the melt [97].

Hydrogen pinholes are often spherical in shape and occur just below the surface of the casting [95]. The outer ring of these pinholes is often surrounded by a ferrite microstructure with minute quantities of flake graphite coating the inner surface of the pinhole [95,96].

2.2.3.3 Effect of Nitrogen on the Formation of Pinhole Porosity

Nitrogen gas is inert and generally remains in solution [97]. Nitrogen concentrations in cast iron typical range from 0.0015% to 0.01% [99]. Nitrogen contents in excess of this range will cause holes to form [96]. This defect becomes more pronounced in thicker sections due to the low rate of diffusion of nitrogen through iron, thus drawing the distinction between nitrogen and hydrogen (having a high rate of diffusion through iron) induced defects. Liquid iron nitrogen contents can increase through the absorption and dissociation of ammonia from nitrogen-rich resin-bonded moulds [95]. The decomposition product of the binder is ammonia (NH_3) and the reaction to produce N and H follows through as [95,103]:

$$NH_3 \rightarrow N + 3H$$ Equation 2.23

2.2.3.4 Effect of Aluminum on the Formation of Pinhole Porosity

Aluminum contributes to the formation of pinholes by producing free hydrogen [96,97]. Aluminum produces hydrogen by reducing the water vapour created during pouring of the metal (Equation 2.9). It has been shown that pinhole formation subsides when aluminum levels are below 0.01wt.% [104]. It was also shown that aluminum concentrations above 0.2wt.% eliminated much of the pinholes in ductile irons [105]. Carter et al. [106] further supported this finding when they concluded that pinholes did not exist at aluminum

concentrations of 0.33wt.%. The severity of pinhole formation is known to increase when aluminum is in the range 0.045 to 0.060wt.% [86].

2.2.3.5 Effect of Carbon on Formation of Pinhole Porosity

Carbon reacts with oxygen to form carbon monoxide (CO). During processing, entrapment of this gaseous compound will create pinholes [96]. Some investigators have suggested that CO is the primary pinhole producer, ahead of hydrogen [107,108]. When alloying additions were made to reduce the oxidation of carbon, it was observed that the castings produced were free of pinholes, even though the hydrogen concentration was high [95]. The literature suggests melts with high carbon readily react with the slag (Equation 2.17) to produce CO. If this gas becomes entrapped in the solidifying melt, pinholes will nucleate [86,90,96].

2.2.4 Shrinkage Defects

Metal and mould conditions influence the onset of shrinkage in cast irons [109-111]. Contributing metal variables include carbon equivalent, inoculation, nodule count and pouring temperature. The contributing mould variables are geometry and stability.

It was shown by Henderson [32] that if the *CE* (Equation 2.1) was below 3.9, shrinkage would subsist. Wallace et al. [109] and Li et al. [110] reconfirmed this from their experiments. However, Wallace et al. [109] observed that a large casting (approximately 11.5mm in diameter) with high *CE* values (4.2 to 4.4) experienced a considerable amount of shrinkage, especially in a green sand mould. This occurrence was related to the high *CE* in iron and the consequent inability to overcome the effect of mould expansion, particularly in large sections. As a result, Wallace et al. [109] concluded that the shrinkage difference experienced from variations in mould dilation was much more significant than variations attributed to *CE*.

Wallace et al. [109] also reported that the pouring temperature had some effect on the shrinkage behaviour of cast irons. It was suggested that higher pouring temperatures could increase the occurrence of liquid contraction, which may contribute to shrinkage. But, this effect is generally compensated by risers. Pouring temperatures also affect the stability of

the mould. The thermal expansion of the mould can increase at higher temperatures, thereby increasing the probability of developing shrinkage.

Inoculation of cast iron has a significant impact on shrinkage as well. Wallace et al. [109] showed that higher inoculation resulted in the formation of shrinkage. A well inoculated melt increases the nodule count. When the nodule count is too high, resistance to metal flow dilates the mould cavity, thereby increasing the susceptibility to shrinkage. Castings with nodule counts exceeding 200 nodules per square millimetre showed a higher susceptibility to shrinkage than irons containing fewer nodules.

When shrinkage defects are analyzed, they are divided into two categories: microshrinkage and macroshrinkage. Microshrinkage (Figure 2.15(a)) occurs in the late stages of solidification [111]. Thickness of the mushy molten iron alloy restricts metal flow to the interdendritic regions. Microshrinkage typically develops between the eutectic cells. Macroshrinkage (Figure 2.15(b)) forms during the initial stages of eutectic solidification when feeding of the molten metal stops [111].

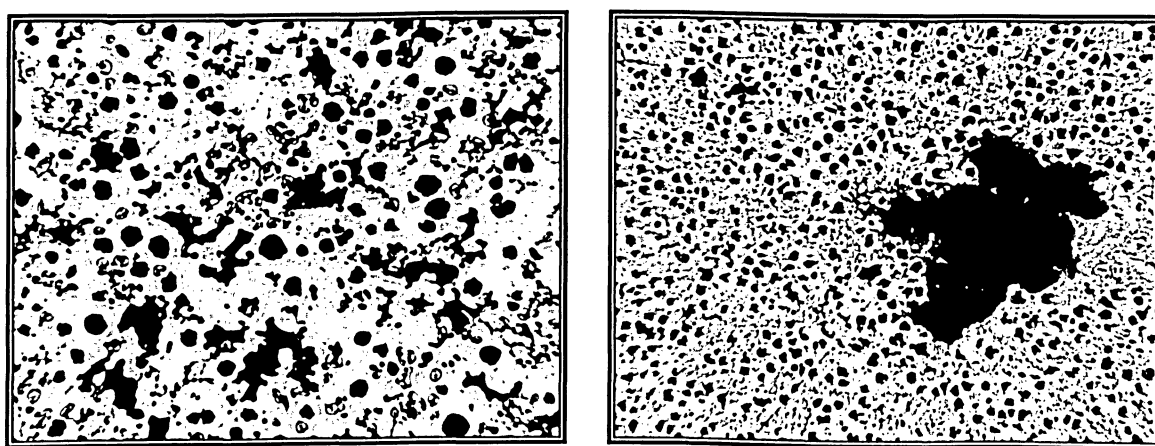

Figure 2.15: Optical micrographs of (a) microshrinkage and (b) macroshrinkage [current research]. 50X.

2.3 OXIDATION CHARACTERISTICS of DUCTILE IRON ALLOYS

2.3.1 Thermodynamics of Metal-Oxide Stability

Metal-oxide stability can be quantitatively determined from Ellingham's [93] plot, illustrated in Figure 2.16. This diagram illustrates the standard free energy of formation (ΔG°) [J] of metal oxides per mole of O_2 as a function of temperature. The variation of ΔG° with temperature can be expressed as [112]:

$$\Delta G^{o} = \Delta H^{o} - T\Delta S^{o} \qquad \text{Equation 2.24}$$

where ΔH° is the temperature-independent standard enthalpy change for the reaction [J] and ΔS° is the negative of the temperature-independent standard entropy change for the reaction [J/K]. On the Ellingham diagram, the length of the intercept parallel with the temperature axis represents the enthalpy of the system. The entropy term is represented by the slope of the reaction line.

The stability of oxides can also be expressed in terms of oxygen pressure (p_{O_2}) of the gas phase with which the metal and its lowest oxide coexist in equilibrium. The partial pressure of oxygen is related to the free energy of formation through the following relation [112]:

$$\Delta G^{o} = RT \ln p_{O_2} \qquad \text{Equation 2.25}$$

where ΔG° is the standard free energy of formation [J], R is the universal gas constant [8.314 J/mol-K], T is the temperature [K] and p_{O_2} is the oxygen gas at 1 atmosphere pressure.

When a metal (Mg, Fe, Al or Si) reacts with a gas (O_2) to form an oxide (MgO, FeO, Al_2O_3, SiO_2) the disappearance of the gas phase will cause the entropy of the system to decrease. If ΔS° becomes negative, then ΔG° will be less negative with increasing temperature.

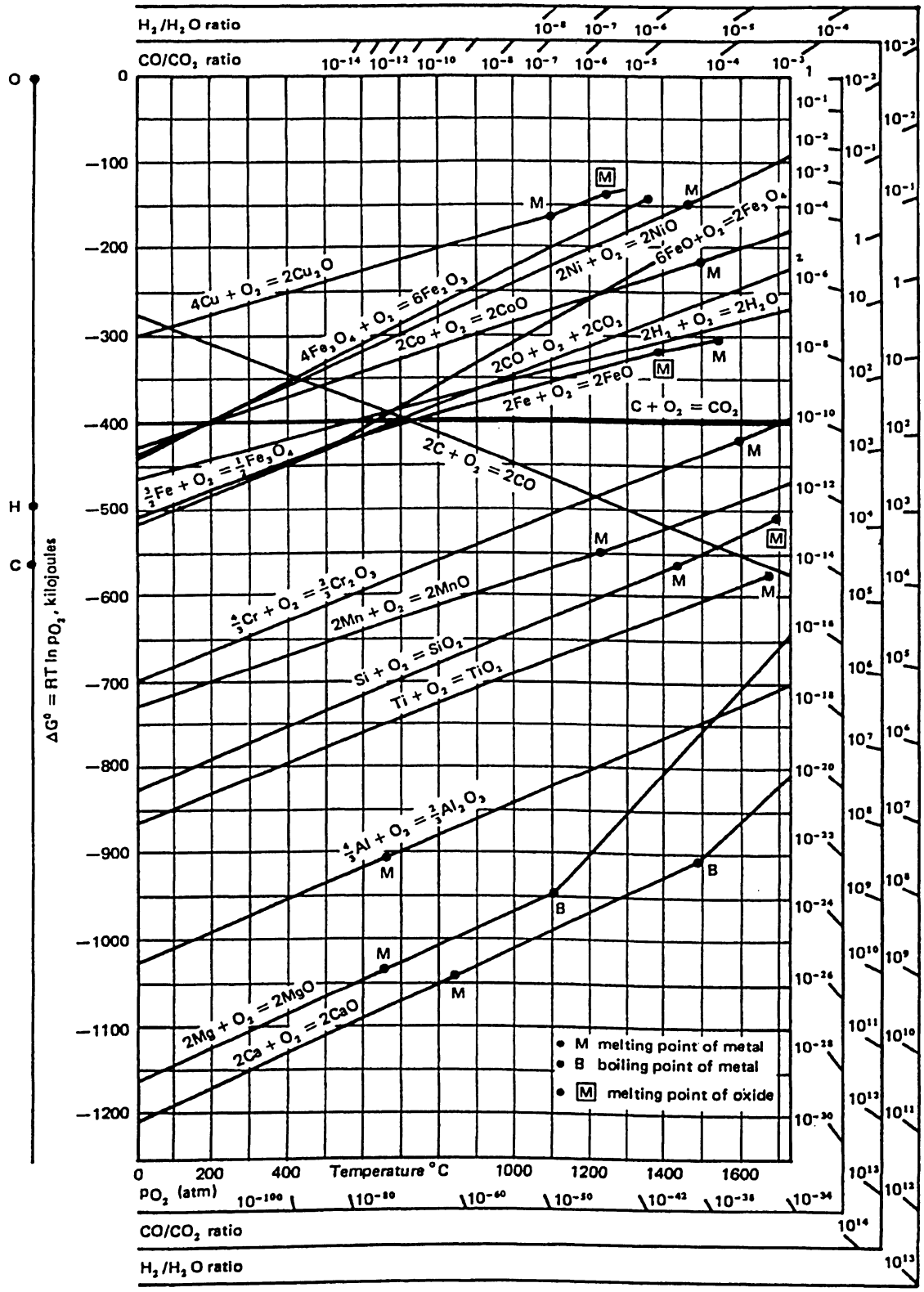

Figure 2.16: The Ellingham diagram for selected oxides (Gaskell [112]).

This will result in a positive slope of the free energy curve (i.e., CaO, MgO, FeO, Fe_2O_3, Fe_3O_4, Al_2O_3, SiO_2, MnO, etc.). When one mole of gas (CO_2) is formed for each mole of gas (O_2) that reacts, the ΔS° of the system will remain at zero. This will result in a horizontal ΔG° curve (i.e., pure metal and gas are in equilibrium). When two moles of gas (2CO) are formed for each mole of gas (O_2) consumed, the ΔS° of the system will increase and become positive. This will result in a ΔG° curve with a negative slope [112]. The curve of 2CO demonstrates that at high temperatures, carbon is a much stronger reducing agent for oxides than at low temperatures.

At the top of the Ellingham diagram, ΔG°=0 because the free energy of formation is negative for most metal oxides. The oxygen partial pressure (p_{O_2}) is taken as 1 atmosphere. As ΔG° becomes a negative quantity, p_{O_2} will be less than 1 atmosphere. For any oxidation process, the value of ΔG° is the measure of the chemical affinity of the metal for oxygen. As ΔG° becomes more negative, the stability of an oxide increases. A detailed discussion on the Ellingham diagram is given by Gaskell [112].

2.3.2 Oxidation Kinetics of As-Cast Ductile Iron Alloys

The oxidation behaviour of cast iron in air or oxygen has been studied by many investigators [13,14,28,113-115]. High-temperature oxidation of iron is considered to be a special phase of metallic corrosion [113]. Corrosion of metallic materials can occur in either aqueous solutions or gaseous atmospheres during low or high temperature regimes.

When cast iron is exposed to an oxygen rich atmosphere at temperatures in excess of 700°C, a thin oxide layer develops on the surface that gradually increases in thickness with increasing temperatures [116]. During the initial stages, oxidation of cast iron proceeds intensely at the eutectic cells and graphite which are protruding along the surface of the specimen [13].

Once the oxide layer matures, further oxidation is restricted [13]. The oxide scale formed on cast iron is composed of FeO (wüstite), Fe_3O_4 (magnetite) and Fe_2O_3 (haematite) [113]. The oxide content of this scale changes with the addition of alloying elements (i.e., Al, Si, Mg, etc.). Formation of the oxide layer occurs by the diffusion of metal ions away

from the metal-scale interface while oxygen ions simultaneously diffuse towards this interface [117]. This electro-chemical process is represented schematically in Figure 2.17.

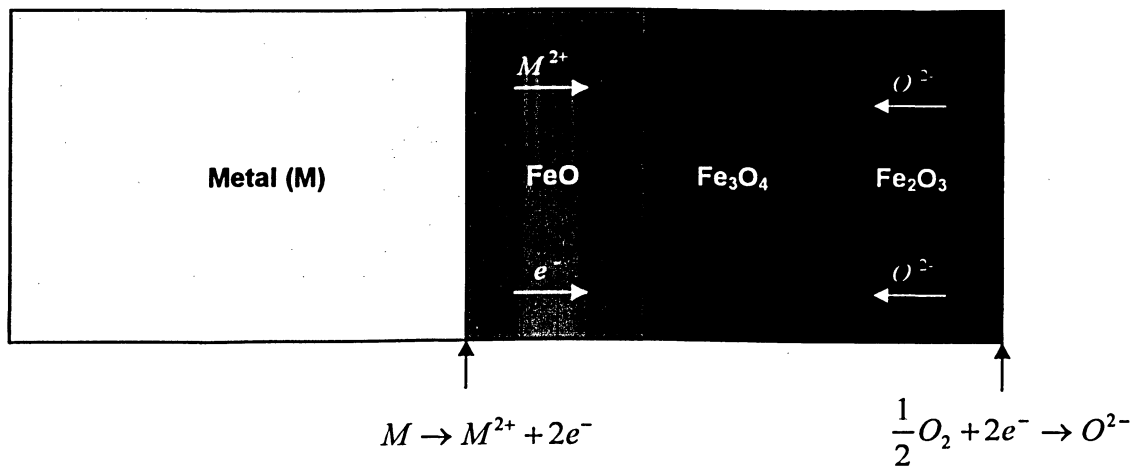

Figure 2.17: Schematic representing the direction and exchange of metal and oxygen ions during the oxidation and reduction reactions [current research].

The active reaction mechanisms in the oxidation of iron are [113,116]:

$$M \rightarrow M^{2+} + 2e^- \qquad \text{Equation 2.26}$$

$$\frac{1}{2}O_2 + 2e^- \rightarrow O^{2-} \qquad \text{Equation 2.27}$$

where M^{2+} are the metal ions, O^{2-} are the oxygen ions and $2e^-$ are the electrons.

When cast iron is alloyed with silicon and aluminum, the internal scale or sub-scale layer will contain multiple oxide systems that can combine with FeO to form Fe_2SiO_4 (fayalite) and $FeAl_2O_4$. It is not uncommon for internal double phase scales such as $FeO+Fe_2SiO_4$ and $FeO+FeAl_2O_4$ to form [118]. These oxide systems give high-temperature resistance to cast irons alloyed with silicon and aluminum. They produce a compact non-permeable scale that reduces the amount oxygen ions diffusing through to the interior, consequently hindering further oxidation of the iron [13].

During the initial stages of oxidation, intense decarburization of cast iron occurs. Measurable carbon loss typically occurs at temperatures in excess of 800°C [119,120].

During oxidation, carbon reacts with the scale according to Equation 2.17 [119,120]. CO may react further with FeO to produce CO_2 [119,120]:

$$CO + FeO \rightarrow Fe + CO_2 \qquad \text{Equation 2.28}$$

These reactions can only proceed when CO and CO_2 are allowed to escape through the oxide layer. If release of the CO gas is prohibited, the oxide scale can rupture. Once the protective scale is ruptured, the kinetics of oxidation can be reactivated [120].

2.3.2.1 Diffusion in Metals and Oxides

Diffusion is the transport of material by atomic motion. The net flux of species (atoms, ions, electrons and molecules) depends on the initial concentration gradient and temperature. The ability of migrating species to diffuse through matter increases as the temperature or thermal energy of the species increases. Stepwise migration of atoms or ions can occur either by moving to a nearby vacancy within the crystal lattice or by moving from one interstitial lattice site to another [47,116,121]. The latter diffusion mechanism applies to atoms small enough (e.g., hydrogen, carbon, nitrogen and oxygen) to fit into the interstitial positions of the host lattice (e.g., iron).

The magnitude of the self-diffusion coefficient is related to temperature through the Arrhenius relation [122]:

$$D = D_o \exp\left(\frac{-Q}{RT}\right) \qquad \text{Equation 2.29}$$

where D is the self-diffusion coefficient [m^2/s], D_o is a frequency factor [m^2/s], Q is the activation energy [J/mol], R is the universal gas constant [8.314 J/mol-K] and T is the absolute temperature [K]. Q is the activation energy required to overcome the energy necessary to move the atoms or ions from one position to another. It can also be used to relate the migration and formation energy of the defect in the case of a vacancy mechanism [116].

The diffusion of atoms may occur either by steady-state or non-steady state. In steady-state diffusion, the diffusion flux is proportional to the concentration gradient. This is expressed using Fick's first law [116]:

$$J = -D\frac{dC}{dx} \qquad \text{Equation 2.30}$$

where J is the diffusion flux [kg/m^2-s], D is the self-diffusion coefficient [m^2/s], dC is the change in the concentration gradient [kg/m^3] and dx is the change in distance. In most cases the initial magnitude of the flux is high and decreases with time. For transient diffusion to progress, the diffusion flux and the concentration gradient at some particular point within the solid must vary with time. This phenomenon is expressed using Fick's second law [116]:

$$\frac{\partial C}{\partial t} = \frac{\partial}{\partial x}\left(D\frac{\partial C}{\partial x}\right) \qquad \text{Equation 2.31}$$

If the diffusion coefficient is assumed not to be a function of x and c of the diffusing species, Equation 2.31 simplifies to:

$$\frac{\partial C}{\partial t} = D\frac{\partial^2 C}{\partial x^2} \qquad \text{Equation 2.32}$$

Arrhenius plots of metal and oxygen self diffusion coefficients are given in Figure 2.18. From the Arrhenius plots, the difference in magnitude of the diffusion coefficients for metal and oxygen in iron oxides can be shown as:

$$D_{\frac{Fe}{Fe_2O_3}} < D_{\frac{O}{Fe_2O_3}} < D_{\frac{Fe}{Fe_3O_4}} < D_{\frac{Fe}{FeO}} < D_{\frac{O}{FeO}} \qquad \text{Equation 2.33}$$

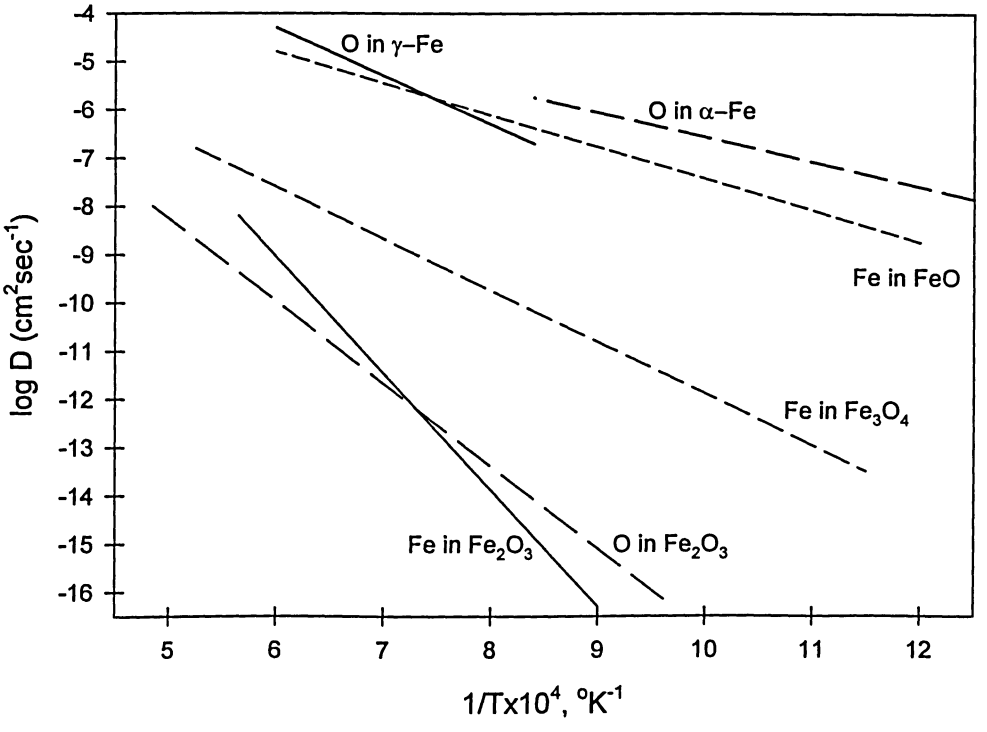

Figure 2.18: Arrhenius plots of metal and oxygen self-diffusion coefficients in iron and iron oxides [116].

2.3.2.2 Oxide Layer Formation at High Temperatures

When iron is exposed to very high temperatures, a complex multi-layered oxide film composed of wüstite (FeO), magnetite (Fe_3O_4) and haematite (Fe_2O_3) develops. The iron-oxygen phase diagram in Figure 2.19 illustrates the regions in which particular iron oxides develop. The initial oxide film protects the metallic surface from further contact with oxygen. If the volume of the initial film is less then the metal it replaces, a cellular scale will form; if the opposite occurs, a homogeneous oxide layer will form. A volumetric ratio relating the volume of oxidizing metal to the volume of oxides forming was developed by Pilling and Bedworth [113]:

$$\frac{M_{oxide}\rho_{metal}}{M_{metal}\rho_{oxide}} \qquad \text{Equation 2.34}$$

where M_{oxide} is the molecular weight of the oxide, M_{metal} is the molecular weight of the metal, ρ_{oxide} is the density of the oxide and ρ_{metal} is the density of the metal. A metal may form a uniformly thick oxide scale when the volume ratio is greater than 1. If it is less then 1, the scale will contain a cellular structure.

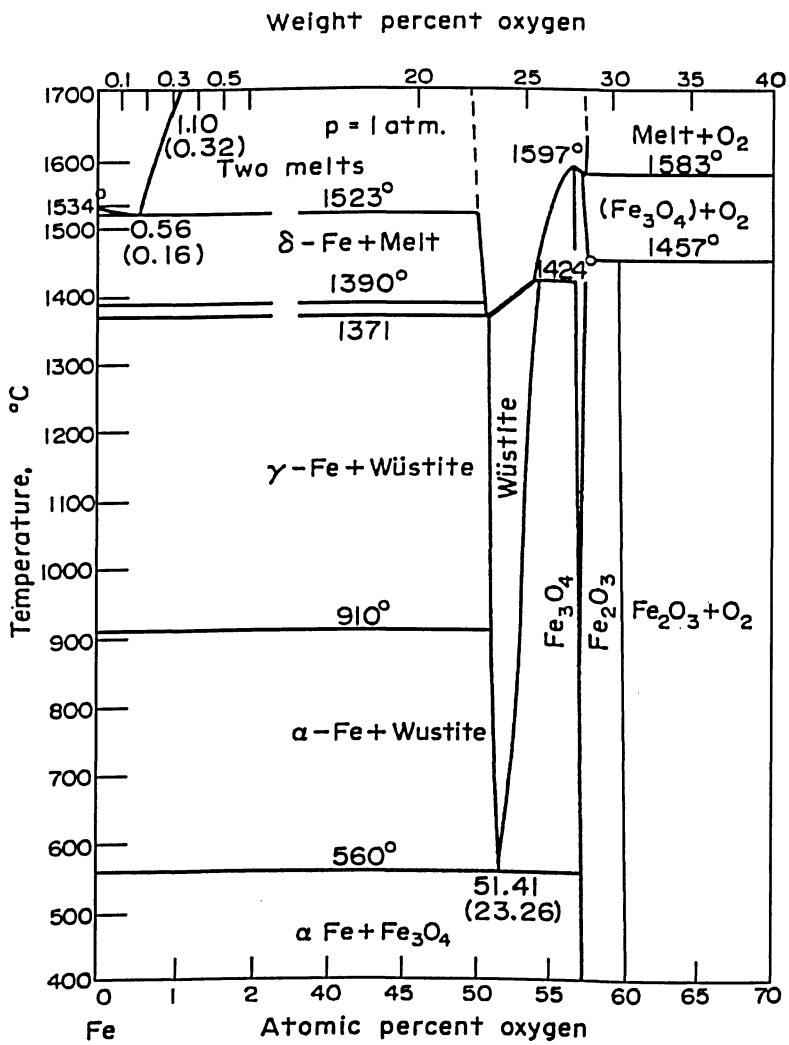

Figure 2.19: Iron-oxygen phase diagram [123].

When iron is exposed to temperatures ranging from 700 to 1250°C, a parabolic relationship exists between the weight gain of the oxide scale per unit area and time [120]. The isothermal parabolic oxidation kinetics of iron during steady-state migration of reactants can be described using Tammann's [124] relationship:

$$\frac{dy}{dt} = \frac{p}{y} \qquad \text{Equation 2.35}$$

$$y^2 = 2pt \qquad \text{Equation 2.36}$$

where y denotes the total scale thickness, t is the oxidation time and $2p$ is the parabolic rate constant measured in cm^2sec^{-1}. The parabolic rate constant is exponentially dependent on temperature and can be expressed as [120]:

$$k_T = k_o \exp\left(\frac{-Q}{RT}\right) \qquad \text{Equation 2.37}$$

where $k_T=2p$ [m^2/s], k_o is a constant [m^2/s], Q is the activation energy [J/mol], T is temperature [K] and R is the universal gas constant [8.314 J/mol-K]. Wagner [125] demonstrated that the activation energy required to oxidize iron was equivalent to the activation energy required for iron diffusion in FeO (wüstite) [125]. Furthermore, the diffusion coefficient of iron in wüstite is much larger than in magnetite and the diffusion of oxygen and iron through the haematite layer is very small (Figure 2.18 and Equation 2.33). This constitutes the relative thickness of each layer. Following Tammann's approach, Païdassi [115] showed that for the parabolic temperature range, the relative thickness ratio of Fe_2O_3, Fe_3O_4 and FeO layers versus the total thickness of the oxide layer was constant at 1:4:95, respectively. The rate constant was also determined as:

$$k_T = 6.1 \exp\left(\frac{-169452}{RT}\right) \qquad \text{Equation 2.38}$$

Later, Pilling and Bedworth [113] developed a parabolic relationship based on the diffusion path for a given concentration difference of migrating species. They postulated that the rate of diffusion was inversely proportional to the length of the diffusion path. Based on the understanding that the oxygen that diffuses through the oxide layer is used to increase the volume of the oxide layer, Pilling and Bedworth [113] proposed the following relationship:

$$\frac{dW_{PB}}{dt} \propto \frac{1}{H} \qquad \text{Equation 2.39}$$

where W_{PB} is the quantity of oxygen and H is the thickness of the scale:

$$W_{PB} \propto H \qquad \text{Equation 2.40}$$

$$\frac{dW_{PB}}{dt} = k_{PB}\left(\frac{1}{W_{PB}}\right) \qquad \text{Equation 2.41}$$

$$W_{PB}^{\ 2} = 2k_{PB}t \qquad \text{Equation 2.42}$$

where k_{PB} is the constant of proportionality measured in $mg^2\text{-}cm^{-4}sec^{-1}$. By measuring the weight gain per unit area (W_{PB}) of a sample after time t, the parabolic oxidation constant k_{PB} can be calculated.

Theories advanced by Wagner have been proposed to account for the parabolic growth of scales based on ambipolar diffusion (charge migration under local electroneutrality) of the reactants. These theories are, however, beyond the scope of this review and will not be discussed any further. A detailed review on Wagner's theory is given by Smeltzer and Young [116].

Chapter 3

Experimental Procedure

3.1 Experimental Plan

Ductile cast iron alloyed with 1.5wt.% molybdenum and different combinations of silicon and aluminum was cast at three different pouring temperatures (i.e., 1350, 1400 and 1450°C). This is schematically represented in Figure 3.1. The criteria used for evaluating these experimental ductile iron alloys were microstructure, oxidation resistance and transformation temperatures. In the as-cast condition, the effects of pouring temperature, chemical composition and section thickness on the microstructure of these castings were studied (Figure 3.2). At 700, 800, 900, 1000 and 1100°C for 500 hours, the oxidation characteristics of these castings were studied through weight change, oxidation rate and x-ray mapping of the oxide scale (Figure 3.3).

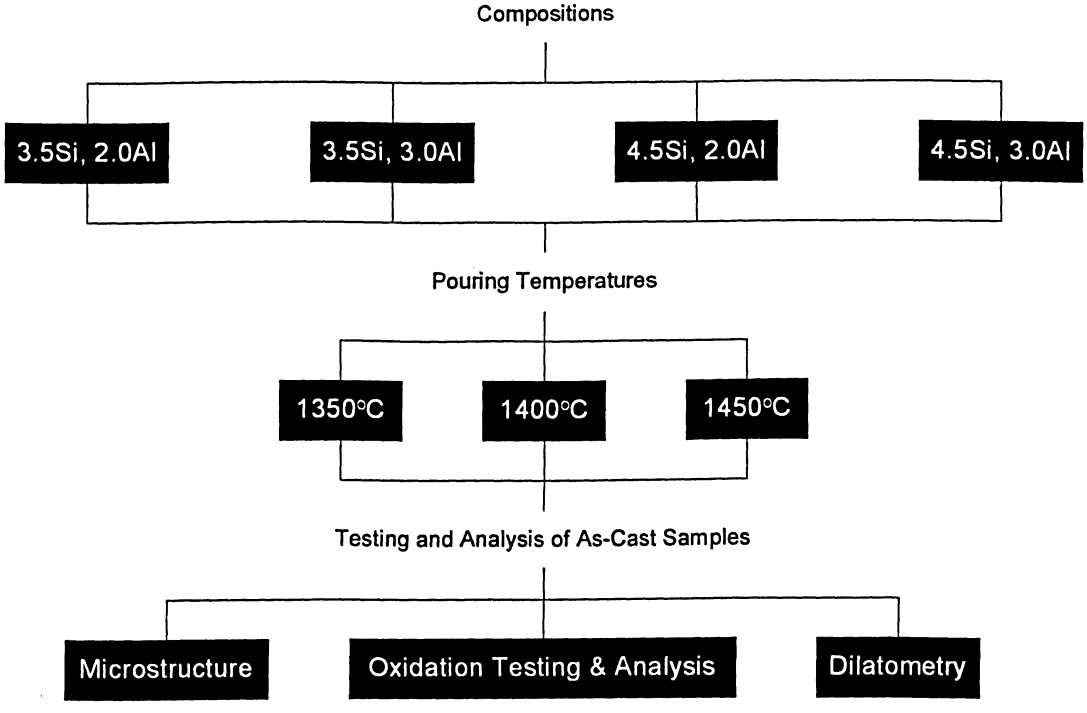

Figure 3.1: Flowchart of the experimental plan.

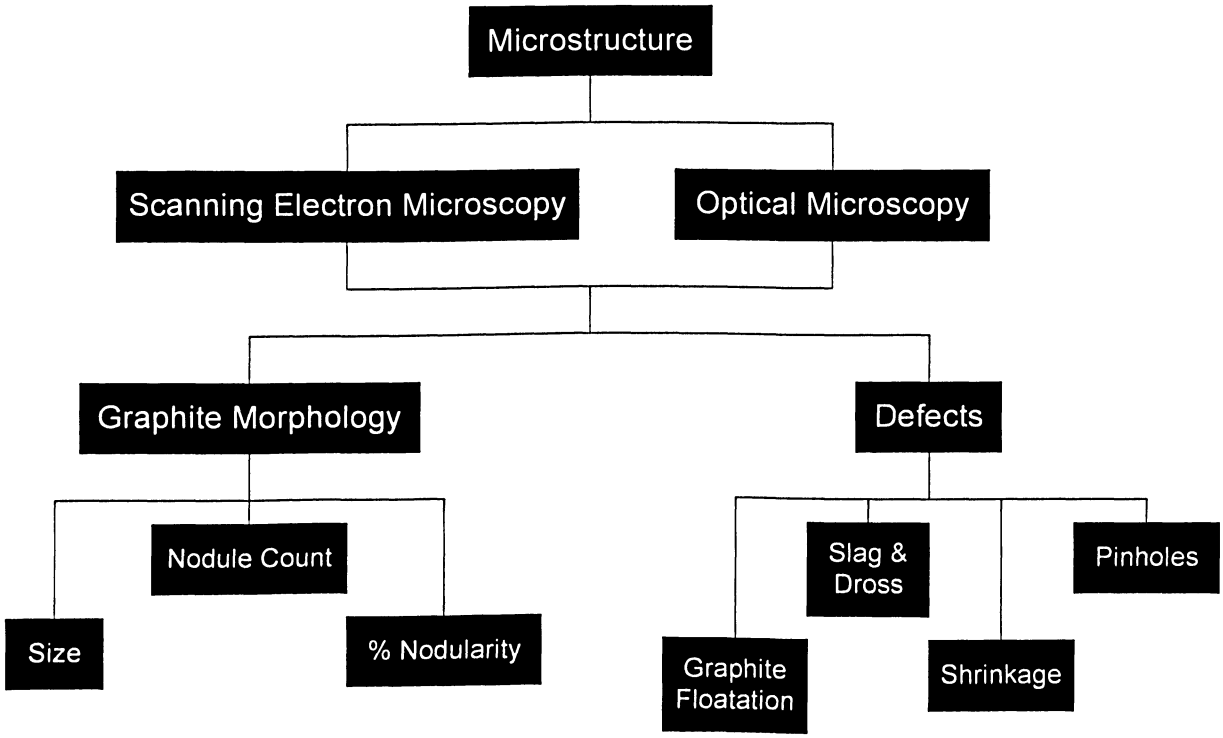

Figure 3.2: Flowchart representing characterization of as-cast samples.

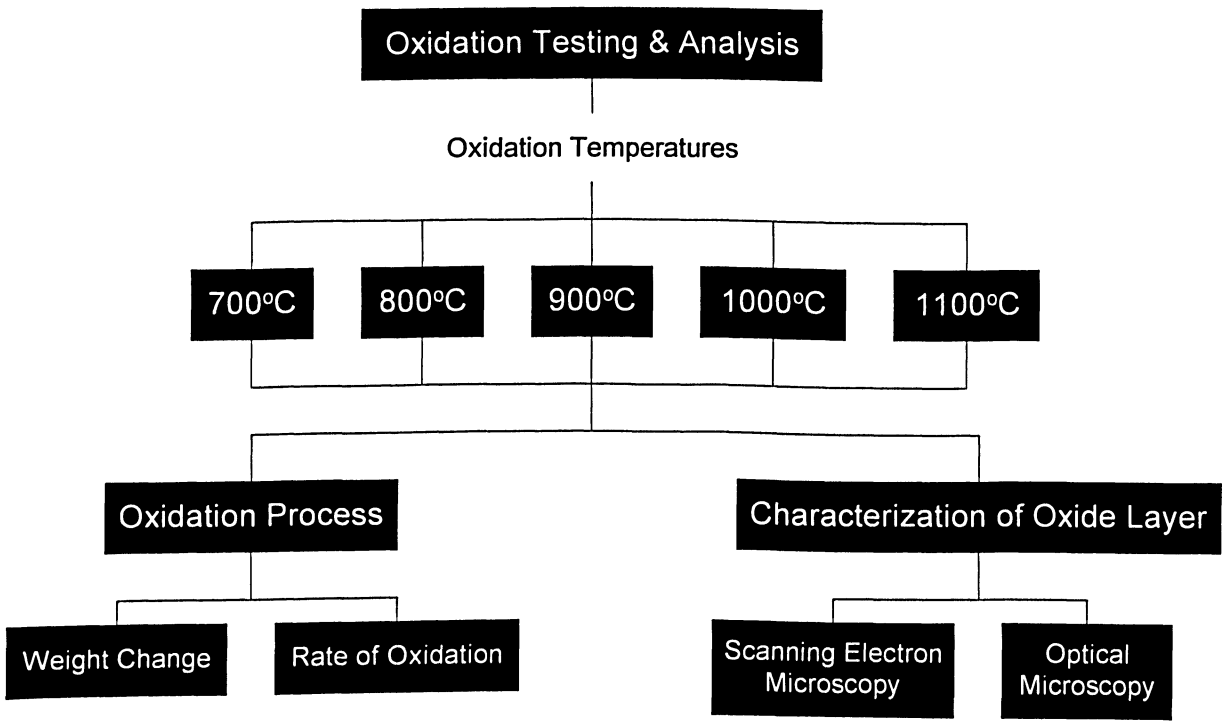

Figure 3.3: Flowchart of testing and analysis of oxidized samples.

3.2 MOULD MEDIUM and GEOMETRY

The iron specimens were cast into a stepped green sand mould with section thicknesses of 4, 7, 14, 22 and 34mm. The stepped mould was developed by Wescast Industries Inc. and is illustrated in Figure 3.4(a). The final cast product is shown in Figure 3.4(b). Detailed dimensioning of the mould is given in Appendix A.

To include a repeat casting under identical conditions, two stepped moulds were simultaneously cast using one sprue and a common runner bar.

Once the green sand was prepared for moulding, the H_2O content and compression strength were tested. Using an electronic MB40 Moisture Content Analyzer (*MCA*), the green sand was subjected to an enclosed atmosphere temperature of 110°C. The released H_2O vapours were analyzed and measured. The moisture content ranged from approximately 2.99% to 3.54%.

The green sand strength was analyzed using the 490A Sand Strength Machine (*SSM*). A 165g sample was compacted into a cylinder 50mm in diameter and 50mm in length. The compacted cylindrical sample was subjected to a compression test. The compressive strength of the green sand used for moulding was in the range of 150.31kPa to 153.07kPa.

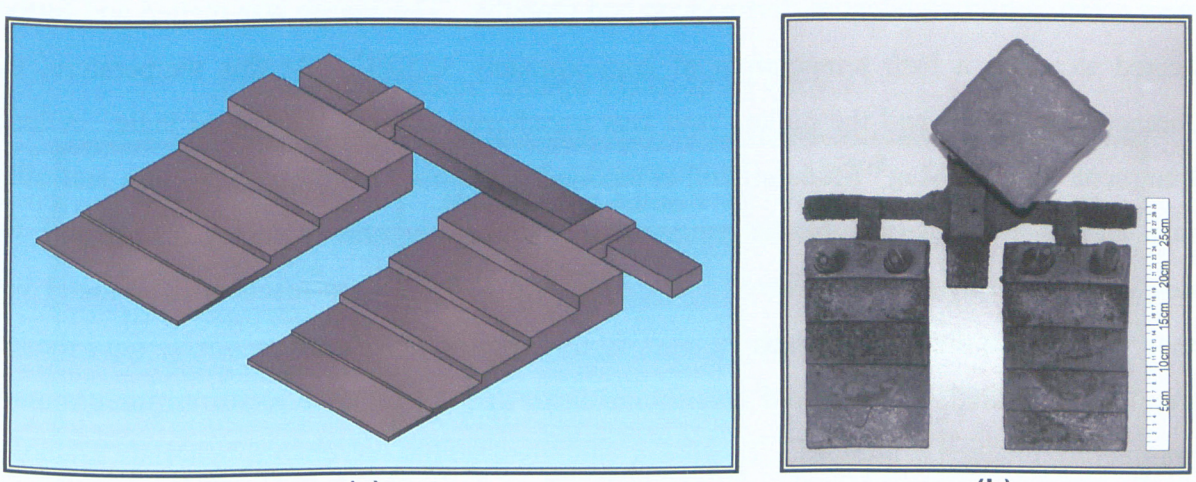

Figure 3.4: (a) A model of step block pattern used to produce experimental castings and (b) final casting produced in green sand.

3.3 MELTING and CASTING

Four heats of the new ductile cast iron alloys were produced using an induction furnace. The procedure consisted of producing cast samples at three different pouring temperatures (i.e., 1350, 1400 and 1450°C) and four different chemistries. The aim chemistry for each alloy is tabulated in Table 3.1. A *CE* value of 4.6 was maintained for each alloy.

Table 3.1: Chemical composition of iron for each heat.

Element	Chemical Composition (wt.%)			
	Alloy 1	Alloy 2	Alloy 3	Alloy 4
Si	3.5	3.5	4.5	4.5
C	3.43	3.43	3.10	3.10
Al	2.0	3.0	2.0	3.0
Mo	1.5	1.5	1.5	1.5

The induction furnace was charged with pig iron, SiMo ductile cast iron returns, 1010 steel scrap, ferromolybdenum, ferrosilicon and graphite. The charge was melted and further heated to reach a bath temperature of approximately 1550°C. At this temperature, the furnace was tapped and the molten iron was transferred into the pre-heated ladle. A ladle treatment with Re-Mag® (nodularizing compound containing magnesium, cerium and other rare earths) was made. After tapping, the ladle temperature was monitored until the designated pouring temperatures of 1450, 1400 and 1350°C were reached. The metal was then poured into the basin of each mould. Monitoring the time from tap out, t_o, until the last mould was poured, t_f, monitored magnesium fade. The target time to fill all three moulds was approximately 8 minutes. The basin contained additional charge materials including aluminum, cerium and Ultraseed® (75% Si, 1.75% Ce, 1% Al, 1% Ca with the rest being Fe coated with S to increase inoculation potential). The detailed charge make up is in Tables 3.2-3.5.

When the molten metal was poured into the basin a ceramic stopper closed the exit to the downsprue until the basin was filled. Once the basin was full, the melt was allowed to settle for approximately three seconds. This allowed the molten bath from the ladle to dissolve additional elements added to the basin, thus ensuring the necessary chemistry to produce cast iron samples for a given heat.

Table 3.2: Charge make-up for Alloy 1.

Charge Material	Weight (lbs)	Furnace Addition	Ladle Addition	Basin Addition
Si-Mo Returns	210			
1010 Steel Slugs	90			
Ferromoly	5.84			
Ferrosilicon	1.700			
Graphite	4.340			
RE-mag®	1.862			
Ultraseed®	0.018			
Cerium	0.026			
Aluminum	0.632			

Table 3.3: Charge make-up for Alloy 2.

Charge Material	Weight (lbs)	Furnace Addition	Ladle Addition	Basin Addition
Si-Mo Returns	105			
1010 Steel Slugs	45			
Ferromoly	2.920			
Ferrosilicon	0.850			
Graphite	2.170			
RE-mag®	1.793			
Ultraseed®	0.018			
Cerium	0.039			
Aluminum	0.949			

Table 3.4: Charge make-up for Alloy 3.

Charge Material	Weight (lbs)	Furnace Addition	Ladle Addition	Basin Addition
Si-Mo Returns	105			
1010 Steel Slugs	45			
Ferromoly	2.970			
Ferrosilicon	3.110			
Graphite	1.670			
RE-mag®	1.814			
Ultraseed®	0.018			
Cerium	0.026			
Aluminum	0.632			

Table 3.5: Charge make-up for Alloy 4.

Charge Material	Weight (lbs)	Furnace Addition	Ladle Addition	Basin Addition
Si-Mo Returns	105			
1010 Steel Slugs	45			
Ferromoly	2.970			
Ferrosilicon	3.110			
Graphite	1.670			
RE-mag®	1.814			
Ultraseed®	0.018			
Cerium	0.039			
Aluminum	0.949			

Prior to pouring the molten bath into the basin, a sample of the melt was taken and analyzed using an emission spectrometer. The sample was cast into a disk, 40mm in diameter and 2mm thick, using a copper chill. The disc was analyzed for carbon, silicon, molybdenum and magnesium, essentially the main constituents of the ladle chemistry.

3.4 HIGH-TEMPERATURE OXIDATION TESTING

With a view to understanding the effects of chemical composition, pouring temperature and section thickness on the oxidation properties of iron; specimens were heated in an ambient air heat treatment furnace to 700, 800, 900, 1000 and 1100°C for 500 hours. Figure 3.5 shows the approximate location where the specimens were extracted from for each particular test. The oxidation tests were carried out according to the ASTM G54-84 standard for static oxidation testing.

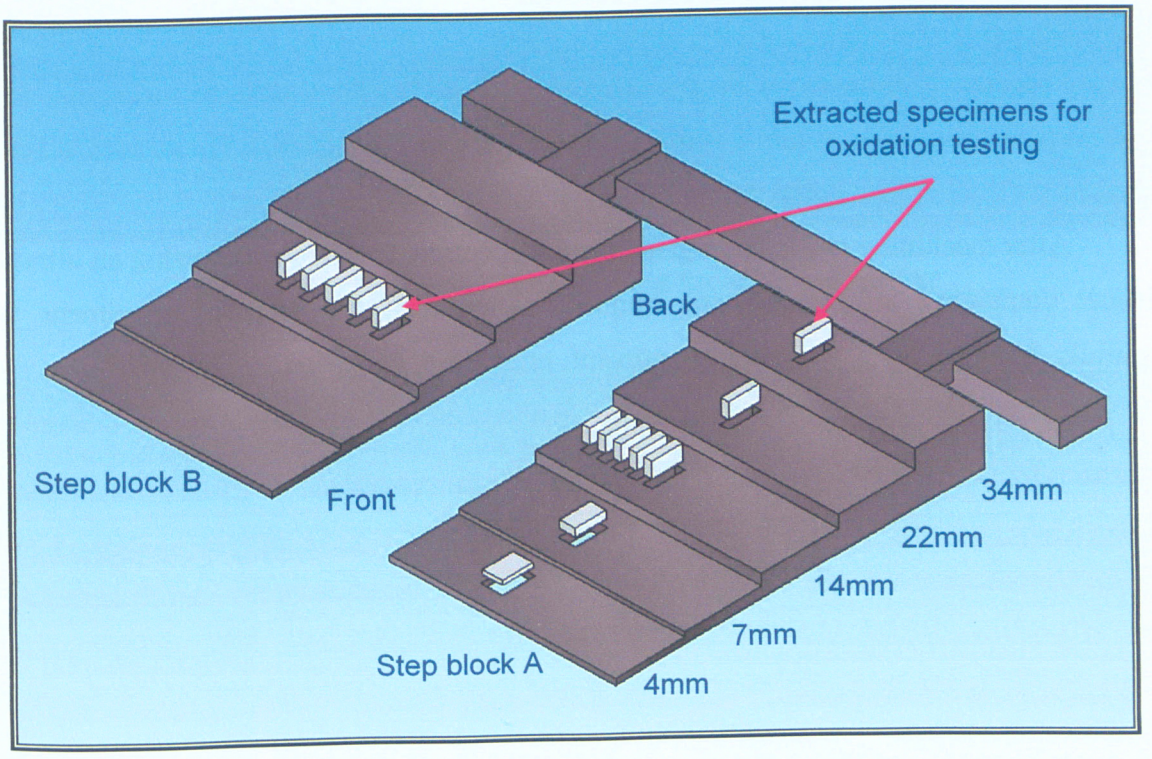

Figure 3.5: Specimens extracted from Step Blocks A and B for oxidation testing (only specimens extracted from Step Block B were used for repeatability studies).

The effect of chemical composition on the iron's resistance to oxidation was studied by carrying out high temperature oxidation tests on specimens taken from the 14mm section (Figure 3.5) of four different alloys (Table 3.1) cast at 1400°C. Each specimen was machined and surface ground on all sides to 5x10x20mm, thereby allowing exposure of 700mm^2 of total surface area to the oxidizing atmosphere. Two more specimens were

subjected to oxidation tests from each composition. Thus, each test was carried out three times. All samples were selected at random from those with the same composition.

The effect of pouring temperature on the iron's resistance to oxidation was determined using 5x10x20mm specimens obtained from the 14mm section of each casting. Specimens were also randomly picked from a particular pouring temperature population for the oxidation tests. These tests were not repeated, as the pouring temperatures did not have an effect on the iron's resistance to oxidation (discussed in Chapter 4).

Oxidation tests were also carried out to determine the effect of section thickness on the iron's resistance to oxidation. 5x10x20mm specimens were obtained from the 7, 14, 22 and 34mm sections (Figure 3.5) of Alloy 4 (Table 3.1) poured at 1450°C. This alloy was selected because it did not contain any misruns. 2.75x13x20mm sub-size specimens with a total surface are of 701.50mm^2 were taken from the 4mm section. These tests were not repeated for the reasons explained in Chapter 4.

After machining and surface grinding, the specimens were cleaned using an ultrasonic cleaner containing acetone for one minute. Thereafter, the prepared specimens were carefully handled with tweezers to prevent premature corrosion. The specimens were individually weighed and then placed into pre-baked ceramic crucibles. The individual mass of each crucible was weighed before and after the specimens were placed inside of them. The orientation of the specimens in the crucibles was such that the maximum surface area of the specimens was exposed to the surrounding atmosphere at all times. The crucibles were then placed on firebricks and inserted into the furnace (Figure 3.6). The temperature at the centre of the firebrick was constantly monitored throughout the duration of the experiment using a thermocouple. A detailed CAD-model of the firebricks position in the furnace is given in Appendix B.

Several steps were taken to ensure a controlled experiment. The data acquisition system (*DAS*) used to monitor the furnace temperature was calibrated. The constant temperature zone inside the three furnaces used was determined using an assembly referred to as the 'Snail', which is illustrated in Figure 3.7. The thermocouples were positioned in the exact location of a crucible on the firebrick. Furnace testing was carried out at the oxidizing test temperatures of 700, 800, 900, 1000 and 1100°C. The temperature distribution within each furnace at the respective oxidizing temperatures is given in Appendix C.

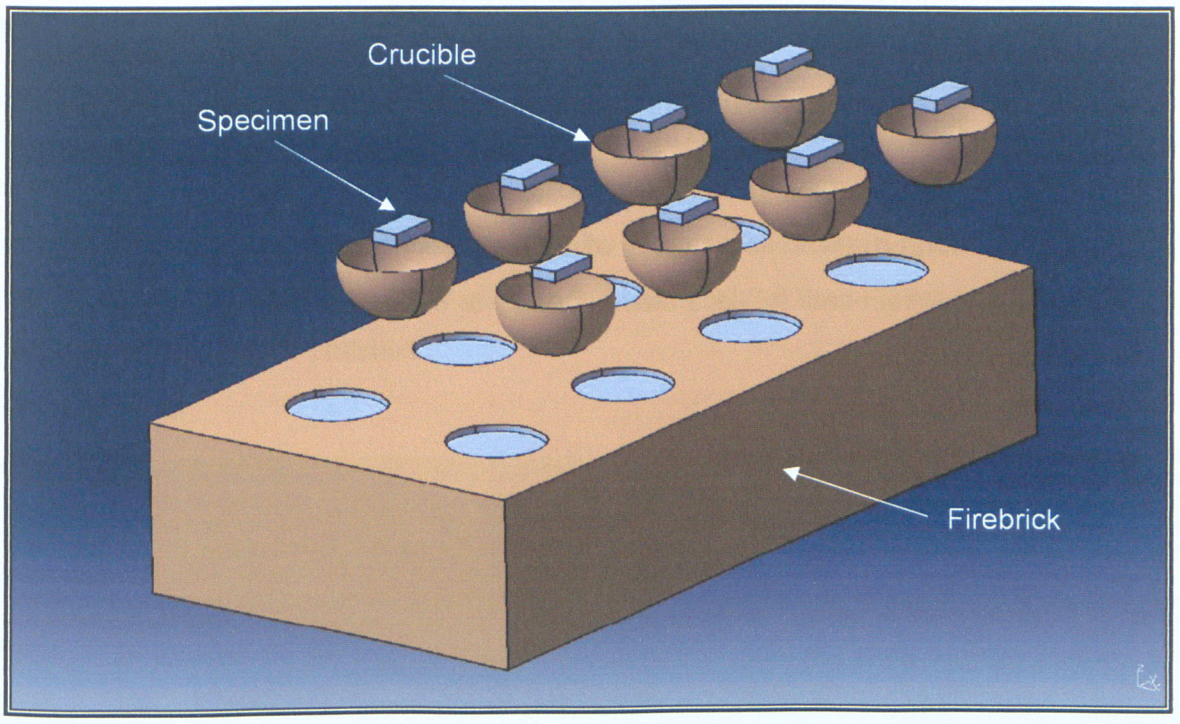

Figure 3.6: Assembly of specimens for oxidation testing.

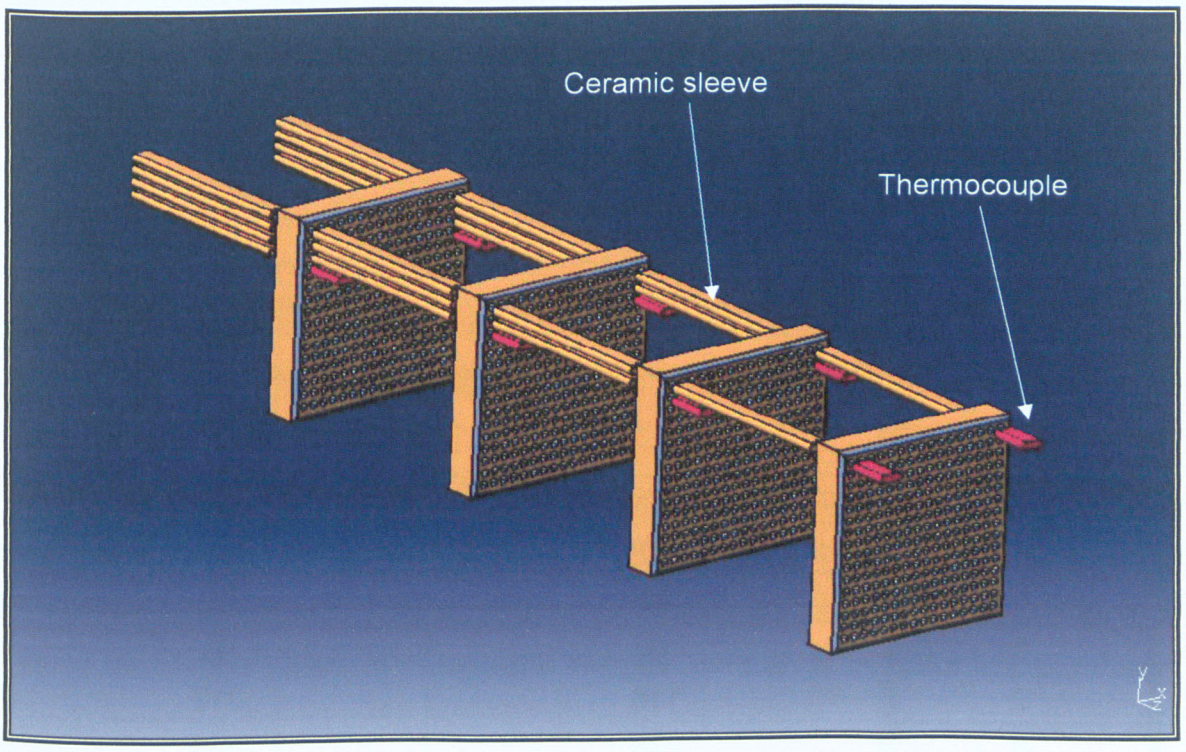

Figure 3.7: The 'Snail' apparatus used to determine the temperature distribution within the furnaces used specifically for oxidation testing.

After necessary calibration and verification (i.e., thermocouples, data acquisition system and furnaces), the firebricks were inserted into electric resistance furnaces and cycled for a cumulative time of 500 hours. The specimens were oxidized for 500 hours following the schedule in Table 3.6. At every cycle, the specimens were removed, cooled to room temperature and weighed (with an accuracy of ±0.1mg) and then placed back in the furnace. The mass change per unit area for each time interval was determined:

$$C = \frac{W_F - W_O}{A} \qquad \text{Equation 3.1}$$

where C is the mass change per unit area (mg/cm^2), W_F is the final mass (mg), W_O is the original mass (mg) and A is the original surface area (cm^2). The mass change per unit area was plotted against the cycle time. The weight change after 500 hours was also used to determine the parabolic rate constant $2k_{PB}$ (g^2/cm^{4}sec) from Pilling-Bedworth's relation (Equation 2.42).

The microstructure of the oxide layer was also studied using optical and scanning electron microscopes. X-ray mappings of the oxide scales were produced to depict the concentration and distribution of particular elements.

Table 3.6: Oxidation schedule.

Cycle #	Time Duration in Furnace (hours)	Cumulative Cycle Time (hours)
1	1	1
2	1	2
3	2	4
4	20	24
5	24	48
6	48	96
7	116	212
8	288	500

3.5 MICROSTRUCTURAL ANALYSIS

3.5.1 Preparation of the As-Cast and Oxidized Samples

Since this research partly focused on reducing the weight of components cast from the new ductile iron alloy, as-cast iron samples were analyzed from relatively thin sections (i.e., 4, 7 and 14mm) of the castings. Figure 3.8 shows where the samples were extracted and on which side they were polished.

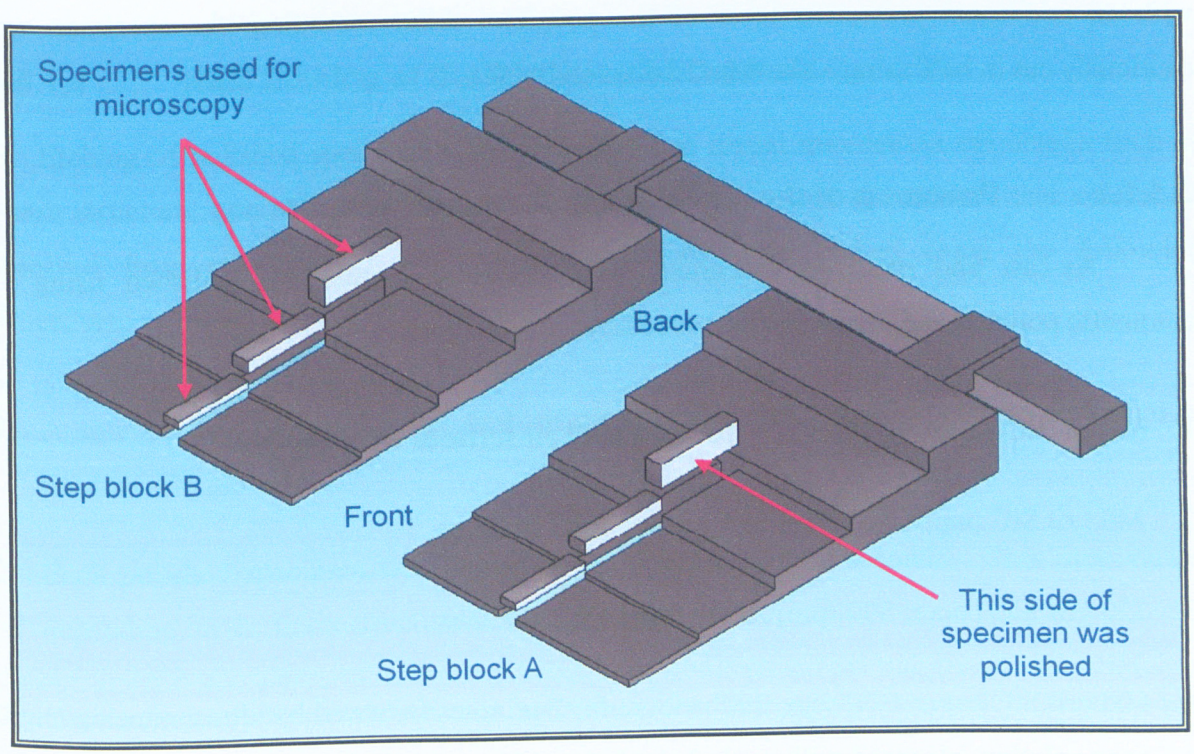

Figure 3.8: Specimen extraction locations for microscopy.

Using optical and scanning electron microscopes, these samples were analyzed for the graphite morphology and the defects (i.e., porosity, dross and slag). Samples obtained from the oxidized iron were only used to analyze the amount and chemical concentration of the oxide scale. In each case, metallographic samples were prepared according to principals outlined in sections 3.5.1.1 to 3.5.1.5.

3.5.1.1 Mounting As-Cast Samples

The specimens were cut from the 4, 7 and 14mm sections, and mounted in lucite. This allowed for coplanar polishing of each specimen.

3.5.1.2 Mounting Oxidized Samples

The conventional mounting method was modified to obviate the spalling of the oxide layer during mounting. The specimen was placed on a bed of lucite powder and topped up with an additional protective layer of the powder. After mounting, the specimen was cautiously cut in half using a slow-speed diamond blade.

3.5.1.3 Polishing of the As-Cast and Oxidized Samples

As-cast and oxidized specimens were carefully ground and polished using an automatic polisher and the following procedure:

1. 60 grit SiC paper, 300 rpm, 25 lbs force until all surfaces were coplanar.
2. 240 grit SiC paper, 300 rpm, 25 lbs force for 3 minutes.
3. 320 grit SiC paper, 300 rpm, 25 lbs force for 2 minutes.
4. 600 grit SiC paper, 300 rpm, 25 lbs force for 2 minutes followed by ultrasonic cleaning in soap solution, cleansed with methyl alcohol and blow dried.
5. 3 μm METADI II® Diamond Paste on a TEXTMET® 1000 pad lubricated with soap solution, 150 rpm, 25 lbs force for 2 minutes followed by ultrasonic cleaning in soap solution, cleansed with methyl alcohol and blow dried.
6. 1 μm METADI® Diamond Paste on a TEXTMET® 1000 pad lubricated with soap solution, 150 rpm, 20 lbs force for 2 minutes followed by ultrasonic cleaning in soap solution, cleansed with methyl alcohol and blow dried.

7. 0.5 μm METADI® Diamond Paste on a TEXTMET® 1000 pad lubricated with soap solution, 150 rpm, 20 lbs force for 2 minutes followed by ultrasonic cleaning in soap solution, cleansed with methyl alcohol and blow dried.

8. MASTERPREP™ Alumina Polishing Suspension used on a MASTERTEX® Polishing Cloth, 150 rpm, 15 lbs force for 1 minute, cleansed with methyl alcohol followed by ultrasonic cleaning in soap solution, cleansed once again with acetone and swabbed lightly with cotton until dried.

3.5.1.4 Nital Etching of the As-Cast and Oxidized Samples

Etching of polished specimens was carried out to reveal microstructural details such as phase structure, grain boundaries, dendrites, carbides and other precipitates that cannot be resolved from conventional polishing. Specimens were etched using the following procedure:

1. A solution was prepared using 4mL of nitric acid added to 100mL of ethyl alcohol to produce 4% nitric acid.

2. Each polished specimen was placed in the solution for 60 seconds. This time varied depending on the microstructure to be analyzed.

3. Once removed from solution, the specimen was thoroughly cleansed in acetone and swabbed with cotton until dried.

3.5.1.5 Etching via the SPEED Technique

To reveal the details of phases embedded within the ferritic matrix, such as dross and nodularity of graphite, a special technique referred to as selective potentiostatic etching by electrolytic dissolution (SPEED) was used [126]. This etching technique allowed for the removal of the ferritic matrix without destroying or removing specific oxides and graphite nodules, thus allowing for a three dimensional analysis of the phases without ambiguity (e.g., phase misrepresentation due to edge retention).

The SPEED etching technique was used to etch specimens in non-aqueous solutions at a predetermined electrical potential. The components to perform SPEED includes the electric control instrument (SPEED Analyser) and the electrolytic cell. The samples were polished as described earlier.

The composition of the electrolyte used depends on the type of metal to be etched. A suitable electrical potential vs. current density curve must be used to determine the optimum composition of the electrolyte needed to etch the specimens. For cast iron, 400mL of the electrolyte was composed of 10% acetylacetone (40mL) and 1% tetra-ethyl ammonium chloride (4g solid powder), the balance being methyl alcohol.

The procedure for etching a specimen using SPEED is as follows:

1. The specimen was placed into the apparatus such that the polishing surface faced the active module of the reference calomel electrode. The distance between these two devices had to be within 1 to 4mm. The sample was then immersed into the electrolyte.

2. The electric control unit was wired such that the red lead is for the cathode, black is for the anode (sample) and white is for the reference electrode.

3. The specimen was then immersed into the electrolyte.

4. The electric unit was adjusted to -500mV. The potential was increased by a factor of 50mV every 5 minutes until the voltage reached 500mV. The current density was recorded for each increment of potential.

5. Once the etching was finished, the specimen was cleansed with methyl alcohol, placed into the ultrasonic cleaner and dried.

6. Intricate microstructural details could then be observed using the scanning electron microscope.

3.5.2 Optical Microscopy

Optical microscopy was used to study the graphite morphology, pearlite, dendrites, dross and slag, shrinkage and pinholes in as-cast and oxidized specimens. Using image analysis software, various phases, precipitates and defects were studied.

3.5.3 Electron Microscopy

The scanning electron microscope (SEM) was also used to study the graphite morphology, pearlite, dendrites and various defects. Chemical analysis using energy dispersive spectrometry (EDS) was carried out on specific phases of unknown composition. The beryllium window on the SEM was removed to analyze the relative concentration of lighter elements in the cast iron. X-ray mapping of the oxide layer on select samples was carried out to study the relative phase distributions and concentrations of various oxide contributing elements.

3.5.4 Computational Digital Image Analysis

Micrographs obtained from the optical and scanning electron microscopes were analyzed using Buehler's Omnimet® software. Every image imported into the software was calibrated and specific software programs were developed to quantify graphite nodules (nodule area fraction, size and distribution) and to determine the extent of certain defects.

3.6 DILATOMETRY TESTS

Dilatometry tests were conducted to determine the coefficient of thermal expansion (α_{exp}) and the critical α-ferrite to γ-austenite phase transformation temperature. The apparatus used is illustrated in Figures 3.9 and 3.10.

A representative specimen from each chemical composition (3.5Si-2.0Al, 3.5Si-3.0Al, 4.5Si-2.0Al and 4.5Si-3.0Al) was tested. The specimens were machined into cylinders (6mm in diameter and 30mm in height) and surface ground. The iron specimens

and an alumina reference specimen were heated and cooled at a rate of 2°C/min. The specimens were heated to a maximum temperature of 1000°C.

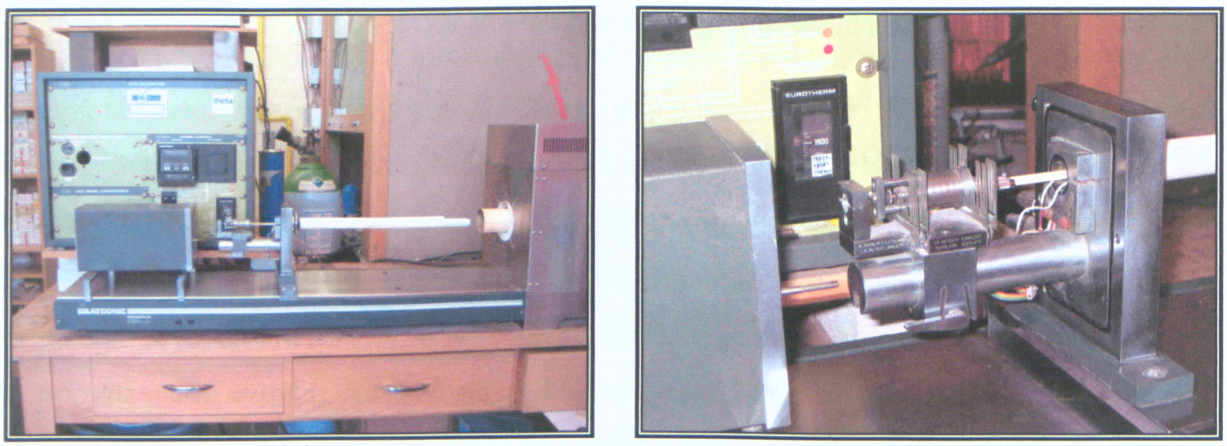

(a) (b)

Figure 3.9: (a) Dilatometer and (b) linear variable displacement transducer (LVDT).

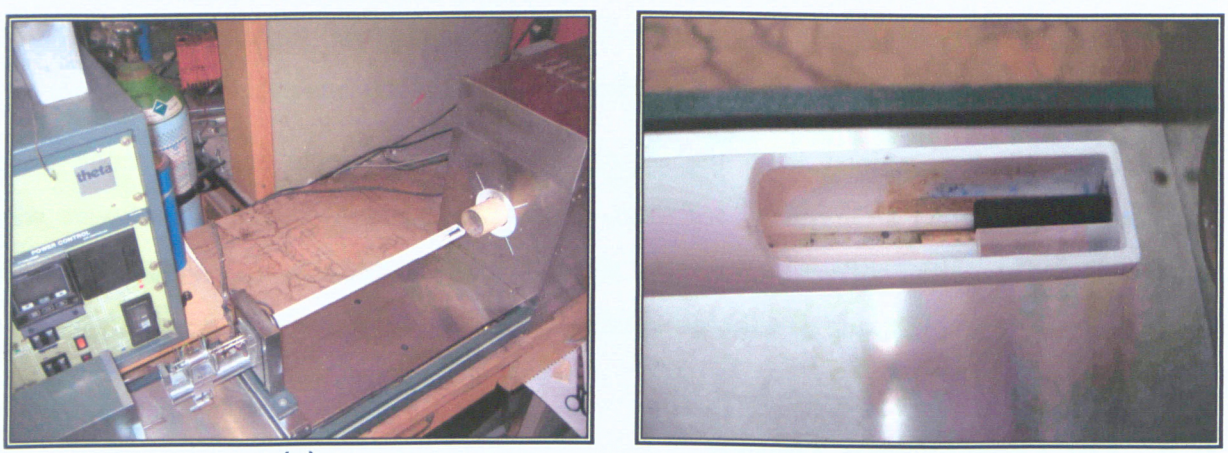

(a) (b)

Figure 3.10: (a) Ceramic tube holding the specimens prior to inserting into furnace and (b) magnification of ceramic specimen holder.

Chapter 4

Results and Discussion

4.1 SOLIDIFICATION CHARACTERISTICS and MICROSTRUCTURAL FEATURES in the AS-CAST CONDTION of DUCTILE IRON ALLOYED with Al, Si and Mo

4.1.1 Chemistry

The actual ladle chemistry for each alloy is given in Table 4.1. The magnesium contents in Alloys 1, 2, 3 and 4 were 0.021, 0.028, 0.028 and 0.025wt.%. In general, the cerium content was slightly higher at 0.03wt.% for each alloy. Boron, chromium, copper, manganese, nickel, phosphorus, sulphur, titanium, vanadium and zirconium were also present in very small concentrations. All chemical analyses were carried out at the Wescast Research and Development Laboratory using an emission spectrometer.

Table 4.1: Comparison of ladle chemistry to target chemistry.

Element	Chemical Composition (wt.%)							
	Alloy 1		Alloy 2		Alloy 3		Alloy 4	
	Target	Ladle	Target	Ladle	Target	Ladle	Target	Ladle
Si	3.50	3.48	3.50	3.54	4.50	4.76	4.50	4.82
C	3.43	3.23	3.43	3.29	3.10	3.13	3.10	3.15
Al	2.00	N/A	3.00	N/A	2.00	N/A	3.00	N/A
Mo	1.50	1.45	1.50	1.47	1.50	1.35	1.50	1.53

4.1.2 Graphite Morphology

Using Buehler's Omnimet® software, graphite nodule size, count per mm^2 and shape were studied. This study was carried out on ten micrographs (100X magnification) from the 4mm and 14mm specimens poured at 1350, 1400 and 1450°C.

4.1.2.1 Nodule Size

The nodules in the 14mm thick specimens were distinctly larger than those in the 4mm thick specimens (Figure 4.1). Lower cooling rates and longer solidification times allowed the graphite nodules to grow in the thick specimens. The size of some nodules in the 14mm section was as high as 31μm, compared to 21μm in the 4mm specimen (based on specimens extracted from step blocks cast at 1450°C).

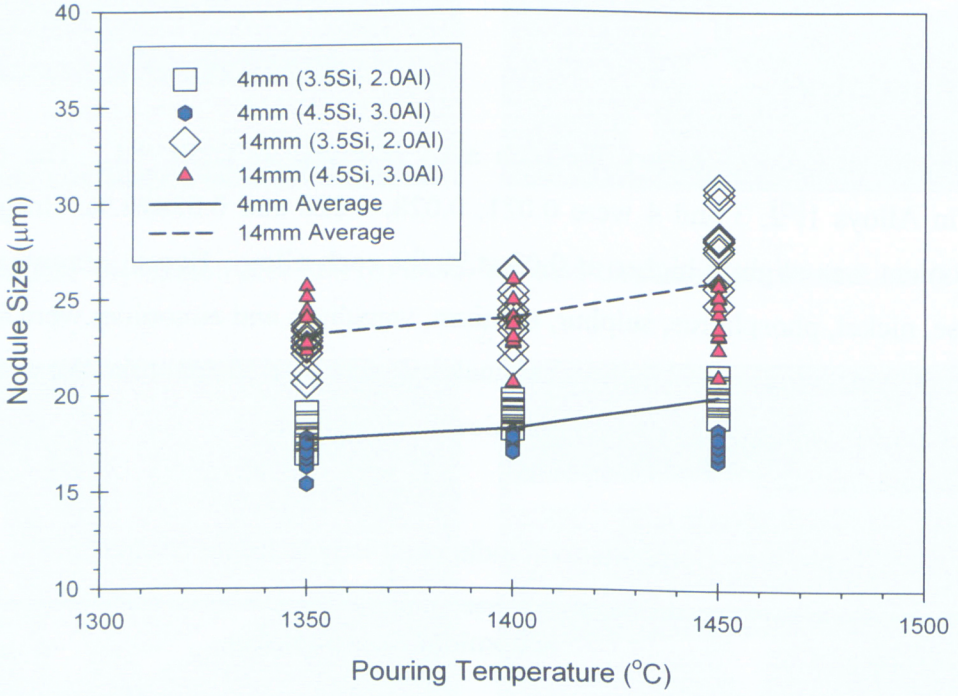

Figure 4.1: Effect of pouring temperature, casting thickness and metal chemistry on nodule size.

The data in Figure 4.1 suggests that the pouring temperature did not have a major effect on nodule size. In the pouring temperature range of 1350 to 1450°C, the average difference in nodule size in the 4mm as well as 14mm thick specimens was only 1.5μm. However, there was a difference of 6μm in the average nodule size between the 4mm and 14mm thick specimens for the same pouring temperature. Figure 4.2 illustrates the effect of pouring temperature on the size and quality (e.g., uniformity and roundness) of the graphite

nodules. It should be noted that the quality of the graphite nodule improved with increasing pouring temperature.

Comparing Alloy 1 (3.5Si-2.0Al) with Alloy 4 (4.5Si-3.0Al), the data points for the 14mm thick specimen in Figure 4.1 indicate that the nodule size decreased with an increase in silicon contents. This effect is more pronounced in the thin (4mm) specimens.

Figure 4.2: SEM micrographs of select graphite nodules from a 14mm thick Alloy 1 (3.5Si-2.0Al) specimen poured at (a) 1350°C (b) 1400°C and (c) 1450°C. 800X. SPEED etched.

4.1.2.2 Nodule Count

The section thickness had a significant impact on nodule count. The nodule count number decreased with an increase in section thickness (Figures 4.3 and Figure 4.4). This effect is attributed to the difference in the cooling during solidification [21,23,45].

Increased solidification cooling rates promote a fine graphitic structure consisting of a large number of nodules [23,24,29,45,85]. As cooling rates decrease, transformation to a coarser structure results in a lower nodule count. A maximum nodule count of 550 nodules/mm^2 was recorded for the 4mm thick specimen cast at 1350°C, compared to 250 nodules/mm^2 for the 14mm thick specimen.

Pouring temperature influences the nodule count. The largest variation was observed between the 1350 and 1400°C temperatures in the 4mm thick specimens, where the nodule

count decreased from an average of 500 to 350 nodules/mm^2 (Figure 4.4). A corresponding decrease of 40 nodules/mm^2 was observed in the 14mm thick specimens.

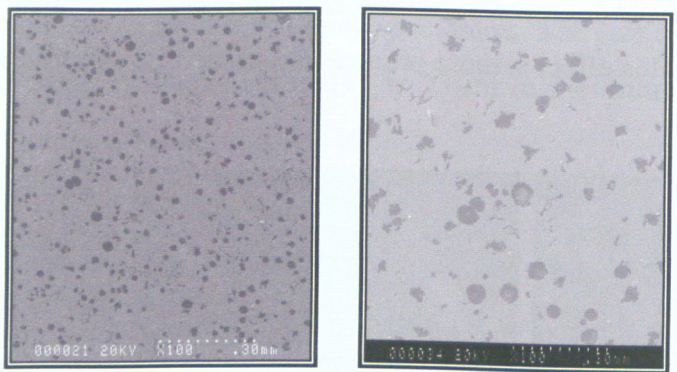

Figure 4.3: SEM micrographs showing nodule density in (a) 4mm and (b) 14mm thick specimens. 100X.

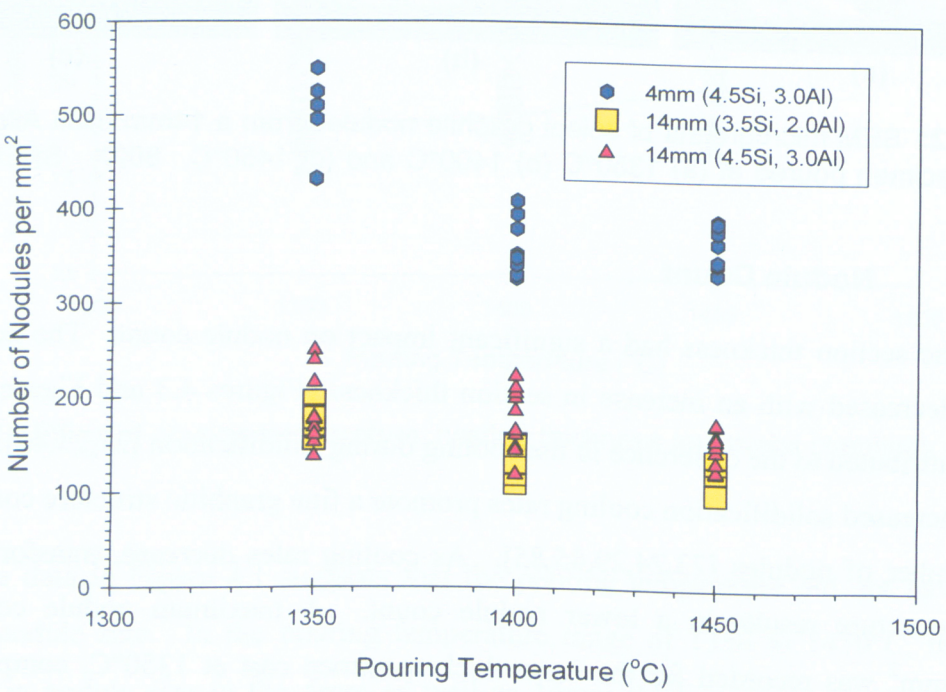

Figure 4.4: Effect of pouring temperature, casting thickness and metal chemistry on nodule count.

Alloys containing high silicon contents and high *CE* (typically 4.6) had high nodule counts and a higher percentage of ferrite with minute traces of carbides, particularly in the

4mm thick specimens. This is in agreement with the observations of other researchers [23,29,85]. A high nodule density will enhance ambient and elevated temperature properties. Alloys containing a low nodule count consisting of large, widely spaced nodules will have a tendency of promoting internodular pearlite. The presence of pearlite will decrease the dimensional stability of iron alloys at higher temperatures. However, very high nodule counts can be detrimental. If the graphite nodules are densely populated thus causing nodule-to-nodule contact, resistance to internal oxidation can diminish. In grey cast irons, graphite forms a skeleton throughout the casting, along which the diffusion of oxygen is possible deep into the interior [13]. In ductile irons, the graphite nodules are relatively isolated from one another. Thus, oxidation by this mechanism cannot occur. However, if nodule-to-nodule contact occurs within the casting, a network of nodules can produce a path for oxygen ions deep into the core of the casting.

4.1.2.3 Percent Nodularity of Graphite

Additions of aluminum to the ductile iron alloy did not degenerate (i.e., affect the shape) the graphite. High aluminum content (3wt.%) in the alloy resulted in a relatively high percentage of spherical nodules. It was observed that the percent of nodules was greatest when the Si/Al ratio was 1.2 (3.5Si-3.0Al). The percentage of nodules decreased as the ratio increased from 1.5 (4.5Si-3.0Al) to 2.25 (4.5Si-2.0Al). This general effect is shown in Figure 4.5 for 4mm and 14mm thick specimens. However, such a trend is not explicit for the Si/Al ratio of 1.75 (3.5Si-2.0Al). The graphite sphericity in 4mm thick specimens was higher than that in the 14mm thick specimens when the Si/Al ratio was close to 1.

The pouring temperature did not affect graphite sphericity significantly in the 14mm thick specimens (Figure 4.6). However, this was not so in the 4mm specimens. Maximum percentage of nodules was observed when the liquid metal was poured at 1450°C and the minimum was observed at 1350°C. Factors responsible include prolonged holding times (e.g., to enable cooling of the melt from the tapping temperature of 1550°C to the pouring temperature of 1350°C), resulting in magnesium fade, and higher cooling rates associated with lower pouring temperatures. These factors possibly prevented the spheroidizing elements from completely reacting with graphite.

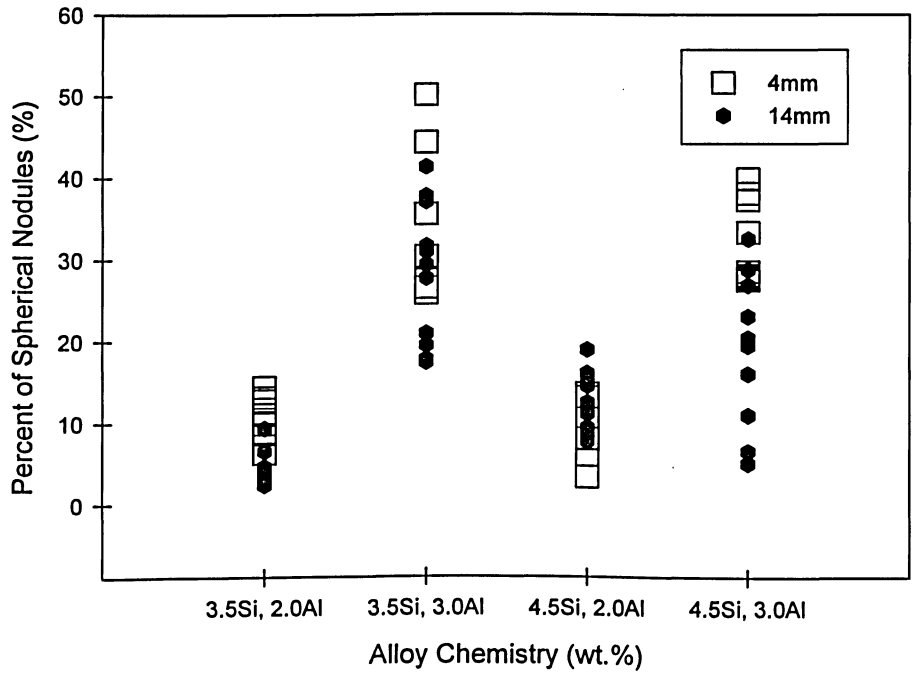

Figure 4.5: Effect of chemical composition on the percent nodularity of graphite in the 4mm and 14mm thick specimens cast at 1400°C.

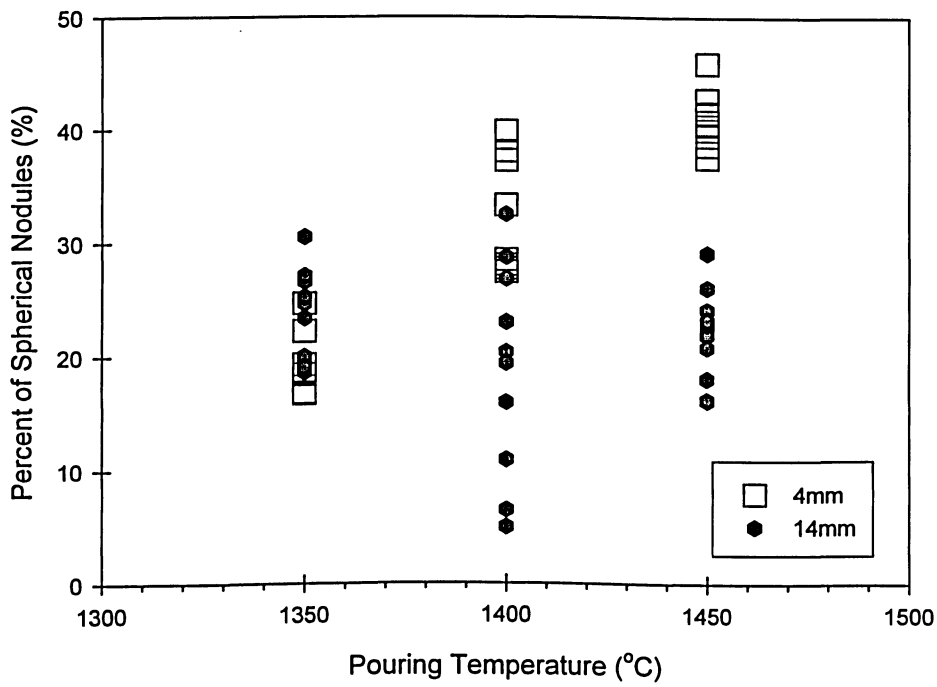

Figure 4.6: Effect of pouring temperature on the sphericity of graphite in the 4mm and 14mm thick specimens extracted from Alloy 4 (4.5Si-3.0Al).

4.1.3 Casting Defects

4.1.3.1 General Casting Features

The step block castings were sound except for a few misruns in the thin section. Preventing misruns indeed is one of the biggest challenges in producing thin-wall castings. Cast step blocks produced are shown in Figures 4.7 to 4.10.

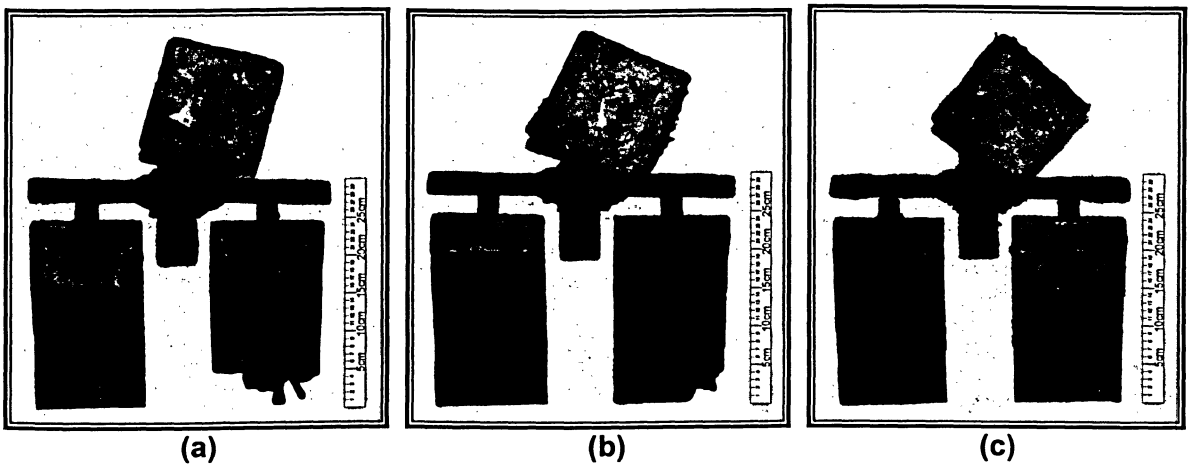

Figure 4.7: Step block castings of Alloy 1 (3.5Si-2.0Al) poured at (a) 1350°C (b) 1400°C and (c) 1450°C.

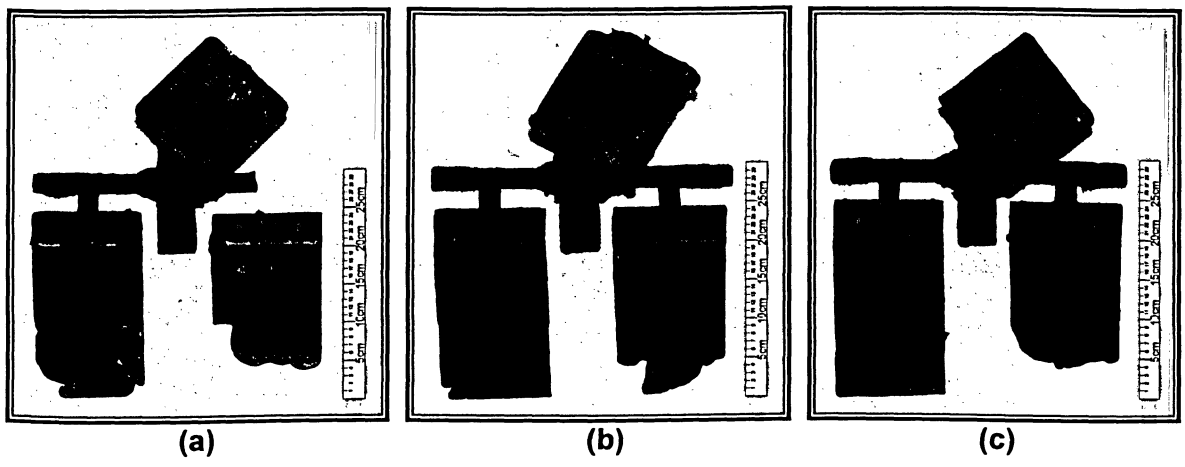

Figure 4.8: Step block castings of Alloy 2 (3.5Si-3.0Al) poured at (a) 1350°C (b) 1400°C and (c) 1450°C.

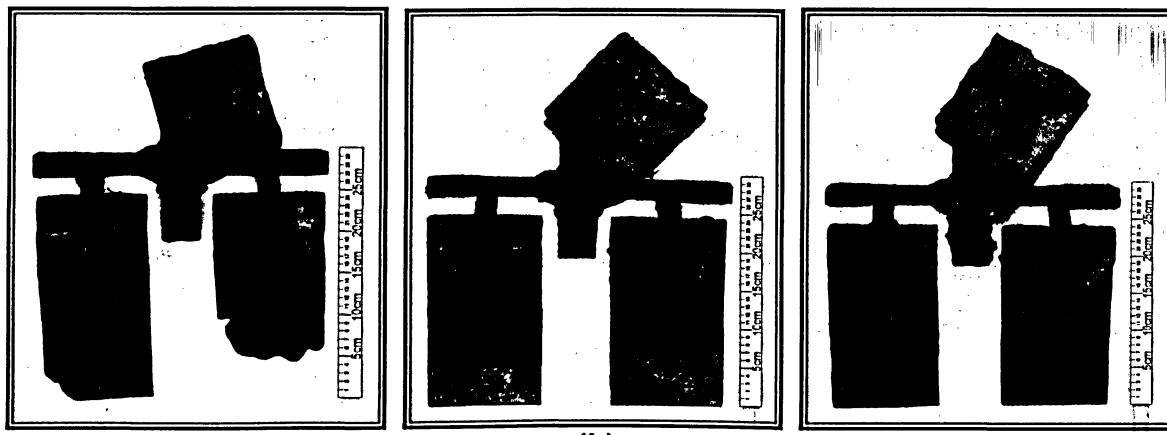

(a) (b) (c)

Figure 4.9: Step block castings of Alloy 3 (4.5Si-2.0Al) poured at (a) 1350°C (b) 1400°C and (c) 1450°C.

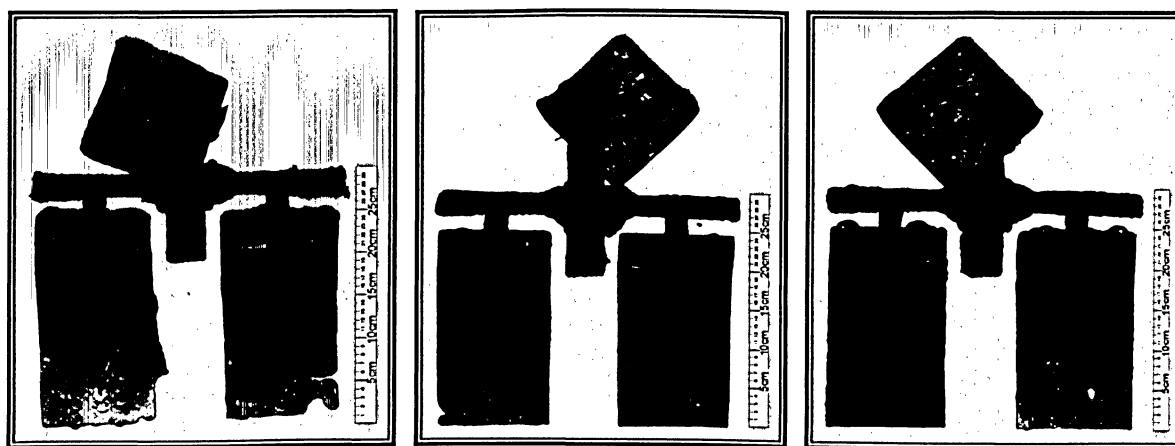

(a) (b) (c)

Figure 4.10: Step block castings of Alloy 4 (4.5Si-3.0Al) poured at (a) 1350°C (b) 1400°C and (c) 1450°C.

The pouring temperatures and the aluminum and silicon contents largely influenced the size of a misrun. Step blocks of Alloy 3 (4.5Si-2.0Al) showed misruns when poured at 1350°C (Figure 4.9(a)). The same alloy poured at 1400 and 1450°C did not show any misrun (Figures 4.9(b) and 4.9(c)). When the silicon content decreased to 3.5wt.%, misruns were observed in castings poured at 1350 and 1400°C (Figures 4.7(a), 4.7(b) and 4.8). Step blocks produced with Alloy 4 (4.5Si-3.0Al) showed similar degree of misruns as those of Alloy 3 (Figures 4.10(b) and 4.10(c)). However, fold defects were observed in Alloy 4 (4.5Si-3.0Al)

(Figure 4.10(b)). Castings produced from Alloy 2 (3.5Si-3.0Al) experienced large misruns (Figure 4.8). Also, a glassy oxide film was observed to envelope the surfaces of castings containing the highest levels of aluminum. These castings experienced severe misruns.

4.1.3.2 Graphite Floatation

Graphite floatation was not observed in the 4, 7 and 14mm thick samples. Micrographs showing the distribution of graphite in these sections are in Figure 4.11.

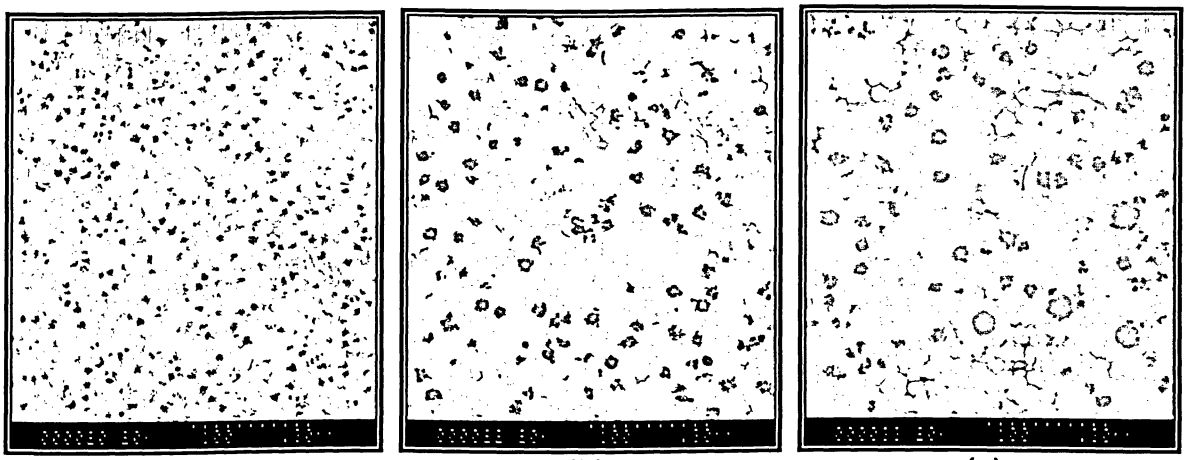

Figure 4.11: SEM micrographs showing the distribution of graphite nodules in the (a) 4mm, (b) 7mm and (c) 14mm thick specimens. 100X.

4.1.3.3 Dross and Slag

4.1.3.3.1 Alloy 1 (3.5Si-2.0Al)

Strings of slag were observed along the centreline of 4mm thick specimens cast at 1350°C. In the specimen location, only 2% of the total surface area was covered with slag (Figures 4.12(a) and 4.12(b)). Similar observations were made in the 7mm thick specimens (Figure 4.13(a)). However, the strings of slag found in the latter samples were positioned above the centerline of casting section.

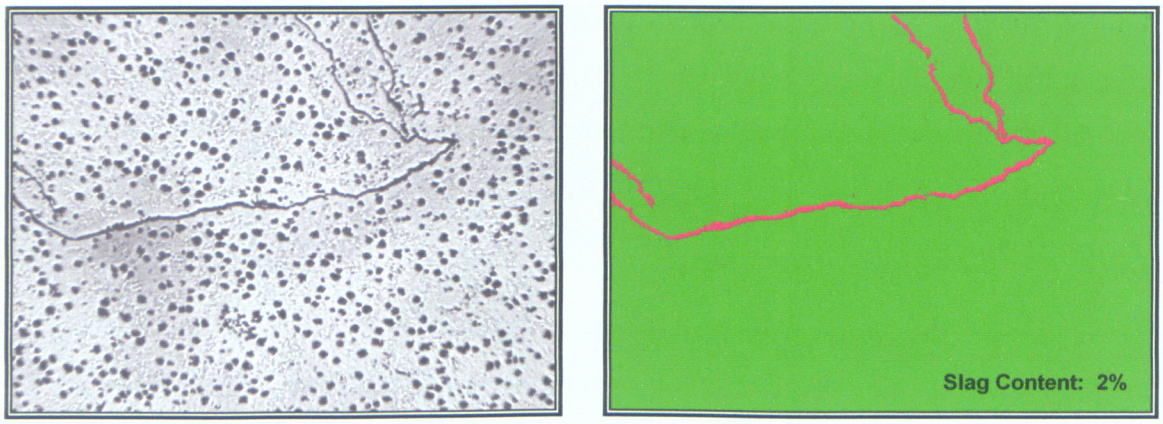

Figure 4.12: (a) Optical micrograph of slag strings along the centreline of a 4mm thick specimen cast at 1350°C (50X) and (b) digital image analysis of Figure 4.12(a).

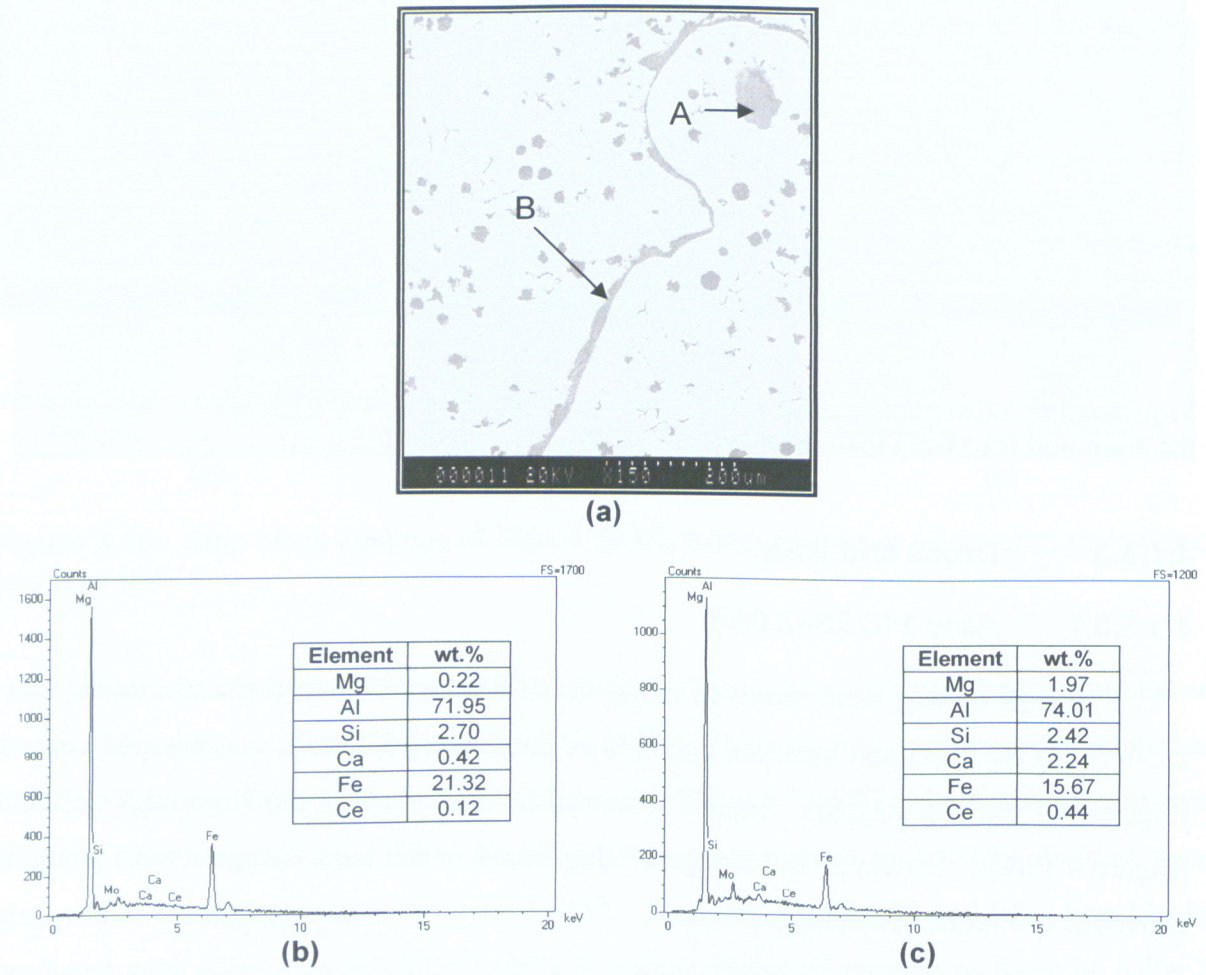

Element	wt.%
Mg	0.22
Al	71.95
Si	2.70
Ca	0.42
Fe	21.32
Ce	0.12

Element	wt.%
Mg	1.97
Al	74.01
Si	2.42
Ca	2.24
Fe	15.67
Ce	0.44

Figure 4.13: (a) SEM micrograph of slag and dross in a 7mm thick specimen cast at 1350°C. EDS spectrum analysis of (b) point A and (c) point B in Figure 4.13(a) above.

Chemical analysis of the slag composition showed presence of oxides of magnesium, aluminum, silicon, calcium, cerium and iron (Figures 4.13(b) and 4.13(c)).

Strings of slag associated with dross dominated the cope side of the 14mm thick specimens poured at 1350°C (Figure 4.14). In the specimen location, 26% of the total upper surface area was occupied with this type of defect.

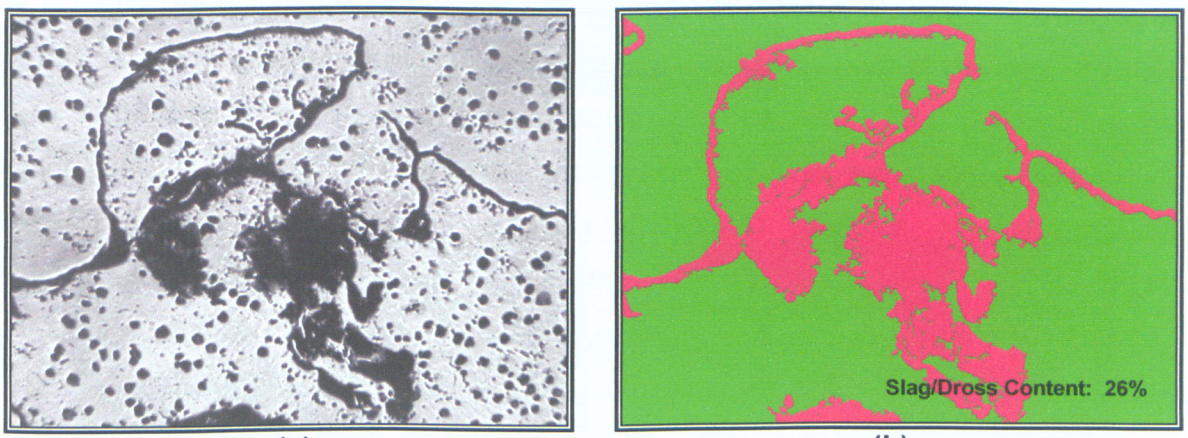

Figure 4.14: (a) Optical micrograph of slag and dross in a 14mm thick specimen cast at 1350°C (50X) and (b) digital image analysis of Figure 4.14(a).

Two different types of slag and dross films can be observed during pouring, fluid and semi-solid [127]. During pouring, fluid slag films can be absorbed by the moulding medium or trapped by filters placed within the mould. Oxide films which enter the mould will float to the top surface of the melt during filling. These films eventually envelope the outside surface of the casting. This interesting phenomenon was observed and the films can be seen in Figures 4.8 and 4.10. Semi-solid slag and dross films consist of solid phases bound weakly in the stream of a more fluid phase. When the semi-solid slag enters the mould cavity, it breaks up. The resulting clusters of slag and dross become trapped beneath the surface of the casting and result in defects illustrated in Figure 4.14 above. Even more detrimental is the entrapment of these clusters within the melt inside the mould, as illustrated in Figures 4.12(a) and 4.13(a). This occurs when the melt solidifies rapidly, thereby not allowing the slag and dross to float to the cope.

Depending on oxygen availability and dwell time, as the melt temperature decreases, a two phase mixture (slag) of SiO_2 (solid) and FeO (liquid) will form [21]. Slag may also include MgO, Al_2O_3, CaO and Ce oxides from charge materials, inoculants and furnace refractories [21,90,91]. Other film related defects such as dross may precipitate from lower melting slags, which may appear as a chunky or powdery substance on or near the surface of a casting. Since iron (the element) is the major constituent (90%) of the cast iron, as the temperature decreases, FeO becomes the dominant constituent found in all slags [21,90]. High FeO contents in the slag can produce defects such as pinholes when it reacts with free carbon (Equation 2.17). Complex iron-silicon oxide systems may react with MgO, Al_2O_3, CaO and Ce oxides to prevent SiO_2-FeO type slags from developing [21]. This may include the formation of forsterite (Mg_2SiO_4), enstatite ($MgSiO_3$) and fayalite (Fe_2SiO_4) [21,90,91,127]. This is indicated in the chemical analysis obtained from slag (Figures 4.13(b) and 4.13(c)), where high magnesium, aluminum, calcium and cerium contents were observed.

As the pouring temperature increased to 1400°C, the slag strings observed earlier in the 4mm thick specimens were no longer positioned along the centreline, but above it (Figure 4.15). The amount of slag in the 4mm thick specimen decreased with increasing pouring temperatures. Increasing the temperature well above 1400°C (prior to pouring) prevented slag from forming on the surface of the melt [21]. Raising and holding the temperature above the equilibrium oxidation-reduction temperature will result in rapid oxidation of carbon [128] (Elingham Diagram, section 2.3.1). As a result, silicon will not oxidize unless carbon contents fall below 1wt.% and more free oxygen is made available.

Slag and dross were not observed in the 7mm thick specimens. With increased pouring temperatures and solidification times, the slag had ample time to float to the surface. As a result, a thin discontinuous film of dross lined the surface of the casting.

In the 14mm thick specimens, dross was present below the skin of the casting. This occurred as a result of a larger section thickness and longer solidification times, which allowed clusters of dross to accumulate below the surface of the casting. However, a 6% reduction in dross was observed for a casting temperature of 1400°C (Figure 4.16) compared to 1350°C (Figure 4.14). This occurred for reasons discussed earlier. The SEM micrograph in Figure 4.17 illustrates typical dross topography in a 14mm thick specimen cast at 1400°C.

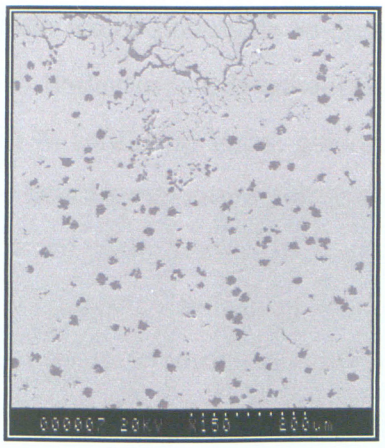

Figure 4.15: SEM micrograph of slag in a 4mm thick specimen cast at 1400°C. 100X.

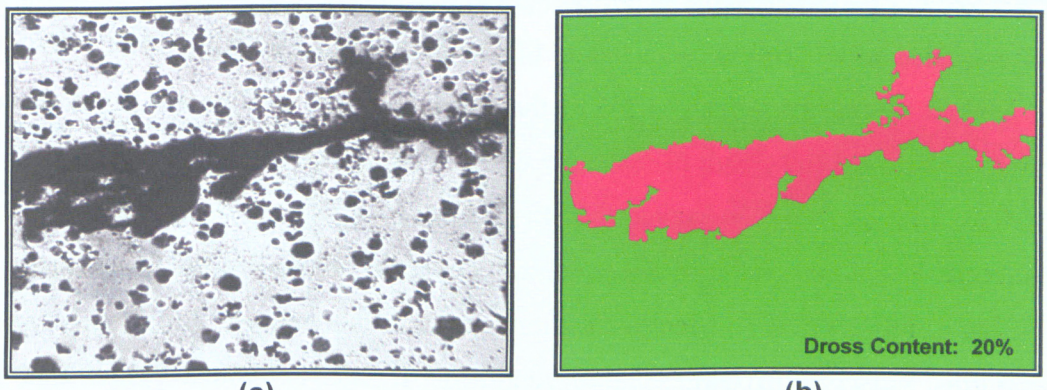

(a) (b)

Figure 4.16: (a) Optical micrograph of dross in a 14mm thick specimen cast at 1400°C (50X) and (b) digital image analysis of Figure 4.16(a).

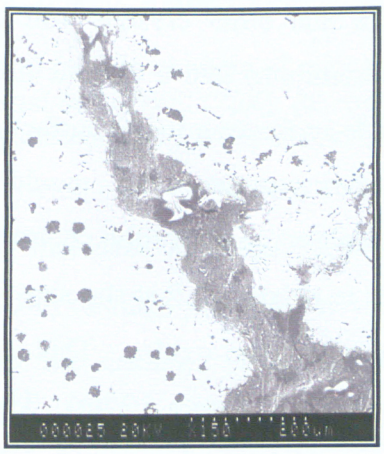

Figure 4.17: SEM micrograph of dross below the skin in a 14mm thick specimen cast at 1400°C. 150X.

A region containing a lump of dross was found along the centreline of a 4mm thick specimen poured at 1450°C. Following the observation of Heine [21], it is suggested that higher pouring temperatures allowing larger quantities of dissolved oxygen possibly caused this defect. In the sample location, this region constituted 12% of total surface area (Figure 4.18). Only two such regions were identified along the centreline. Upon repolishing and etching with nital, detrimental micro-cracks were revealed (Figure 4.19). These micro-cracks were within the oxide film and along the perimeter of the oxide-metal interface. Such cracks could potentially limit the fatigue life of the material [129]. The sample was further etched using SPEED, and it was further observed that dross was trapped within a shrinkage pore during solidification (Figures 4.20(a), 4.20(b) and 4.20(c)). It is thus possible that the entrapped dross was unable to float to the surface during the late stages of solidification, in spite of extended solidification times due to higher pouring temperatures.

Chemical analysis (Figure 4.21) of the shrinkage pore in Figure 4.20(c) showed that the cast iron was relatively high in carbon and low in aluminum, silicon and iron. Wallace et al. [109] and Li et al. [110] suggested that the amount of shrinkage decreased with increasing carbon content. Since graphite precipitation depends on the carbon equivalent (%C + %Si/7), increasing the *CE* to precipitate more graphite has become an attractive means for compensating liquid contraction in thin sections. It was explained earlier that graphite nucleation causes expansion of the mould (section 2.2.4). In thicker sections, high *CE* iron cannot overcome amplified mould dilations [109]. However, in thinner sections, such as 4mm, the primary cause for shrinkage occurs during solidification [111]. The formation of complex Fe, Si and Al oxides and other crystals will transform the liquid metal (now deficient in iron, silicon and aluminum) into a viscous fluid, thus impeding its flow. As a result, dross will be prevented from floating to the surface and become trapped in shrinkage pores developed as a result of other parameters (i.e., mould dilation and dendrites).

Discontinuous slag was observed above the centreline in a 7mm thick specimen cast at 1450°C (Figure 4.22(a)). It is suggested that the slag was a complex ternary compound composed of iron, silicon and aluminum oxides. This was determined from the chemical analysis (Figure 4.22(b)) of point A in Figure 4.22(a). The amount of slag in this specimen was similar to that in the 7mm thick specimen cast at 1350°C. However, rapid cooling during holding, pouring and moulding could have produced large quantities of iron, silicon

and magnesium oxides and silicon rich compounds such as forsterite (Mg_2SiO_4), enstatite ($MgSiO_3$) and fayalite (Fe_2SiO_4).

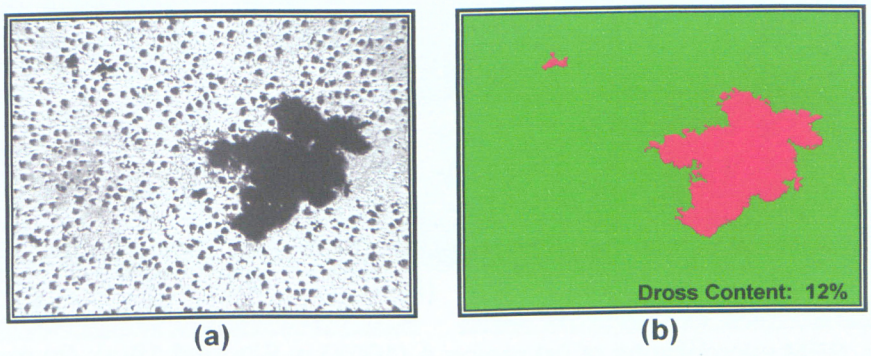

Figure 4.18: (a) Optical micrograph of dross in a 4mm thick specimen cast at 1450°C (50X) and (b) digital image analysis of Figure 4.18(a).

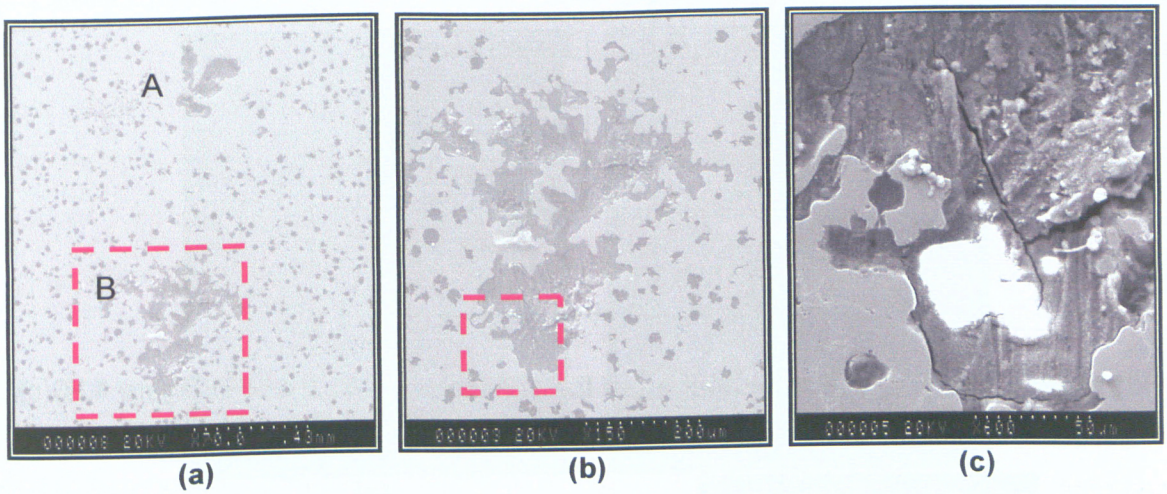

Figure 4.19: SEM micrographs of (a) two clusters of slag and dross at the centre along the centreline of a 4mm specimen cast at 1450°C (70X), (b) magnified area (150X) enclosed by box in Figure 4.19(a) and (c) magnified area (600X) enclosed by box in Figure 4.19(b).

As the section thickness increased to 14mm, specimens cast at 1450°C exhibited much of the same trend observed in castings produced at 1350 and 1400°C. Slag and dross accumulated below the skin of the casting. Slag and dross concentrations at higher temperatures were reduced by 1%, compared to 14mm thick specimens cast at 1400°C. The higher pouring temperature prevented silicon dioxide and other oxides from forming. This is in agreement with the earlier observation of Heine [21].

Figure 4.20: SEM micrographs of (a) region A (100X) in Figure 4.19(a), (b) magnified area (400X) in Figure 4.20(a) and (c) region B (100X) in Figure 4.19(a). SPEED etched.

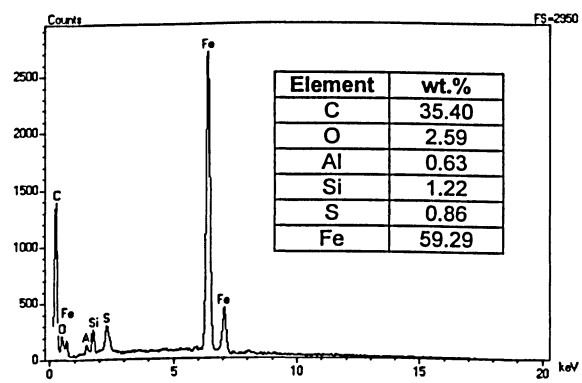

Element	wt.%
C	35.40
O	2.59
Al	0.63
Si	1.22
S	0.86
Fe	59.29

Figure 4.21: EDS spectrum analysis of the shrinkage pore surface in Figure 4.20(c).

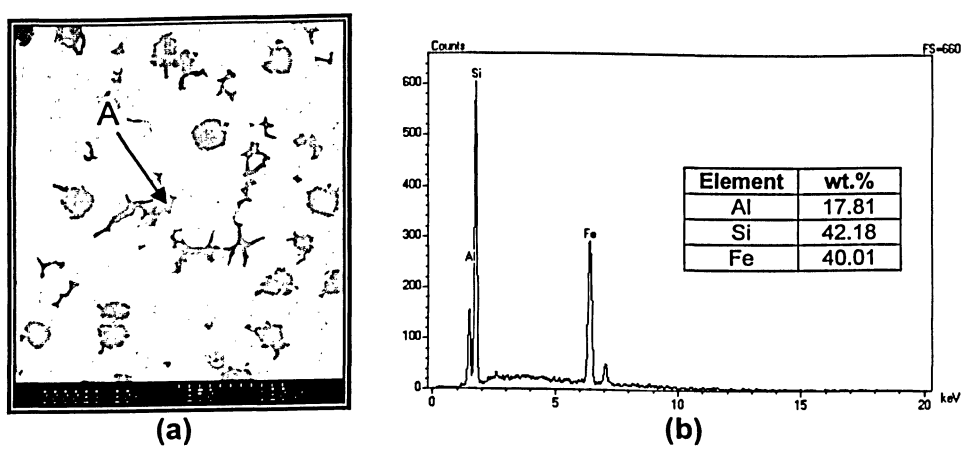

Element	wt.%
Al	17.81
Si	42.18
Fe	40.01

Figure 4.22: (a) SEM micrograph of slag clusters in a 7mm thick specimen cast at 1450°C (150X) and (b) EDS spectrum analysis of point A in Figure 4.22(a).

In the specimen location, 19% of total surface area was contaminated with slag and dross (Figure 4.23). SEM micrographs of these defects are shown in Figure 4.24.

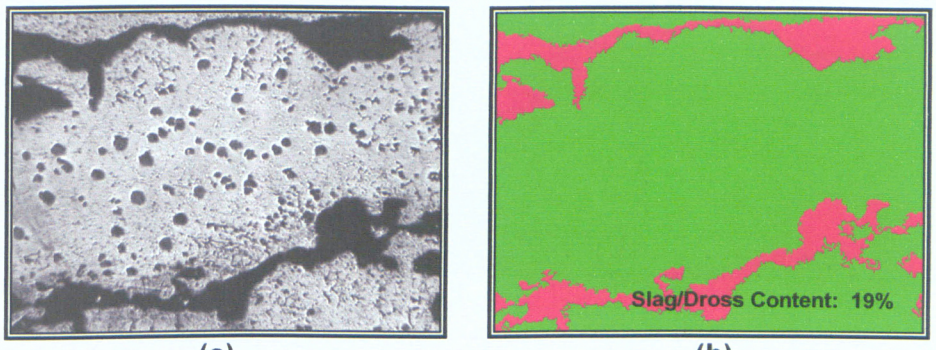

Figure 4.23: (a) Optical micrograph of subsurface dross in a 14mm thick specimen cast at 1450°C (50X) and (b) digital image analysis of Figure 4.23(a).

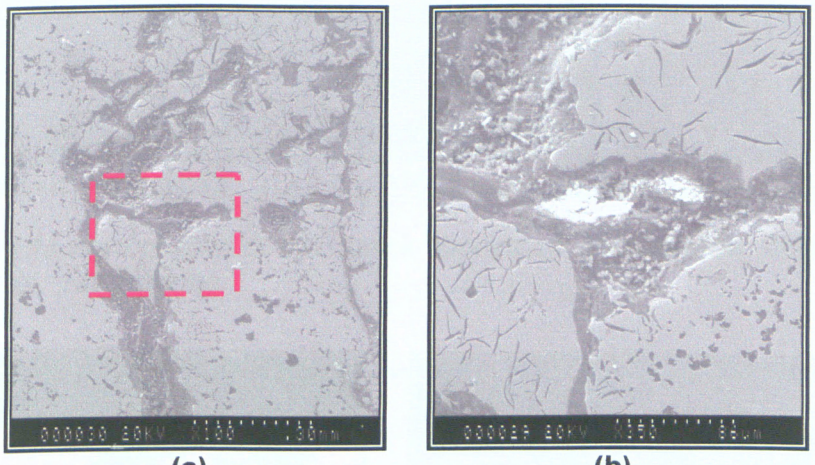

Figure 4.24: SEM micrographs of (a) subsurface dross in a 14mm thick specimen cast at 1450°C (100X) and (b) magnified area (350X) enclosed by box in Figure 4.24(a).

4.1.3.3.2 Alloy 2 (3.5Si-3.0Al)

Slag was identified along the centreline of 4mm thick specimens cast at 1350°C (Figure 4.25(a)). Slag was not observed along the centreline of 4mm thick specimens cast at 1400°C (Figure 4.25(b)). A network of slag strings was identified below the top surface in specimens cast at 1450°C (Figure 4.25(c)). On all 4mm thick specimens, slag coagulated at the surface producing a brittle glassy film. This can be observed in Figure 4.8.

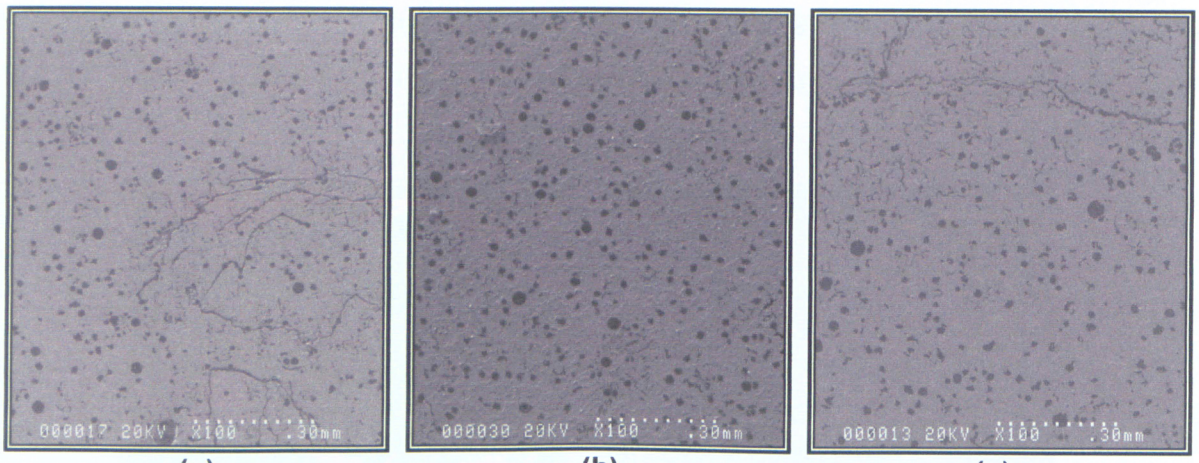

Figure 4.25: SEM micrographs of 4mm thick specimens poured at (a) 1350 (b) 1400 and (c) 1450°C. 100X. Nital etched.

All 7mm thick specimens exhibited microstructures similar to those observed in specimens cast from Alloy 1 (3.5Si-2Al) at 1350, 1400 and 1450°C.

14mm thick specimens cast at 1350, 1400 and 1450°C contained subsurface slag and dross (Figure 4.26(a)). Larger amounts of dross and slag were observed in these specimens than in specimens extracted from Alloy 1 (3.5Si-2.0Al). Image analysis of these defects is shown in Figure 4.26(b).

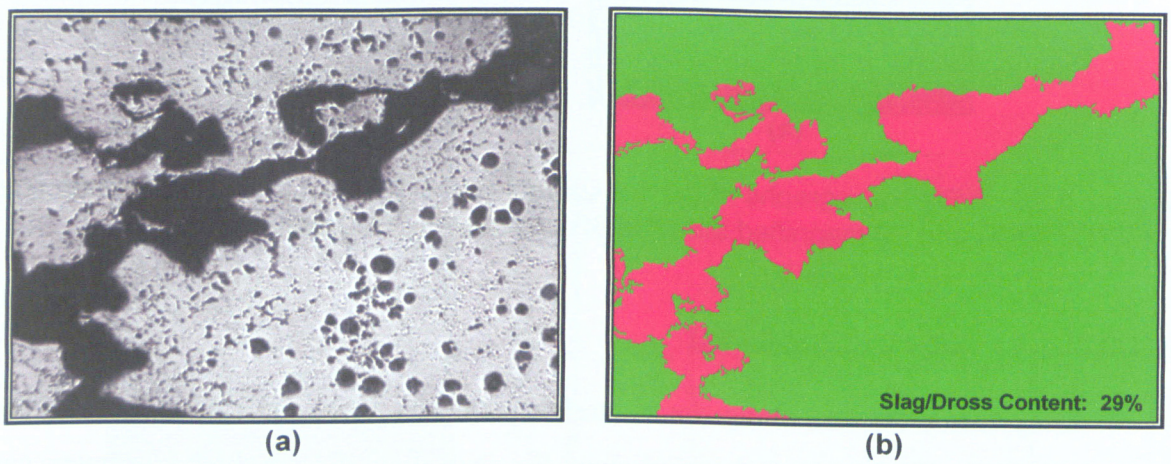

Figure 4.26: (a) Optical micrograph of subsurface slag and dross in 14mm thick specimens poured at 1350, 1400 and 1450°C (50X) and (b) image analysis of Figure 4.26(a).

4.1.3.3.3 Alloy 3 (4.5Si-2.0Al)

Slag and dross were not observed in the 4 and 7mm thick specimens cast at 1350, 1400 and 1450°C (Figure 4.27). 14mm thick specimens cast at 1350°C contained strings of slag and dross below the skin of the casting (Figure 4.28(a)). A small quantity of slag strings were observed in specimens cast at 1400°C (Figure 4.28(b)). 14mm thick specimens cast at 1450°C were free of slag and dross (Figure 4.28(c)).

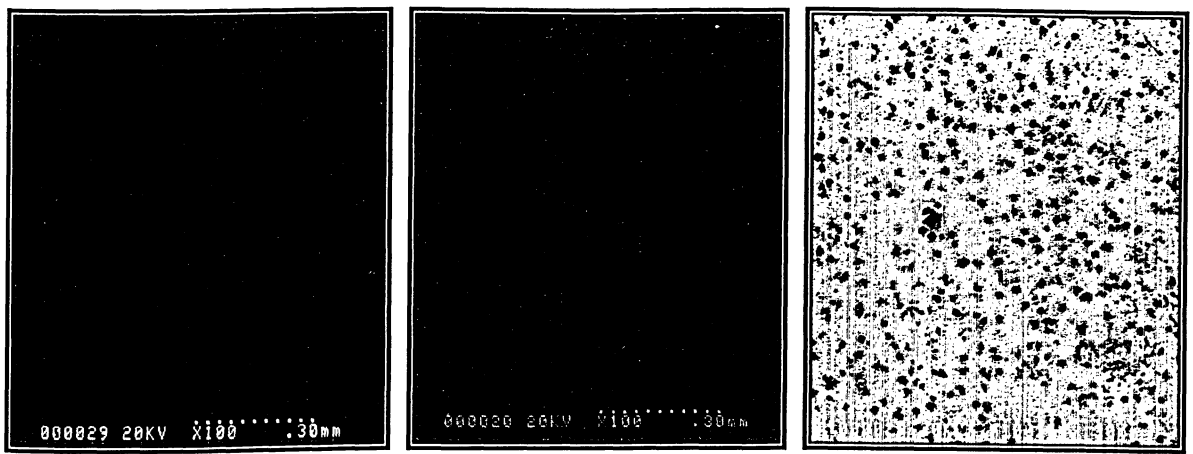

(a) (b) (c)

Figure 4.27: SEM micrographs of 4mm thick specimens poured at (a) 1350 (b) 1400 and (c) 1450°C. 100X. Nital etched.

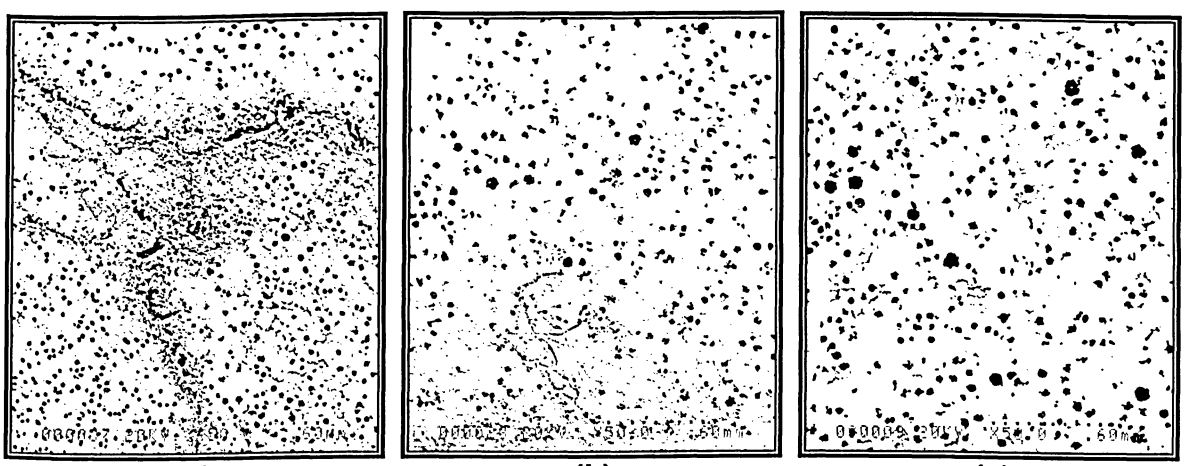

(a) (b) (c)

Figure 4.28: SEM micrographs of 14mm thick specimens poured at (a) 1350 (b) 1400 and (c) 1450°C. 50X. Nital etched.

4.1.3.3.4 Alloy 4 (4.5Si-3.0Al)

Slag strings were observed in 4mm thick specimens cast at 1350°C (Figure 4.29(a)). They were not observed in 4mm thick specimens cast at 1400 and 1450°C (Figures 4.29(b) and 4.29(c)). Isolated regions of slag (similar to the ones observed in Figure 4.22) were identified in the 7mm thick specimens. The 14mm samples cast at 1350°C exhibited regions of slag similar to the ones observed in the 7mm specimens. 14mm samples cast at 1400 and 1450°C contained significant amounts of subsurface slag, dross and blowholes (Figure 4.30).

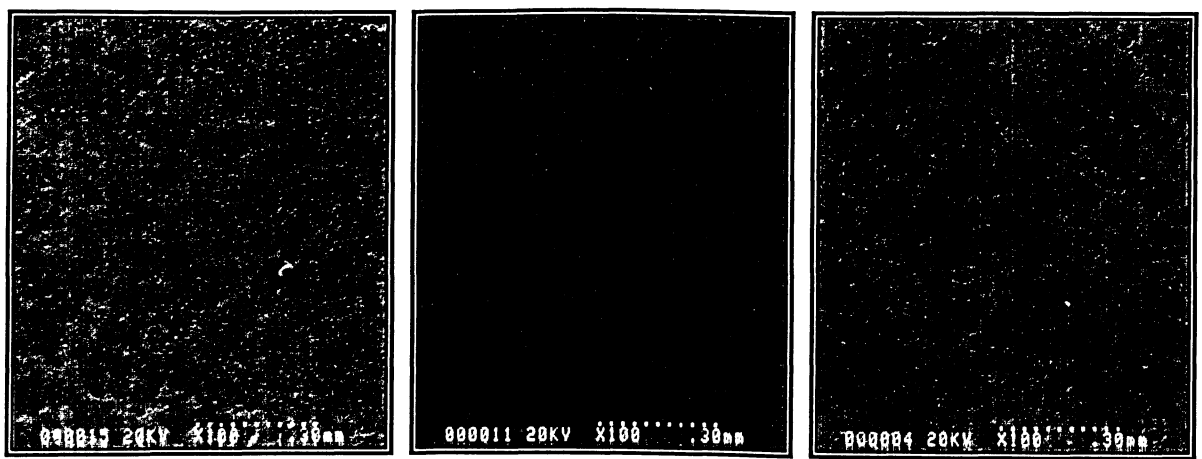

Figure 4.29: SEM micrographs of 4mm thick specimens poured at (a) 1350 (b) 1400 and (c) 1450°C. 100X. Nital etched.

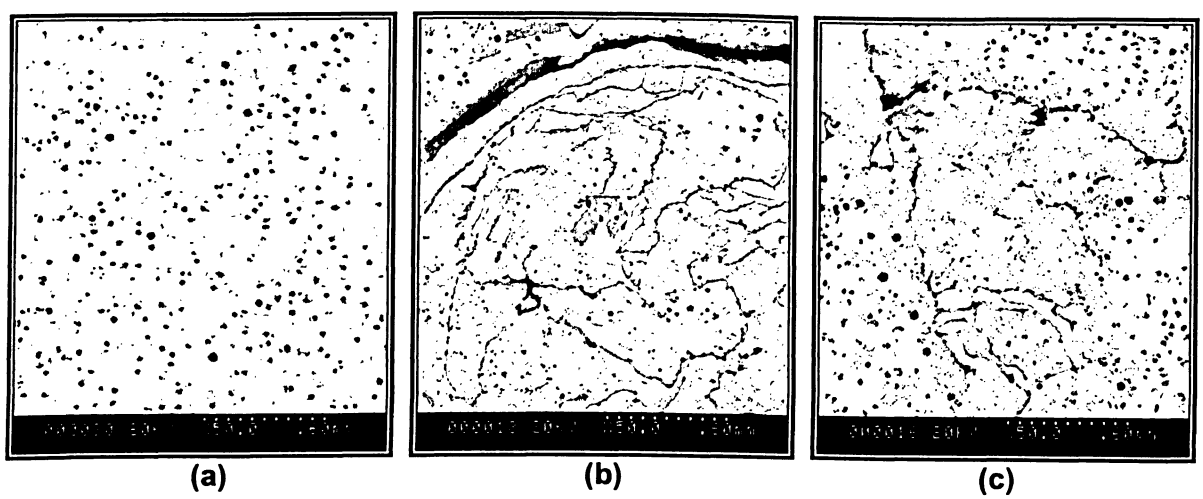

Figure 4.30: SEM micrographs of 14mm thick specimens poured at (a) 1350 (b) 1400 and (c) 1450°C. 50X. Nital etched.

4.1.3.4 Pinhole Porosity

The pouring temperature (i.e., 1350, 1400 and 1450°C) did not affect the formation of pinholes.

Pinholes were observed in Alloy 1 (3.5Si-2.0Al) and Alloy 2 (3.5Si-3.0Al). The average size of a pinhole pore in Alloys 1 and 2 was 0.9 and 1.7μm, respectively. These pinholes, magnified 1700X and 1500X, are shown in Figures 4.31(a) and 4.31(b). The alloy with a higher aluminum content showed larger pinholes. Further, the number of pinholes observed in Alloy 2 increased (relative to Alloy 1).

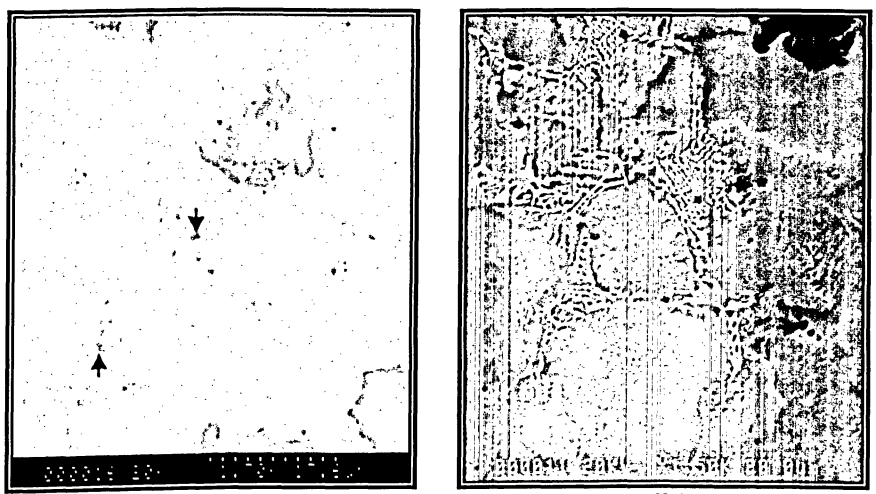

Figure 4.31: SEM micrographs of 4mm thick specimens obtained from (a) Alloy 1 (1700X) and (b) Alloy 2 (1500X). Select pinholes are indicated by arrows.

The pinholes observed in Alloys 3 (4.5Si-2.0Al) and 4 (4.5Si-3.0Al) increased in size and quantity. This is shown in Figures 4.32(a) and 4.32(b). The average size of a pinhole in Alloys 3 and 4 was 6 and 6.5μm, respectively. It was determined that pinhole counts increased with an increasing aluminum content. Also, the pinhole distributions were random and no distinct patterns could be resolved. But, the size and number of pinholes observed in Alloys 3 and 4 (relative to Alloys 1 and 2) were higher. This feature is attributed to the moisture content in the mould and an oxygen saturated liquid metal (section 2.2.3.5)

Pinholes were not observed in 14mm thick specimens. However, porosity and blowholes associated with slag and dross developed below the surface of the casting.

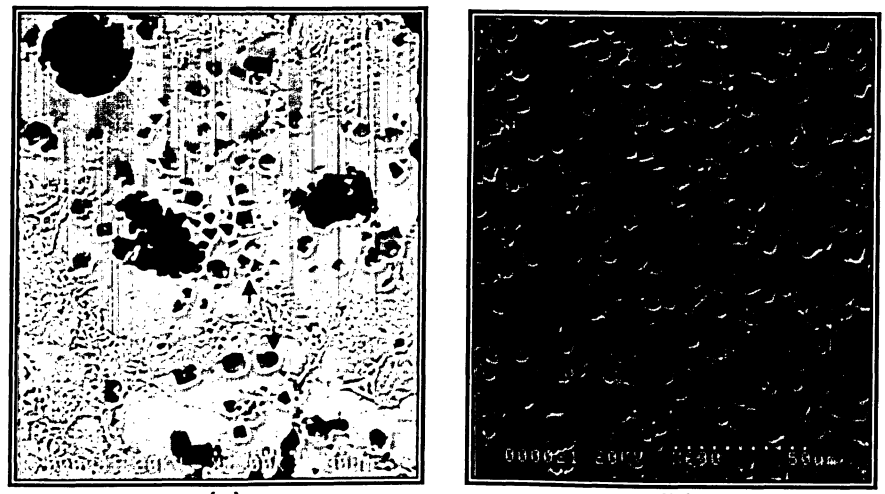

Figure 4.32: SEM micrographs of 4mm thick specimens obtained from (a) Alloy 3 (600X) and (b) Alloy 4 (1000X). Select pinholes are indicated by arrows.

Reaction porosity [90] or pinholes that resulted from carbon monoxide (CO) associated with large amounts of slag was observed in every specimen containing clusters of slag and dross. Polishing and etching removed slag and dross in local regions, thus revealing subsurface pinholes (Figure 4.33).

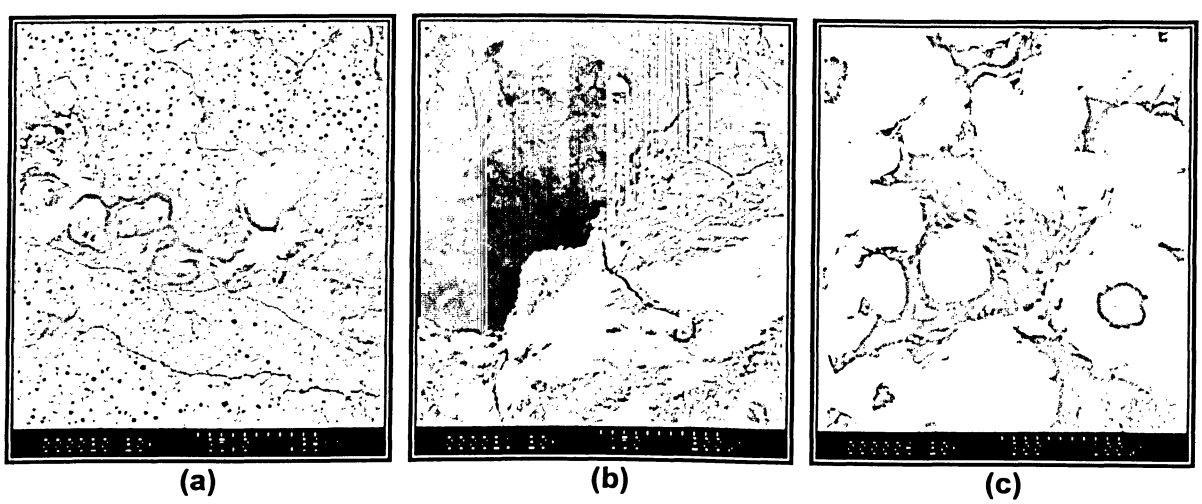

Figure 4.33: SEM micrographs of (a) reaction porosity (35X), (b) 150X micrograph of Figure 4.33(a) and (c) two reaction pinholes uncovered along the centre of a specimen (300X).

4.1.3.5 Shrinkage Defects

The section thickness and pouring temperature affected the degree of shrinkage. Shrinkage defects were observed in the 4mm thick specimens and, to a lesser extent, in the 7 and 14mm thick specimens. Shrinkage defects observed in the 4mm thick specimens are attributed to high cooling rates. This can be observed in Figures 4.34 to 4.37 for the alloy poured at 1350, 1400 and 1450°C. There was no clear observed effect of concentrations of silicon and aluminum on the formation of shrinkage cavities. It is thus suggested that a *CE* of 4.6 was maintained in every casting, and the observed shrinkage was not a result of composition.

Shrinkage was more pronounced in 4mm thick specimens cast at 1350 and 1400°C. Increased cooling rate and the degree of graphite nucleation in the molten ductile iron influenced the amount shrinkage produced in these specimens.

Excellent inoculation and rapid cooling rates in these castings resulted in higher nodule counts. This was determined earlier in Figure 4.4. Higher nodule counts increase the fineness of the intermixed liquid-solid solidifying mass, thereby making it very mushy [109]. The increased viscosity and the pressure of the expanding eutectic graphite together restrict the flow of the solidifying mass.

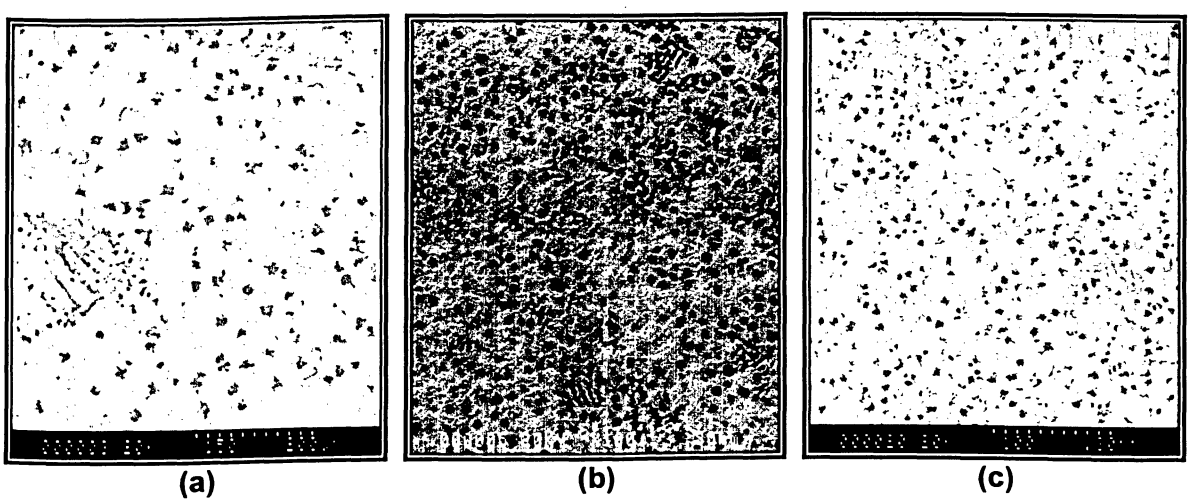

Figure 4.34: SEM micrographs of shrinkage in 4mm thick specimens cast from Alloy 1 (3.5Si-2.0Al) at (a) 1350°C (150X), (b) 1400°C (100X), nital etched, and (c) 1450°C (100X).

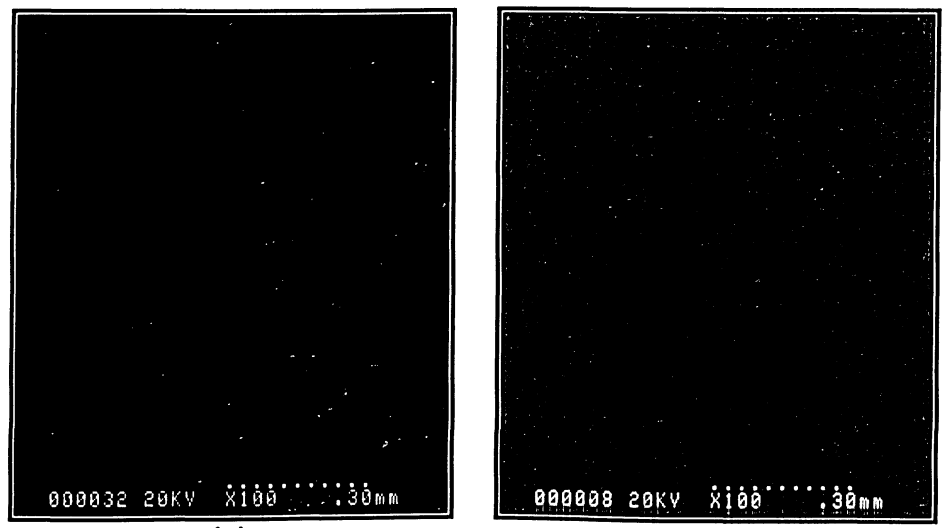

Figure 4.35: SEM micrographs of shrinkage in 4mm thick specimens cast from Alloy 2 (3.5Si-3.0Al) at (a) 1400°C and (b) 1450°C. 100X. Nital etched.

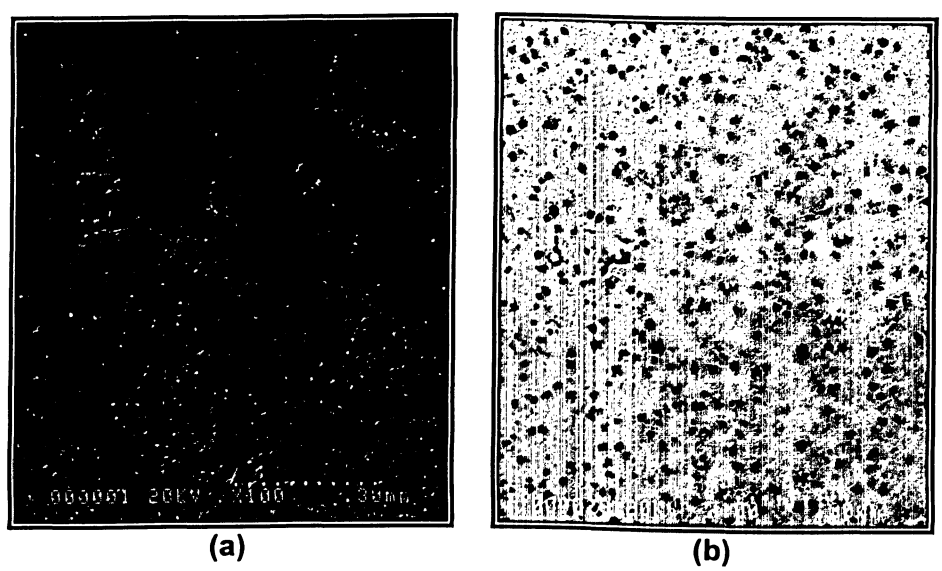

Figure 4.36: SEM micrographs of shrinkage in 4mm thick specimens cast from Alloy 3 (4.5Si-2.0Al) at (a) 1400°C and (b) 1450°C. 100X. Nital etched.

The increasing pressure from the eutectic graphite on the mould wall will cause the mould to expand and allow for shrinkage cavities to prevail. Wallace et al. [109] observed that nodule counts in excess of 200 nodules/mm^2 produced shrinkage cavities in cylindrical moulds 63.5mm in diameter and 31.75mm in height. In addition, dendrites can also increase the melt viscosity.

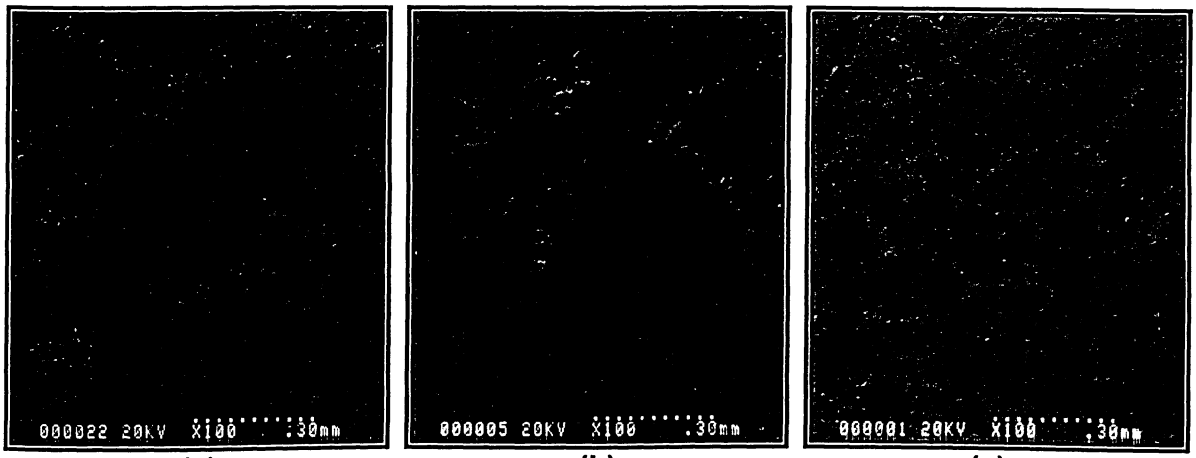

Figure 4.37: SEM micrographs of shrinkage in 4mm thick specimens cast from Alloy 4 (4.5Si-3.0Al) at (a) 1350°C, (b) 1400°C and (c) 1450°C. 100X. Nital etched.

A dendritic structure is characterized by long and thin spikes oriented in specific crystallographic directions. These spikes constitute branches containing primary, secondary, tertiary and even higher order arms. When metal cools rapidly, particularly along the mould walls, a vast number of fine dendrites will form. This was observed in Figure 4.38.

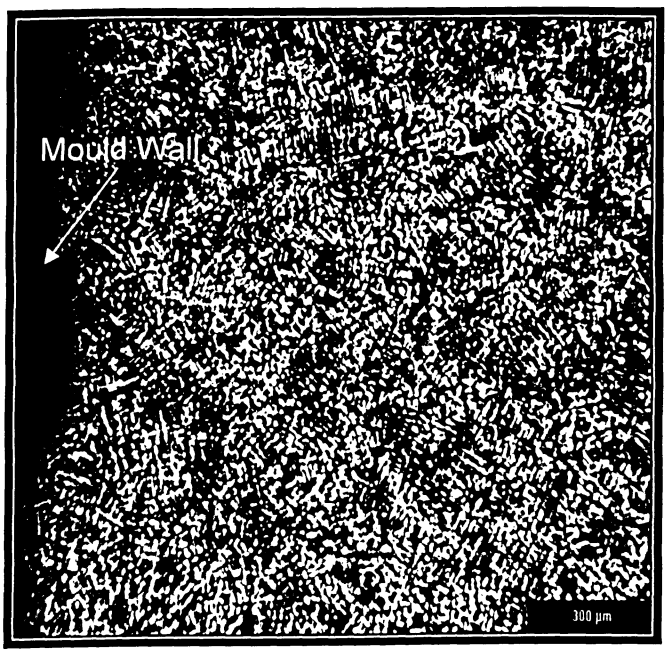

Figure 4.38: Optical micrograph of dendrites in a 4mm thick specimen cast at 1400°C. 50X. Nital etched.

During solidification, the expansion of graphite and the collision of dendrites with dendrites will cause the fragile higher order dendrite arms to break. These solid fragments will increase the viscosity of the melt [130]. These solutes will segregate in the liquid and cause shrinkage pores, particularly along the casting centreline to form. Centreline shrinkage typically occurs from the entrapment of a solute-rich interdendritic liquid from surrounding areas into a low pressure unfilled region [131]. This will ultimately form a defect that can be referred to as interdendritic shrinkage. Examples of interdendritic shrinkage pores were found in 4mm thick specimens, and these are illustrated in Figures 4.39, 4.40 and 4.41.

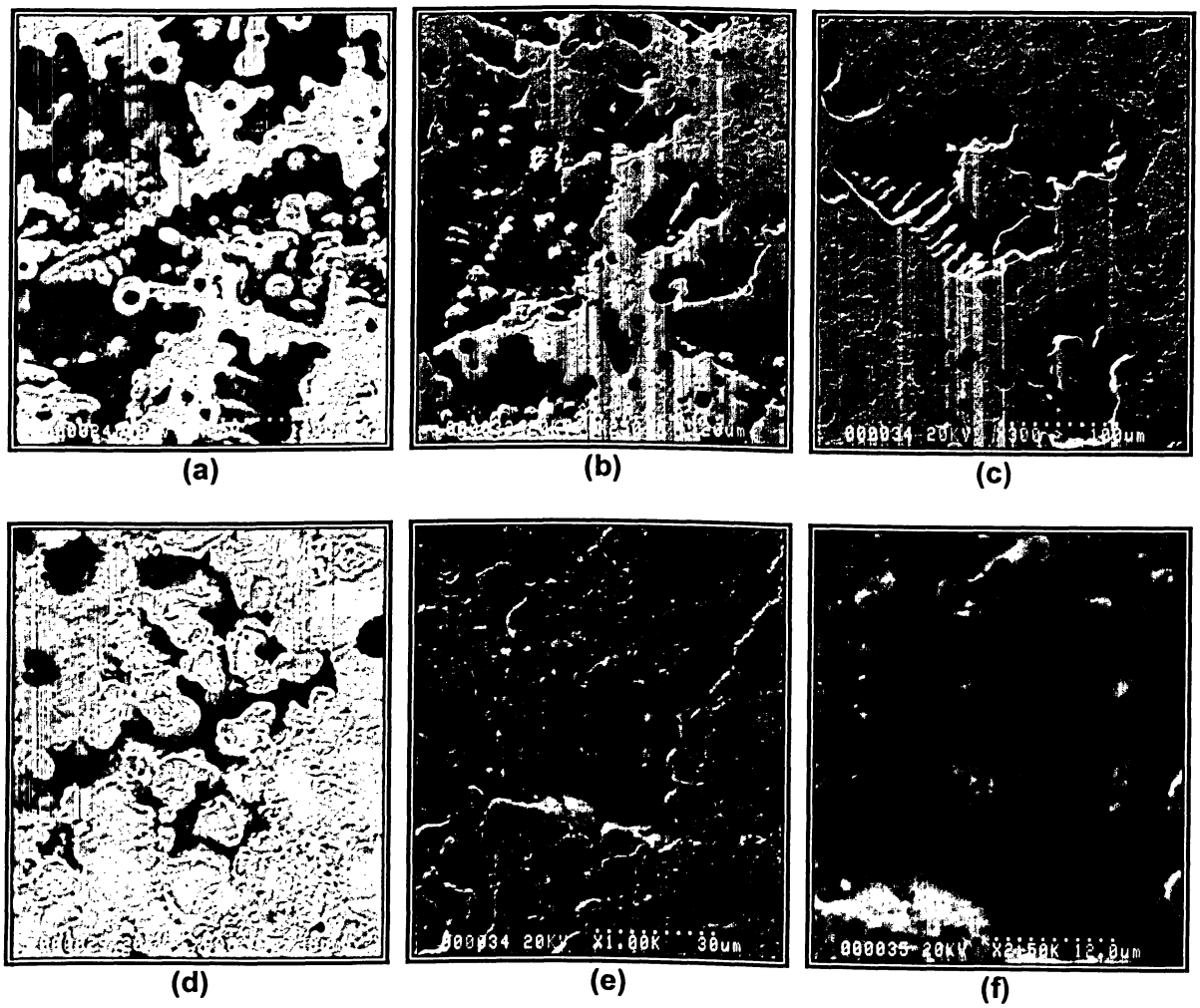

Figure 4.39: SEM micrographs showing examples of interdendritic shrinkage found in 4mm thick specimens cast from Alloy 2 (3.5Si-3.0Al) at 1400°C (a) 250X, (b) 250X, (c) 300X, (d) 800X, (e) 1000X and (f) 2500X magnification of Figure 4.39(e). Nital etched.

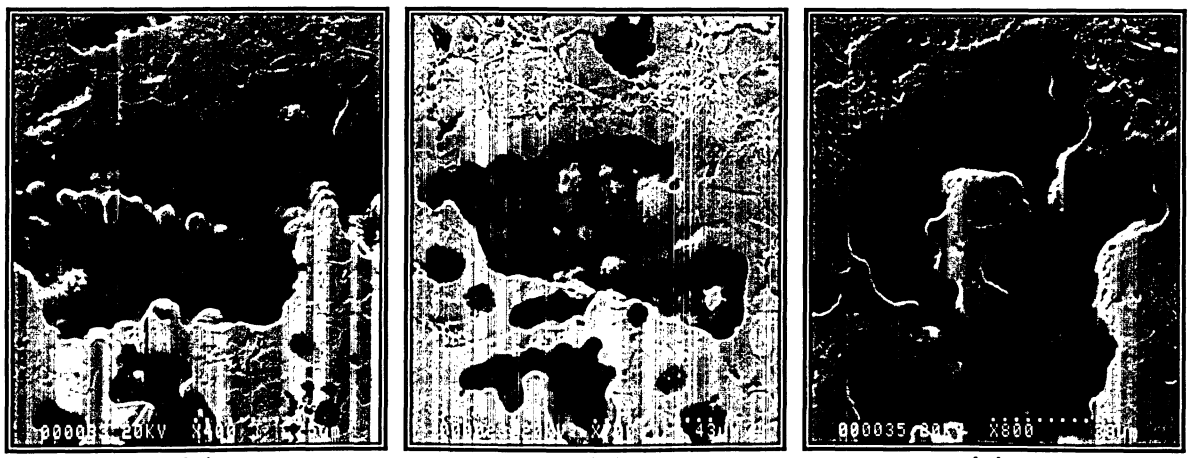

Figure 4.40: SEM micrographs showing examples of interdendritic shrinkage found in 4mm thick specimens cast from Alloy 3 (4.5Si-2.0Al) at 1450°C (a) 400X, (b) 700X and (c) 800X. Nital etched.

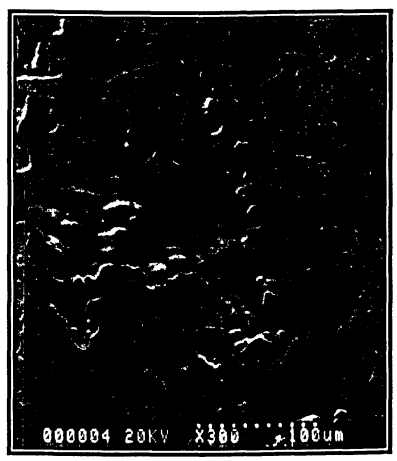

Figure 4.41: SEM micrographs showing examples of interdendritic shrinkage found in 4mm thick specimens cast from Alloy 4 (4.5Si-3.0Al) at 1400°C. 300X. Nital etched.

4.2 OXIDATION CHARACTERISTICS and MICROSTRUCTURAL FEATURES of DUCTILE IRON ALLOYS OXIDIZED for 500 hours at 700, 800, 900, 1000 and 1100°C

Factors affecting the oxidation behaviour of Alloys 1, 2, 3 and 4 were studied. All the experiments on the effect of alloy composition were repeated twice. The experimental results and the statistical analyses of these tests are given in Appendix D. Data obtained from single trial tests (effects of pouring temperature and section thickness) are not included in the appendix. The results are presented as weight lost (i.e., due to decarburization) and gained (i.e., due to formation of metal oxides) per unit area. The total weight gain of a specimen represents the addition of the absolute value of weight lost and weight gained (i.e., |weight lost (-ve)| + |weight gained (+ve)|) (Appendix E).

4.2.1 Effect of Composition on Oxidation Behaviour

Three ductile iron specimens were taken from Alloy 1 (3.5Si-2.0Al), Alloy 2 (3.5Si-3.0Al), Alloy 3 (4.5Si-2.0Al) and Alloy 4 (4.5Si-3.0Al) for this test. These specimens were exposed at atmospheric pressure in air at a temperature of 700, 800, 900, 1000 and 1100°C and cycled for 500 hours.

The oxidation kinetics of each alloy followed the parabolic time law. The results of the loss or gain in weight as a function of time were plotted and are shown in sections 4.2.1.1 to 4.2.1.5. Every alloy experienced weight loss during the early stages of testing. This resulted from the oxidation of surface graphite and surrounding carbon. The extent of weight loss progressively decreased as a direct consequence of the formation of a very thin protective oxide scale on the surface, which inhibited further oxidation. Similar observations were made by other researchers [8,9,13,14,114].

The growth of scales proceeded rapidly becoming several micrometers thick in alloys containing lower silicon and aluminum contents. Non-steady state oxidation (section 2.3.2.1) occurred during the initial hours of testing. However, upon reaching a steady state the thickness of the oxide scale was constant (which is expected for diffusion controlled oxidation) [116]. At temperatures exceeding 1000°C, abundant spalling of the oxide scale occurred during cooling.

4.2.1.1 Oxidation at 700°C for 500 hours

A thin adherent oxide layer was observed on specimens from Alloys 1, 2, 3 and 4. It can be observed from Figures 4.42(a) to 4.42(d) that specimens containing the lowest aluminum and silicon content exhibited minute oxide nodules scattered across the surface. This effect diminished as the aluminum and silicon content increased.

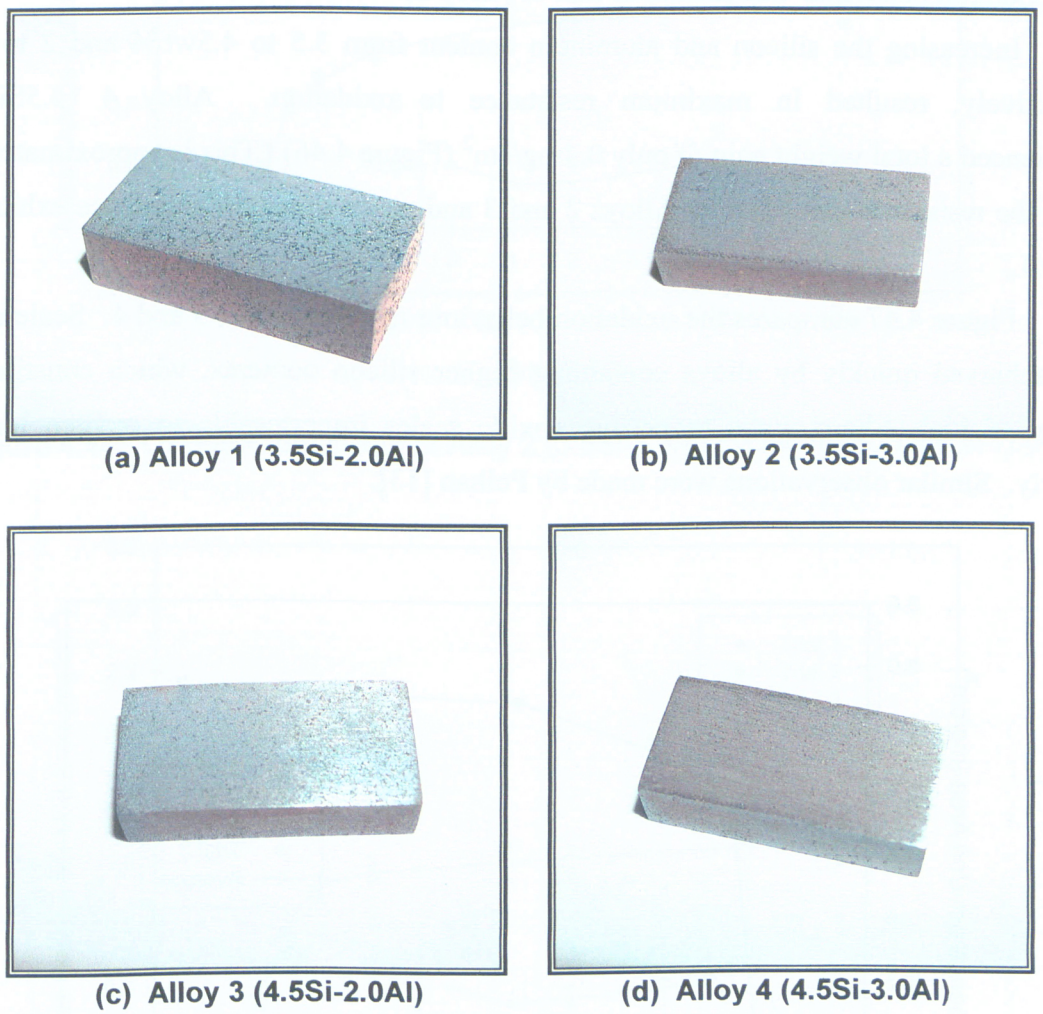

(a) Alloy 1 (3.5Si-2.0Al) **(b) Alloy 2 (3.5Si-3.0Al)**

(c) Alloy 3 (4.5Si-2.0Al) **(d) Alloy 4 (4.5Si-3.0Al)**

Figure 4.42: The extent of oxidation due to thermal cycling at 700°C.

Alloy 1 (3.5Si-2.0Al) experienced a total weight gain of 3.0mg/cm^2 after 500 hours at 700°C (Figure 4.43). The maximum weight change was experienced during the initial 24

hours, where oxidation proceeded rapidly. The rate of oxidation decreased thereafter, eventually reaching a plateau.

Alloy 2 (3.5Si-3.0Al) oxidized moderately with a total weight gain of 1.4mg/cm^2 after 500 hours (Figure 4.44). An increase in the aluminum content from 2 to 3wt.% almost doubled the alloys resistance to oxidation.

Alloy 3 (4.5Si-2.0Al) experienced a total weight gain of 1.2mg/cm^2 (Figure 4.45). The oxidation behaviour was similar to that of Alloy 2.

Increasing the silicon and aluminum content from 3.5 to 4.5wt.% and 2 to 3wt.% respectively, resulted in maximum resistance to oxidation. Alloy 4 (4.5Si-3.0Al) experienced a total weight gain of only 0.4mg/cm^2 (Figure 4.46). This is approximately three times the resistance exhibited by Alloys 2 and 3 and seven times the resistance exhibited by Alloy 1.

Figure 4.47 compares the oxidation behaviour of Alloys 1, 2, 3 and 4. Scale stability was achieved quickly by alloys containing higher silicon contents, which constitutes the ability of high silicon irons to produce oxide scales impermeable to oxygen ions very quickly. Similar observations were made by Pelhan [13].

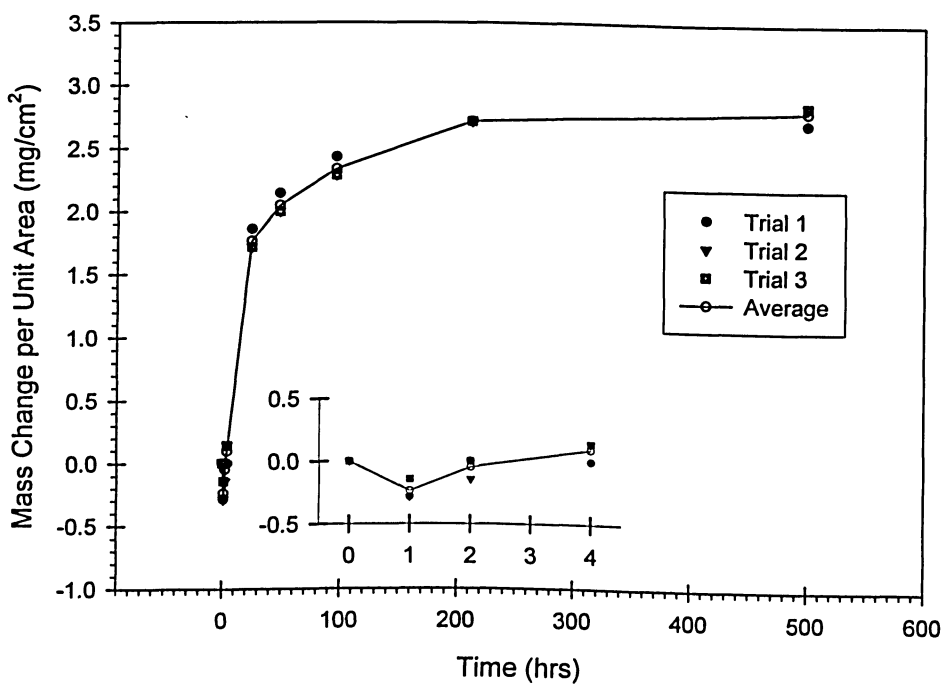

Figure 4.43: Oxidation behaviour of Alloy 1 (3.5Si-2.0Al) cycled for 500 hrs at 700°C.

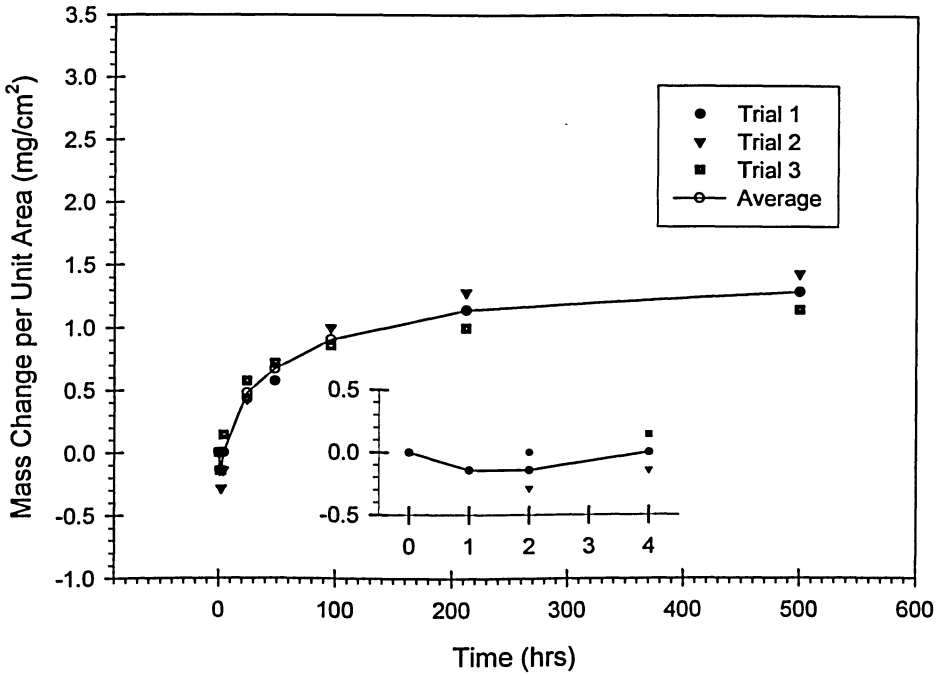

Figure 4.44: Oxidation behaviour of Alloy 2 (3.5Si-3.0Al) cycled for 500 hrs at 700°C.

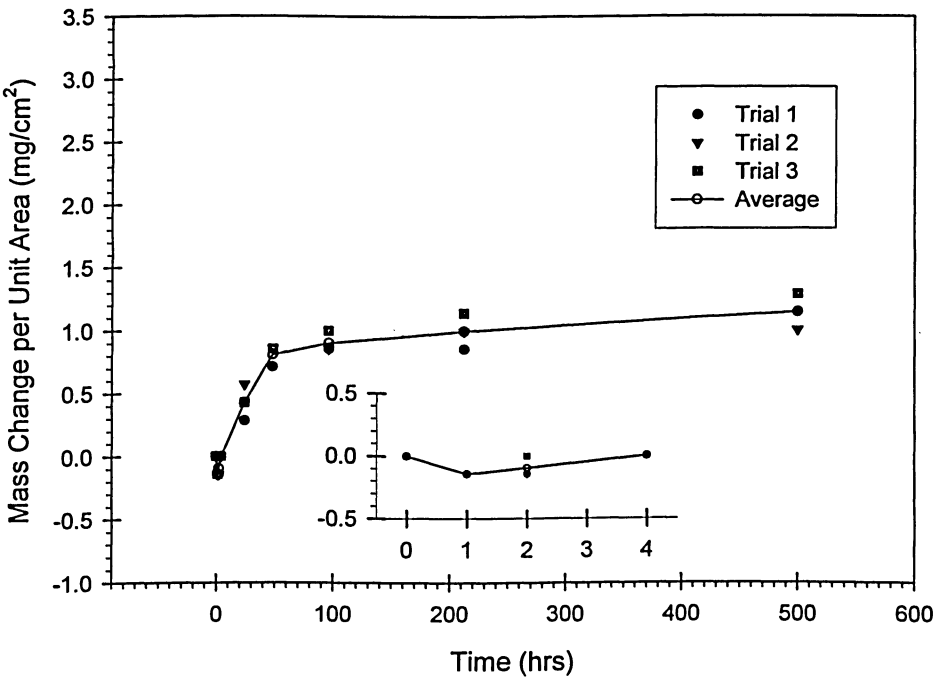

Figure 4.45: Oxidation behaviour of Alloy 3 (4.5Si-2.0Al) cycled for 500 hrs at 700°C.

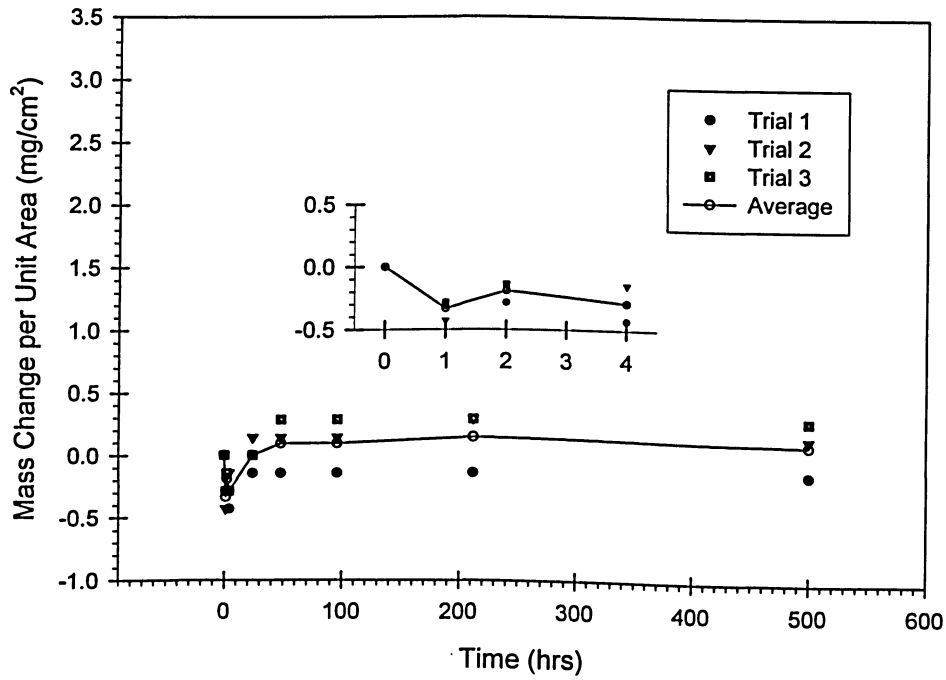

Figure 4.46: Oxidation behaviour of Alloy 4 (4.5Si-3.0Al) cycled for 500 hrs at 700°C.

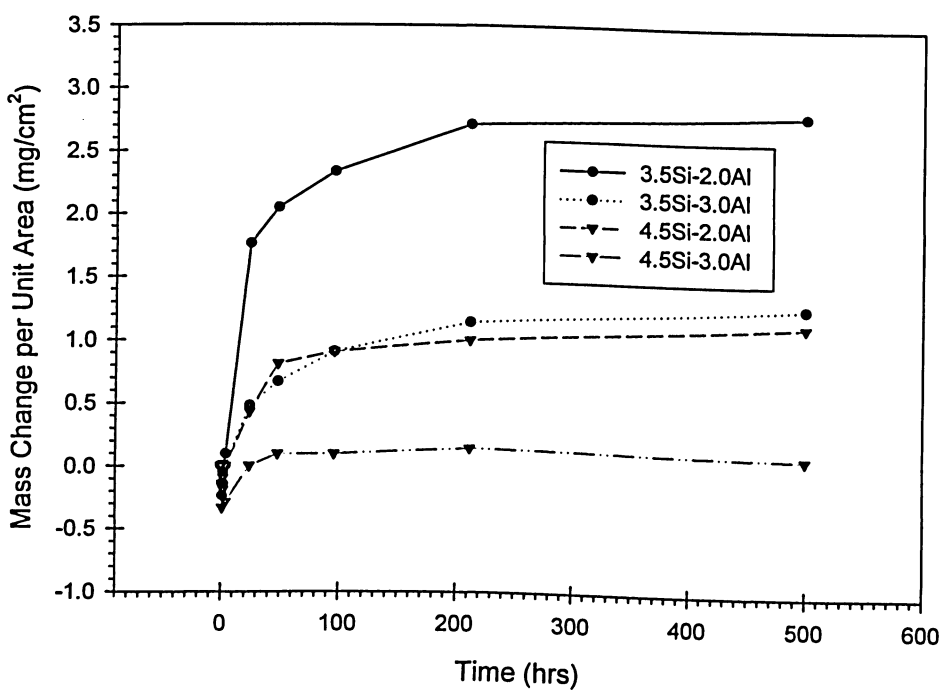

Figure 4.47: Effect of different combinations of Al and Si on the oxidation behaviour of ductile iron specimens cycled for 500 hrs at 700°C.

4.2.1.2 Oxidation at 800°C for 500 hours

The oxide scale became progressively thinner as the silicon and aluminum content increased. These trends are shown in Figures 4.48(a) to 4.48(d). Also, the size of the oxide nodules on the surface of Alloy 1 increased with an increase in the oxidation temperature.

X-ray analysis of the oxide scales was performed. X-ray maps of the oxide scale produced on Alloy 2 (3.5Si-3.0Al) are given in Figure 4.49. The mapping revealed that the oxide scale consisted of several layers, an external layer composed of iron oxides and an internal layer composed of oxides of iron, silicon and aluminum. Traces of molybdenum rich precipitates were also identified below the oxide scale.

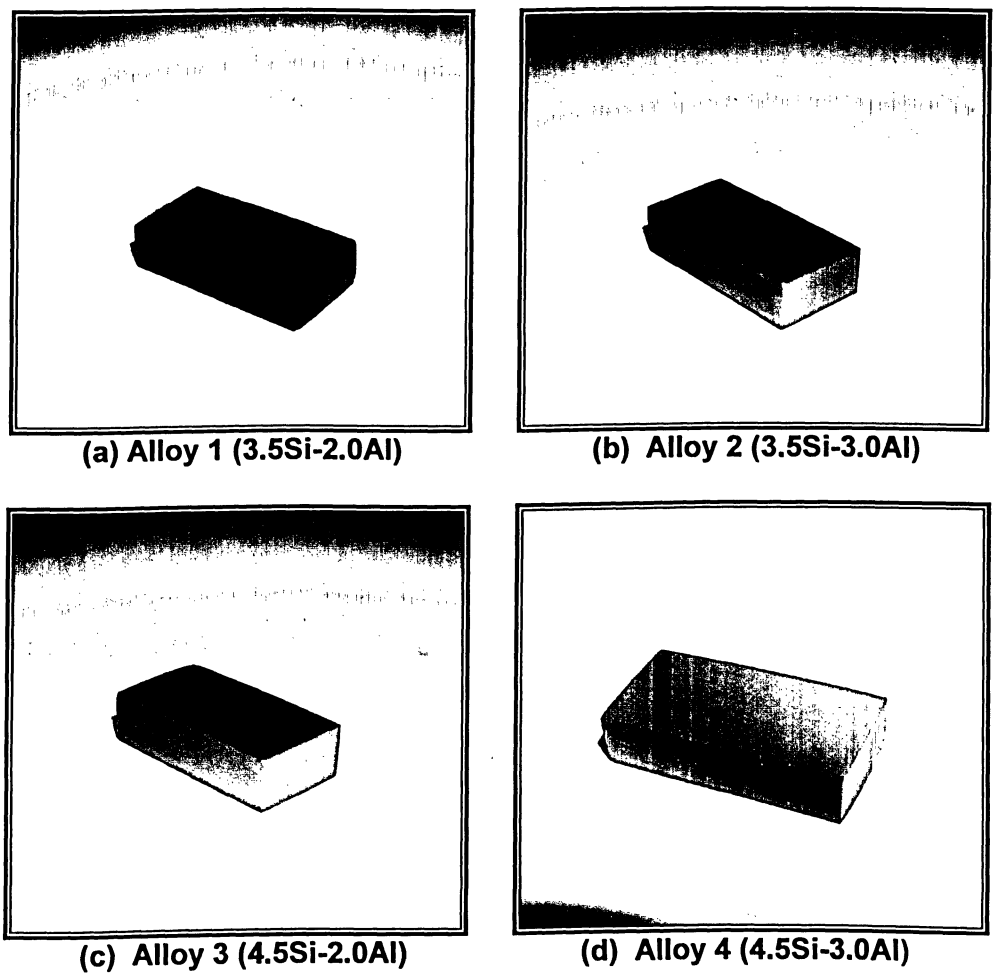

(a) Alloy 1 (3.5Si-2.0Al)

(b) Alloy 2 (3.5Si-3.0Al)

(c) Alloy 3 (4.5Si-2.0Al)

(d) Alloy 4 (4.5Si-3.0Al)

Figure 4.48: The extent of oxidation due to thermal cycling at 800°C.

Alloy 1 (3.5Si-2.0Al) exhibited a total weight gain of 0.6mg/cm^2 after 500 hours (Figure 4.50). A plateau was not observed and oxidation continually progressed throughout the duration of the test. Oxide ridges were accompanied by micro-cracks on the scale surface, and these possibly provide an explanation for the continued corrosion of the sample. These cracks suggest that dilation of the specimen occurred during thermal cycling, thus breaking the scale and continuously exposing the metal to oxygen. Sample dilation could have resulted from the difference in expansion coefficient of the individual oxides and metal as well as the evolution of gases arising from the thermal oxidation of carbon (i.e., CO and CO_2). Similar observations were made by Nofal et al. [8]. Further, the volumetric stability of the specimen can be compromised through the decomposition of pearlite, which could cause the scale to rupture. During cyclic oxidation testing, all these factors generate stresses that contribute to cracking of the scale. Once ruptured, oxygen can penetrate into the metal, thus forming a fresh oxide scale. This process could repeat itself indefinitely. However, the effect of pearlite decomposition is temperature-time dependent and will diminish after a specific number of cycles (Figure 2.7, section 2.1.8.2).

Alloy 2 (3.5Si-3.0Al) showed a total weight gain of 0.4mg/cm^2 (Figure 4.51). However, a significantly high initial weight loss of 0.3mg/cm^2 was observed. Electron microscopy and x-ray analysis of the metal-oxide interface suggests that the initial weight loss was related to the size of the remaining cavity when graphite nodules oxidized. Also, the extent of weight loss can increase appreciably if the cavity is accompanied by a defect, such as a shrinkage pore, a series of pinholes or cellular slag and dross. Such a phenomenon is readily illustrated in Figure 4.52. When a cavity develops, oxygen can use this path to diffuse into the internal core of the casting. If this path leads to the surface of an internal pore, the graphite and surrounding carbon can oxidize preferentially. Internal oxidation will continue until a protective oxide scale develops and lines the surface of the pore. X-ray maps (Figure 4.49) of the same area in Figure 4.52 show that the pores were lined with oxides of aluminum, silicon and iron. In addition, the oxidation of iron can result in the formation of an iron oxide nodule above the pore. From this analysis it was suggested that oxide nodules developed as a result of internal defects. From the x-ray analysis in Figure 4.49, it was suggested that the nodule was primarily composed of oxides of iron.

(a) SEM micrograph of area mapped using x-rays

(b) Oxygen

(c) Iron

(d) Aluminum

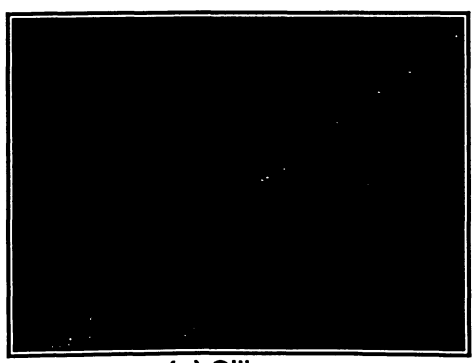

(e) Silicon

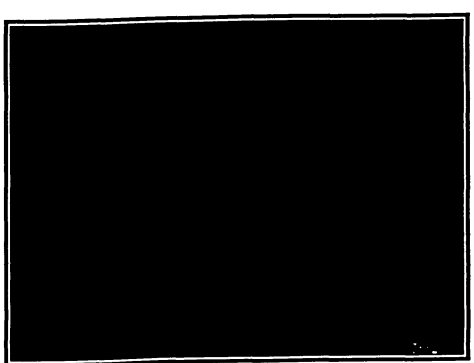

(f) Molybdenum

(g) Background Noise

Figure 4.49: X-ray mapping of the oxide scale on Alloy 2 (3.5Si-3.0Al) oxidized at 800°C.

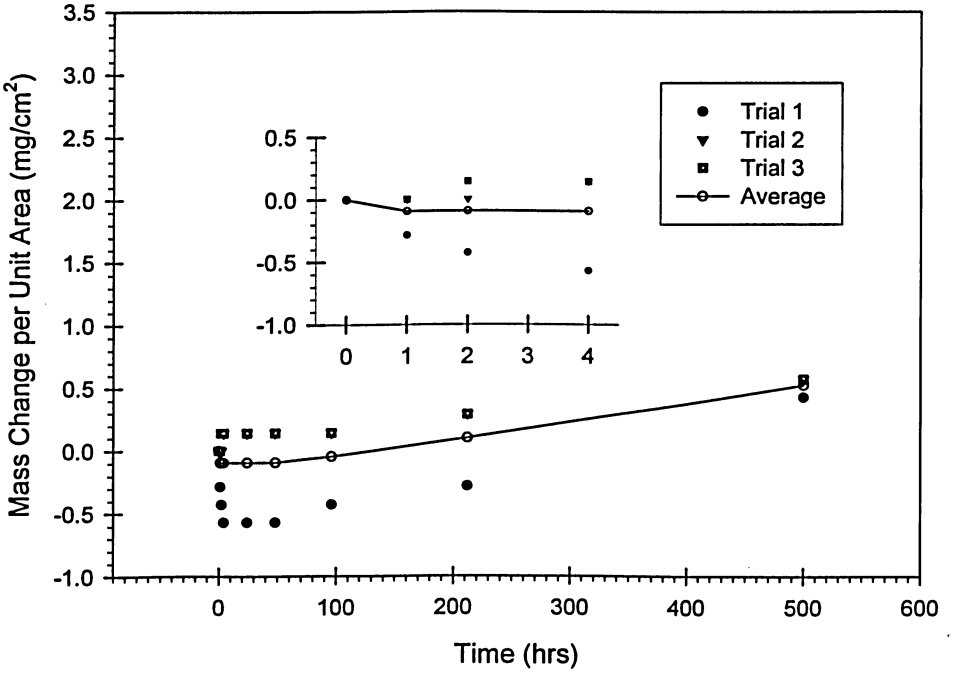

Figure 4.50: Oxidation behaviour of Alloy 1 (3.5Si-2.0Al) cycled for 500 hrs at 800°C.

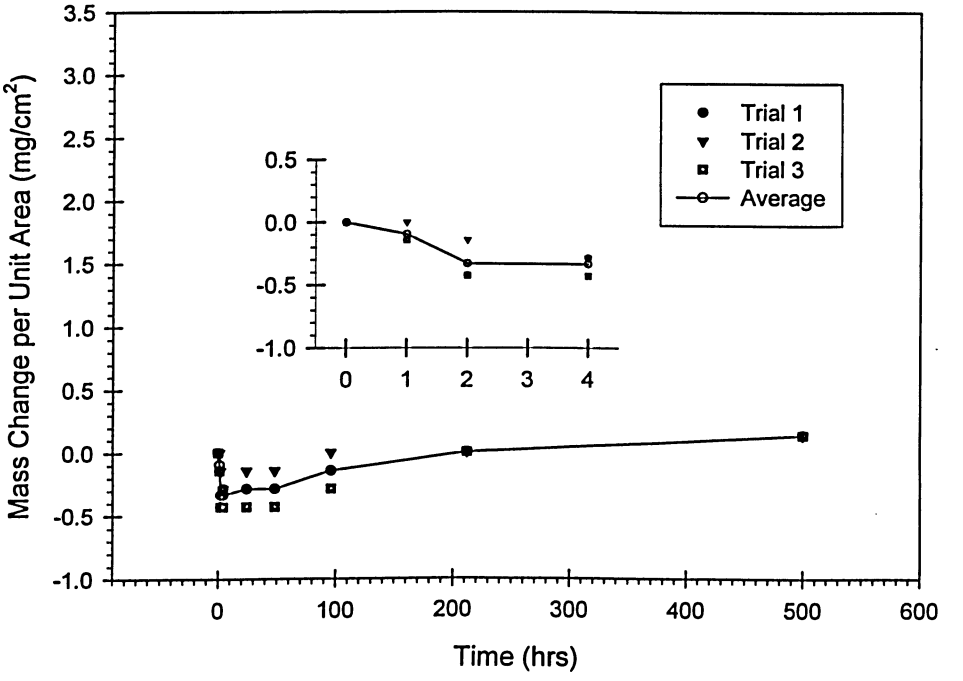

Figure 4.51: Oxidation behaviour of Alloy 2 (3.5Si-3.0Al) cycled for 500 hrs at 800°C.

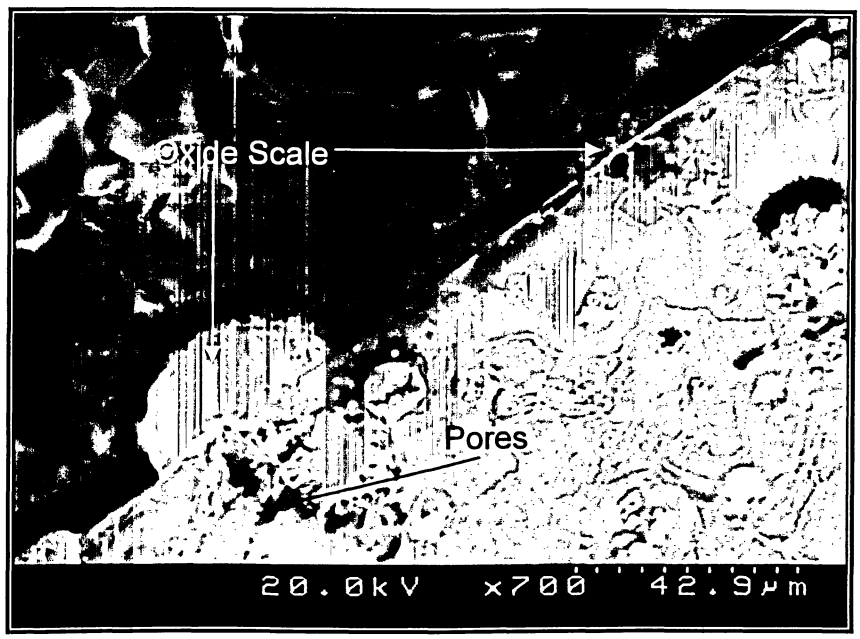

Figure 4.52: SEM micrograph of an oxide nodule that formed over a subsurface defect pore in Alloy 1 (3.5Si-2.0Al) oxidized at 800°C. 700X. Nital etched.

The excess iron from the internal surface of the crevice yielded more oxidizable iron per unit of external surface area, thus producing a layer several times thicker at that particular point, compared to a layer formed elsewhere along the external surface of the sample. As a result, it is suggested that a correlation may exist between the size of the oxide nodule and the size of the crevice. Mapping of the developed oxide nodules could eventually provide a map of subsurface defects and ultimately determine the materials resistance to oxidation, at a fraction of the time currently required. In general, samples containing internal defects close to the surface will experience a high initial weight loss provided everything else remains constant (i.e., size, surface area, surface finish and oxidizing temperature). Furthermore, subsurface crevices could result in forming an external scale composed of oxide nodules. Figure 4.53 illustrates this phenomenon on one of the specimens from Alloy 1 (3.5Si-2.0Al) oxidized at 800°C.

Alloy 3 (4.5Si-2.0Al) exhibited a total weight gain of 0.6mg/cm^2 (Figure 4.54). However, the initial weight loss was high. This was attributed to the possible presence of subsurface defects.

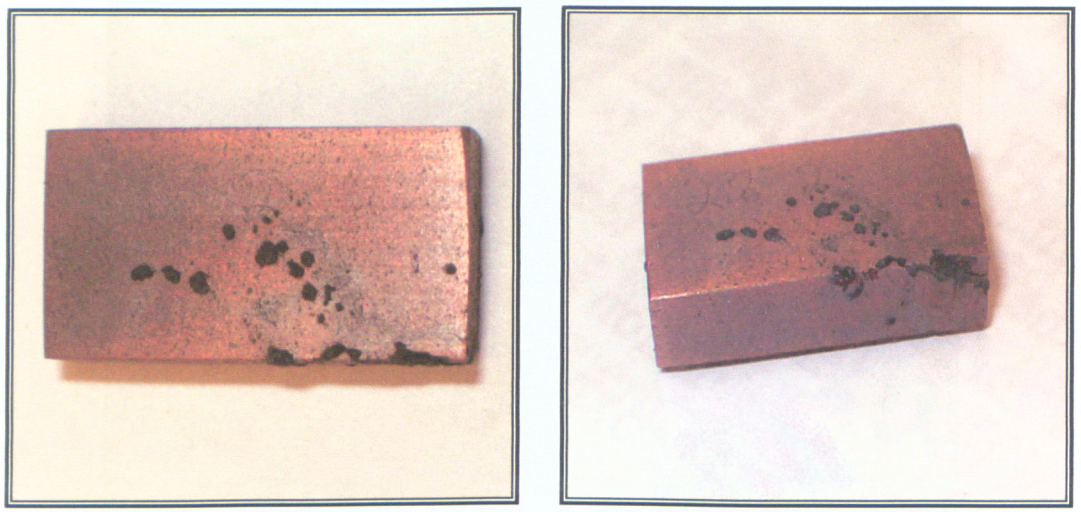

(a) Top View **(b)** Isometric View

Figure 4.53: Oxide nodules on one of the specimens from Alloy 1 oxidized at 800°C.

Alloy 4 (4.5Si-3.0Al) showed excellent oxidation resistance. After 500 hours, this alloy had a total weight gain of 0.3mg/cm^2 (Figure 4.55).

The four alloys showed much greater resistance to oxidation at 800°C then at 700°C. This phenomenon was possibly due to the greater mobility of atoms at higher temperatures. This allowed the alloying elements to oxidize more rapidly, thereby producing a protective scale during the early stages of testing.

The effect of increasing the silicon and aluminum content on the oxidation resistance of each alloy at 800°C for 500 hours is shown in Figure 4.56. In general, the resistance to oxidation at 800°C was enhanced as the silicon and aluminum content increased.

Work by Sponseller et al. [14] on the oxidation behaviour of ductile irons alloyed with aluminum, silicon and molybdenum showed that respectable resistance to oxidation could be achieved. They showed that ductile iron alloyed with 4wt.% silicon, 2wt.% molybdenum and 0.9wt.% aluminum had a weight gain of 6.24mg/cm^2 after 500 hours at 816°C. This is a ten fold increase in mass per unit area compared to Alloy 1, which exhibited the poorest resistance to oxidation among the alloys studied. In the current study, significant improvement to the oxidation resistance of ductile iron at 800°C was achieved.

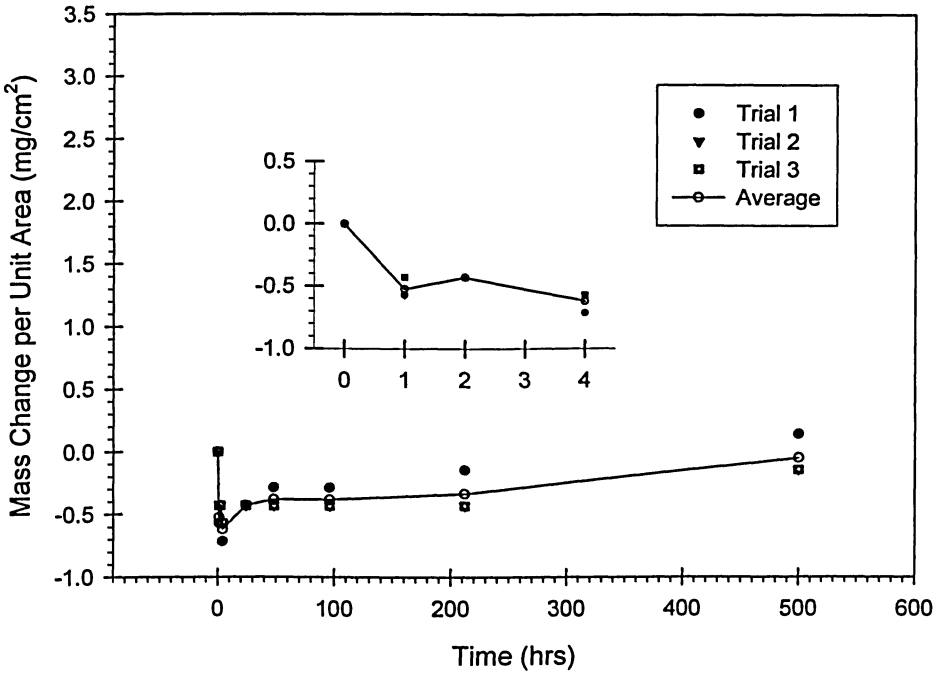

Figure 4.54: Oxidation behaviour of Alloy 3 (4.5Si-2.0Al) cycled for 500 hrs at 800°C.

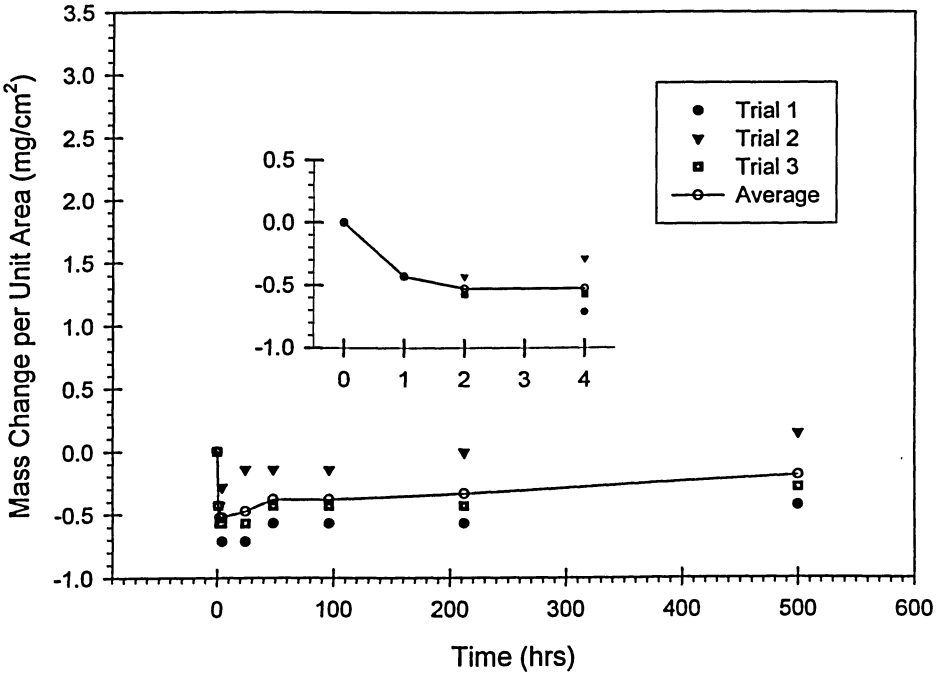

Figure 4.55: Oxidation behaviour of Alloy 4 (4.5Si-3.0Al) cycled for 500 hrs at 800°C.

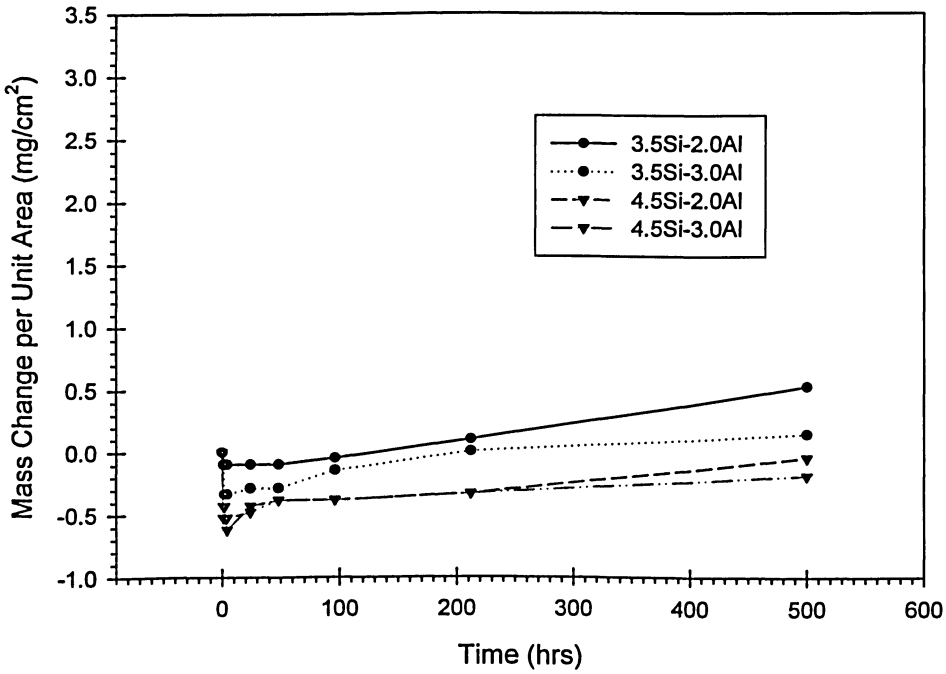

Figure 4.56: Effect of different combinations of Al and Si on the oxidation behaviour of ductile iron specimens cycled for 500 hrs at 800°C.

4.2.1.3 Oxidation at 900°C for 500 hours

Alloy 1 developed a thick dark oxide scale consisting of densely populated oxide nodules (Figure 4.57(a)). Surface spalling was not observed. This alloy showed a total weight gain of 45mg/cm^2 (Figure 4.58). This sample oxidized continuously during the 500 hours of cycling. A plateau was not reached and the rate of oxidation was observed to remain constant (the slope did not change) throughout the test.

When Alloy 1 was sectioned, porous oxide scales were observed, as illustrated in Figures 4.59(a), 4.60 and 4.61. Large fissure defects accompanied by blistering were observed along the edges of the sample. It is suggested that these subscale defects resulted from the combustion of graphite and surrounding carbon. If the oxide scale cracks during the course of testing and allows oxygen to penetrate to the metal, graphite and the surrounding carbon will oxidize. Typically, for every mole of oxygen consumed by carbon, two moles of carbon monoxide gas will form.

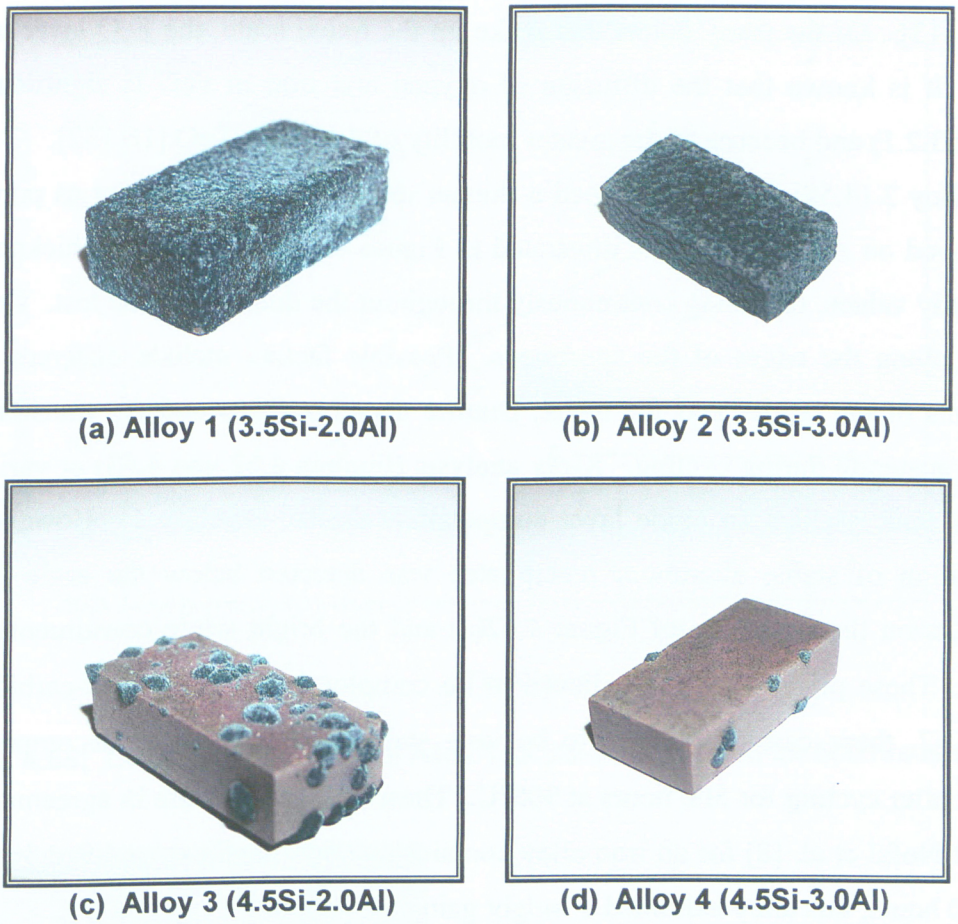

Figure 4.57: The extent of oxidation due to thermal cycling at 900°C.

Further, carbon can react with FeO (Equation 2.17) to produce CO. Also, reaction between CO and FeO can produce CO_2 (Equation 2.28). These reactions can occur only when the gases can escape through the porous scale. When the scale matures and mass transport is ceased, the pressure due to CO and CO_2 gases can cause the oxide scale to blister [120].

The chemical analysis (Figure 4.59(b)) of the scale in Figure 4.59(a) showed a combination of iron, aluminum and silicon oxides, in addition to molybdenum rich precipitates. X-ray mapping (Figures 4.60 and 4.61) of the scale along the side and at the corner of the specimen (Figure 4.61) shows the relative amounts of aluminum, silicon, iron and molybdenum present. The scale consisted of a very thick external layer of iron oxide composed of FeO (wüstite), Fe_3O_4 (magnetite) and Fe_2O_3 (haematite), according to the iron-oxygen phase diagram (Figure 2.19). An internal layer of aluminum (possibly composed of

Al_2O_3 and $FeAl_2O_4$) and silicon (possibly composed of SiO_2 and Fe_2SiO_4) oxides was observed [13]. Of the many layers that make up the oxide scale, the FeO layer will be the thickest. It is known that the diffusion of oxygen and iron in FeO is significantly large (section 2.3.2.1) and because of the greater mobility of defects in FeO [16,132].

Alloy 2 (4.5Si-3.0Al) developed a thinner oxide layer that was not as porous as the one observed on Alloy 1. This is illustrated in Figure 4.57(b). The scale thickness did not reach steady values, oxidizing continuously throughout the duration of the test. Cracks were observed along the edges of the specimens. Possible factors include different expansion coefficients of the oxides and the metal, pearlite decomposition and the transformation of ferrite to austenite during cycling. X-ray analysis (Figures 4.62 and 4.63) at various points along the scale yielded an oxide layer composition similar to Alloy 1. However, a large concentration of stable aluminum precipitates was detected below the scale (i.e., black precipitates on the right side of Figure 4.62(a) and the bright white constituents in Figure 4.62(d)). These precipitates are believed to be complex iron-aluminum ε-carbides. From Figure 4.62, these carbides appear to be very stable and no sign of decomposition was observed after cycling for 500 hours at 900°C. These observations are in agreement with the results of Nofal et al. [8] for an iron alloy containing 3.5wt.% silicon and 9wt.% aluminum. After 500 hours, this alloy exhibited a weight gain of $3.6mg/cm^2$ (Figure 4.64).

A thin oxide scale covered with large oxide nodules developed on Alloy 3 (Figure 4.57(c)). Chemical analysis of these nodules yielded a high content of iron, thereby possibly composed of oxides of iron. Similar observations were made by Tholence and Norell [28]. It was discussed earlier (section 4.2.1.2) that the position and size of these nodules could be related to the size and number of subsurface defects in the sample. Thus, it is suggested that Alloy 3 contained an appreciable amount of subsurface defects. The scale thickness of Alloy 3 quickly attained steady values. After 500 hours at 900°C, Alloy 3 experienced a total weight gain of $0.1mg/cm^2$ (Figure 4.65).

Alloy 4 developed a thin adherent scale containing oxide nodules (Figure 4.57(d)). The number of oxide nodules covering the surface of the sample was significantly lower than exhibited by Alloy 3. The scale thickness of Alloy 4 quickly attained steady values. The total weight gain was $0.25mg/cm^2$ (Figure 4.66), which is approximately twice as high relative to Alloy 3.

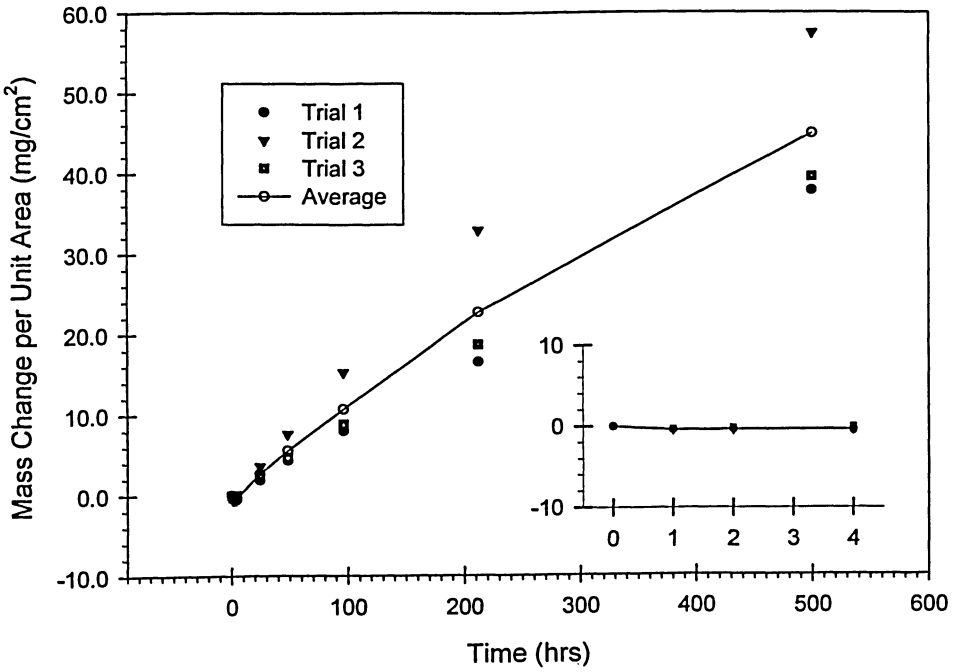

Figure 4.58: Oxidation behaviour of Alloy 1 (3.5Si-2.0Al) cycled for 500 hrs at 900°C.

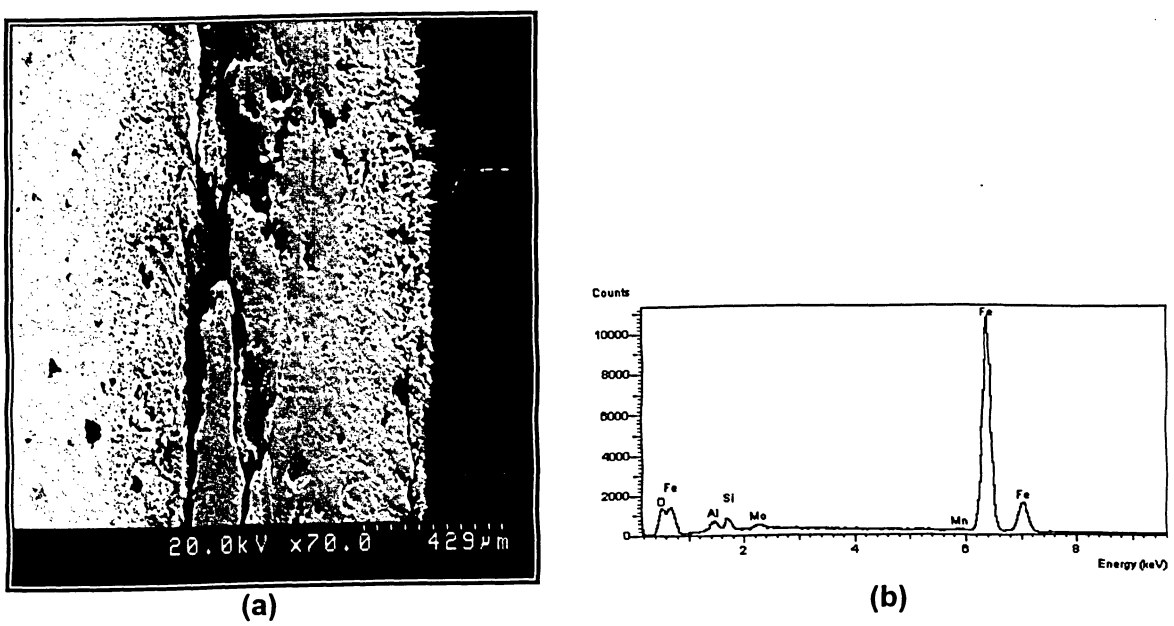

(a) (b)

Figure 4.59: SEM micrograph of oxide scale on Alloy 1 (3.5Si-2.0Al) oxidized at 900°C (70X) and (b) EDS spectrum analysis of scale. 70X. Nital etched.

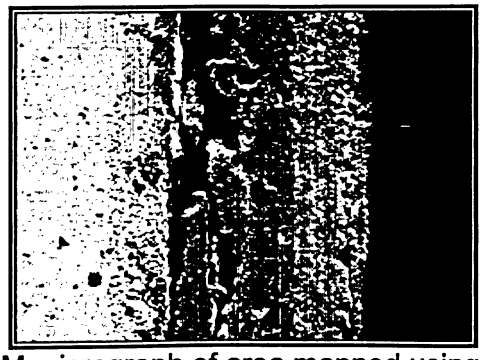

(a) SEM micrograph of area mapped using x-rays

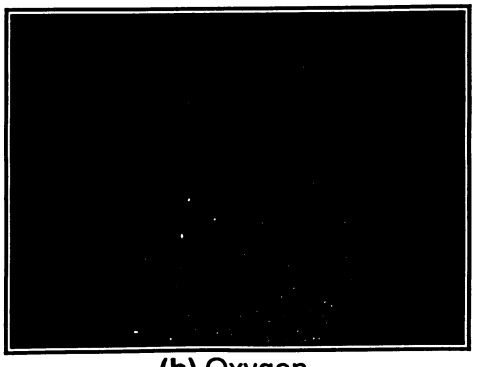

(b) Oxygen

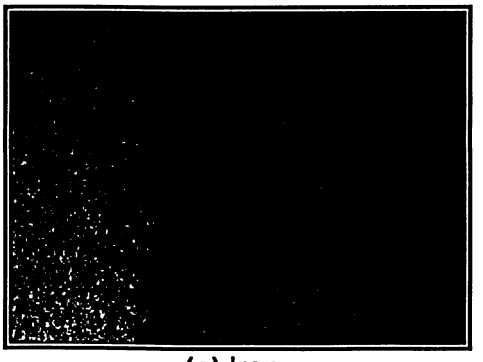

(c) Iron

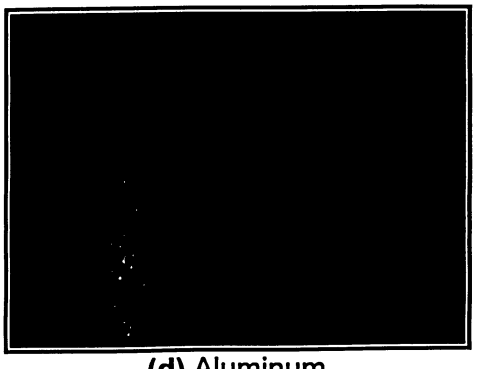

(d) Aluminum

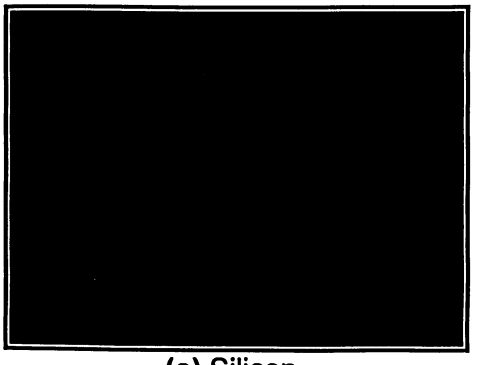

(e) Silicon

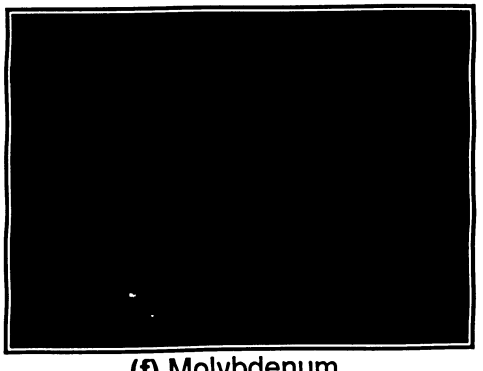

(f) Molybdenum

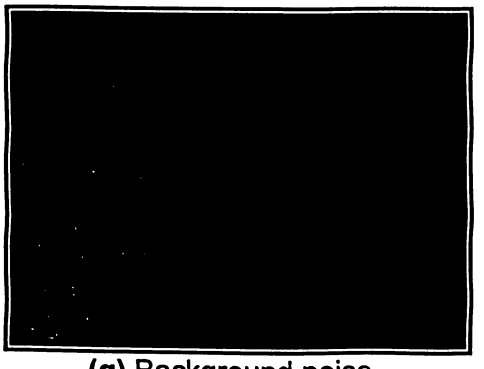

(g) Background noise

Figure 4.60: X-ray mapping of scale along side of Alloy 1 (3.5Si-2.0Al) oxidized at 900°C.

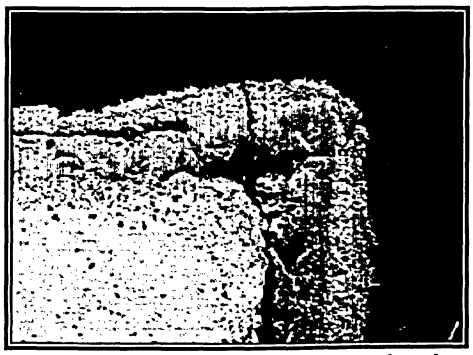

(a) SEM micrograph of area mapped using x-rays

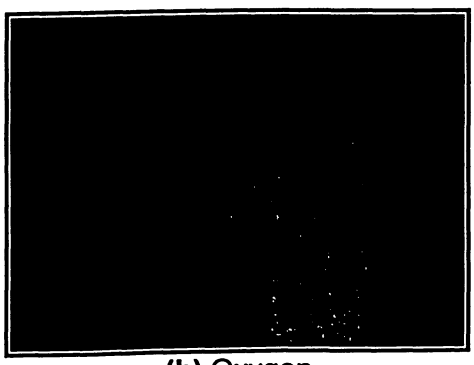

(b) Oxygen

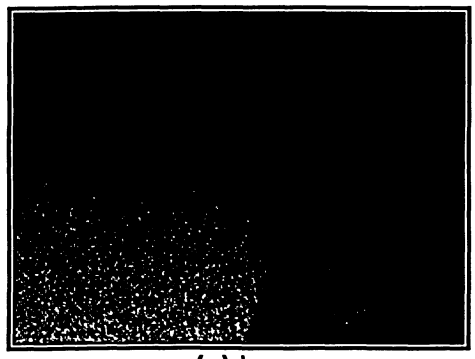

(c) Iron

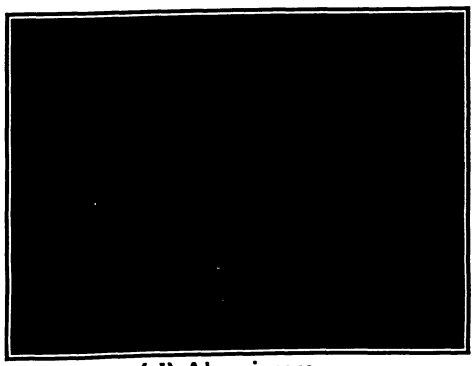

(d) Aluminum

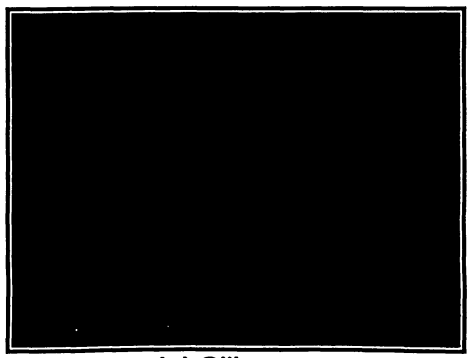

(e) Silicon

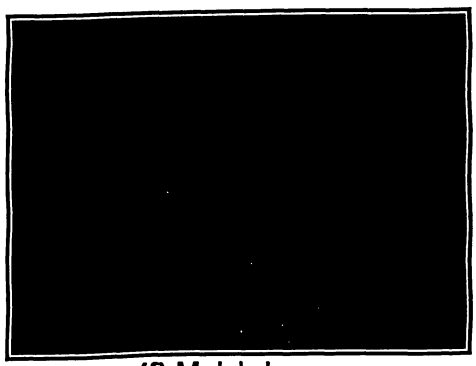

(f) Molybdenum

(g) Background noise

Figure 4.61: X-ray mapping of scale at corner of Alloy 1 (3.5Si-2.0Al) oxidized at 900°C.

(a) SEM micrograph of area mapped using x-rays

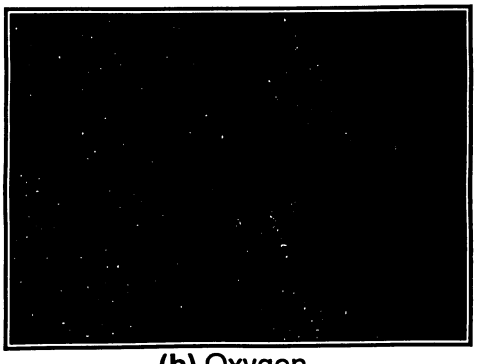

(b) Oxygen

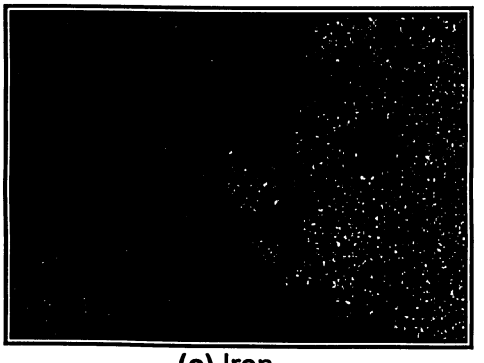

(c) Iron

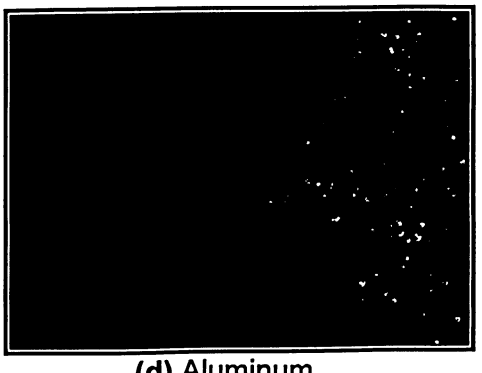

(d) Aluminum

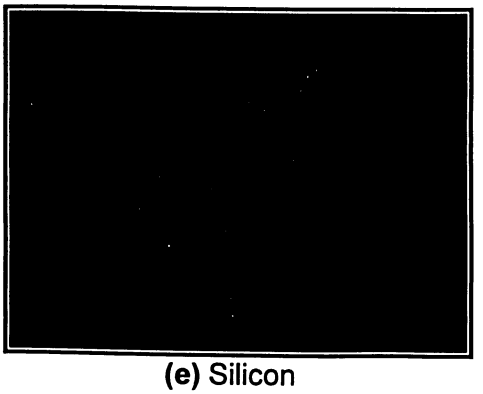

(e) Silicon

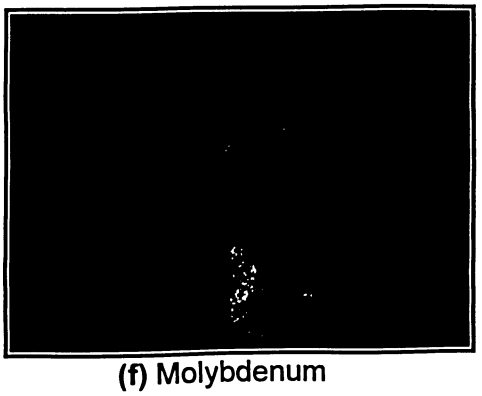

(f) Molybdenum

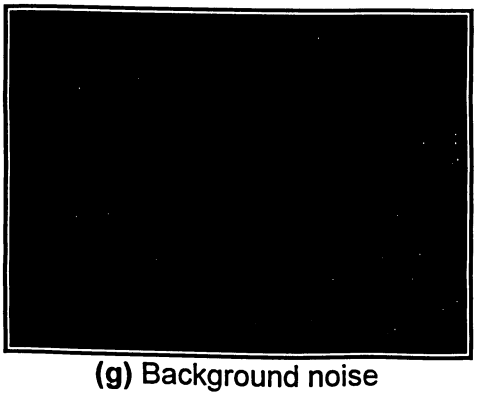

(g) Background noise

Figure 4.62: X-ray mapping of oxide scale on Alloy 2 (3.5Si-3.0Al) oxidized at 900°C.

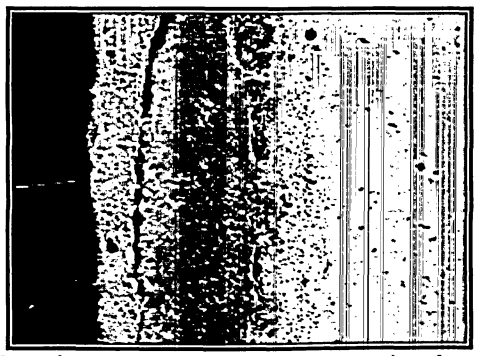

(a) SEM micrograph of area mapped using x-rays

(b) Oxygen

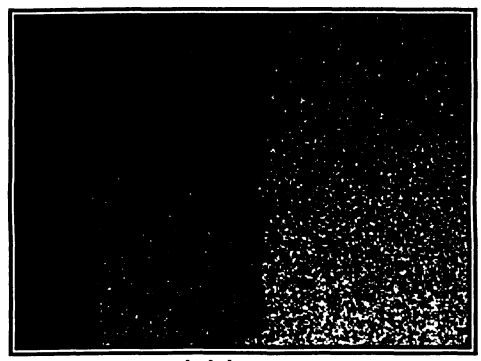

(c) Iron

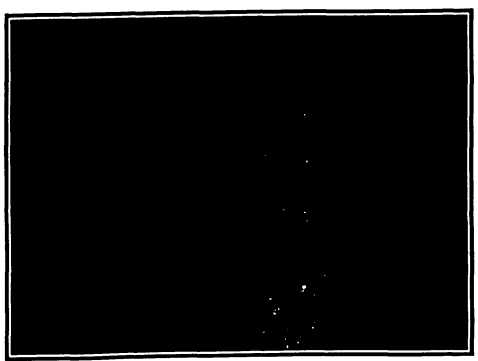

(d) Aluminum

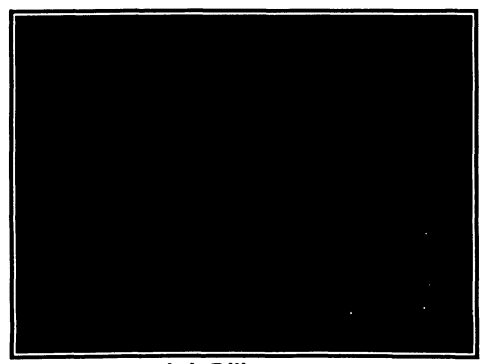

(e) Silicon

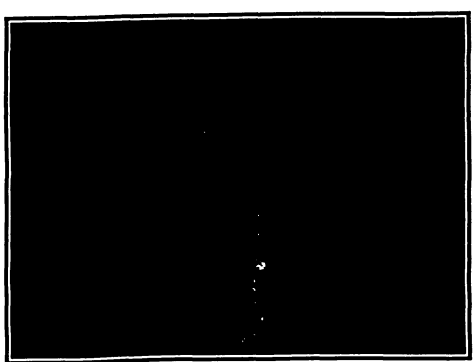

(f) Molybdenum

(g) Background noise

Figure 4.63: X-ray mapping of oxide scale on Alloy 2 (3.5Si-3.0Al) oxidized at 900°C.

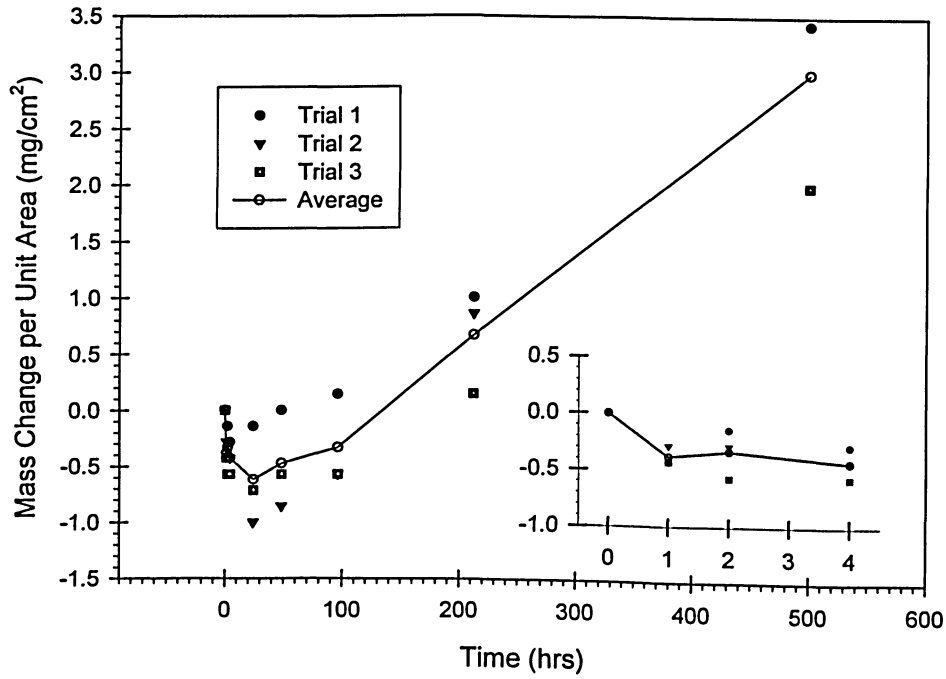

Figure 4.64: Oxidation behaviour of Alloy 2 (3.5Si-3.0Al) cycled for 500 hrs at 900°C.

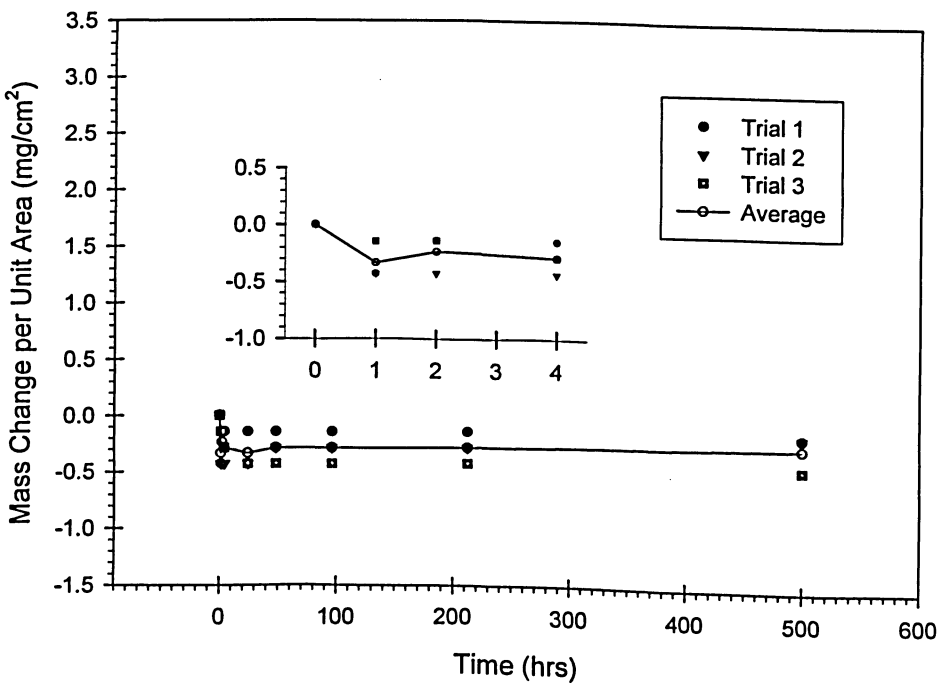

Figure 4.65: Oxidation behaviour of Alloy 3 (4.5Si-2.0Al) cycled for 500 hrs at 900°C.

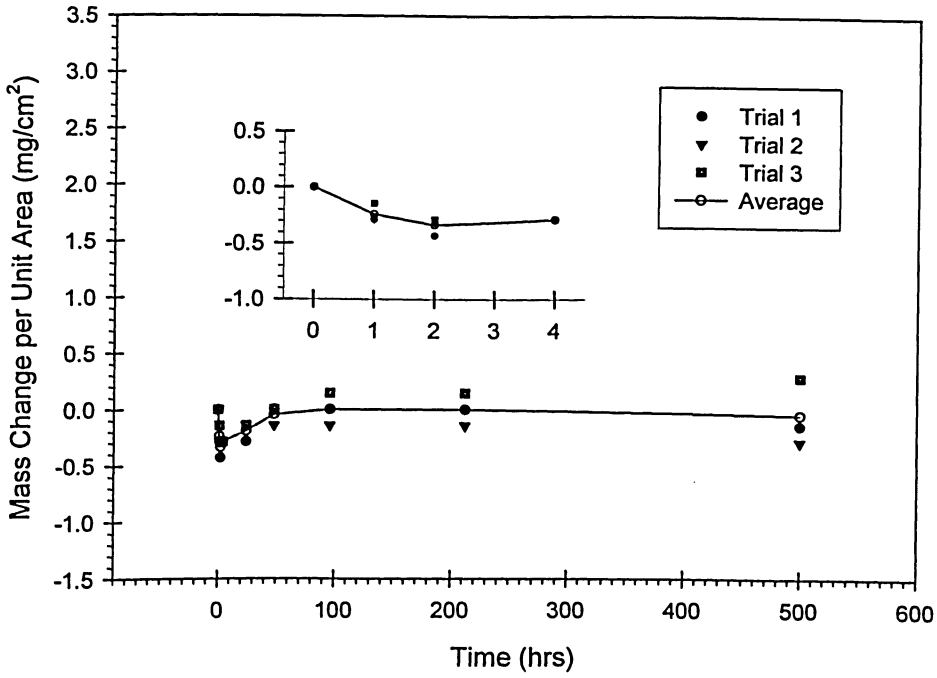

Figure 4.66: Oxidation behaviour of Alloy 4 (4.5Si-3.0Al) cycled for 500 hrs at 900°C.

Figure 4.67 shows the relative oxidation characteristics of Alloys 1, 2, 3 and 4. At 900°C, alloys containing the highest silicon content exhibited superior resistance to oxidation. However, alloys containing the highest aluminum and silicon content contained a lower amount of oxide nodules on the scale surface. This observation suggests that aluminum might play a key role in the size and amount of oxide nodules formed.

Li et al. [16] studied the oxidation kinetics of ductile irons containing silicon and molybdenum. Following 500 hours of testing at 900°C, their results showed a total weight gain of 7mg/cm^2 for an alloy containing 4wt.% silicon and a weight gain of 1.5mg/cm^2 for an alloy containing 4.8wt.% silicon. However, a total weight gain of 3.6mg/cm^2 was exhibited by Alloy 2 and negligible weight gain by Alloys 3 and 4. Thus, the current research suggests that relatively low silicon contents (i.e., 4.5wt.%) supplemented by controlled additions of aluminum can yield an alloy exhibiting excellent resistance to oxidation.

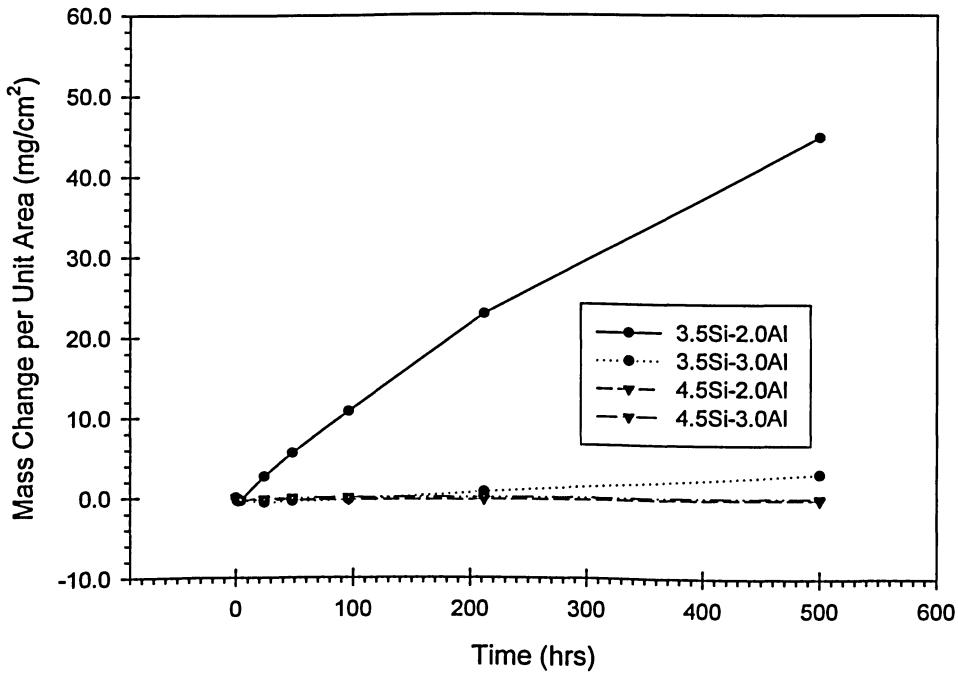

Figure 4.67: Effect of different combinations of Al and Si on the oxidation behaviour of ductile iron specimens cycled for 500 hrs at 900°C.

4.2.1.4 Oxidation at 1000°C for 500 hours

Alloy 1 developed an oxide scale which delaminated from the specimen (Figure 4.68(a)). The suggested causes for the deleterious scale include the different expansion coefficient of the individual oxides and metal, and the ferrite to austenite phase transformation. The total weight gain of this alloy after 500 hours was 48mg/cm^2 (Figure 4.69).

Alloy 2 developed a scale covered with regions containing oxide nodules (Figure 4.68(b)). Severe spalling occurred during cooling. The total weight gain of this alloy after 500 hours was 19mg/cm^2 (Figure 4.70).

Alloy 3 developed a scale containing a finer distribution of oxide nodules (Figure 4.68(c)). Surface spallation was observed to occur only at the site of the precipitated oxide nodules during cooling. After 500 hours, the total weight gain of Alloy 3 was 5mg/cm^2 (Figure 4.71).

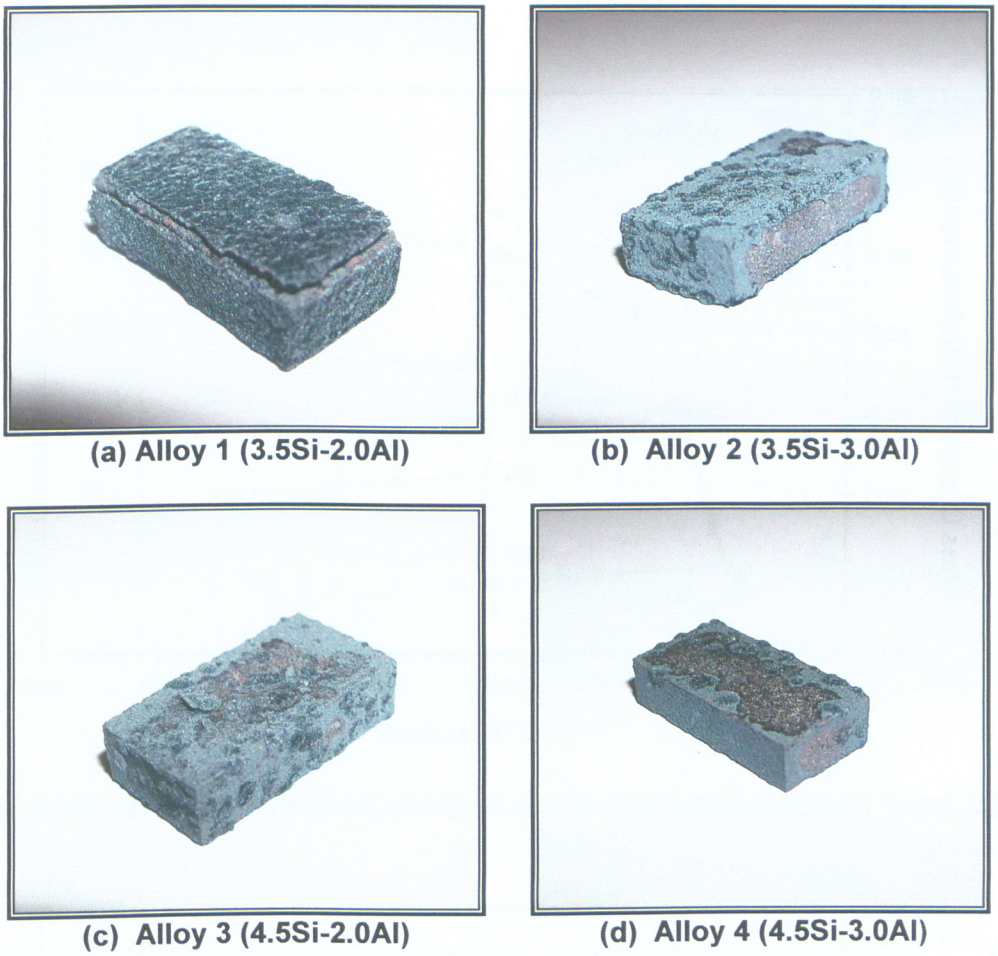

(a) Alloy 1 (3.5Si-2.0Al) (b) Alloy 2 (3.5Si-3.0Al)

(c) Alloy 3 (4.5Si-2.0Al) (d) Alloy 4 (4.5Si-3.0Al)

Figure 4.68: The extent of oxidation due to thermal cycling at 1000°C.

Alloy 4 developed a thin scale. Only the top surface of the sample contained a network of oxide nodules (Figure 4.68(d)). Interestingly, surface spalling occurred only on the surface containing the oxide nodules. The total weight gain of this alloy after 500 hours was 3.5mg/cm^2 (Figure 4.72).

The oxidation resistance of Alloys 1, 2, 3 and 4 is compared in Figure 4.73. Poor resistance to oxidation was exhibited by Alloys 1 and 2 at 1000°C. Superior resistance to oxidation was exhibited by Alloys 3 and 4 at 1000°C. Spalling was confined to only one side of Alloy 4 whereas spalling occurred over the entire surface of Alloy 3. Such spalling was more pronounced in regions containing an interconnected network of oxide nodules. Controlling this feature could enable a ductile iron alloy capable of withstanding over 1000°C.

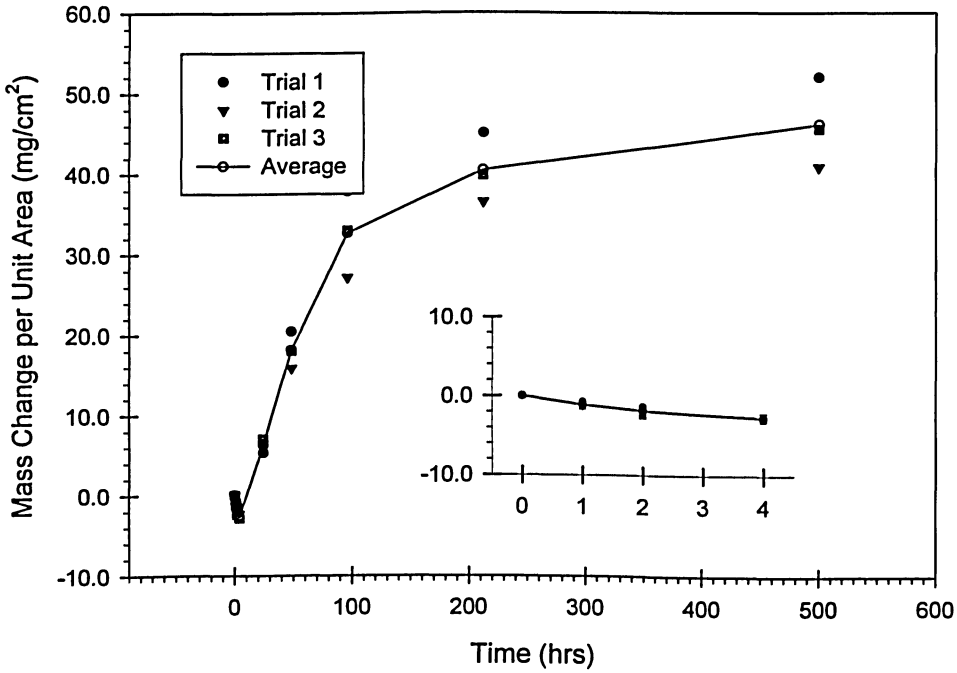

Figure 4.69: Oxidation behaviour of Alloy 1 (3.5Si-2.0Al) cycled for 500 hrs at 1000°C.

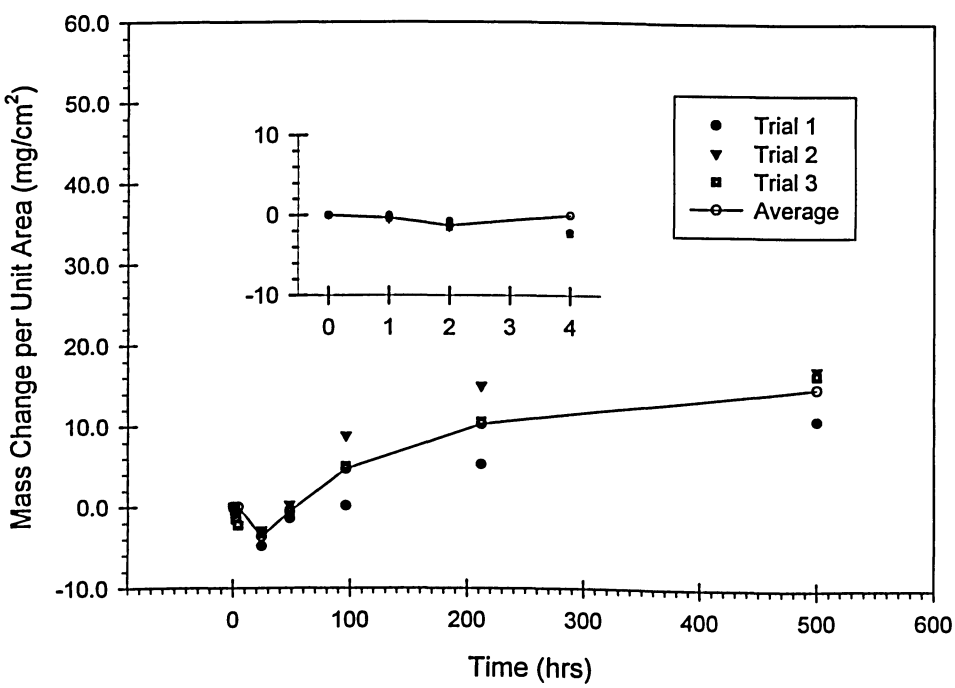

Figure 4.70: Oxidation behaviour of Alloy 2 (3.5Si-3.0Al) cycled for 500 hrs at 1000°C.

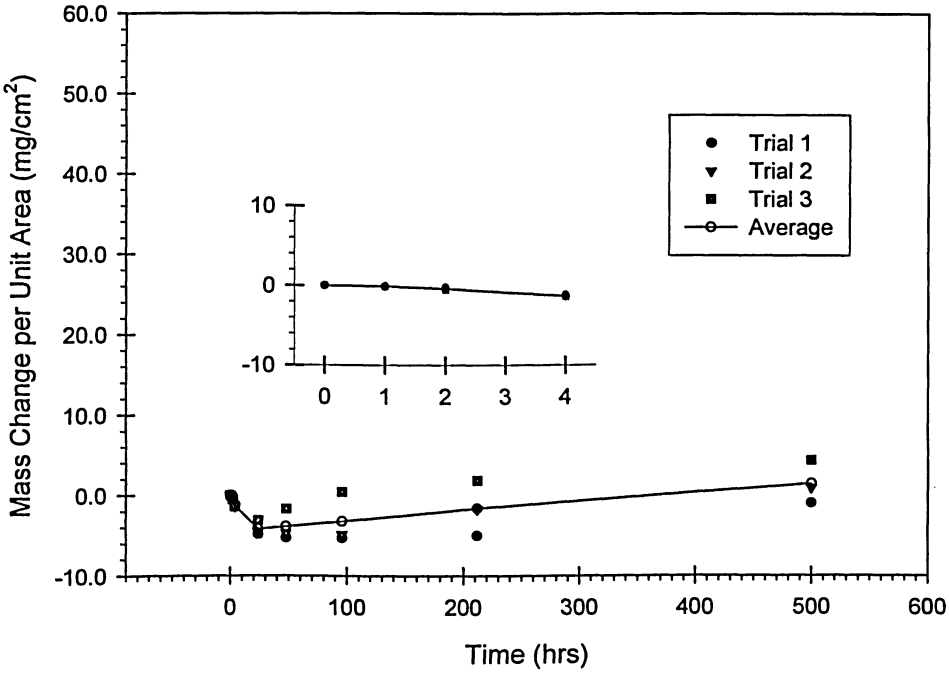

Figure 4.71: Oxidation behaviour of Alloy 3 (4.5Si-2.0Al) cycled for 500 hrs at 1000°C.

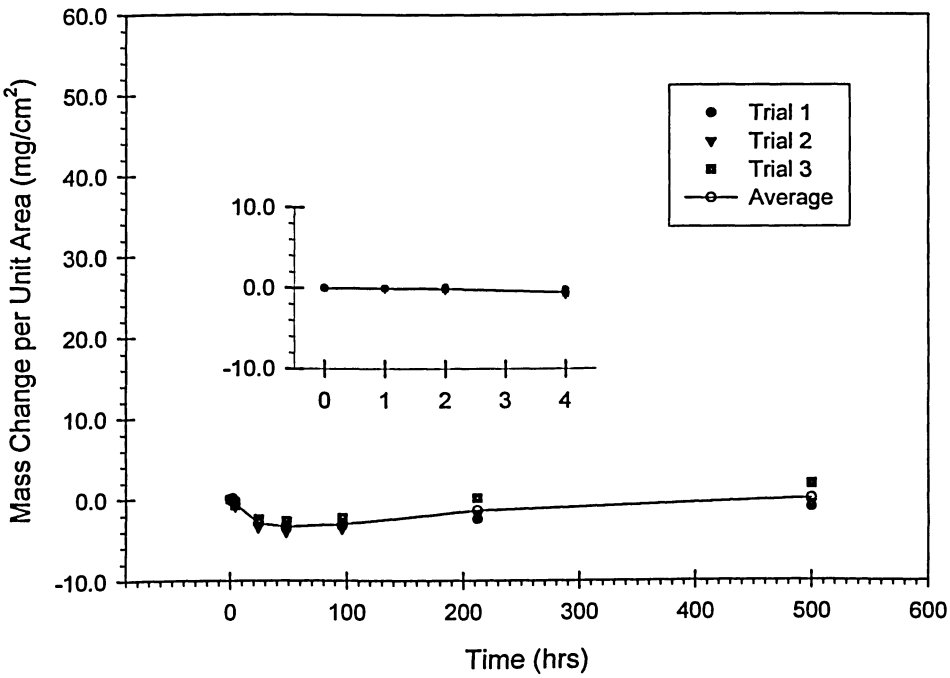

Figure 4.72: Oxidation behaviour of Alloy 4 (4.5Si-3.0Al) cycled for 500 hrs at 1000°C.

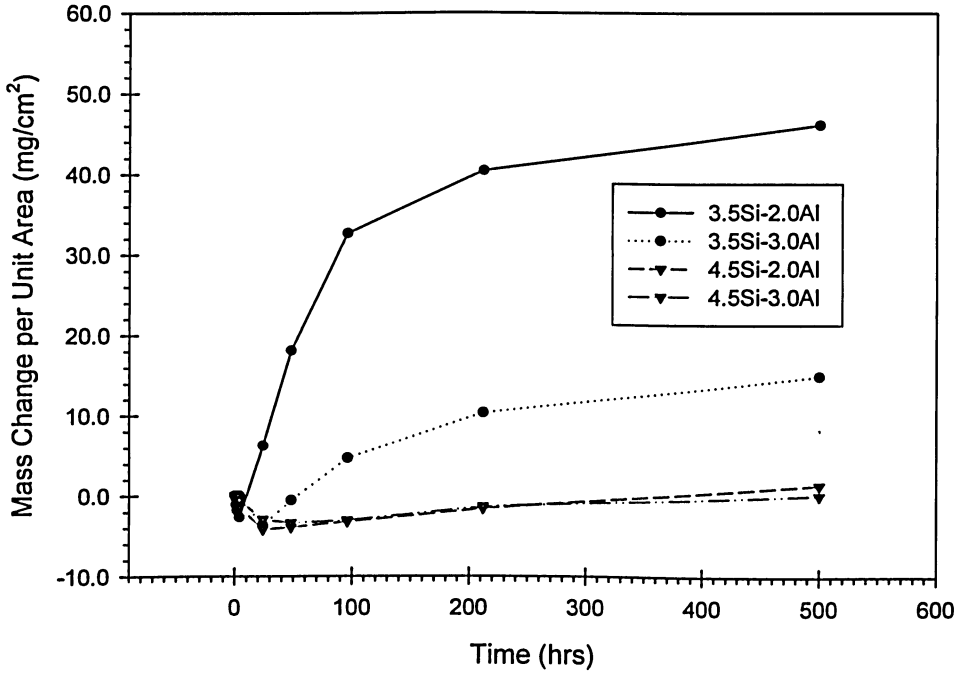

Figure 4.73: Effect of different combinations of Al and Si on the oxidation behaviour of ductile iron specimens cycled for 500 hrs at 1000°C.

4.2.1.5 Oxidation at 1100°C for 500 hours

Alloys 1, 2, 3 and 4 exhibited very poor resistance to oxidation. Excessive temperatures causing phase transformation (α-ferrite to γ-austenite) and high thermal expansion gradients between the individual oxide layers and between the oxides and the base metal completely destroyed the samples.

Alloy 1 developed a very thick scale that delaminated several times over during the course of the experiment (Figure 4.74(a)). This alloy experienced a total weight gain of 387mg/cm^2 (Figure 4.75).

Alloy 2 exhibited a scale that cracked and then spalled (Figure 4.74(b)). A total weight gain of 399mg/cm^2 was experienced by Alloy 2 (Figure 4.75).

Alloy 3 developed a very thick scale (Figure 4.74(c)). The outer shell of the scale flaked off during cooling. This alloy exhibited a total weight gain of 396mg/cm^2 (Figure 4.75).

(a) Alloy 1 (3.5Si-2.0Al) **(b) Alloy 2 (3.5Si-3.0Al)**

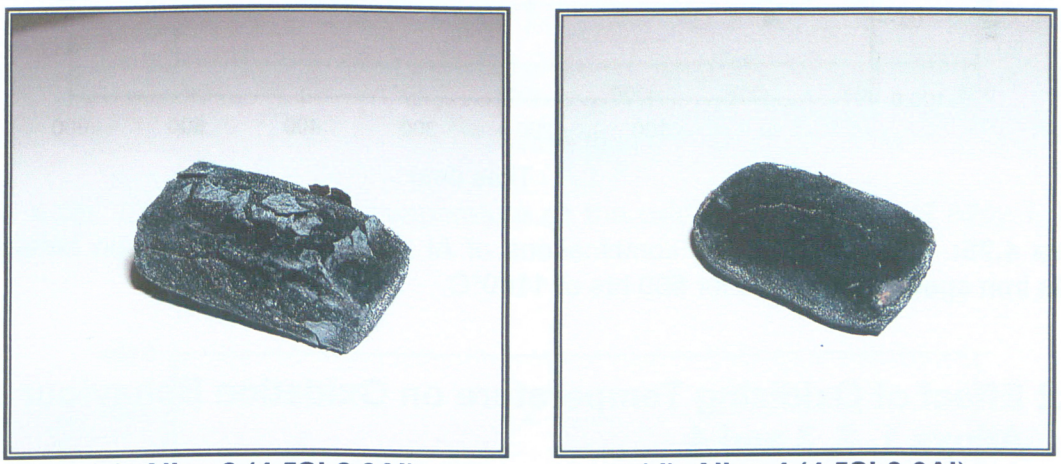

(c) Alloy 3 (4.5Si-2.0Al) **(d) Alloy 4 (4.5Si-3.0Al)**

Figure 4.74: The extent of oxidation due to thermal cycling at 1100°C.

Alloy 4 exhibited a thick, porous scale which was tightly packed (Figure 4.74(d)). Micro-cracks along the surface of the scale were observed but no spalling occurred. Alloy 4 experienced a total weight gain of 401mg/cm^2 (Figure 4.75).

Due to close and unequivocal correlation between the observations in Figure 4.74 and the results in Figure 4.75, these tests were not repeated and further analysis of the samples was not carried out.

Alloys 1, 2, 3 and 4 are clearly not suitable for operating temperatures in excess of 1000°C. The silicon and aluminum contents used were insufficient to provide oxidation resistance above these temperatures.

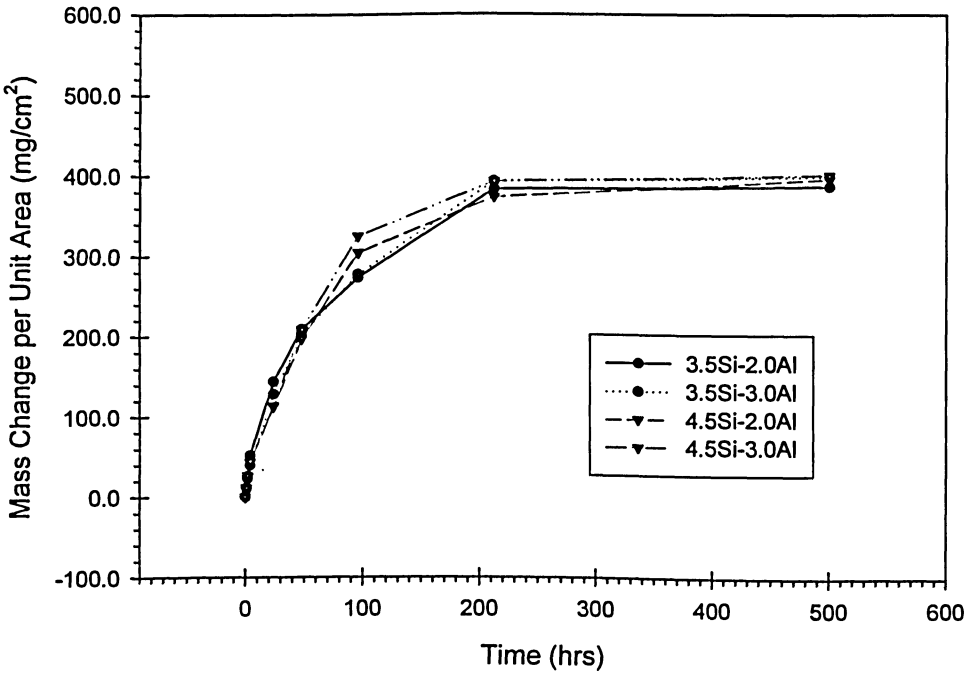

Figure 4.75: Effect of different combinations of Al and Si on the oxidation behaviour of ductile iron specimens cycled for 500 hrs at 1100°C.

4.2.2 Effect of Oxidizing Temperature on Oxidation Behaviour of Alloys 1, 2, 3 and 4

The effect of the oxidizing temperature on Alloys 1, 2, 3 and 4 was studied. Plots were made to observe the relative effects of temperature on the oxidation kinetics of each alloy.

Alloy 1 (3.5Si-2.0Al) exhibited a fair amount of resistance to oxidation at 700 and 800°C (Figure 4.76). Alloy 2 exhibited a higher degree of resistance to oxidation at 700, 800 and 900°C (Figure 4.77). Alloy 3 (4.5Si-2.0Al) maintained an acceptable amount of resistance to oxidation (i.e., no degradation) ranging from 700 to 1000°C (Figure 4.78). Alloy 4 (4.5Si-3.0Al) maintained excellent oxidation characteristics from 700 to 1000°C (Figure 4.79). All the four alloys practically showed no resistance to oxidation at 1100°C.

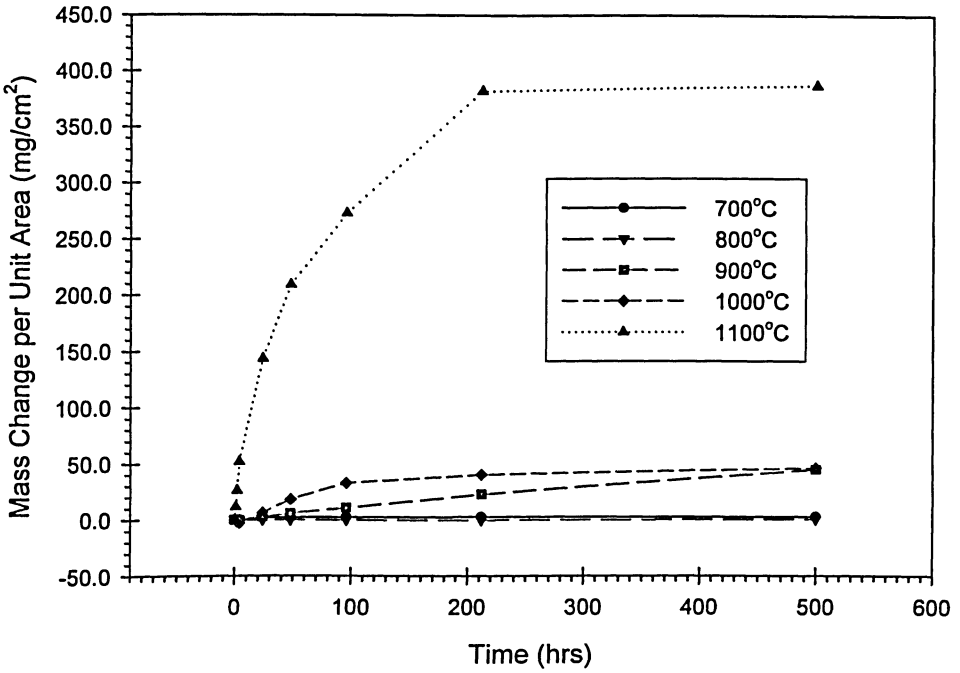

Figure 4.76: Effect of oxidizing temperature on the oxidation behaviour of Alloy 1 (3.5Si-2.0Al).

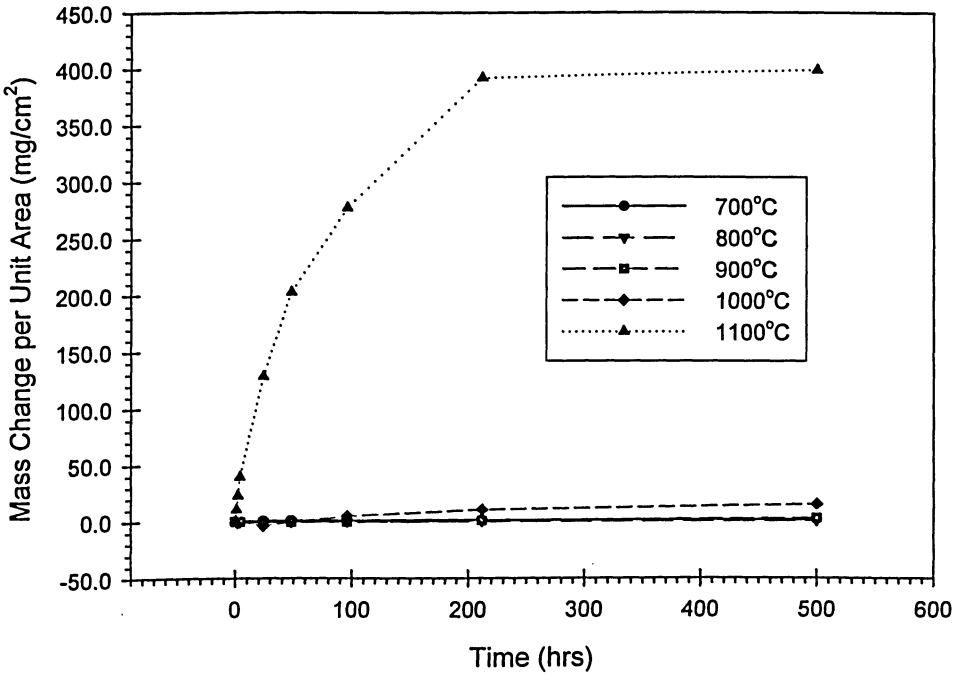

Figure 4.77: Effect of oxidizing temperature on the oxidation behaviour of Alloy 2 (3.5Si-3.0Al).

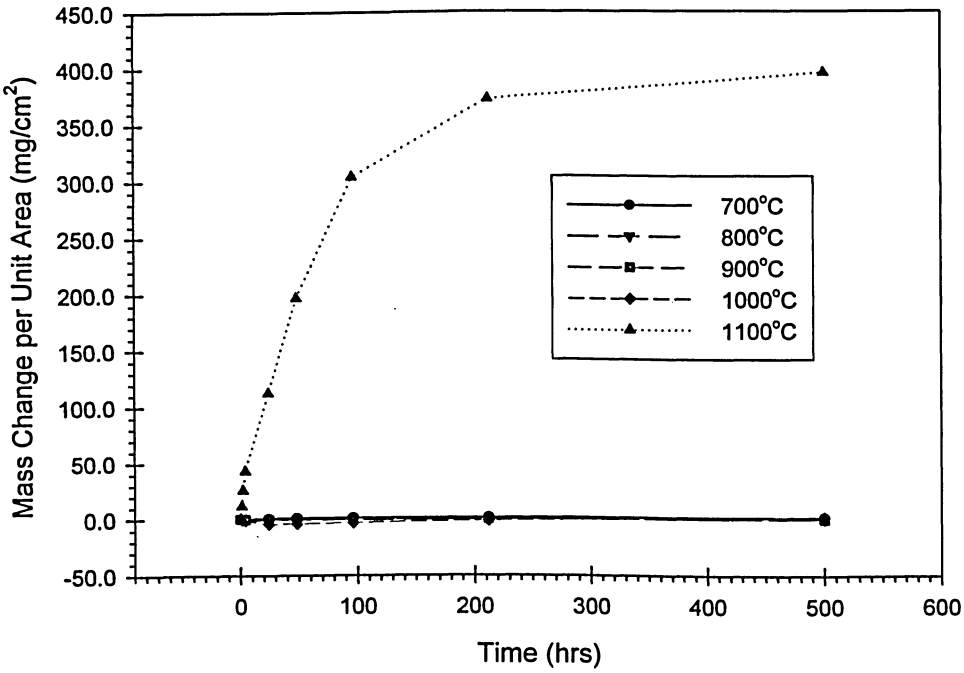

Figure 4.78: Effect of oxidizing temperature on the oxidation behaviour of Alloy 3 (4.5Si-2.0Al).

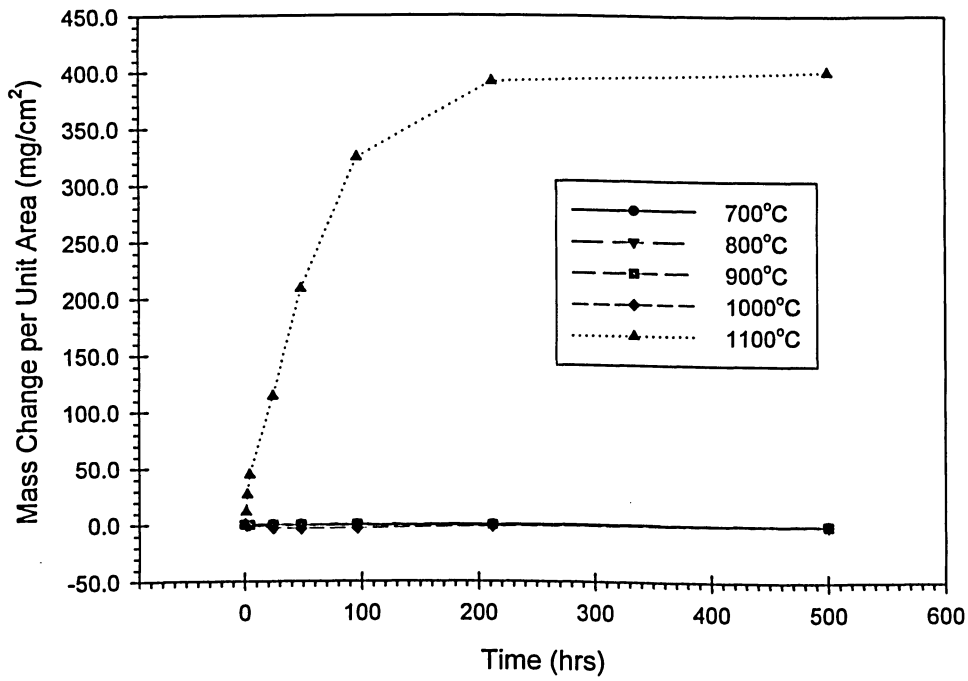

Figure 4.79: Effect of oxidizing temperature on the oxidation behaviour of Alloy 4 (4.5Si-3.0Al).

4.2.3 Effect of Pouring Temperature and Section Thickness on Oxidation Behaviour

The effect of pouring temperature on the oxidation characteristics of Alloys 1, 2, 3 and 4 was studied. Further, the effect of section thickness was also studied, but this test was only carried out on Alloy 4. These tests were carried out at 800°C.

From Figures 4.80 to 4.83, it was observed that the pouring temperature did not affect the oxidation characteristics of the alloys. The only observable effect was an increased resistance to oxidation (lower total weight gains) as the aluminum and silicon content was increased. There was some scatter in the data; however, the data was not sufficient to conclude that pouring temperatures influenced the oxidation kinetics.

Increasing the section thickness did not affect the oxidation characteristics of the alloys. Every section thickness exhibited similar trends in weight loss and gain. This is shown in Figure 4.84. Further, some data scatter was observed, but the data was not sufficient to conclude that section thickness affected the resistance to oxidation in the range of thickness studied.

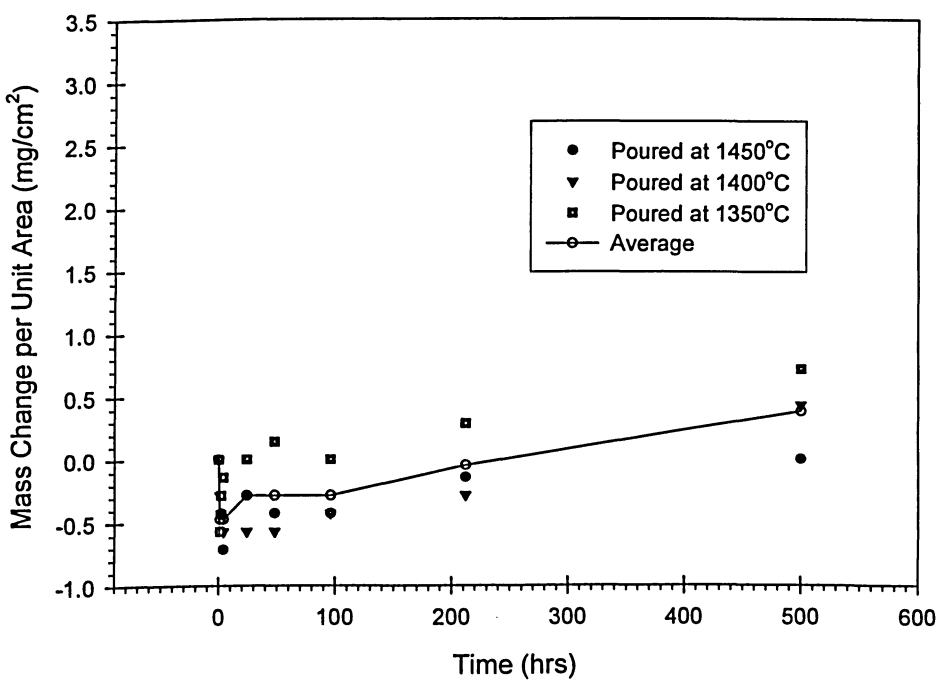

Figure 4.80: Effect of pouring temperature on the oxidation behaviour of Alloy 1 (3.5Si-2.0Al) oxidized for 500 hrs at 800°C.

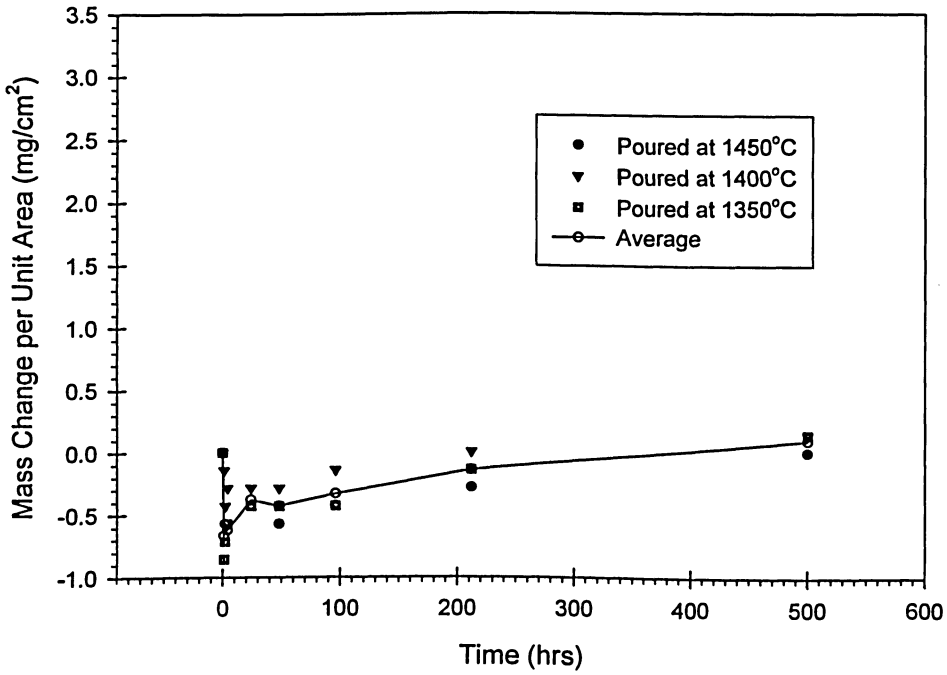

Figure 4.81: Effect of pouring temperature on the oxidation behaviour of Alloy 2 (3.5Si-3.0Al) oxidized for 500 hrs at 800°C.

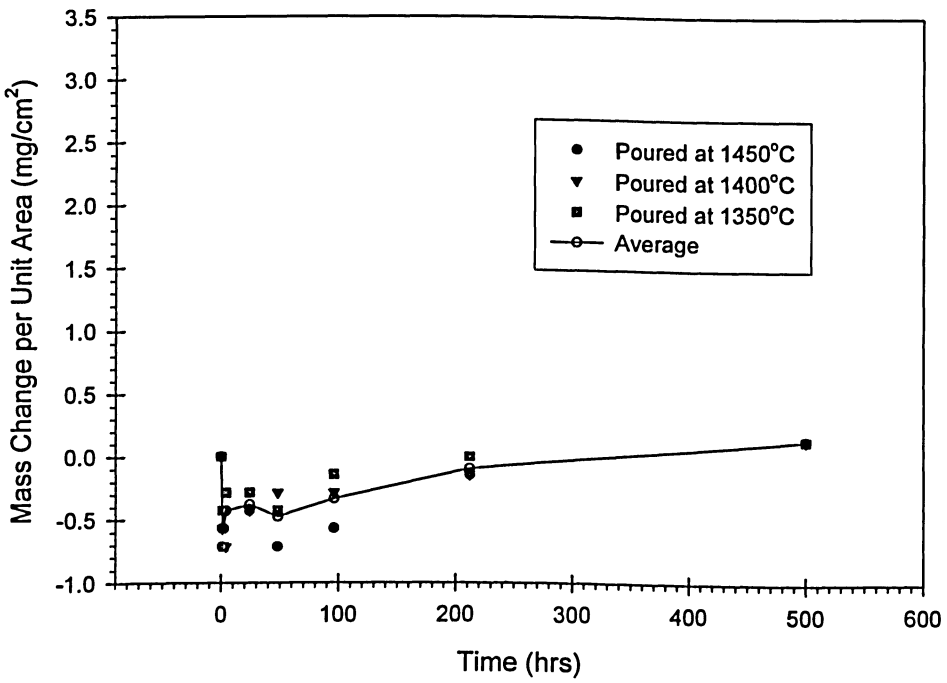

Figure 4.82: Effect of pouring temperature on the oxidation behaviour of Alloy 3 (4.5Si-2.0Al) oxidized for 500 hrs at 800°C.

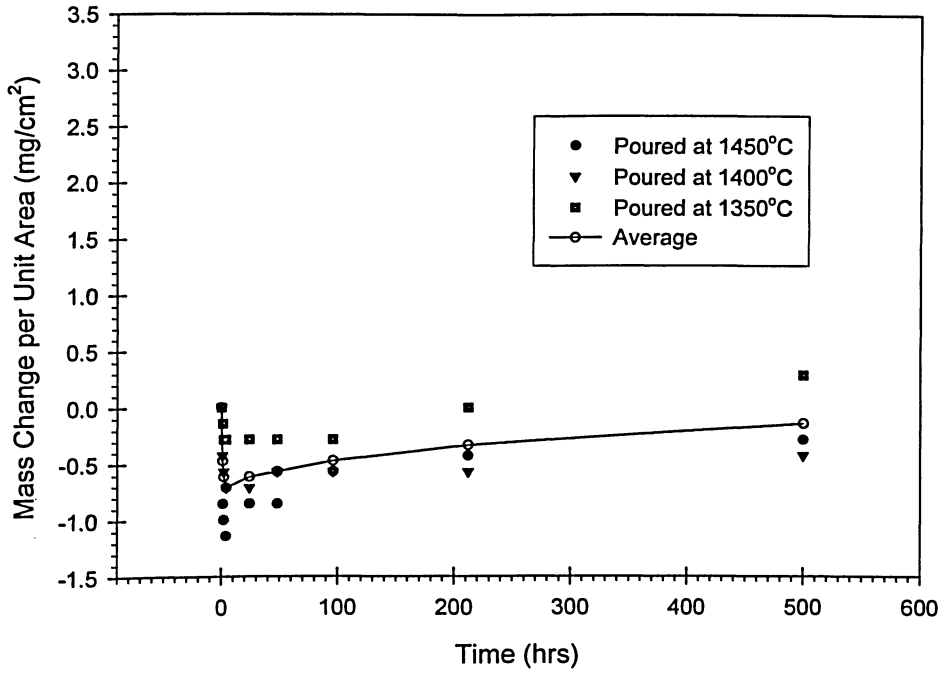

Figure 4.83: Effect of pouring temperature on the oxidation behaviour of Alloy 4 (4.5Si-3.0Al) oxidized for 500 hrs at 800°C.

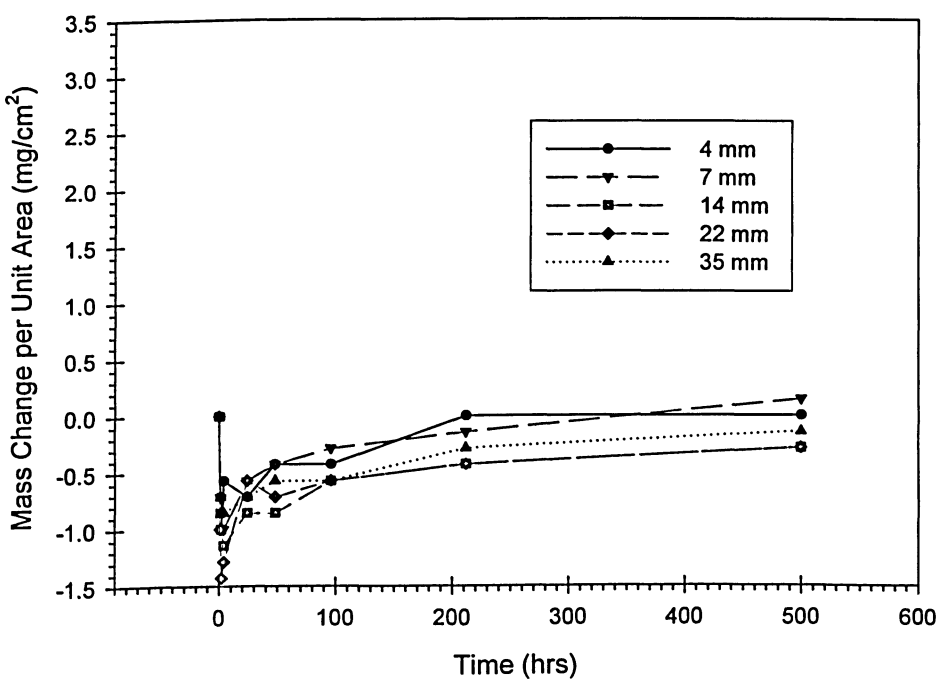

Figure 4.84: Effect of section size on the oxidation behaviour of Alloy 4 (4.5Si-3.0Al) oxidized for 500 hrs at 800°C.

4.2.4 Parabolic Oxidation Rate Constant

Using the Pilling and Bedworth [113] relationship (Equation 2.42), the parabolic oxidation rate constant $2k_{PB}$ was determined to compare the rate of oxidation with increasing temperatures and increasing silicon and aluminum contents. Linear regression analysis of the scattered data was plotted to illustrate these trends.

The rate of oxidation decreased appreciably as the silicon and aluminum content increased. This is readily observed in Figure 4.85.

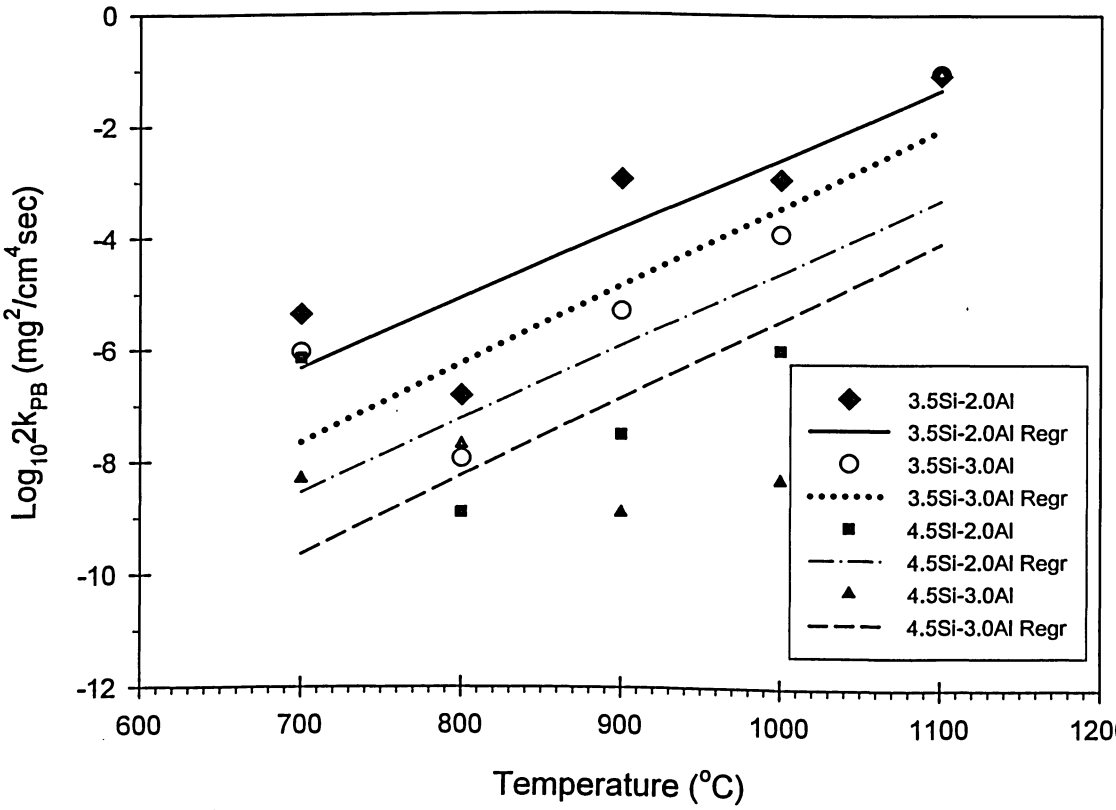

Figure 4.85: Oxidation rate of Alloys 1, 2, 3 and 4 after 500 hours.

4.3 DILATOMETRY ANALYSIS

The coefficient of thermal expansion and the α-ferrite to γ-austenite phase transformation temperature for Alloys 1, 2, 3 and 4 was determined using a dilatometer. Samples were slowly heated and cooled at a constant rate of 2°C/min. The subsequent

heating and cooling curves for each alloy are illustrated in Figures 4.87 to 4.89. Differentiation of the heating curves yielded the thermal expansion coefficient and the transformation temperature range for each alloy (Figures 4.90 to 4.93).

There were no significant differences in the coefficients of thermal expansion for Alloys 1, 2, 3 and 4. However, the coefficient of thermal expansion for each alloy progressively increased with an increase in temperature.

The critical α-ferrite to γ-austenite phase transformation temperature was determined from the inflection point in Figures 4.90 to 4.93. With increasing silicon and aluminum contents, the critical transformation temperature increased by approximately 115°C. This can be seen by the data for Alloy 1 (3.5Si-2.0Al) and that for Alloy 4 (4.5Si-3.0Al). Details of the effect of compositional changes on the phase transformation temperature are shown in Table 4.2.

The transformation studies suggest that Alloys 1, 2, 3 and 4 did not form austenite up to an operating temperature of about 860°C. Alloys 2, 3 and 4 maintained an austenite free structure up to about 950°C. Alloys 3 and 4 did not undergo a phase transformation up to about 980°C. The addition of 1wt.% aluminum can increase the critical phase transformation temperature by about 80°C. The addition of 1wt.% silicon can enable an increase of the operating temperature by 30°C to approximately 110°C. Silicon and aluminum, together had a significant role in increasing the transformation temperature.

Table 4.2: Transformation ranges during heating determined by differential thermal analysis for Alloys 1, 2, 3 and 4.

Alloy	α-ferrite → γ-austenite Transformation Temperature [Range] (°C)
Alloy 1 (3.5Si-2.0Al)	870 [860-880]
Alloy 2 (3.5Si-3.0Al)	950 [940-960]
Alloy 3 (4.5Si-2.0Al)	980 [975-985]
Alloy 4 (4.5Si-3.0Al)	985 [980-990]

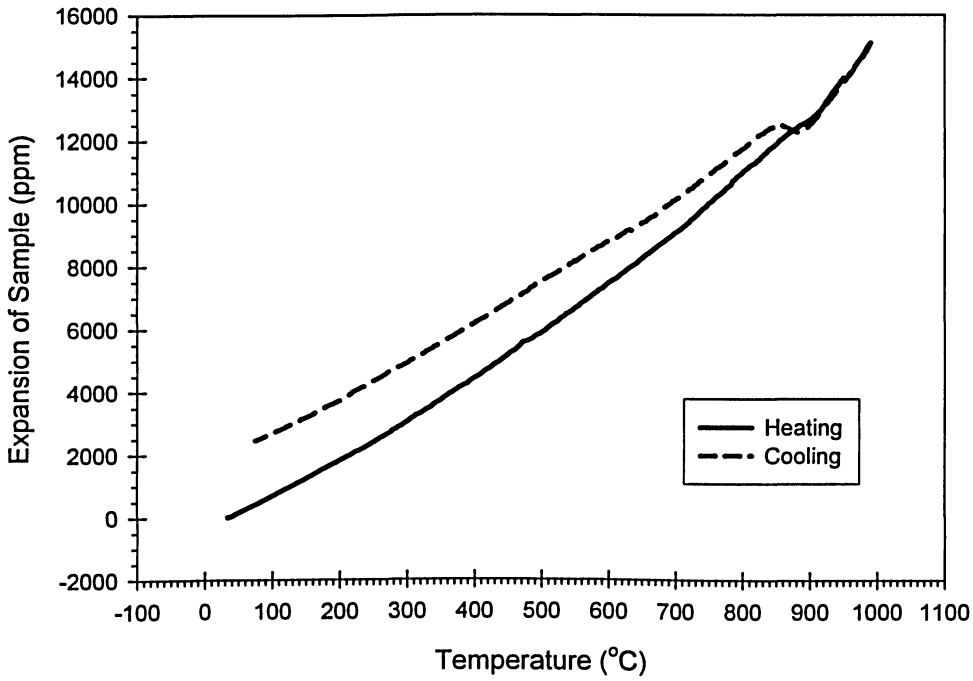

Figure 4.86: Dilatometry test of Alloy 1 (3.5Si-2.0Al).

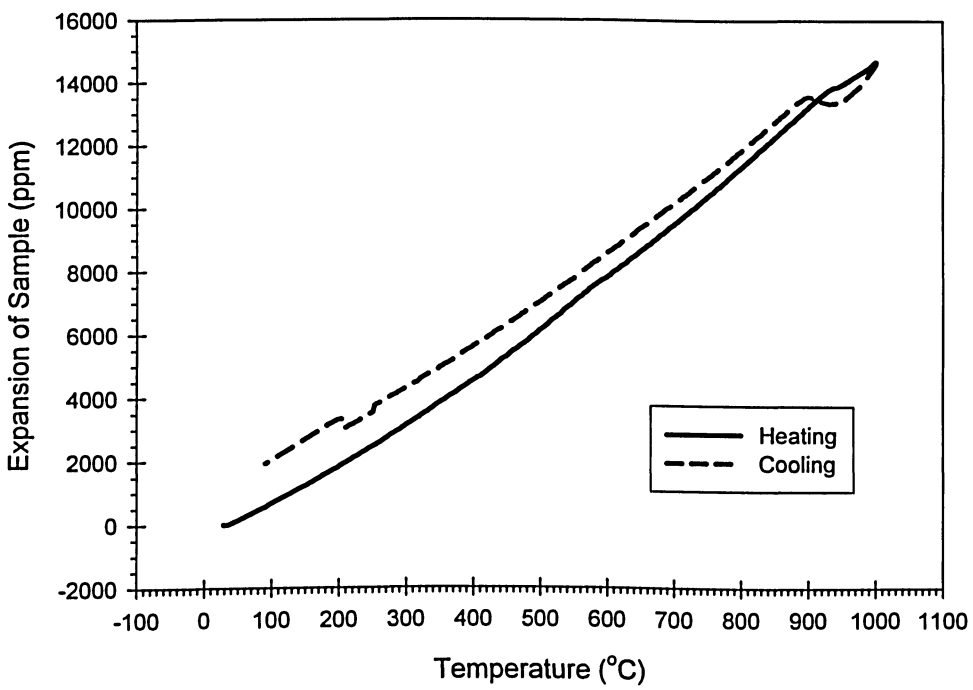

Figure 4.87: Dilatometry test of Alloy 2 (3.5Si-3.0Al).

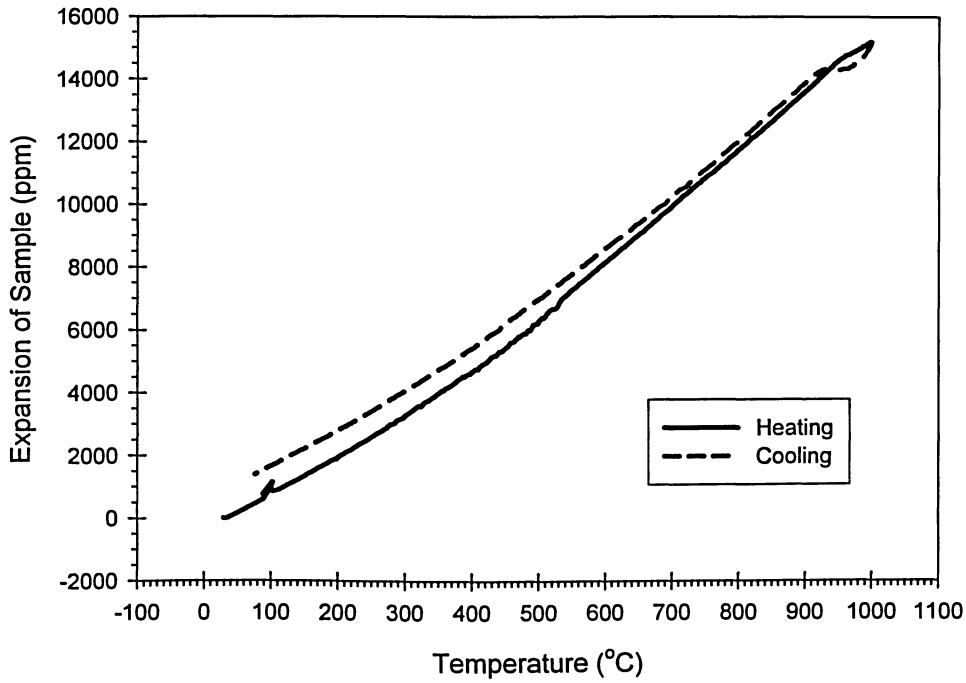

Figure 4.88: Dilatometry test of Alloy 3 (4.5Si-2.0Al).

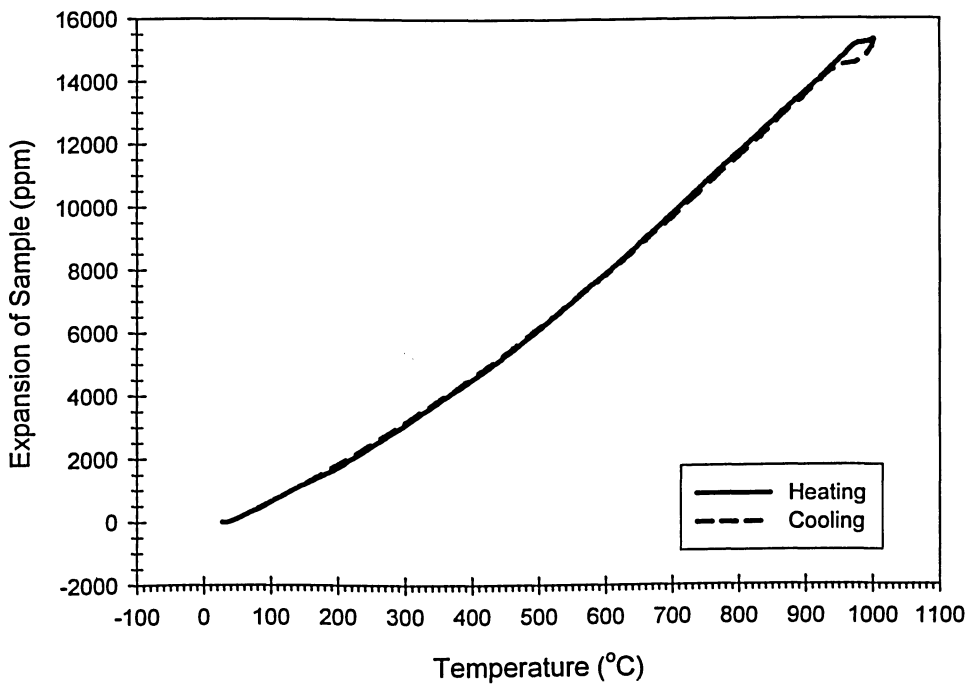

Figure 4.89: Dilatometry test of Alloy 4 (4.5Si-3.0Al).

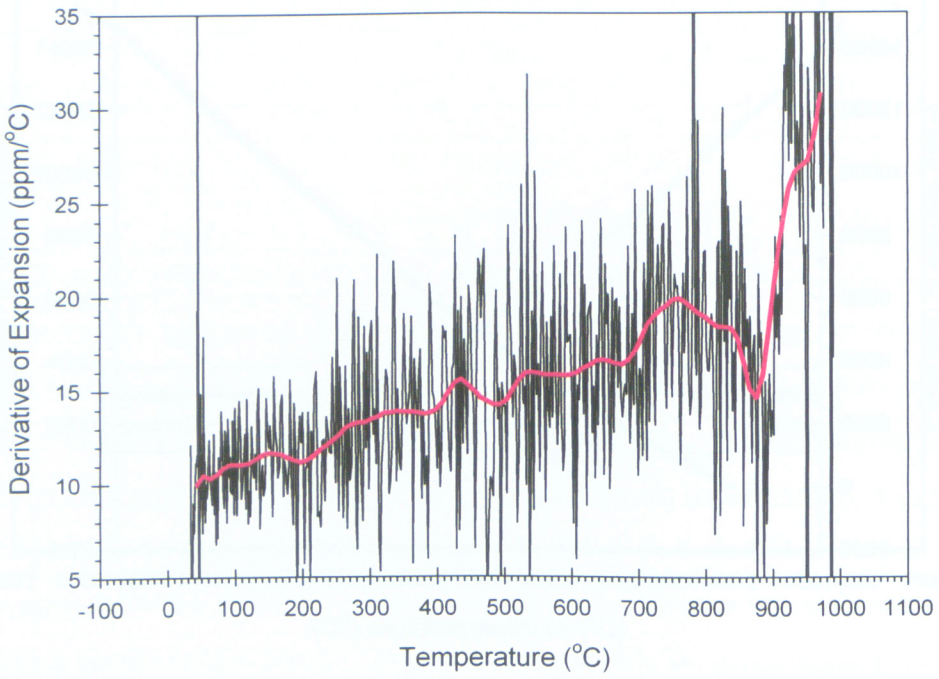

Figure 4.90: First derivative analysis of heating curve in Figure 4.86 for Alloy 1 (3.5Si-2.0Al).

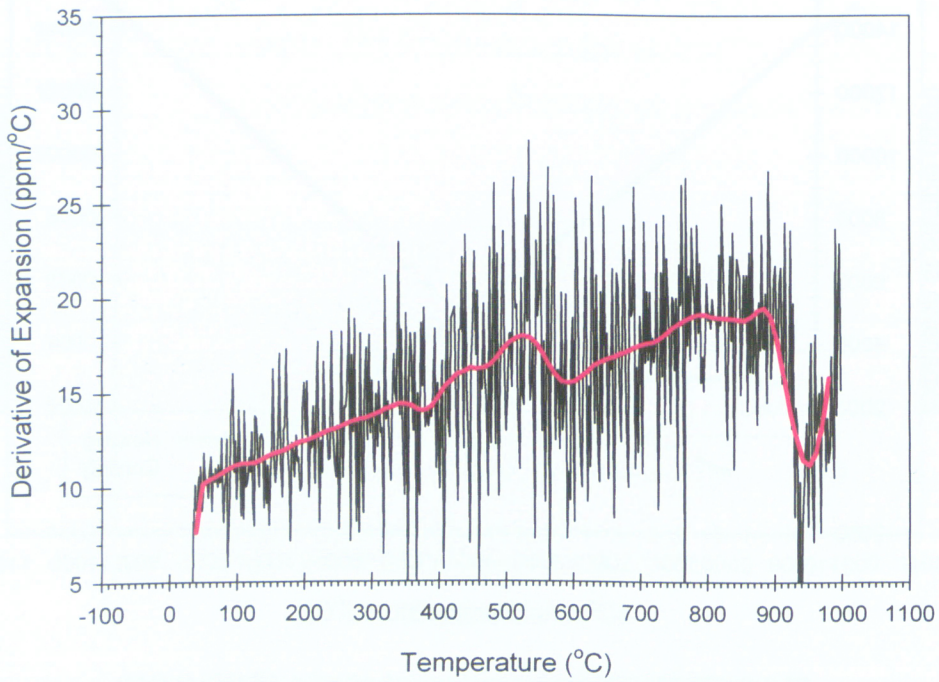

Figure 4.91: First derivative analysis of heating curve in Figure 4.87 for Alloy 2 (3.5Si-3.0Al).

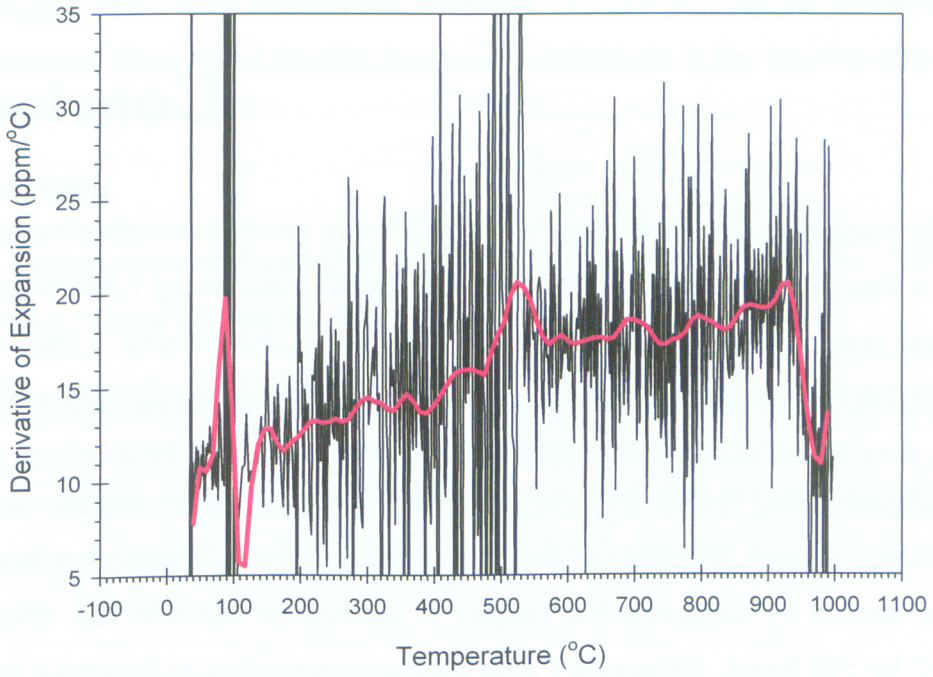

Figure 4.92: First derivative analysis of heating curve in Figure 4.88 for Alloy 3 (4.5Si-2.0Al).

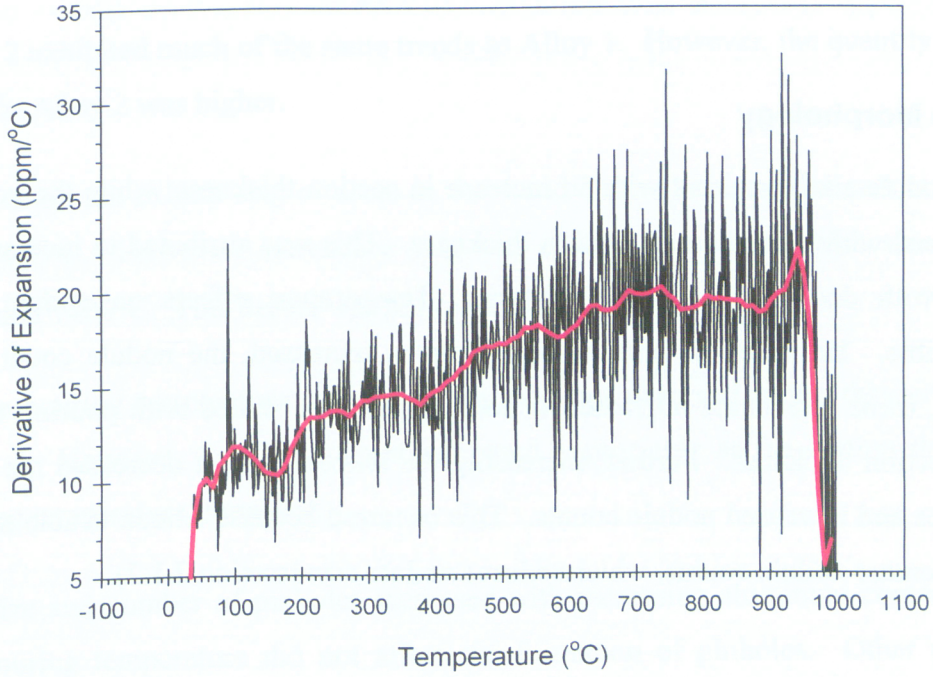

Figure 4.93: First derivative analysis of heating curve in Figure 4.89 for Alloy 4 (4.5Si-3.0Al).

Chapter 5

Conclusions

This thesis focused on developing ductile irons for high temperature applications. Four ductile iron alloys poured at 1350, 1400 and 1450°C containing 1.5wt.% molybdenum and different concentrations of aluminum and silicon (i.e., 3.5Si-2.0Al, 3.5Si-3.0Al, 4.5Si-2.0Al, 4.5Si-3.0Al) were characterized in the as-cast and oxidized states. The effects of alloy chemistry, pouring temperature and section thickness on graphite morphology and defects were investigated using optical and scanning electron microscopes. Further, the effects of alloy chemistry, pouring temperature and section thickness on the oxidation kinetics of the alloys were studied by subjecting the samples to thermal oxidation at 700, 800, 900, 1000 and 1100°C for 500 hours. Dilatometry tests were also carried out to determine the effects of different silicon and aluminum contents on the critical α-ferrite to γ-austenite phase transformation temperature and the coefficient of thermal expansion. On the basis of this research work, the following conclusions were developed.

Graphite Morphology

1. The nodule size increased with an increase in section thickness, while the nodule count increased with a decrease in section thickness. This was attributed to increased cooling rates with decreased section thickness. Temperature effects on nodule size were negligible. However, as pouring temperatures increased, the nodule count decreased. Again, these effects are attributed to cooling rates associated with pouring temperature and section thickness. Further, increasing the silicon content decreased the size of the nodules and increased nodule counts. This occurred because silicon is able to graphitize and increase nodule counts, which reduces nodule size (section 2.1.2).

2. Maximum percentage of spherical graphite was attained when the Si/Al ratio was close to 1.0. Higher Si/Al ratios reduced the sphericity. As the pouring temperatures increased, the percentage of spherical graphite increased, particularly in the 4mm specimens.

Defect Analysis

1. Sound castings were produced from Alloy 3 poured at 1400 and 1450°C. Alloys 1, 2 and 4 exhibited varying degrees of misruns.

2. Graphite floatation was not observed in any alloy in the 4, 7 and 14mm thick specimens.

3. As the aluminum content increased, the amounts of both slag and dross increased. This is particularly evidenced by SEM analysis of Alloy 2 (relative to Alloy 1) and Alloy 4 (relative to Alloy 3).

4. Alloy 1 contained slag and dross in the 4, 7 and 14mm thick specimens. As the section thickness and pouring temperature increased, the slag and dross moved from the centre of the specimens to regions below the top surface.

5. Alloy 2 exhibited much of the same trends as Alloy 1. However, the quantity of slag and dross in Alloy 2 was higher.

6. Alloy 3 did not exhibit slag or dross in the 4 and 7mm thick samples cast at 1350, 1400 and 1450°C. However, subsurface slag was observed in 14mm thick samples cast at 1350 and 1400°C. This defect was not observed at 1450°C.

7. As the pouring temperature increased, slag was not observed in the thinner sections of Alloy 4. However, the slag content increased appreciably as the section thickness and pouring temperature increased.

8. The size and number of pinholes increased with increasing aluminum content. Further, the pouring temperature did not affect the formation of pinholes. Other pinhole like defects included the presence of porosity below slag scales.

9. The section thickness and pouring temperature affected the degree of shrinkage. Shrinkage defects were more readily observed in the 4mm than in the 7 and 14mm thick specimens. The shrinkage in the 4mm thick specimens was attributed to rapid cooling rates and high viscosity of the liquid metal, which resulted from high nodule counts and dendrites. There was no clear observed effect of alloy chemistry on the formation of shrinkage cavities.

Oxidation Kinetics and Dilatometry

1. As the silicon and aluminum contents increased from 3.5 to 4.5wt.% and from 2.0 to 3.0wt.%, respectively, the resistance to oxidation increased appreciably, particularly at higher temperatures. This is attributed to greater mobility of atoms at higher temperatures resulting in greater resistance to oxidation at 800°C (relative to 700°C). This in turn possibly allowed the protective oxide layer to develop more rapidly. However, this effect diminished with higher temperatures and scaling tendencies due to specimen dilation (caused by decomposition and transformation of phases) and the relative coefficients of expansion of the base metal and oxides. These factors also allowed some specimens to continuously oxidize throughout the course of the test, thus not allowing the scale to reach steady values. This effect was more pronounced in Alloys 1 and 2.

2. The extent of initial weight loss in the oxidation specimens was attributed to subsurface defects. Further, it was suggested that there was a correlation between oxide nodule counts and the concentration of subsurface defects. However, the extent of oxide nodule formation was dependent on the ability of the alloying elements to produce an adherent non-permeable scale.

3. X-ray mapping of the oxide scales revealed an external layer composed of oxides of iron (i.e., FeO, Fe_3O_4 and Fe_2O_3) and an internal layer composed of oxides of aluminum and silicon. These scales became progressively thicker as the oxidizing temperature increased. Further, the presence of a fine distribution of stable molybdenum and aluminum carbide precipitates was identified.

4. Acceptable oxidation resistance was exhibited by Alloys 3 (4.5Si-2.0Al) and 4 (4.5Si-3.0Al) at 1000°C; the α-ferrite to γ-austenite phase transformation temperatures were 980 and 985°C. Alloy 2 (3.5Si-3.0Al) exhibited oxidation resistance up to 900°C and a phase transformation temperature of 950°C. Alloy 1 (3.5Si-2.0Al) exhibited oxidation resistance up to 800°C and a phase transformation temperature of 870°C. Further, as the silicon and aluminum contents increased, the oxidation rate constant decreased (i.e., increased resistance to oxidation). The pouring temperature and section thickness did not affect the oxidation kinetics of the alloys.

Alloy Recommendation

1. The results of this research suggest that the most promising alloy for high temperature applications is Alloy 3 (4.5Si-2.0Al) poured at 1400°C. This alloy exhibited superior resistance to oxidation up to 1000°C and a high critical phase transformation temperature of 980°C. It provided a balance of good nodule morphology, limited number of defects and thin section (4mm) castability.

Chapter 6

Suggestions for Future Study

On the basis of current investigative work, the following suggestions have been made for future study:

1. Creep-rupture testing of alloys used in current study.

2. Diffraction study of the oxide scale formed in the current alloys using transmission electron microscopy, thus enabling proper characterization and identification.

3. Diffraction studies and kinetic characterization of the molybdenum and aluminum carbide precipitates and their influence on ambient and high temperature properties.

4. Study of the growth kinetics of oxide nodules with a view to determining correlation between oxide nodule count and subsurface flaws.

5. Study of the interaction of silicon and aluminum and its effect on enhancing graphite sphericity.

References

1. J.R. Davis, ASM Specialty Handbook: Cast Irons, ASM Int., Ohio, 1996.

2. H.T. Angus, Cast Iron: Physical and Engineering Properties 2nd ed., Butterworth & Co Ltd., London, 1976.

3. A.M. Sage and J.V. Dawson, "A High-Carbon, V-Mo, High Strength Gray Cast Iron for Castings Subjected to Thermal Fatigue", AFS Transactions, Vol. 100, 1992, p. 253.

4. L.A. Neumeier and B.A. Betts, "Ductile Iron Containing Tin, Copper and Other Contaminants", AFS Transactions, Vol. 84, 1976, p. 265.

5. W. Scholz and M. Semchyshen, "Effect of Molybdenum on the Hardenability of Ductile Cast Iron", AFS Transactions, Vol. 76, 1968, p. 1.

6. M. Takanezawa, Y. Tomota and Y. Kobayashi, "A New Heat Resistant Cast Iron for Thin Wall Exhaust Manifold", ISIJ Int., Vol. 38, 1998, p. 106.

7. R.G. Baligidad and A. Radhakrishna, "Effect of B, Zr, Ce and Nb addition on structure and mechanical properties of high carbon Fe-10.5 wt% Al alloy", Journal of Materials Science Letters, Kluwer Academic Publishers, 2002, p. 1231.

8. A.A. Nofal, N.S. Felix and A.S. Rezk, "Cast Iron Alloyed with 9% Aluminum", 50th International Foundry Conference, Cairo, 1983, p. 1.

9. J.A. Yaker, L.E. Byrnes, W.C. Leslie, A. Arbor and E.U. Petitbon "Microstructures and Strength of Aluminum-Containing Gray and Nodular Irons in the Temperature Range 1200-1800F (649-982C)", AFS Transactions, Vol. 84, 1976, p. 305.

10. E.P. Babich, N.S. Sevast'yanov and V.P. Saburov, "Mechanical Properties of Heat Resistant Modified Iron Containing 20-24 per cent Aluminum", Russian Castings Production, Vol. 7, 1964, p. 293.

11. R.P. Walson, "Aluminum Alloyed Cast Iron Properties Used in Design", AFS Transactions, Vol. 85, 1977, p. 51.

12. E.U. Petitbon and J.F. Wallace, "Aluminum Alloyed Gray Iron – Properties at Room and Elevated Temperature", AFS Cast Metals Research Journal, Vol. 9, 1973, p. 127.

13. C. Pelhan, "Comparison between the Oxidation of Unalloyed and Low-Alloyed Cast Iron with Lamellar and Spheroidal Graphite", The Metallurgy of Cast Iron, Proceedings of the 2nd International Symposium on the Metallurgy of Cast Iron, Switzerland, 1974, p. 841.

14. D.L. Sponseller, W.G. Scholz and D.F. Rundle, "Development of Low-Alloy Ductile Irons for Service at 1200-1500°F (650-815°C)", AFS Transactions, Vol. 76, 1968, p. 353.

15. B. Black, G. Burger, R. Logan, R. Perrin and R. Gundlach, "Microstructure and Dimensional Stability in Si-Mo Ductile Irons for Elevated Temperature Applications", SAE Int., 2002.

16. D. Li, R. Perrin, G. Burger, D. McFarlan, B. Black, R. Logan and R. Williams, "Solidification Behavior, Microstructure, Mechanical Properties, Hot Oxidation and Thermal Fatigue Resistance of High-Silicon SiMo Nodular Cast Irons", SAE Int., 2004.

17. A. Reynauld and J.L. Roberge, "Application of High Temperature Spheroidal Graphite Cast Irons in Exhaust Manifolds", CTIF, Fonderie-Fondeur d'aujourd'hui, Vol. 182, 1999, p. 37.

18. D. Venugopalan and A. Alagarsamy, "Influence of Microstructure and Chemical Composition on the Mechanical Properties of Ductile Iron", Materials Research Society, 1990, p. 321.

19. P.R. Bridenbaugh, "Casting will Play a Major Role in the Future of Transportation," Modern Casting, Vol. 86, July 1996, p. 31.

20. K. Hornung, "Thin Section Ductile Iron Castings," Technical Forum 61st World Foundry Congress, Beijing, 1995, p. 75.

21. R.W. Heine, "Major Aspects of Processing Cast Irons", AFS Transactions, Vol. 102, 1994, p. 985.

22. R.B. Gundlach, C.R. Loper Jr. and B. Morgensteren, "Composition of Ductile Irons", Ductile Iron Handbook, AFS, Des Plaines, Illinois, 1999, p. 66.

23. G.S. Cole, "Solidification of Ductile Iron", AFS Transactions, Vol. 80, 1972, p. 335.

24. C.R. Loper, "Processing and Control of Ductile Cast Iron", AFS Transactions, Vol. 77, 1969, p. 1.

25. C.F. Walton and T.J. Opar, Iron Castings Handbook, Iron Castings Society, Inc., Tennessee, 1981.

26. R.L. Naro and J.F. Wallace, "Trace Elements in Cast Irons", AFS Transactions, Vol. 77, 1969, p. 311.

27. I.C.H. Hughes, "The Role of Gases in the Structure of Cast Iron", AFS Transactions, Vol. 77, 1969, p. 121.

28. F. Tholence and M. Norell, "High Temperature Corrosion of Cast Irons and Cast Steels in Dry Air", 5th Int. Symposium on High Temperature Corrosion and Protection of Materials, Vols. 369-372, 2001, p. 197.

29. R.C. Voigt and C.R. Loper Jr., "Matrix Structure Development in Ductile Cast Irons," AFS Transactions, Vol. 97, 1989, p. 595.

30. R.W. Heine, "Carbon, Silicon, Carbon Equivalent, Solidification, and Thermal Analysis Relationships in Gray and Ductile Cast Irons", AFS Transactions, Vol. 81, 1973, p. 462.

31. J.R. Marks, "Metallography of Ductile Iron", AFS Transactions, Vol. 107, 1999, p. 819.

32. H.E. Henderson, "Compliance with Specifications for Ductile Iron Castings Assures Quality", Metal Progress, Vol. 99, 1966, p. 82.

33. J.D. Mullins, "Engineering Properties, Specifications and Physical Constants of Specific Ductile Irons", Ductile Iron Handbook, AFS, Des Plaines, Illinois, 1999, p. 20.

34. D.L. Torkington, "Ductile Irons for Elevated Temperature Service", Metal Progress, Vol. 119, no. 6, 1981, p. 38.

35. Metals Handbook 8th ed., Metallography, Structures and Phase Diagrams, Vol. 8, ASM, 1973.

36. R.J. Maitland and I.C.H. Hughes, "Influence of Silicon Content on Growth and Scaling Resistance of Cast Iron with Nodular Graphite", BCIRA Journal, 1958, p. 203.

37. C.O. Burgess, "Heat Treatment of Gray Iron", Gray Iron's Founders' Society, Cleveland, 1954, p. 117.

38. W.G. Scholz, D.V. Doane and G.A. Timmons, "Effects of Molybdenum on Stability and High Temperature Properties of Pearlitic Malleable Iron", AFS Transactions, Vol. 63, 1955, p. 251.

39. F.R. Morral, "The Constitution of Iron-Rich Fe-Al-C Alloys", Journal of Iron Steel Institute, Vol. 130, 1934, p. 418.

40. R. Vogel and H. Mader, "Das System Eisen-Aluminium-Kohlenstoff", Archiv fur das Eisenhuttenwessen, 1935-1936, p. 333.

41. K. Loehberg and W. Schmidt, "Die Eisenecke des System Eisen-Aluminium-Kohlenstoff", Archiv fur das Eisenhuttenwessen, Vol. 20, 1938, p. 607.

42. M. Vyklicky and H. Tuma, "Krystallisace Technickych Slitin Fe-Al-C vOblasti Tuheho Roztoku", Hutnicke Listy, Vol. 14, 1959, p. 218.

43. A.B. Everest, "The Influence of Aluminum on an Iron Carbon Alloy", Foundry Trade Journal, Vol. 36, 1927, p. 169.

44. R. Herbertson and A.M Sage, "The Virtues of Vanadium", 1st International Ferro-Alloys Conference Zurich, Metal Bulletin Ltd., London, 1977, p. 102.

45. R.W. Heine, "Nodule Count: The Benchmark of Ductile Iron Solidification," AFS Transactions, Vol. 101, 1993, p. 879.

46. S.Gosh, A. Prodhan, A.K. Chakrabarti, and O.N. Mohanty, "Effect of Alloy Composition and Inoculation on Microstructure and Cracking Susceptibility of Aluminum Cast Irons", AFS Transactions Vol. 104, 1996, p. 67-73.

47. W. D. Callister Jr., Materials Science and Engineering an Introduction 4th ed., John Wiley & Sons, Inc., 1997.

48. U. Ekpoom and R.W. Heine, "Austenite Transformation Temperature Range in Cast Irons", AFS Transactions, Vol. 86, 1978, p. 281.

49. G.M. Goodrich and R.W. Lobenhofer, "Effect of Cooling Rate on Ductile Iron Mechanical Properties", AFS Transactions, Vol. 110, 2002, p. 1006.

50. F. Lieteart, "The Eutectoid Transformation in Ductile Iron Castings", La Fonderie, no.4, Belge, 1979, p. 12.

51. G.N.J. Gilbert, "The Growth and Scaling Characteristics of Cast Irons in Air and Steam", BCIRA Journal, 1959, p. 478.

52. K. Roehrig, "Thermal Fatigue of Gray and Ductile Irons", AFS Transactions, Vol. 86, 1978, p. 75.

53. M.C.M Santos, A.M. P. Pinto, M.C.P.L. Jacinto and C.P.M. Sà, "Supporting the Model of Ductile Iron Dendritic Solidification", Advanced Engineering Materials, Vol. 2, no. 8, 2000, p. 514.

54. C.F. Yeung, H. Zhao and W.B. Lee, "The Morphology of Solidification of Thin-Section Ductile Iron Castings", Materials Characterization, Vol. 40, 1998, p. 201.

55. J. Verlinden and L.J. Kikkert, "Dendritisches Gefüge in Gusseisen mit Kugelgraphit," Eine Zwischenbilanz, Meehanite Research Report, Nr. 1375/G, November 1982.

56. S. Engler and R. Ellerbrok, "Über die Bildung von Austenithüllen um Graphitkugein während der Erstarrung von Eisen-Kohlenstoff-Silicium-Schmelzen", Giesserei-Forschung, Heft 4, 1977, p. 141.

57. D.M. Stefanescu and D.K. Bandyopadhyay, "On the Solidification Kinetics of Spheroidal Graphite Cast Iron," Conference Proceedings Cast Iron IV, Materials Research Society, 1990, p. 15.

58. R.W. Heine, "Spiking Solidification and Defects in White Cast Iron," AFS Transactions, Vol. 74, 1966, p. 734.

59. C.R. Loper Jr. and R.W. Heine, "Dendritic Structure and Spiking in Ductile Iron", AFS Transactions, Vol. 76, 1968, p. 547.

60. R.W. Heine and C.R. Loper Jr., "On Dendrites and Eutectic Cells in Gray Iron," AFS Transactions, Vol. 77, 1969, p.185.

61. T.W. Parks and C.R. Loper Jr., "A Study of Conditions Promoting Dendritic Growth in Ductile Iron," AFS Transactions, Vol. 77, 1969, p. 90.

62. M. Gagne and R. Goller, "Plate Fracture in Ductile Iron Castings," AFS Transactions, Vol. 91, 1983, p.37.

63. J.F. Wallace, M.H. Mulazrimoglu, Y.M. Yang, N.X. Ding and J.L. Merrer, "Solidification Studies of Spiking and Large-Small Nodule Formation in Ductile Cast Iron by the In-Mold Process," AFS Transactions, Vol. 93, 1985, p. 627.

64. H. Morrogh and W.J. Williams, "Graphite Formation in Cast Irons, Journal of Iron and Steel Institute, Vol. 155, 1947, p. 321.

65. R.P. Dunphy and W.S. Pellini, "Nodule Genesis and Growth in Magnesium-Treated Hypoeutectic Irons", Foundry 80, 1952, p. 82.

66. A.L. De Sy, "Graphite Spherulite Formation and Growth", Foundry, November 1953, p. 100.

67. A. Wittmoser, "A Propos de la Formation des Nodules de Graphite", Intern. Gieterij Congres, Bruxelles, 1951, p. 433.

68. G. Falkenhagen and W. Hofmann, "Beobachtungen an schroff abgeschreckten Eisen-Kohlenstoff-Schmelzen", Archiv für das Eisenhüttenwesen, Heft 1/2, 1952, p. 73.

69. E. Scheil and L. Hutter, "Untersuchungen über die Kristallisation des Gusseisens mit Kugelgraphit", Archiv fur das Eisenhuttenwesen, Mai/Juni 1953, p. 237.

70. C.R. Loper Jr. and R.W. Heine, "Graphite Formation During Solidification of Cast Iron," AFS Transactions, Vol. 70, 1962, p. 583.

71. C.R. Loper Jr. and R.W. Heine, "The Solidification of Cast Iron with Spheroidal Graphite," ASM Transactions, Vol. 56, 1963, p. 135.

72. C.R. Loper Jr. and R.W. Heine, "Graphitization and the Processing Cycle in Producing Ductile Iron," AFS Transactions, Vol. 72, 1964, p. 495.

73. W. Oldfield and J.G. Humphreys, "Formation of Nodular Graphite in Hypo-Eutectic Irons", BCIRA Journal, 1962, p. 315.

74. H. Kempers, "Sphärolitenflotation bei Gusseisen mit Kugelgraphit", Giesserei, Dezember 1966, p. 841.

75. W. Oldfield, G.T. Geering and W.A. Tiller, "Solidifcation of Spheroidal and Flake-Graphite Cast Iron," The Solidification of Metals, ISI Pub. 110, 1968, p. 256.

76. T. Sato, M. Maruyama and T. Ototani, "Formation of Lamellar and Spheroidal Graphite in Relation to the Microsegregation of Silicon," Cast Metals Research Journal, Vol. 7, 1971, p. 70.

77. W. Patterson, "Über den Einfluß von Fremdkeimen auf die Kristallisation von Metallen und Legierungen, insbesondere auf die Ausbildung des Eutectikums in Gußeisen", Giesserei Techn. Wissensch, Beihefte, März 1952, p. 355.

78. C.A. Van de Velde, "The Solidification of Ductile Cast Iron – A New Approach", AFS Special Report, AFS, Des Plaines, Illinois, 1997.

79. D.M. Stefanescu, "Theory of Solidification and Graphite Growth in Ductile Iron", Ductile Iron Handbook, AFS, Des Plaines, Illinois, 1999, p. 1.

80. A.L. De Sy, "The Core of Graphite Spherules in Nodular Cast Iron", Metal Progress, June 1950, p. 774.

81. H. Bakkerus and A.P. von Rosenstiel, "Onderzoeknaardeaanwezigheid van Karmen in Nodulair Grafiet", Metalen, no. 2, 1964, p. 40.

82. H. Itofuji, Y. Kawano, N. Inoyama, S. Yamamoto, B. Chang and T. Nishi, "The Formation Mechanism of Compacted/Vermicular Graphite in Cast Irons", AFS Transactions, 1983, p. 831.

83. M.J. Lalich and J.R. Hitchings, "Characterization of Inclusions as Nuclei for Spheroidal Graphite in Ductile Cast Irons", AFS Transactions, 1976, p. 653.

84. I. Minkoff, The Physical Metallurgy of Cast Iron, John Wiley & Sons Inc., 1983.

85. R.E. Ruxanda, D.M. Stefanescu and T.S. Piwonka, "Microstructure Characterization of Ductile Thin Wall Iron Castings," AFS Transactions, Vol. 110, 2002, p. 1131.

86. G.M. Goodrich, "Ductile Iron Casting Defects", Ductile Iron Handbook, AFS, Des Plaines, Illinois, 1999, p. 222.

87. R.W. Heine and C.R. Loper Jr., "Dross Formation in the Processing of Ductile Iron", AFS Transactions, Vol. 74, 1966, p. 274.

88. R.W. Heine and C.R. Loper Jr., "Principles of Slag and Dross Formation on Molten Cast Iron", AFS Transactions, Vol. 74, 1966, p. 421.

89. M.E. Latona, H.W. Kwon, J.F. Wallace and J.D. Voss, "Factors Influencing Dross Formation in Ductile Iron Castings", AFS Transactions, Vol. 92, 1984, p. 881.

90. E.R. Kaczmarek, R. Leitermann and R.W. Heine, "Pinhole and Slag Casting Defects in Ductile Iron Processing", AFS Transactions, Vol. 105, 1997, p. 67.

91. Z.B. Dwyer, R.D. Griffin and C.E. Bates, "Defects in Ductile Iron Castings", AFS Transactions, Vol. 106, 1996, p. 89.

92. P.K. Trojan, P.J. Griachelsaar, W.N. Bargeson and R.A. Flinn, "An Intensive Investigation of Dross in Nodular Iron", AFS Transactions, Vol. 76, 1968, p. 323.

93. H.J.T. Ellingham, "Reducibility of Oxides and Sulfides in Metallurgical Processes", J. Soc. Chem. Ind., Vol. 63, 1944, p. 125.

94. J. Campbell, Castings, Butterworth-Heinemann Ltd., Scotland, 1991.

95. R.V. Naik and J.F. Wallace, "Surface Tension - Nucleation Relations in Cast Iron Pinhole Formation", AFS Transactions, Vol. 88, 1980, p. 367.

96. J.V. Dawson, J.A. Kilshaw and A.D. Morgan, "The Nature and Origin of Gas Holes in Iron Castings", AFS Transactions, Vol. 73, 1965, p. 224.

97. B. Hernandez and J.F. Wallace, "Mechanisms of Pinhole Formation in Gray Iron", AFS Transactions, Vol. 87, 1979, p. 335.

98. A.D. Morgan, "Blowholes from Slag Inclusions," BCIRA Journal, Vol. 10, 1962, p. 438.

99. I.C.H. Hughes, "The Role of Gases in the Structure of Cast Iron", AFS Transactions, Vol. 77, 1969, p. 121.

100. E.E. Haack, "Pinhole in Gray Iron Castings", Modern Castings, Vol. 51, 1963, p. 50.

101. V.A. Checulin, "Chemical Reactions of Gases from the Mold with Steel and Cast Irons", Gases in Metals, 1965, p. 214.

102. J.F. Wallace and P.F. Wieser, "Pinholes in Gray Iron: A Literature Review", AFS, Des Plaines, Illinois, 1965.

103. M.J. Clifford, "Metal Penetration into Cores, Nitrogen/Hydrogen Pinholes and Defects", The British Foundryman, Vol. 60, November 1967, p. 447.

104. J.V. Dawson, "Avoiding Pinholes in Ductile Iron", Foundry, Vol. 101, June 1973, p. 89.

105. J. Gittus, "Pinholes in Nodular Iron Castings", BCIRA Journal, Vol. 5, 1955, p. 2.

106. S.F. Carter, W.J. Evans, J.C. Harkness and J.F. Wallace, "Factors Influencing the Formation of Pinholes in Gray and Ductile Iron," AFS Transactions, Vol. 87, 1979, p. 245.

107. A. Sahay, "Causes and Cures of Pinhole (Porosity) in Spherical Graphite Iron Castings", Indian Foundry Journal, 1971, p. 29.

108. K.H. Tiegel, "On the Formation of Pinholes in Spheroidal Graphite Cast Iron", Giesseri, Vol. 55, 1968, p. 169.

109. J.F. Wallace, P.K. Samal and J.D. Voss, "Factors Influencing a Shrinkage Cavity Formation in Ductile Iron", AFS Transactions, Vol. 92, 1984, p. 765.

110. J.R. Li, B.C. Liu, C.R. Loper Jr., H.B. Xing, H.J. Tong and Y.T. Xie, "Preliminary Study of Shrinkage Behavior of Ductile Iron in Green Sand Molds", AFS Transactions, Vol. 102, 1994, p. 421.

111. C.A. Bhaskaran and D.J. Wirth, "Ductile Iron Shrinkage Evaluation through Thermal Analysis", Vol. 110, 2002, p. 835.

112. D.R. Gaskell, Introduction to the Thermodynamics of Materials, 4th ed., Taylor & Francis, London, 2003.

113. N.B. Pilling and R.E. Bedworth, "The Oxidation of Metals at High Temperatures", Journal of the Institute of Metals, Vol. 29, 1923, p.529.

114. P. Bastid, P. Pilvin, C. Grente and E. Andrieu, "Microstructural Evolution of Spheroidal Graphite Cast Iron at High Temperature: Consequences on Mechanical Behaviour", Physical Metallurgy of Cast Iron V, Proceedings of the 5th International Symposium on the Physical Metallurgy of Cast Iron, France, 1994, p. 139.

115. J. Païdassi, "The Kinetics of the Air Oxidation of Iron in the Range 700-1250°C", Acta Metallurgica, Vol. 6, March 1958, p. 184.

116. W.W. Smeltzer and D.J. Young, "Oxidation Properties of Transition Metals", Progress in Solid-State Chemistry, Vol. 10, 1975, p. 17.

117. K. Hauffe, Reaktionen in und an festen Stoffen, Springer, Verlag, Berlin, 1966.

118. C. Pelhan, Selektive Oxydation njedrig legierten Gusseisen mit Lamellengraphit, Deutscher, Giessereitag, Düsseldorf, 1973.

119. N. Birks and W. Jackson, "Quantitative Treatment of Simultaneous Scaling and Decarburization of Steels", Journal of Iron and Steel Institute, Vol. 208, January 1970, p. 81.

120. R.Y. Chen and W.Y.D. Yuen, "Review of the High-Temperature Oxidation of Iron and Carbon Steels in Air or Oxygen", Oxidation of Metals, Plenum Publishing Corporation, Vol. 59, June 2003, p. 433.

121. D.R. Askeland and P.P. Phulé, The Science and Engineering of Materials 4th ed., Brooks/Cole, 2003.

122. D. Lazarus, "Diffusion in Body-Centered Cubic Transition Metals – A Theoretical Critique", ASM, 1964, p.155.

123. M. Hansen, Constitution of Binary Alloys, McGraw-Hill Inc., New York, 1958.

124. V.G. Tammann, "Über Anlauffarben von Metallen", Zeitschrift für Anorganische Chemie, Vol. 111-112, 1920, p. 78.

125. C. Wagner, "Equations for Transport in Solid Oxides and Sulfides of Transition Metals", Progress in Solid State Chemistry, Vol. 10, 1975, p. 3.

126. Y. Yang and A. McLean, Private Communication, University of Toronto, 2004.

127. D.R. Askeland, P.K. Trojan and R.A. Flinn, "Dross Forming Reactions in the System Mg-Si-O in Ductile Iron", AFS Transactions, Vol. 80, 1972, p. 349.

128. R.W. Heine, "Oxidation-Reduction Principles Controlling the Composition of Molten Cast Irons", AFS Transactions, Vol. 59, 1951, p. 121.

129. C.R. Cvetnic, A. Varvani-Farahani and C. Ravindran, "Fracture Surface Study of Spur Gears Subjected to Service Loading History", 1st Int. Conference on Fatigue Damage of Materials – Experiment and Analysis, WIT Press, 2003, p. 45.

130. C. Ravindran, Private Communication, Ryerson University, 2003.

131. J.E. Gruzleski, Microstructure Development during Metalcasting, AFS, Des Plaines, Illinois, 2000.

132. N. Birks and G.H. Meier, Introduction to High Temperature Oxidation of Metals, Edward Arnold Ltd., London, UK, 1983.

133. J.E. Freund and R.E. Walpole, Mathematical Statistics 4th ed., Prentice-Hall Inc., Englewood Cliffs, New Jersey, 1987.

Appendix **A**

Mould Dimensions

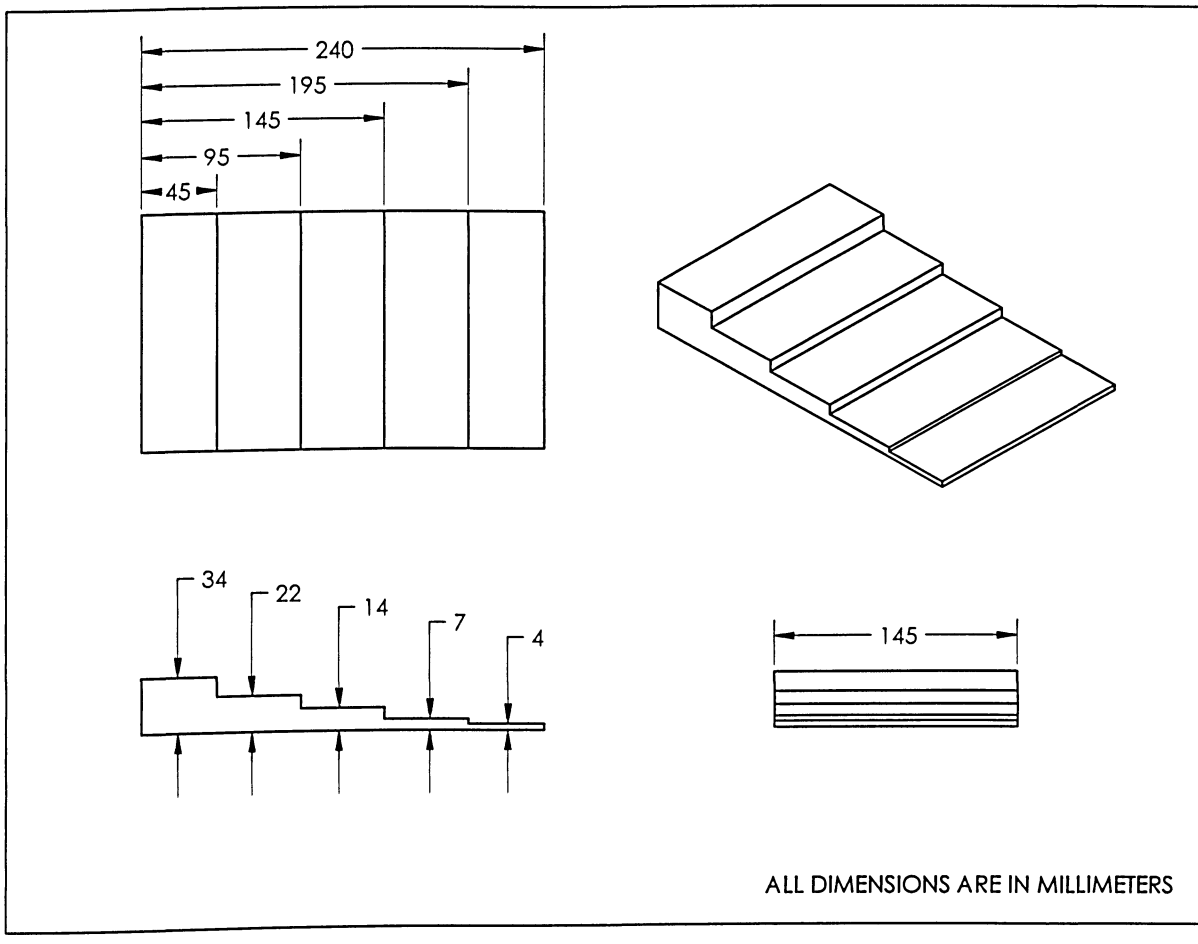

Figure A-1: Dimensions of Step Block mould used to produce experimental castings.

Appendix **B**

Model of Oxidation Testing Equipment

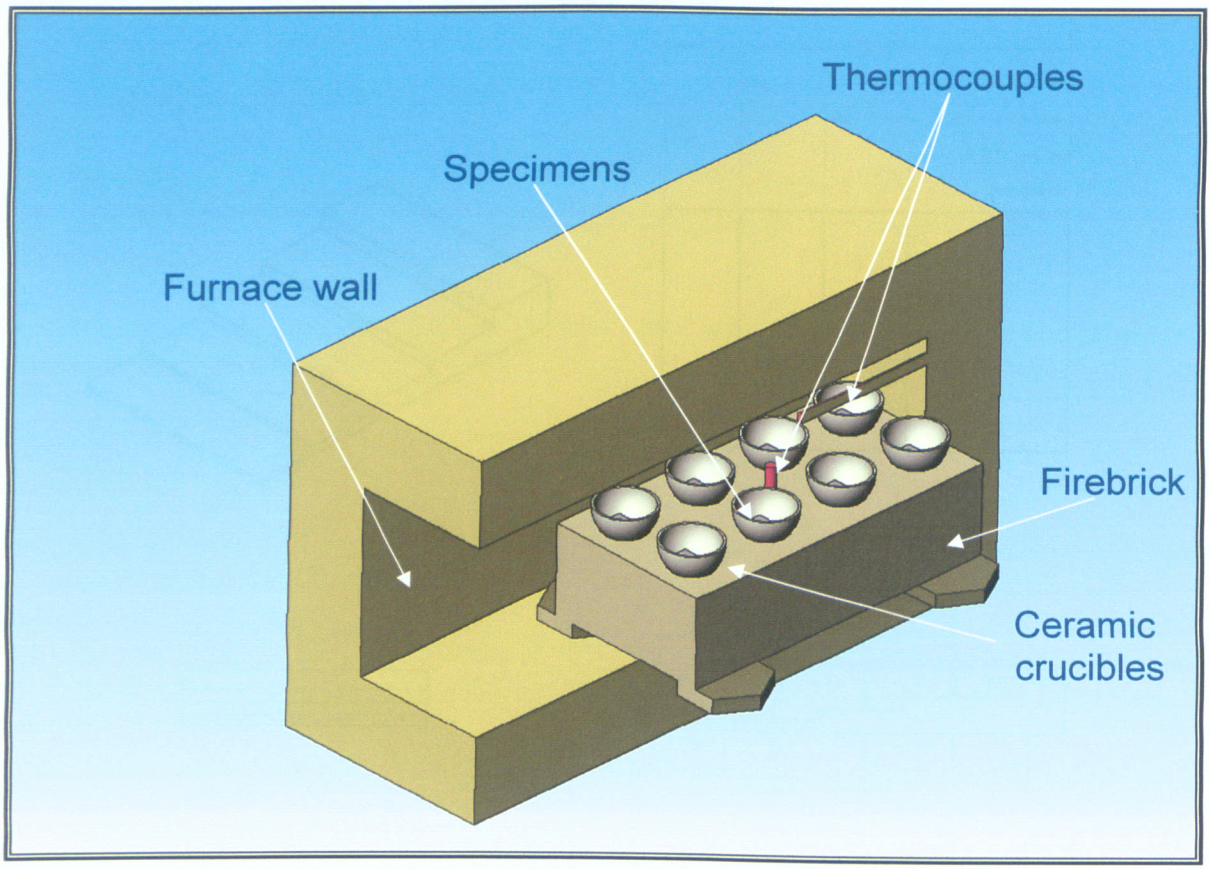

Figure B-1: Position of specimens in furnace during oxidation testing.

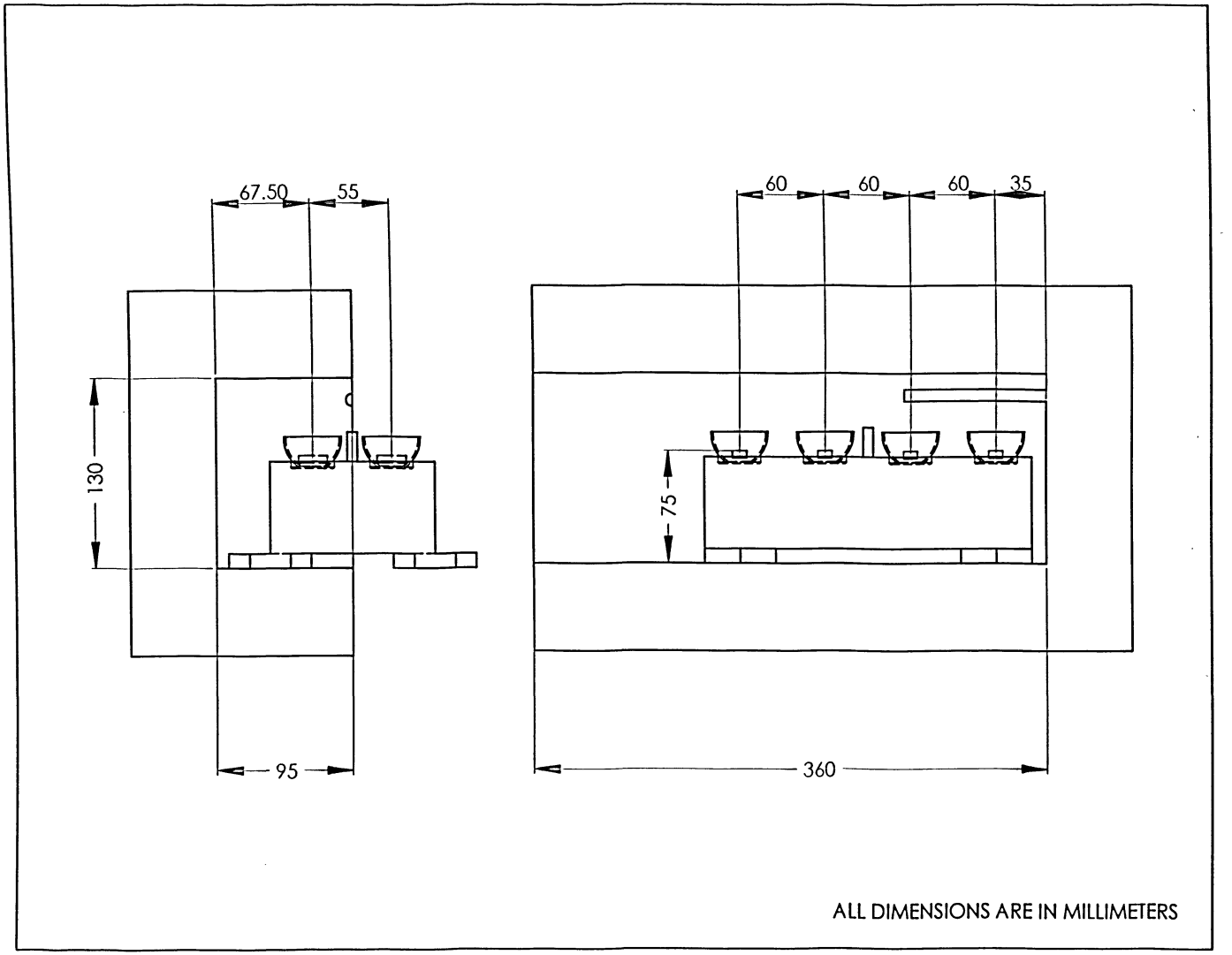

Figure B-2: Dimensioned position of each specimen relative to the furnace.

Appendix **C**

Furnace Temperature Distribution Results

In order to ensure efficiency of the oxidation tests, three furnaces were used (i.e., Furnaces A, B and C) with due consideration to suitability at the test temperature. The data compiled from the tests are illustrated graphically for each furnace. The temperature distribution within the furnaces did not change during the course of the experiment.

FURNACE A

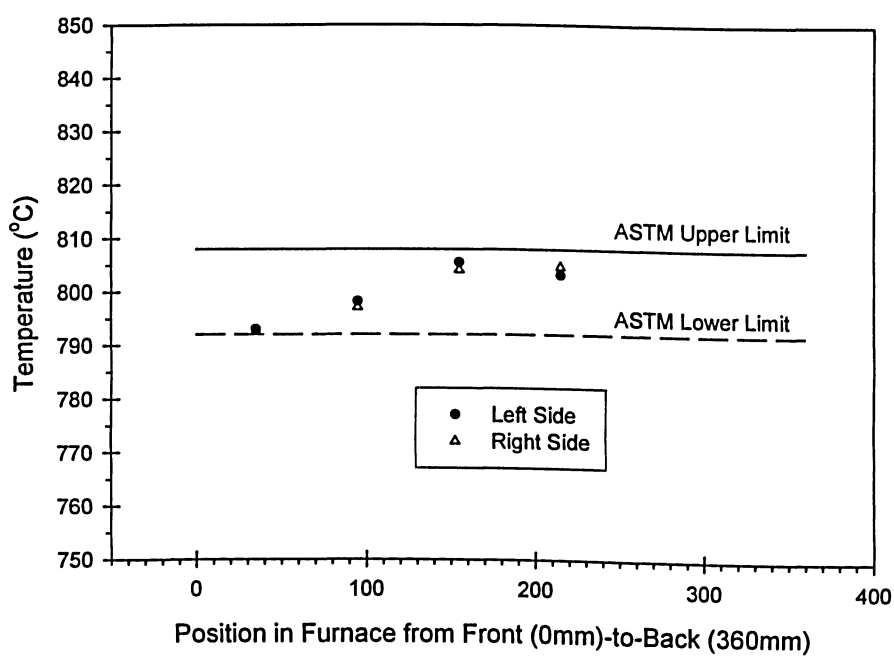

Figure C-1: Temperature distribution curve for Furnace A at 800°C.

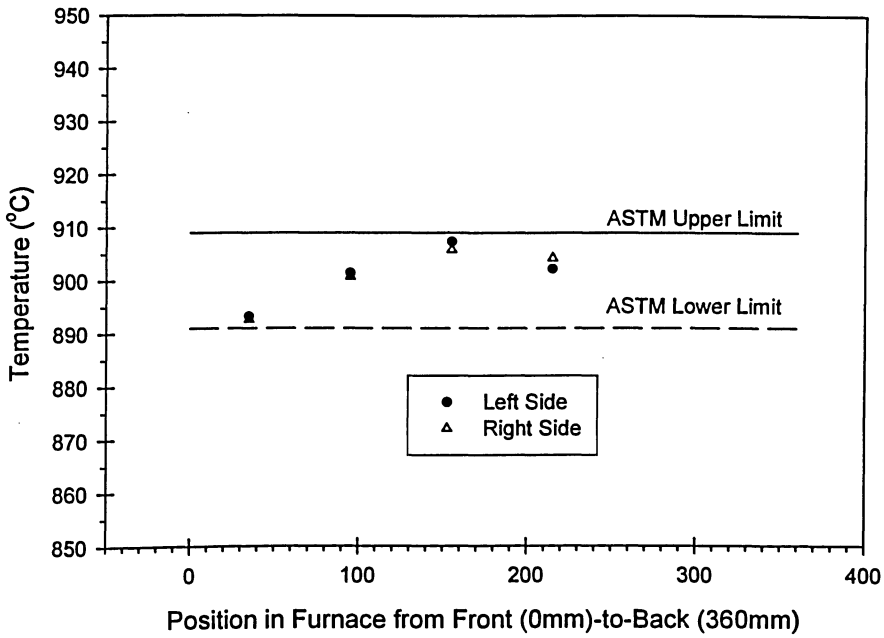

Figure C-2: Temperature distribution curve for Furnace A at 900°C.

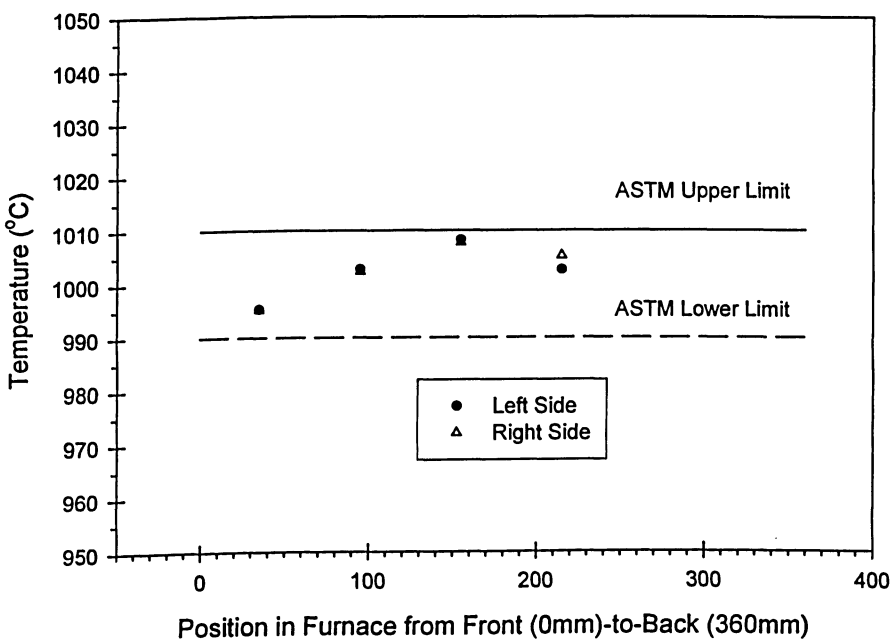

Figure C-3: Temperature distribution curve for Furnace A at 1000°C.

FURNACE B

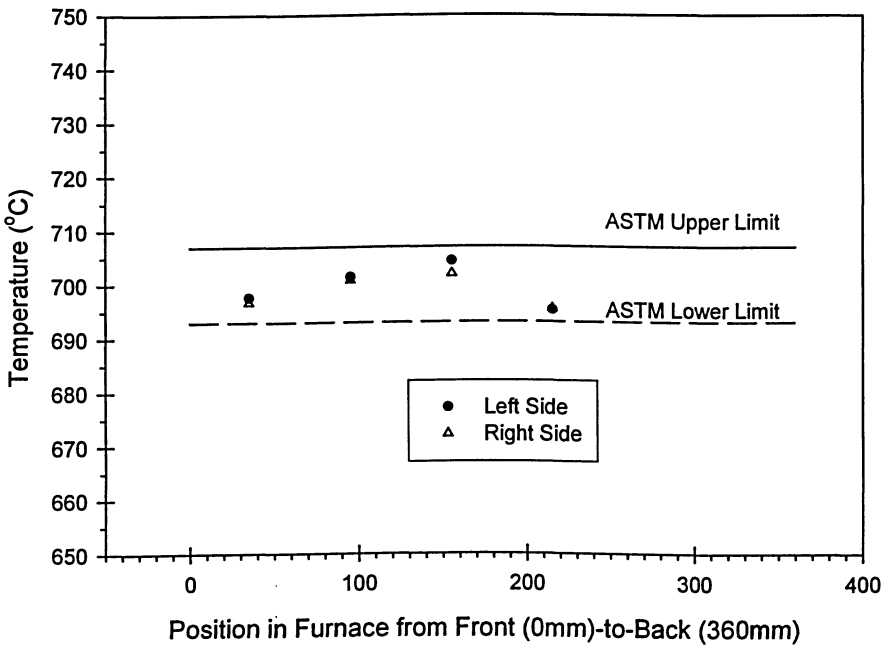

Figure C-4: Temperature distribution curve for Furnace B at 700°C.

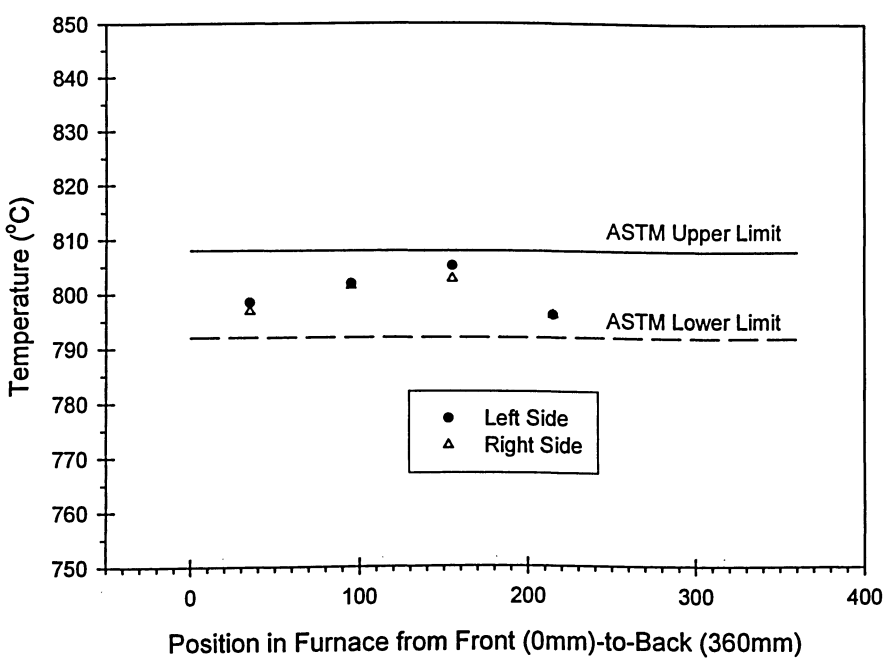

Figure C-5: Temperature distribution curve for Furnace B at 800°C.

FURNACE C

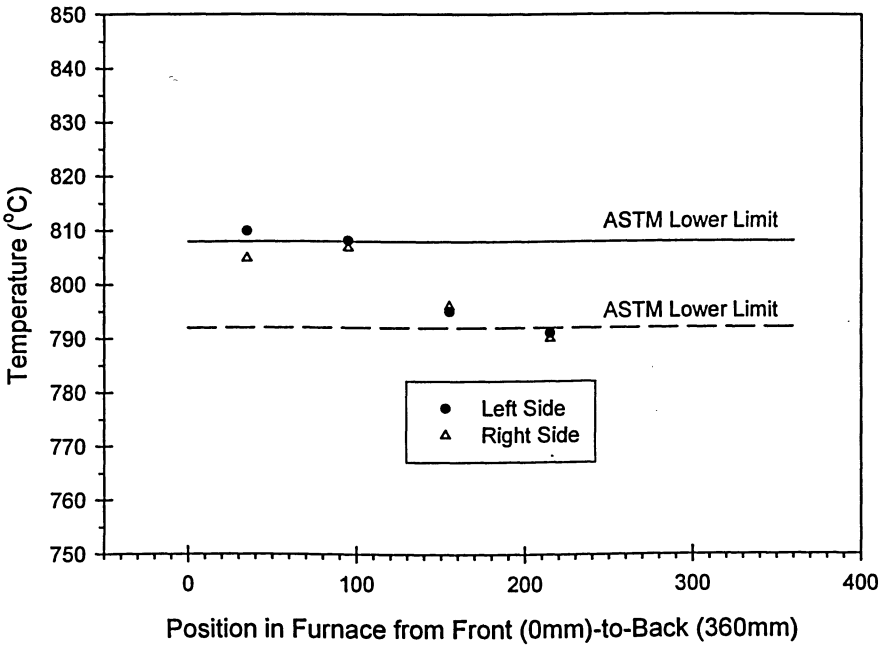

Figure C-6: Temperature distribution curve for Furnace C at 800°C.

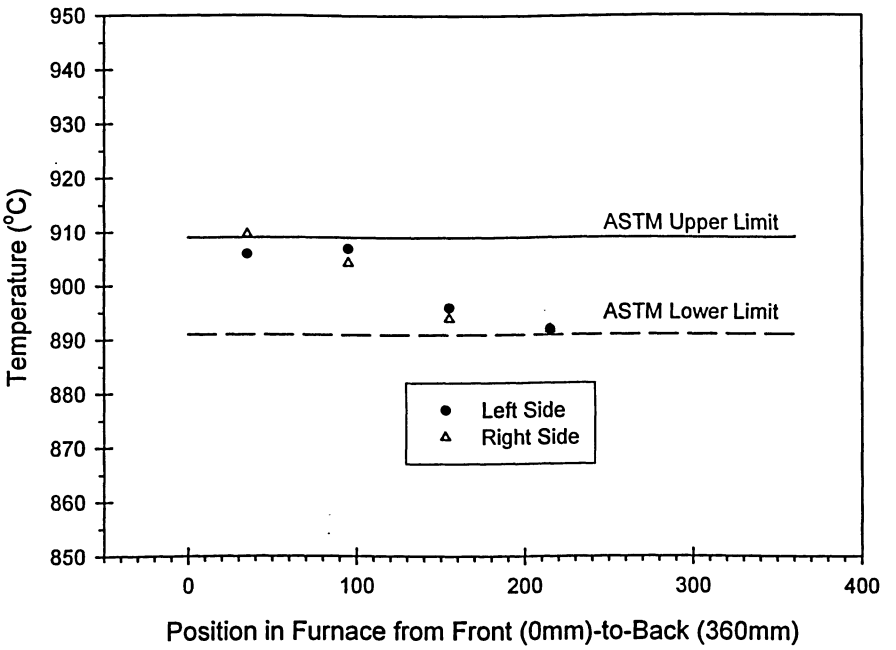

Figure C-7: Temperature distribution curve for Furnace C at 900°C.

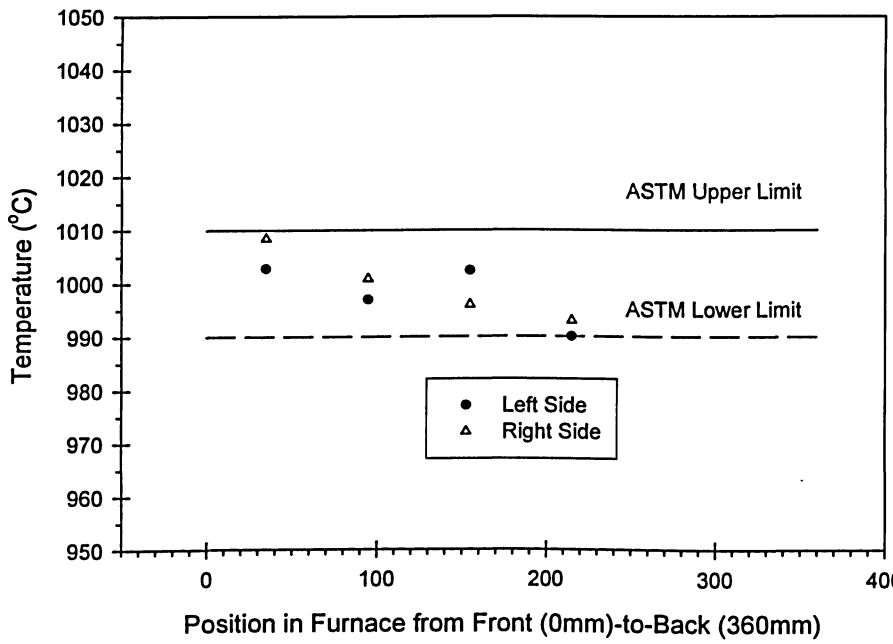

Figure C-8: Temperature distribution curve for Furnace C at 1000°C.

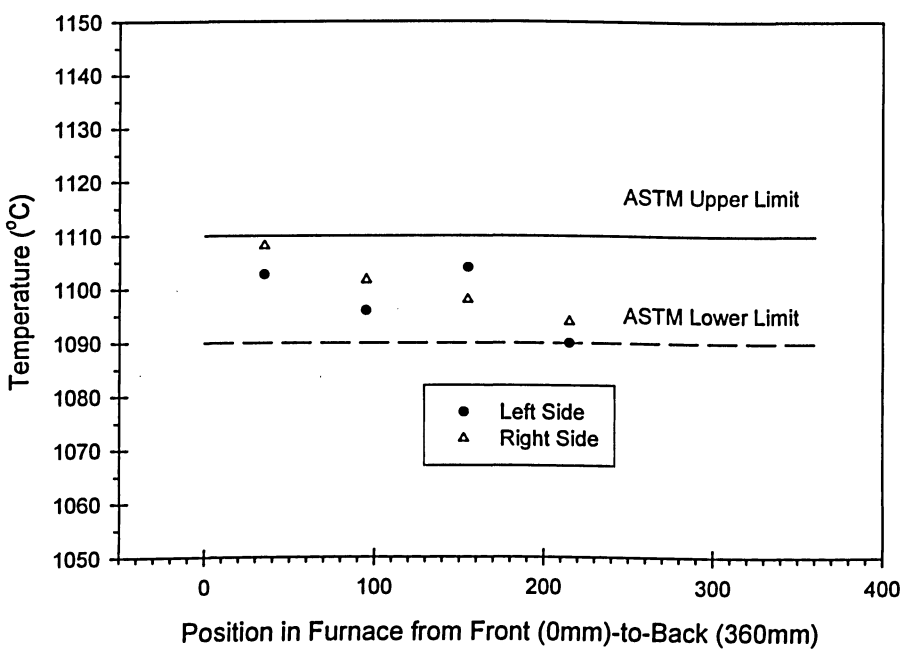

Figure C-9: Temperature distribution curve for Furnace C at 1100°C.

Appendix **D**

Tabulation and Statistical Analysis of Experimental Data

Experimental oxidation data obtained from tests at 700, 800, 900 and 1000°C after 500 hours on Alloy 1 (3.5Si-2.0Al), Alloy 2 (3.5Si-3.0Al), Alloy 3 (4.5Si-2.0Al) and Alloy 4 (4.5Si-3.0Al) was tabulated and statistically analyzed. Tests not repeated were not included in this analysis. The experimental data from the repeatability tests are presented in sections D1 to D4 in the following manner:

(i) Tabulation of Experimental Data

(ii) Mean, Standard Deviation, Standard Error and 95% and 99% Confidence Intervals

(iii) Analysis of Variance

(i) Tabulation of Experimental Data

The weight loss and gain per square centimetre after each cycle was tabulated for every specimen from Trial 1, 2 and 3. This data was organized in table format, as shown below:

Cycle Time (hrs)	Trial 1 (mg/cm^2)	Trial 2 (mg/cm^2)	Trial 3 (mg/cm^2)
0			
1			
2			
4			
24			
48			
96			
212			
500			

(ii) Mean, Standard Deviation, Standard Error and 95% and 99% Confidence Intervals

The mean, standard deviation, standard error and the 95% and 99% confidence intervals were determined using SigmaPlot® software. The confidence intervals were determined using the *t*-statistic.

(iii) Analysis of Variance

Analysis of variance (ANOVA) for a single factor experiment was carried out to test the statistical significance between measurements of the mean and variance of two or more different populations (i.e., cycle times). ANOVA was carried out for each oxidation cycle (e.g., 0-1 hrs, 1-2 hrs ...) and for the overall cycle from 0-500 hours.

Testing of the statistical significance for each temperature was performed using Microsoft® Excel. The critical factors determined are shown in the table below [133]:

Table D-1: ANOVA table for a 1 factor experiment.

Source of Variation	Sum of Squares	Deg. Of Free.	Mean Square Value	α	F	P-Value	$F_{critical}$	H_o
Between Cycles	SS_T	$\nu_T = a-1$	$S_T^2 = \frac{SS_T}{\nu_T}$		$F_T = \frac{S_T^2}{S_R^2}$		$F_{\nu_1;\nu_2;\alpha}$	
Within Cycles	SS_R	$\nu_R = N-a$	$S_R^2 = \frac{SS_R}{\nu_R}$		-	-	-	
Total	SS	$\nu = N-1$	-		-	-	-	

where SS_T is the sum of squares associated with variation between the cycles, SS_R is the sum of squares associated with variation within each cycle and SS is the total sum of squares. ν_T, ν_R and ν are the degrees of freedom associated with variation between and within cycles and the total degrees of freedom involved, respectively. a denotes the number of cycles and N represents the number of replication measurements taken at each cycle multiplied by a. S_T^2 and S_R^2 denotes the variance associated with variation between and within cycles. The α

denotes the level of significance and the *P-Value* represents the smallest pre-set level of significance where the null hypothesis would be rejected. The *P-Value's* in this analysis were generated by the software.

Computed factors were summarized using the following table format:

Cycle Time (hours)	α	F	P-Value	$F_{critical}$	H_o

The test for statistical significance between each cycle was carried out by comparing the *F*-statistic with $F_{critical}$ and α with *P-Value*. If *F* was greater than $F_{critical}$, the null hypothesis H_o was rejected at that specific level of significance α. Thus, it would be concluded that the interactions were significantly large and that the cycle times had a significant effect on the oxidation behaviour of the alloy at that specific temperature. Similarly, if the *P-Value* was determined to be smaller then the α, the H_o was rejected.

D1 OXIDATION DATA for SAMPLES OXIDIZED at 700°C

D1-1 Alloy 1 (3.5Si-2.0Al)

Table D1-1: Experimental data from ductile iron specimens oxidized for 500 hrs at 700°C.

Cycle Time (hrs)	Trial 1 (mg/cm^2)	Trial 2 (mg/cm^2)	Trial 3 (mg/cm^2)
0	0	0	0
1	-0.3	-0.3	-0.1
2	0	-0.1	0
4	0	0.1	0.1
24	1.9	1.7	1.7
48	2.1	2.0	2.0
96	2.4	2.3	2.3
212	2.7	2.7	2.7
500	2.7	2.9	2.9

Table D1-2: Statistical analysis of data in Table D1-1.

Cycle Time (hrs)	Mean (mg/cm^2)	Standard Deviation	Standard Error	95% Conf. Interval	99% Conf. Interval
0	0	0	0	0	0
1	-0.2	0.1	0.07	0.3	0.7
2	-0.03	0.06	0.03	0.1	0.3
4	0.07	0.06	0.03	0.1	0.3
24	1.8	0.12	0.067	0.29	0.65
48	2.0	0.058	0.033	0.14	0.33
96	2.3	0.058	0.033	0.14	0.33
212	2.7	0	0	0	0
500	2.8	0.12	0.067	0.29	0.65

Table D1-3: Analysis of variance from 0 to 500 hrs.

Cycle Time (hours)	α	F	P-Value	$F_{critical}$	H_o
0-1	0.05	12	0.02	8	Reject
1-2	0.05	7	0.06	8	Accept
2-4	0.05	5	0.10	8	Accept
4-24	0.05	520	0.00002	8	Reject
24-48	0.05	13	0.02	8	Reject
48-96	0.05	41	0.003	8	Reject
96-212	0.05	121	0.0004	8	Reject
212-500	0.10	4	0.11	5	Accept
0-500	0.05	852	0	3	Reject

D1-2 Alloy 2 (3.5Si-3.0Al)

Table D1-4: Experimental data from ductile iron specimens oxidized for 500 hrs at 700°C.

Cycle Time (hrs)	Trial 1 (mg/cm^2)	Trial 2 (mg/cm^2)	Trial 3 (mg/cm^2)
0	0.0	0.0	0.0
1	-0.1	-0.1	-0.1
2	0.0	-0.3	-0.1
4	0.0	-0.1	0.1
24	0.4	0.4	0.6
48	0.6	0.7	0.7
96	0.9	1.0	0.9
212	1.1	1.3	1.0
500	1.3	1.4	1.1

Table D1-5: Statistical analysis of data in Table D1-4.

Cycle Time (hrs)	Mean (mg/cm^2)	Standard Deviation	Standard Error	95% Conf. Interval	99% Conf. Interval
0	0	0	0	0	0
1	-0.1	0	0	0	0
2	-0.1	0.1	0.08	0.4	0.8
4	0	0.1	0.08	0.4	0.8
24	0.5	0.08	0.05	0.2	0.5
48	0.7	0.08	0.05	0.2	0.5
96	0.9	0.08	0.05	0.2	0.5
212	1.1	0.14	0.083	0.35	0.81
500	1.3	0.14	0.083	0.35	0.81

Table D1-6: Analysis of variance from 0 to 500 hrs.

Cycle Time (hours)	α	F	P-Value	$F_{critical}$	H_o
0-1	0.20	-2E+16	N/A	2	Accept
1-2	0.20	0.1	0.7	2	Accept
2-4	0.20	2	0.27	2	Accept
4-24	0.05	28	0.006	8	Reject
24-48	0.05	7	0.06	8	Accept
48-96	0.05	32	0.005	8	Reject
96-212	0.05	5	0.10	8	Accept
212-500	0.20	1.1	0.35	2.4	Accept
0-500	0.05	83	0	3	Reject

D1-3 Alloy 3 (4.5Si-2.0Al)

Table D1-7: Experimental data from ductile iron specimens oxidized for 500 hrs at 700°C.

Cycle Time (hrs)	Trial 1 (mg/cm^2)	Trial 2 (mg/cm^2)	Trial 3 (mg/cm^2)
0	0	0	0
1	-0.1	-0.1	-0.1
2	-0.1	-0.1	0
4	0	0	0
24	0.3	0.6	0.4
48	0.7	0.9	0.9
96	0.9	0.9	1
212	0.9	1	1.1
500	1.1	1	1.3

Table D1-8: Statistical analysis of data in Table D1-7.

Cycle Time (hrs)	Mean (mg/cm^2)	Standard Deviation	Standard Error	95% Conf. Interval	99% Conf. Interval
0	0	0	0	0	0
1	-0.1	0	0	0	0
2	-0.1	0.08	0.05	0.2	0.5
4	0	0	0	0	0
24	0.4	0.1	0.08	0.35	0.8
48	0.8	0.08	0.05	0.2	0.5
96	0.9	0.08	0.05	0.2	0.5
212	1	0.1	0.08	0.4	0.8
500	1.1	0.14	0.083	0.35	0.81

Table D1-9: Analysis of variance from 0 to 500 hrs.

Cycle Time (hours)	α	F	P-Value	$F_{critical}$	H_o
0-1	0.20	-2E+16	N/A	2	Accept
1-2	0.20	1	0.4	2	Accept
2-4	0.10	4	0.1	5	Accept
4-24	0.05	24	0.008	8	Reject
24-48	0.05	13	0.02	8	Reject
48-96	0.20	2	0.25	2	Accept
96-212	0.20	1	0.4	2	Accept
212-500	0.20	1.6	0.27	2.4	Accept
0-500	0.05	93	0	2.5	Reject

D1-4 Alloy 4 (4.5Si-3.0Al)

Table D1-10: Experimental data from ductile iron specimens oxidized for 500 hrs at 700°C.

Cycle Time (hrs)	Trial 1 (mg/cm^2)	Trial 2 (mg/cm^2)	Trial 3 (mg/cm^2)
0	0	0	0
1	-0.3	-0.4	-0.3
2	-0.3	-0.1	-0.1
4	-0.4	-0.1	-0.3
24	-0.1	0.1	0
48	-0.1	0.1	0.3
96	-0.1	0.1	0.3
212	-0.1	0.3	0.3
500	-0.1	0.1	0.3

Table D1-11: Statistical analysis of data in Table D1-10.

Cycle Time (hrs)	Mean (mg/cm^2)	Standard Deviation	Standard Error	95% Conf. Interval	99% Conf. Interval
0	0	0	0	0	0
1	-0.3	0.08	0.05	0.2	0.5
2	-0.2	0.08	0.05	0.2	0.5
4	-0.3	0.1	0.08	0.4	0.8
24	0	0.1	0.08	0.4	0.8
48	0.1	0.2	0.1	0.5	1.0
96	0.1	0.2	0.1	0.5	1.0
212	0.1	0.2	0.1	0.6	1.0
500	0.1	0.2	0.1	0.5	1.0

Table D1-12: Analysis of variance from 0 to 500 hrs.

Cycle Time (hours)	α	F	P-Value	$F_{critical}$	H_o
0-1	0.05	100	0.0007	8	Reject
1-2	0.05	5	0.09	8	Accept
2-4	0.20	0.8	0.4	2	Accept
4-24	0.05	6	0.06	8	Accept
24-48	0.05	0.6	0.5	2	Accept
48-96	0.20	0	1	2	Accept
96-212	0.20	0.1	0.7	2	Accept
212-500	0.20	0.1	0.7	2	Accept
0-500	0.05	4	0.008	3	Reject

D2 OXIDATION DATA for SAMPLES OXIDIZED at 800°C

D2-1 Alloy 1 (3.5Si-2.0Al)

Table D2-1: Experimental data from ductile iron specimens oxidized for 500 hrs at 800°C.

Cycle Time (hrs)	Trial 1 (mg/cm^2)	Trial 2 (mg/cm^2)	Trial 3 (mg/cm^2)
0	0	0	0
1	-0.3	0	0
2	-0.4	0	0.1
4	-0.6	0.1	0.1
24	-0.6	0.1	0.1
48	-0.6	0.1	0.1
96	-0.4	0.1	0.1
212	-0.3	0.3	0.3
500	0.4	0.6	0.6

Table D2-2: Statistical analysis of data in Table D2-1.

Cycle Time (hrs)	Mean (mg/cm^2)	Standard Deviation	Standard Error	95% Conf. Interval	99% Conf. Interval
0	0	0	0	0	0
1	-0.1	0.2	0.1	0.4	0.9
2	-0.09	0.3	0.2	0.7	2
4	-0.1	0.4	0.2	1	2
24	-0.1	0.4	0.2	1	2
48	-0.1	0.4	0.2	1	2
96	-0.05	0.3	0.2	0.8	2
212	0.1	0.3	0.2	0.8	2
500	0.5	0.1	0.06	0.2	0.6

Table D2-3: Analysis of variance from 0 to 500 hrs.

Cycle Time (hours)	α	F	P-Value	$F_{critical}$	H_o
0-1	0.20	1	0.4	2	Accept
1-2	0.20	0	N/A	2	Accept
2-4	0.20	0.01	0.9	2	Accept
4-24	0.20	0	1	2	Accept
24-48	0.20	0	1	2	Accept
48-96	0.20	0.05	0.8	2	Accept
96-212	0.20	0.4	0.6	2	Accept
212-500	0.05	4	0.1	8	Accept
0-500	0.10	2	0.2	2	Accept

D2-2 Alloy 2 (3.5Si-3.0Al)

Table D2-4: Experimental data from ductile iron specimens oxidized for 500 hrs at 800°C.

Cycle Time (hrs)	Trial 1 (mg/cm^2)	Trial 2 (mg/cm^2)	Trial 3 (mg/cm^2)
0	0.0	0.0	0.0
1	-0.1	0.0	-0.1
2	-0.4	-0.1	-0.4
4	-0.3	-0.3	-0.4
24	-0.3	-0.1	-0.4
48	-0.3	-0.1	-0.4
96	-0.1	0.0	-0.3
212	0.0	0.0	0.0
500	0.1	0.1	0.1

Table D2-5: Statistical analysis of data in Table D2-4.

Cycle Time (hrs)	Mean (mg/cm^2)	Standard Deviation	Standard Error	95% Conf. Interval	99% Conf. Interval
0	0	0	0	0	0
1	-0.07	0.06	0.03	0.1	0.3
2	-0.3	0.2	0.1	0.4	1
4	-0.3	0.07	0.04	0.2	0.4
24	-0.3	0.1	0.08	0.4	0.8
48	-0.3	0.1	0.08	0.35	0.8
96	-0.1	0.15	0.09	0.4	0.8
212	0	0	0	0	0
500	0.1	0	0	0	1.0

Table D2-6: Analysis of variance from 0 to 500 hrs.

Cycle Time (hours)	α	F	P-Value	$F_{critical}$	H_o
0-1	0.10	4	0.12	5	Accept
1-2	0.05	5	0.09	8	Accept
2-4	0.20	0.1	0.8	2	Accept
4-24	0.20	0.5	0.5	2	Accept
24-48	0.20	0	1	2	Accept
48-96	0.20	1	0.3	2	Accept
96-212	0.10	2	0.2	5	Accept
212-500	0.20	-2E+16	N/A	2	Accept
0-500	0.05	6	0.0006	3	Reject

D2-3 Alloy 3 (4.5Si-2.0Al)

Table D2-7: Experimental data from ductile iron specimens oxidized for 500 hrs at 800°C.

Cycle Time (hrs)	Trial 1 (mg/cm^2)	Trial 2 (mg/cm^2)	Trial 3 (mg/cm^2)
0	0.0	0.0	0.0
1	-0.6	-0.6	-0.4
2	-0.4	-0.4	-0.4
4	-0.7	-0.6	-0.6
24	-0.4	-0.4	-0.4
48	-0.3	-0.4	-0.4
96	-0.3	-0.4	-0.4
212	-0.1	-0.4	-0.4
500	0.1	-0.1	-0.1

Table D2-8: Statistical analysis of data in Table D2-7.

Cycle Time (hrs)	Mean (mg/cm^2)	Standard Deviation	Standard Error	95% Conf. Interval	99% Conf. Interval
0	0	0	0	0	0
1	-0.5	0.08	0.05	0.2	0.5
2	-0.4	0	0	0	0
4	-0.6	0.08	0.05	0.2	0.5
24	-0.4	0	0	0	0
48	-0.4	0.08	0.05	0.2	0.5
96	-0.4	0.08	0.05	0.2	0.5
212	-0.3	0.2	0.1	0.4	0.9
500	-0.06	0.1	0.08	0.3	0.8

Table D2-9: Analysis of variance from 0 to 500 hrs.

Cycle Time (hours)	α	F	P-Value	$F_{critical}$	H_o
0-1	0.05	64	0.001	8	Reject
1-2	0.10	4	0.12	5	Accept
2-4	0.05	49	0.002	8	Reject
4-24	0.05	49	0.002	8	Reject
24-48	0.20	1	0.4	2	Accept
48-96	0.20	0	1	2	Accept
96-212	0.20	0.4	0.6	2	Accept
212-500	0.05	5	0.09	8	Accept
0-500	0.05	17	5E-07	3	Reject

D2-4 Alloy 4 (4.5Si-3.0Al)

Table D2-10: Experimental data from ductile iron specimens oxidized for 500 hrs at 800°C.

Cycle Time (hrs)	Trial 1 (mg/cm^2)	Trial 2 (mg/cm^2)	Trial 3 (mg/cm^2)
0	0.0	0.0	0.0
1	-0.4	-0.4	-0.4
2	-0.6	-0.4	-0.6
4	-0.7	-0.3	-0.6
24	-0.7	-0.1	-0.6
48	-0.6	-0.1	-0.4
96	-0.6	-0.1	-0.4
212	-0.6	0.0	-0.4
500	-0.4	0.1	-0.3

Table D2-11: Statistical analysis of data in Table D2-10.

Cycle Time (hrs)	Mean (mg/cm^2)	Standard Deviation	Standard Error	95% Conf. interval	99% Conf. Interval
0	0	0	0	0	0
1	-0.4	0	0	0	0
2	-0.5	0.08	0.05	0.2	0.5
4	-0.5	0.2	0.1	0.5	1
24	-0.5	0.3	0.2	0.7	2
48	-0.4	0.2	0.1	0.5	1
96	-0.4	0.2	0.1	0.5	1
212	-0.3	0.3	0.2	0.7	2
500	-0.2	0.3	0.2	0.7	2

Table D2-12: Analysis of variance from 0 to 500 hrs.

Cycle Time (hours)	α	F	P-Value	$F_{critical}$	H_o
0-1	0.2	-2E+16	N/A	2	Accept
1-2	0.10	4	0.1	5	Accept
2-4	0.20	0	1	2	Accept
4-24	0.20	0.09	0.8	2	Accept
24-48	0.20	0.2	0.7	2	Accept
48-96	0.20	0	1	2	Accept
96-212	0.20	0.02	0.9	2	Accept
212-500	0.20	0.3	0.6	2	Accept
0-500	0.10	2	0.2	2	Accept

D3 OXIDATION DATA for SAMPLES OXIDIZED at 900°C

D3-1 Alloy 1 (3.5Si-2.0Al)

Table D3-1: Experimental data from ductile iron specimens oxidized for 500 hrs at 900°C.

Cycle Time (hrs)	Trial 1 (mg/cm^2)	Trial 2 (mg/cm^2)	Trial 3 (mg/cm^2)
0	0	0	0
1	-0.4	-0.6	-0.3
2	-0.4	-0.6	-0.1
4	-0.6	-0.6	0
24	1.9	3.6	2.4
48	4.3	7.6	4.7
96	8	15.3	8.9
212	16.6	33	18.7
500	37.7	57.4	39.4

Table D3-2: Statistical analysis of data in Table D3-1.

Cycle Time (hrs)	Mean (mg/cm^2)	Standard Deviation	Standard Error	95% Conf. Interval	99% Conf. Interval
0	0	0	0	0	0
1	-0.4	0.1	0.08	0.4	0.8
2	-0.4	0.2	0.1	0.5	1
4	-0.4	0.3	0.2	0.8	2
24	2.6	0.87	0.50	2.2	4.9
48	5.5	1.8	1.0	4.4	10
96	10	4.0	2.3	9.9	22
212	23	8.9	5.2	22	50
500	45	11	6.3	27	62

Table D3-3: Analysis of variance from 0 to 500 hrs.

Cycle Time (hours)	α	F	P-Value	$F_{critical}$	H_o
0-1	0.05	24	0.008	8	Reject
1-2	0.20	0.2	0.7	2	Accept
2-4	0.20	0.02	0.9	2	Accept
4-24	0.05	31	0.005	8	Reject
24-48	0.05	6.3	0.066	7.7	Accept
48-96	0.10	4.3	0.11	4.5	Accept
96-212	0.05	4.5	0.010	7.7	Accept
212-500	0.05	7.35	0.0535	7.71	Accept
0-500	0.05	28	0	3	Reject

D3-2 Alloy 2 (3.5Si-3.0Al)

Table D3-4: Experimental data from ductile iron specimens oxidized for 500 hrs at 900°C.

Cycle Time (hrs)	Trial 1 (mg/cm^2)	Trial 2 (mg/cm^2)	Trial 3 (mg/cm^2)
0	0	0	0
1	-0.4	-0.3	-0.4
2	-0.1	-0.3	-0.6
4	-0.3	-0.4	-0.6
24	-0.1	-1	-0.7
48	0	-0.9	-0.6
96	0.1	-0.6	-0.6
212	1	0.9	0.1
500	3.4	3.6	2

Table D3-5: Statistical analysis of data in Table D3-4.

Cycle Time (hrs)	Mean (mg/cm^2)	Standard Deviation	Standard Error	95% Conf. Interval	99% Conf. Interval
0	0	0	0	0	0
1	-0.4	0.08	0.05	0.2	0.5
2	-0.3	0.2	0.1	0.5	1
4	-0.4	0.1	0.08	0.4	0.8
24	-0.6	0.4	0.3	1	2
48	-0.5	0.4	0.3	1	2
96	-0.3	0.4	0.2	1	2
212	0.7	0.5	0.3	1	3
500	3	0.87	0.50	2.2	4.9

Table D3-6: Analysis of variance from 0 to 500 hrs.

Cycle Time (hours)	α	F	P-Value	$F_{critical}$	H_o
0-1	0.05	121	0.0004	8	Reject
1-2	0.20	0.05	0.8	2	Accept
2-4	0.20	0.3	0.6	2	Accept
4-24	0.20	0.4	0.6	2	Accept
24-48	0.20	0.07	0.8	2	Accept
48-96	0.20	0.1	0.7	2	Accept
96-212	0.05	8	0.05	8	-
212-500	0.05	16	0.02	8	Accept
0-500	0.05	21	1E-07	3	Reject

D3-3 Alloy 3 (4.5Si-2.0Al)

Table D3-7: Experimental data from ductile iron specimens oxidized for 500 hrs at 900°C.

Cycle Time (hrs)	Trial 1 (mg/cm^2)	Trial 2 (mg/cm^2)	Trial 3 (mg/cm^2)
0	0	0	0
1	-0.4	-0.4	-0.1
2	-0.1	-0.4	-0.1
4	-0.1	-0.4	-0.3
24	-0.1	-0.4	-0.4
48	-0.1	-0.3	-0.4
96	-0.1	-0.3	-0.4
212	-0.1	-0.3	-0.4
500	-0.1	-0.1	-0.4

Table D3-8: Statistical analysis of data in Table D3-7.

Cycle Time (hrs)	Mean (mg/cm^2)	Standard Deviation	Standard Error	95% Conf. Interval	99% Conf. Interval
0	0	0	0	0	0
1	-0.3	0.2	0.1	0.4	0.9
2	-0.2	0.2	0.1	0.4	0.9
4	-0.3	0.1	0.08	0.4	0.8
24	-0.3	0.2	0.1	0.4	0.9
48	-0.3	0.1	0.08	0.4	0.8
96	-0.3	0.1	0.08	0.4	0.8
212	-0.3	0.1	0.08	0.4	0.8
500	-0.2	0.2	0.1	0.4	0.9

Table D3-9: Analysis of variance from 0 to 500 hrs.

Cycle Time (hours)	α	F	P-Value	$F_{critical}$	H_o
0-1	0.05	9	0.04	8	Reject
1-2	0.20	0.5	0.5	2	Accept
2-4	0.20	0.25	0.6	2	Accept
4-24	0.20	0.06	0.8	2	Accept
24-48	0.20	0.06	0.8	2	Accept
48-96	0.20	0	1	2	Accept
96-212	0.20	0	1	2	Accept
212-500	0.05	0.3	0.6	2	Accept
0-500	0.20	1	0.4	2	Accept

D3-4 Alloy 4 (4.5Si-3.0Al)

Table D3-10: Experimental data from ductile iron specimens oxidized for 500 hrs at 900°C.

Cycle Time (hrs)	Trial 1 (mg/cm^2)	Trial 2 (mg/cm^2)	Trial 3 (mg/cm^2)
0	0.0	0.0	0.0
1	-0.3	-0.3	-0.1
2	-0.4	-0.3	-0.3
4	-0.3	-0.3	-0.3
24	-0.3	-0.1	-0.1
48	0.0	-0.1	0.0
96	0.0	-0.1	0.1
212	0.0	-0.1	0.1
500	-0.1	-0.3	0.3

Table D3-11: Statistical analysis of data in Table D3-10.

Cycle Time (hrs)	Mean (mg/cm^2)	Standard Deviation	Standard Error	95% Conf. Interval	99% Conf. Interval
0	0	0	0	0	0
1	-0.2	0.08	0.05	0.2	0.5
2	-0.3	0.08	0.05	0.2	0.5
4	-0.3	0	0	0	0
24	-0.2	0.08	0.05	0.2	0.5
48	-0.05	0.08	0.05	0.2	0.5
96	0	0.1	0.08	0.4	0.8
212	0	0.1	0.08	0.4	0.8
500	-0.05	0.3	0.2	0.7	1.7

Table D3-12: Analysis of variance from 0 to 500 hrs.

Cycle Time (hours)	α	F	P-Value	$F_{critical}$	H_o
0-1	0.05	12	0.02	8	Reject
1-2	0.20	2	0.3	2	Accept
2-4	0.20	1	0.4	2	Accept
4-24	0.10	4	0.1	5	Accept
24-48	0.10	3	0.1	5	Accept
48-96	0.20	0.3	0.6	2	Accept
96-212	0.20	0	1	2	Accept
212-500	0.20	0.03	0.9	2	Accept
0-500	0.05	3	0.01	3	Reject

D4 OXIDATION DATA for SAMPLES OXIDIZED at 1000°C

D4-1 Alloy 1 (3.5Si-2.0Al)

Table D4-1: Experimental data from ductile iron specimens oxidized for 500 hrs at 1000°C.

Cycle Time (hrs)	Trial 1 (mg/cm^2)	Trial 2 (mg/cm^2)	Trial 3 (mg/cm^2)
0	0	0	0
1	-0.7	-1.3	-1.3
2	-1.3	-1.7	-2.4
4	-2.9	-2.3	-2.9
24	5.3	6.4	7
48	20.4	15.9	18
96	37.9	27.1	33
212	45	36.4	39.7
500	52	40.9	45.6

Table D4-2: Statistical analysis of data in Table D3-1.

Cycle Time (hrs)	Mean (mg/cm^2)	Standard Deviation	Standard Error	95% Conf. Interval	99% Conf. Interval
0	0	0	0	0	0
1	-1	0.3	0.2	0.8	2
2	-1.8	0.58	0.33	1.4	3.3
4	-2.7	0.33	0.19	0.82	1.9
24	6.2	0.87	0.50	2.2	4.9
48	18	2.3	1.3	5.7	13
96	33	5.4	3.1	13	30
212	40	4.3	2.5	11	24
500	46	5.6	3.2	14	32

Table D4-3: Analysis of variance from 0 to 500 hrs.

Cycle Time (hours)	α	F	P-Value	$F_{critical}$	H_o
0-1	0.05	30	0.005	8	Reject
1-2	0.10	3	0.1	5	Accept
2-4	0.05	5.7	0.076	7.7	Accept
4-24	0.05	277	0.000076	7.7	Reject
24-48	0.05	73	0.0010	7.7	Reject
48-96	0.05	19	0.013	7.7	Reject
96-212	0.10	3.7	0.13	4.5	Accept
212-500	0.20	2.0	0.23	2.4	Accept
0-500	0.05	122	0	2.5	Reject

D4-2 Alloy 2 (3.5Si-3.0Al)

Table D4-4: Experimental data from ductile iron specimens oxidized for 500 hrs at 1000°C.

Cycle Time (hrs)	Trial 1 (mg/cm^2)	Trial 2 (mg/cm^2)	Trial 3 (mg/cm^2)
0	0	0	0
1	0	-0.6	-0.4
2	-0.7	-1.6	-1.6
4	-2.1	-2.1	-2.3
24	-4.9	-2.9	-3.3
48	-1.4	0.3	-0.6
96	0.1	8.9	5
212	5.3	15	10.6
500	11	17.3	16.6

Table D4-5: Statistical analysis of data in Table D4-4.

Cycle Time (hrs)	Mean (mg/cm^2)	Standard Deviation	Standard Error	95% Conf. Interval	99% Conf. Interval
0	0	0	0	0	0
1	-0.3	0.3	0.2	0.7	2
2	-1	0.5	0.3	1	3
4	-2.2	0.083	0.048	0.20	0.47
24	-3.7	1.1	0.61	2.6	5.9
48	-0.57	0.86	0.49	2.1	4.8
96	4.7	4.4	2.5	11	25
212	10	4.9	2.8	12	27
500	15	3.4	2.0	8.5	19

Table D4-6: Analysis of variance from 0 to 500 hrs.

Cycle Time (hours)	α	F	P-Value	$F_{critical}$	H_o
0-1	0.10	4	0.1	5	Reject
1-2	0.10	8	0.05	5	Reject
2-4	0.10	8	0.05	8	Reject
4-24	0.05	6.2	0.067	7.7	Accept
24-48	0.05	16	0.016	7.7	Reject
48-96	0.10	4.1	0.11	4.5	Accept
96-212	0.20	2.2	0.21	2.4	Accept
212-500	0.20	1.8	0.25	2.4	Accept
0-500	0.05	19	2.9E-07	2.5	Reject

D4-3 Alloy 3 (4.5Si-2.0Al)

Table D4-7: Experimental data from ductile iron specimens oxidized for 500 hrs at 1000°C.

Cycle Time (hrs)	Trial 1 (mg/cm^2)	Trial 2 (mg/cm^2)	Trial 3 (mg/cm^2)
0	0	0	0
1	0	-0.1	-0.1
2	-0.1	-0.4	-0.6
4	-1.1	-1.4	-1.4
24	-4.9	-4.6	-3.1
48	-5.3	-4.7	-1.7
96	-5.3	-4.9	0.4
212	-5	-1.7	1.9
500	-1	0.9	4.3

Table D4-8: Statistical analysis of data in Table D4-7.

Cycle Time (hrs)	Mean (mg/cm^2)	Standard Deviation	Standard Error	95% Conf. Interval	99% Conf. Interval
0	0	0	0	0	0
1	-0.1	0.08	0.05	0.2	0.5
2	-0.4	0.2	0.1	0.5	1
4	-1.3	0.17	0.095	0.41	0.93
24	-4.2	0.92	0.53	2.3	5.2
48	-3.9	1.9	1.1	4.8	11
96	-3.2	3.2	1.8	7.9	18
212	-1.6	3.4	2.0	8.5	19
500	1.4	2.7	1.5	6.6	15

Table D4-9: Analysis of variance from 0 to 500 hrs.

Cycle Time (hours)	α	F	P-Value	$F_{critical}$	H_o
0-1	0.05	4	0.1	8	Accept
1-2	0.10	4	0.1	5	Accept
2-4	0.05	28	0.006	8	Reject
4-24	0.05	26	0.0069	7.7	Reject
24-48	0.20	0.058	0.82	2.4	Accept
48-96	0.20	0.087	0.78	2.4	Accept
96-212	0.20	0.38	0.57	2.4	Accept
212-500	0.20	1.4	0.30	2.4	Accept
0-500	0.05	3.0	0.025	2.5	Reject

D4-4 Alloy 4 (4.5Si-3.0Al)

Table D4-10: Experimental data from ductile iron specimens oxidized for 500 hrs at 1000°C.

Cycle Time (hrs)	Trial 1 (mg/cm^2)	Trial 2 (mg/cm^2)	Trial 3 (mg/cm^2)
0	0	0	0
1	0	-0.1	0
2	0.1	-0.3	-0.1
4	-0.1	-0.9	-0.7
24	-3	-3.4	-2.4
48	-3.4	-4	-2.7
96	-3.3	-3.6	-2.3
212	-2.4	-1.9	0.1
500	-1	-0.6	1.9

Table D4-11: Statistical analysis of data in Table D4-10.

Cycle Time (hrs)	Mean (mg/cm^2)	Standard Deviation	Standard Error	95% Conf. Interval	99% Conf. Interval
0	0	0	0	0	0
1	-0.05	0.08	0.05	0.2	0.5
2	-0.1	0.2	0.1	0.5	1.2
4	-0.6	0.4	0.2	0.9	2
24	-3.0	0.50	0.29	1.2	2.8
48	-3.4	0.64	0.37	1.6	3.6
96	-3.0	0.68	0.39	1.7	3.8
212	-1	1	0.8	3	8
500	0.1	2	0.9	4	9

Table D4-12: Analysis of variance from 0 to 500 hrs.

Cycle Time (hours)	α	F	P-Value	$F_{critical}$	H_o
0-1	0.20	1	0.4	2	Accept
1-2	0.20	0.3	0.6	2	Accept
2-4	0.10	3	0.2	5	Accept
4-24	0.05	39	0.003	8	Reject
24-48	0.20	0.83	0.41	2.4	Accept
48-96	0.20	0.30	0.61	2.4	Accept
96-212	0.10	4	0.1	5	Accept
212-500	0.20	2	0.3	2	Accept
0-500	0.05	10	0.00002	3	Reject

Appendix **E**

Representation of Total Weight Gained

The total weight gain of specimens was determined using the following expression:

$$Total\ Weight\ Gain = |A + B| + |B + C| \qquad \text{Equation E-1}$$

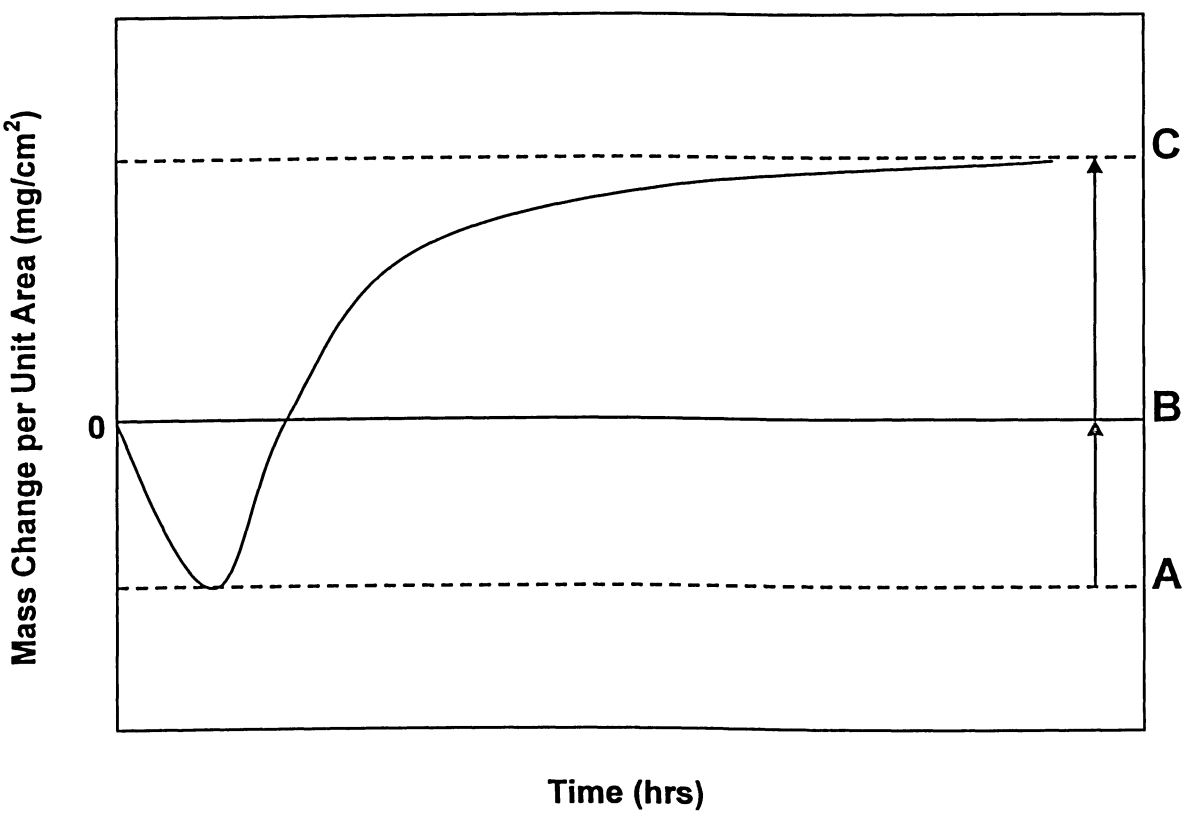

Figure E-1: Schematic of weight gain calculations.